Contrasting deformation styles in the Domeyko Fault System, northern Chile.

Thesis submitted in accordance with the requirements of the University of Liverpool for the Degree of Doctor of Philosophy by Susie McElderry

(August 1998)

Contrasting deformation styles in the Domeyko Fault System, Northern Chile

Susie M^cElderry (University of Liverpool)

Subduction of an oceanic plate under the Pacific margin of South America has been prevalent since Jurassic times. Magmatic and deformation centres have migrated eastward since subduction began. Northern Chile houses two north-south trench linked strike-slip fault systems, the Atacama Fault Zone and the Domeyko Fault System (DFS). The DFS lies within the Chilean Precordillera from 21° to 28°S. Lateral movement began on the DFS in the Eocene. The DFS can be divided into three segments which have apparently undergone differing deformation histories. This study has focused on the central segment of the DFS, to determine fault kinematics and to establish a relative chronology of deformation. Observations have been made in more detail than previous investigations and have been used to infer the deformation history. Shallow level faulting has resulted in heavily fractured zones with occasional slickenline surfaces. It is difficult to infer kinematics of faulting from these. Much effort has been expended in developing techniques to analyse fracture patterns associated with brittle faulting under conditions of plane strain, simple shear.

A novel approach of analysing the shapes of clasts of rock defined by secondary fractures within a fault zone has been used. The clasts approximate ellipses when viewed in 2 dimensions. Combining ellipse orientation and aspect ratio from mutually perpendicular sections through the fault zone allowed calculation of an ellipsoid representative of the clasts of rock in 3 dimensions. Independent determination of the fault kinematics using stratigraphic relationships across the fault, fracture distribution, incremental strain axes and palaeomagnetic analysis has allowed evaluation of the new technique. The shapes of rock clasts are found to be related to the kinematics of the fault system. Up to a critical stage of development of the fault zone the axes of the rock clasts parallel the slip direction, intermediate strain axis and pole to the boundary faults. Which rock clast axis parallels which structural feature depends upon the spacing and curvature of fractures and stage of development of the fault zone. Analysis of the shapes of rock clasts defined by fractures can avoid bias of the data set towards thicker fractures or against irregular fractures, which can occur when measuring fracture orientations directly. The degree of development of the fault zone varies laterally along the fault over short distances. This causes the shape fabric of the rock clasts to change, so predictions of connectivity within a fault zone are limited.

The history of the central segment of the DFS determined from this study is found to concur with earlier workers. The complementary deformation histories produced from two scales of observation verifies the reliability of the chronology. Lateral movements along the DFS are thought to begin in the Eocene with a sinistral transpressive event which occurred along all three segments of the DFS. En echelon folds, east and west verging thrusts and clockwise rotations associated with sinistral faulting along the master fault of the segment are documented. Later, in the Oligocene, dextral faulting occurred. Large clockwise palaeomagnetic rotations, determined from Palaeozoic samples beside the master fault, indicate sinistral displacements have been larger than dextral displacements. It is inferred that only one episode of large lateral transport occurred. This is the Eocene sinistral event. Normal faulting associated with sinistral displacements along the western side of the system are documented. This later sinistral faulting has not been documented before in the central segment of the DFS. After Oligocene age dextral faulting, the three segments of the DFS underwent separate deformation histories, as the main Andean deformation foci had moved eastward.

Table of Contents

Acknowledgements

Chapter 1	Introduction and Regional Geology	1
1.1	Pre-Andean History	3
1.2	The Andean Cycle	6
1.3	History of the Domeyko Fault System	10
1.4	Aims of this Study	12
Chapter 2	Structural Analysis of Folds and Faults	13
2.1	Deformation within Jurassic Sediments	13
2.2	Analysis of Brittle Fault Data	22
2.3	Fault Data from Agua el oro	26
2.4	Summary of Chapter 2	28
Chapter 3	Palaeomagnetism	29
3.1	Sampling, Treatment and Analysis	30
3.2	Results	32
3.3	Individual Site Results	33
	Significance of sites	38
Chapter 4	Detailed Fault Analysis	40
4.1	Description of the Fault Zone	41
4.2	Kinematic Analysis of the Slip Surfaces	47
4.3	Argon Dating	53
4.4	Palaeomagnetic Analysis	60
4.5	Model of the Fault Zone	63
Chapter 5	Analysis of the Localised Fault Zone	66
5.1	Fracture Analysis	66
5.2	Methodology	69
5.3	Results	71
5.4	Significance of the Clast Shapes	73
5.5	Comparison of Results with Model	76
5.6	Discussion	79
5.7	Conclusions	84
Chapter 6	Regional Synthesis	88
Conclusions		93

References
Appendices
Foldouts 2.1, 2.2 and 4.1

ACKNOWLEDGMENTS

A debt of gratitude is owing to Dave Prior and Graham Potts, who have supervised me through the enthusiastic, disillusioned, confused and re-enthused stages of my research. Steve Flint has generously provided support, logistical expertise, advice and even a computer when mine failed days before my deadline! Guillermo Chong of Universidad Católica del Norte, shared his wide and detailed knowledge of the Domeyko, directing me towards useful outcrops and identifying numerous fossils. For his hospitality I am also grateful.

Palaeomagnetic analyses were undertaken in the Geomagnetic Laboratories, Liverpool University. John Piper, John Shaw, Steve Openshaw all deserve thanks for the invaluable advice, patience and constructive criticism they provided. Argon analyses were carried out at SURRC in East Kilbride, with Malcolm Pringle at the helm. Discussions with Steve Reddy helped with the interpretation of the results.

Whilst in Chile RTZ provided logistical support. In particular Dave Andrews and Alasdaire Pope, who shared their structural knowledge and provided satellite images, were very helpful. I am grateful also to Oswaldo, who patiently found and supplied whatever field equipment I lacked.

In Chile, John Ardill proved an excellent guide to Antofagasta and the desert - for an unforgettable first field season and two years of office japes I'm grateful (?!). For all their carrying, walking, cooking and drinking I'd like to thank my field assistants: Malcolm who was driven to cycle the length of Chile after the experience; Matt who also felt compelled to remain in Chile; and Kev who returned as the Strat-Cowboy and continued to support my research by salvaging files from my ailing computer.

Back in the 'Pool Caroline, Rachel and Pam shared a house with me and were still my friends. Rachel has provided solidarity in the darker stages of writing-up. Mikee and MarkR provided many an absurd conversation and Fran, Andy and John supplied quality office banter. Pete and Martin who have taken on the mantle of office inmates and endured my writing-up-phase deserve recognition. To Pat who has coped remarkably well with 7 years of anecdotes and even supplied his own - watch out, there's more to come. To everyone else - Sophie, Nick, MJD, Mooresy, Anne, Sam, Paul, Matt, Maria and Carlos....thanks! Marie and Fawzy deserve a special mention for all the cups of tea, chocolate bars and cash forwards - as well as adding a wealth of character to the department. Helen and Kay have fulfilled the vital role of friends who are not interested in geology but in enjoying life.

My Mum, Dad, Thomas and William have all coped with a daughter/sister with an absent sense of humour for a year and still been wonderful to me. Thanks also to Jenny who has kept me laughing and in touch with an alternative reality.

And Thomas.....à la folie!

When the Queen, over the
magnetic lines of force
on Faraday's rough table, asked
And what use is it?
Faraday replied,
gazing lower than her
lace collar:

And what use, Ma'am is a child?

It was a high point of science
in history, because

modern mankind is divided into those
who understand gravitation and those
who understand braces,

we either ask about everything,
or we ask about nothing,
in which case the universe originated
in the Square of the Republic
through the condensation of
Saint Nicholas' deodorant.

Magnetism, by Miroslav Holub.

We shall not cease from exploration
And the end of all our exploring
Will be to arrive where we started
And know the place for the first time.

Little Gidding, T S Eliot.

Chapter 1

Introduction and Regional Geology

CHAPTER 1 INTRODUCTION AND REGIONAL GEOLOGY

The Chilean margin has long been recognised as an active plate boundary, where the South American plate is overriding the subducting Pacific plate. This situation has been prevalent since Jurassic times (Mpodozis and Ramos, 1990). In Northern Chile two strike slip fault systems have been designated trench linked strike slip fault systems sensu Woodcock (1986), The Atacama Fault Zone and the Domeyko Fault System, Figure 1.1. At 25°S a west-east transect across Chile can be divided into north-south trending morphotectonic units, Figure 1.2. Along the Pacific margin the Coastal Cordillera rises to a maximum height of 3000m, across a maximum width of 40 km. The Coastal Cordillera is bound to the west by a cliff up to 500m high, which locally reaches altitudes of 6000m above the bottom of the trench. To the east the Coastal Cordillera descends gradually to Longitudinal or Central Valley, which has a gentle west dipping slope and an average width of 80 km. This basin is either a well developed graben (Pampa del Tamarugal) or is interrupted by longitudinal and transversal ranges. The Chilean Precordillera, or Domeyko Range, to the east of Longitudinal Valley, has a width of 25 km and a maximum height of 4150m. To the east the Pre-Andean depression is represented by the Salar de Punta Negra and the surrounding drainage basin. A Tertiary volcanic cover with an altitude of 4000m a.s.l. is recognised immediately before the High Cordillera, also referred to as the Western Cordillera. To the east of the High Cordillera the Altiplano (or Puna), Eastern Cordillera and sub-Andean ranges are found. The morphotectonic units of the North Chilean Andes extend to Peru, Bolivia and Argentina, resulting in more than one name for the same feature. In this study, the Domeyko or Precordillera refers to the mountain range west of the High Andes and the Puna is equivalent to the Altiplano.

These fault systems are significant on two levels. A detailed history of the fault systems will improve understanding of continental margin deformation. The fault systems are also associated with significant Cu, Au and Ag mineralization. The study area of this project is within a southern portion of the central segment of one of these fault systems, The Domeyko Fault System (DFS), also referred to as the West Fissure Fault System, after the main strike-slip fault in the northern segment, Falla Oeste, and Precordilleran Fault System (Reutter et al, 1991). The Domeyko Range is the name of the Chilean Precordillera in Northern Chile. Different segments of the DFS have been studied to different levels. Many workers have tried to relate the kinematics of the fault system directly to relative plate motion vectors. The local deformation sequence and how it relates to the larger scale deformation across the foreland needs to be understood, before such correlations can be proposed with any degree of confidence. This project aims to understand the local deformation within the DFS.

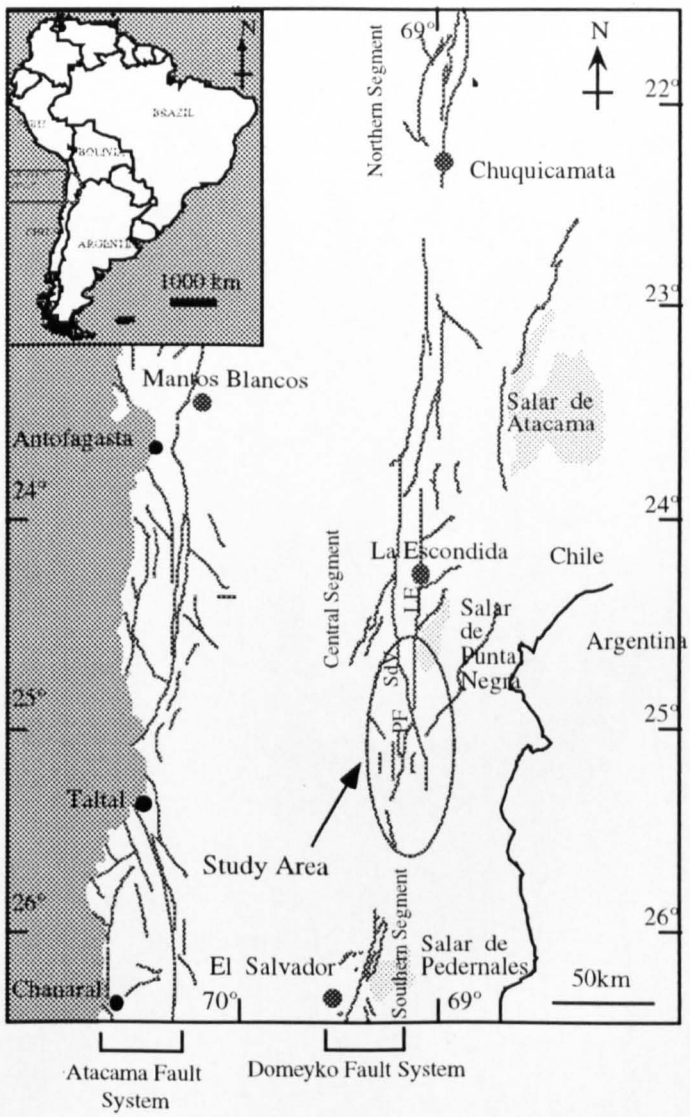

Figure 1.1 (modified from Prinz et al 1994), showing location of study area and fault systems. The larger mines are shown along the fault systems, towns Taltal and Antofagasta are at the coast.

PT: Profeta Thrust
LE: La Escondida Fault
SdV: Sierra de Varas strike-slip fault.

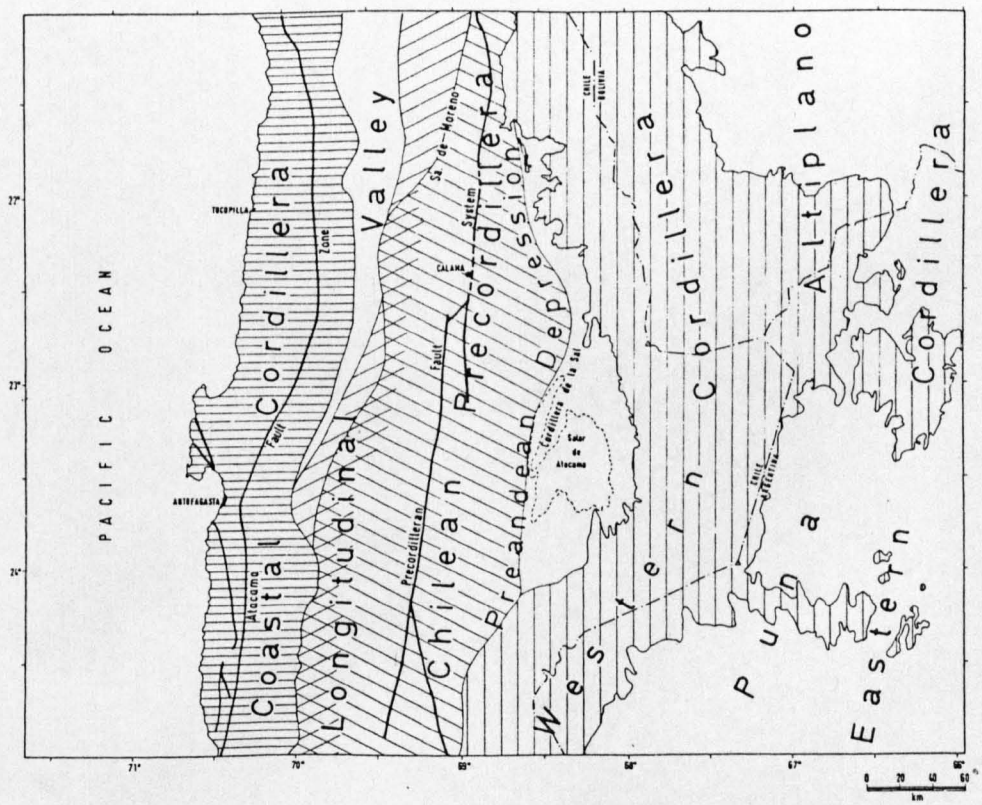

Figure 1.2 Morphotectonic units of the North Chilean Andes, Reutter et al, 1994.

The following sections provide a brief over view of the tectonics of Chile, followed by a history of the DFS.

1.1 Pre-Andean history

1.2 The Andean Cycle

1.3 History of the DFS

1.4 Aims of this study.

1.1 Pre-Andean History

The Pre-Andean history of Chile is relevant to this study as it establishes whether any structural grain existed within the crust, which may have constrained the location and or orientation of Andean structures.

In the Late Proterozoic - Early Cambrian, present day South America was part of an ancestral supercontinent comprising Gondwana, Laurentia, Baltica and Siberia (Piper, 1976; 1983; Ziegler et al, 1981; Morel and Irving, 1978), Figure 1.1.1. This has been recognised on the basis of faunal, stratigraphic and glacial evidence and supported by correlation between Precambrian structures and rift-related sediments(Gallagher, 1989). Between 625 and 555 Ma break up of the supercontinent occurred as the Iapetus ocean opened to the western margin of proto-South America (Bond et al, 1984).

Nance et al (1988) built on the Wilson cycle by which continents rift to form ocean basins and later close to reassemble the continents. They concluded that the processes of plate tectonics are governed by a regular, cyclic process, noting that the margins of North Atlantic have undergone a series of Wilson cycles during the past billion years; the regions bordering the Pacific have apparently undergone none. Scotese and McKerrow (1990) suggested from palaeobiology and palaeoclimatology that the Upper Proterozoic supercontinent was composed of Laurentia, Baltica and Siberia which disintegrated as Gondwana formed, about 600 Ma. They support the interpretation of Nance et al (1988), stating that the western margin of South America has always been adjacent to oceanic crust, hence not having undergone a complete Wilson Cycle.

Gallagher (1989), Mpodozis and Ramos (1990), Dalziel et al (1994) and Bahlberg (1987) are some of the proponents of a model involving Palaeozoic collisions between proto - South America and North-America and microcontinents. The latter model may better explain the structural grain within the Andes.

Mpodozis and Ramos (1990) recognise the Famatinian Cycle in the Early Palaeozoic, which involves subduction, accretion of microcontinents and magmatic activity.

Famatinian Cycle

Mpodozis and Ramos (1990) define the SW margin of a continent (Gondwana) in Early Palaeozoic to lie at the western side of the present day Sierra Pampeanas in NW Argentina. The Sierra Pampeanas have a north-south trend. The current Precordillera was a carbonate platform lying eastward of the ocean, Figure 1.1.2. This is supported by Breitkreuz and Zeil (1984), Cobbing (1985) and Vicente (1985). They cite the

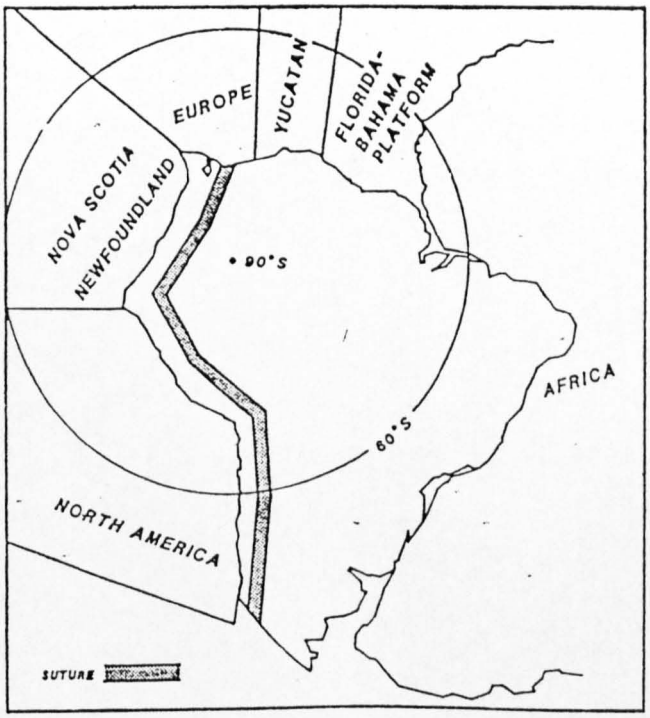

Figure 1.11 Hypothetical plate tectonic reconstruction for 600 Ma. Schematic showing continents adjacent to South America. Taken from Gallagher 1989.

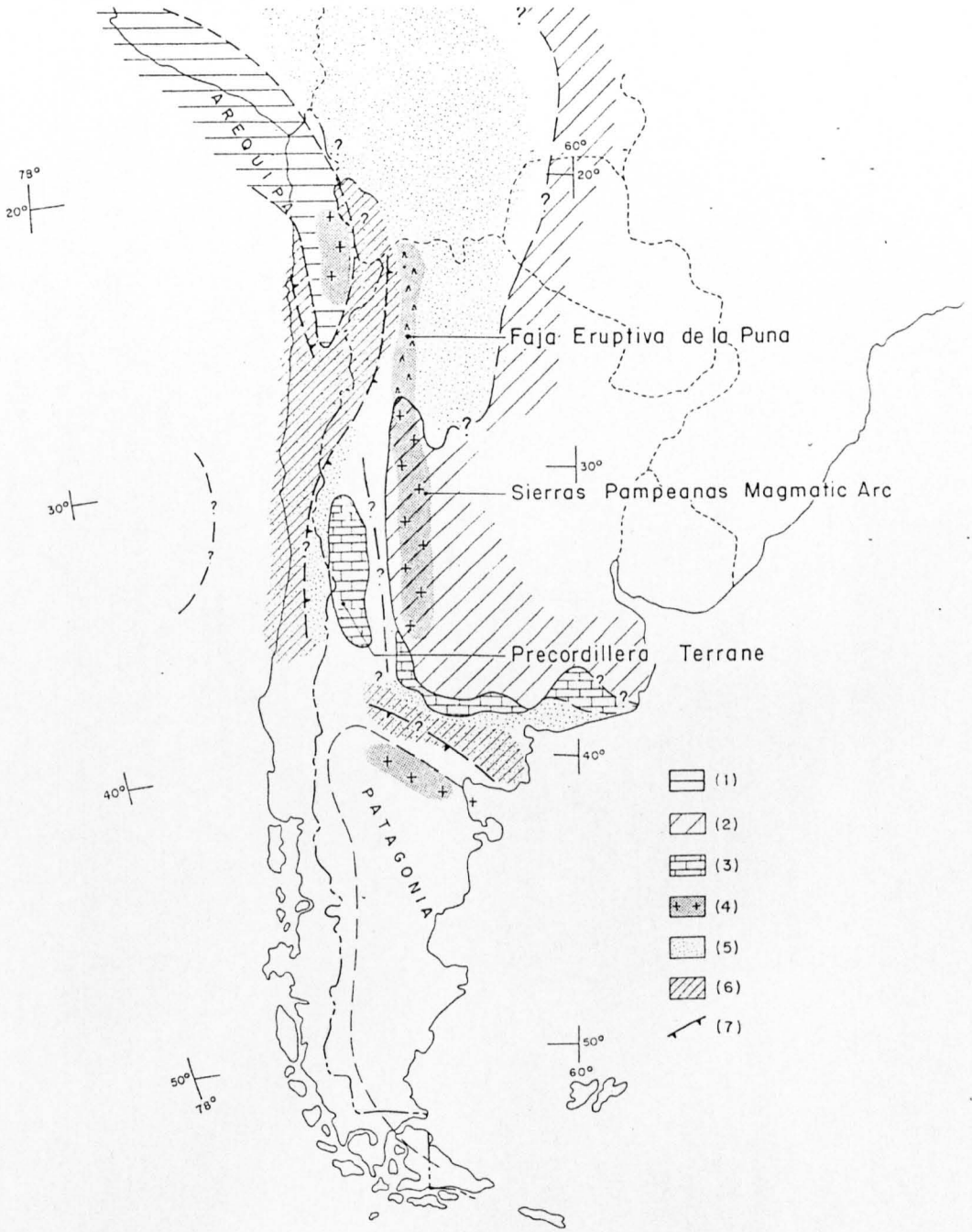

Figure 1.1.2 Cambrian-Ordovician palaeogeography: (1) Precambrain basement of the Arequipa-Belen-Antofalla block; (2) emerged land areas along the ancestral South American continental margin; (3) carbonate platforms; (4) magmatic "arcs"; (5) marine terriginous sediments accumulated over a continental basement; (6) sediments deposited on "oceanic" basement; and (7) axis of palaeotrench. Taken from Mpodozis and Ramos, 1990.

presence of Precambrian granitic rocks from the Proterozoic - Archean craton up to the western limit of the eastern Cordillera, Puna and Altiplano.

An oceanic complex has been recognised in the Pampean ranges, Argentine Puna and North Patagonian Massif (Kay, Ramos and Kay, 1984; Ramos et al, 1986). This belt of Precambrian - Early Palaeozoic mafic - ultramafic high grade metamorphic rocks are taken as evidence of a tectonothermal event. This region lies between two calc-alkaline magmatic arcs, both with a north-south trend, one in the Puna, thè Faja Eruptiva, and one in the Arequipa - Belén - Antofalla block. The Arequipa - Belén - Antofalla block, along with isolated blocks in the region between the present Coastal Cordillera and Western Cordillera are similar to the basement blocks of the Proterozoic Archean craton found further east (Thornburg and Kulm, 1981, Breitkreutz and Zeil, 1984 and Cobbing, 1985). Mpodozis and Ramos interpret this oceanic complex to have been accreted between the "South American" continent and microcontinents during subduction along an easterly dipping subduction zone which consumed the ocean basin that lay between the land masses. The eastward dipping subduction boundary is supported by identification of a deep east-dipping structure beneath the present day Sierra Pampeanas on seismic reflection profiles, by Cominguez and Ramos (1991). Dalla-Salda et al (1992) interpret the accreted material to reflect the docking of Laurentia beside Gondwana. In this interpretation the Arequipa-Belén-Antofalla block was part of Laurentia. The magmatic arcs were deformed in the Oclóyic orogen at the Ordovician - Silurian boundary as magmatic activity ceased (Turner and Méndez, 1979; Kay, Ramos and Kay, 1984; Ramos et al , 1986). The accretion of the suspect terranes (wherever their origin) is assumed to be contemporaneous with the Oclóyic phase. This collision is marked by a climax in volcanic and plutonic activity, with final emplacement of granites along the Faja Eruptiva and uplift of the Arco Puneño topographic high (Coira et al, 1982). The Faja Eruptiva rocks are characterised by north-south striking sinistral sub vertical shear zones (Bahlberg, 1994), possibly in response to oblique subduction to the south east.

Mid - Late Palaeozoic

Two marine passive margin basins had formed by Early Devonian times (Bahlberg, 1993), Figure 1.1.3, following continued rifting along lines of pre-existing weakness. Silurian - Carboniferous deposition occurred in two centres, separated by the Arco Puneño topographic high. The eastern depocentre records mid-Silurian to mid-Devonian sediments in the region of the eastern Cordillera and sub-Andean ranges (Coira et al, 1982). The western depocentre records a marine basin which deepened to the west (Bahlberg and Breitkreuz, 1991). There are no Silurian or Devonian sediments in the Puna, indicating it was a topographic high. The eastern basin comprises more than 2500m of shallow marine shales and mudstones. The western basin comprises shallow marine sediments at Sierra Almeida in the Chilean Precordillera and deep marine turbidites at the site of the present Coastal Cordillera (Bahlberg and Breitkreuz, 1991). The

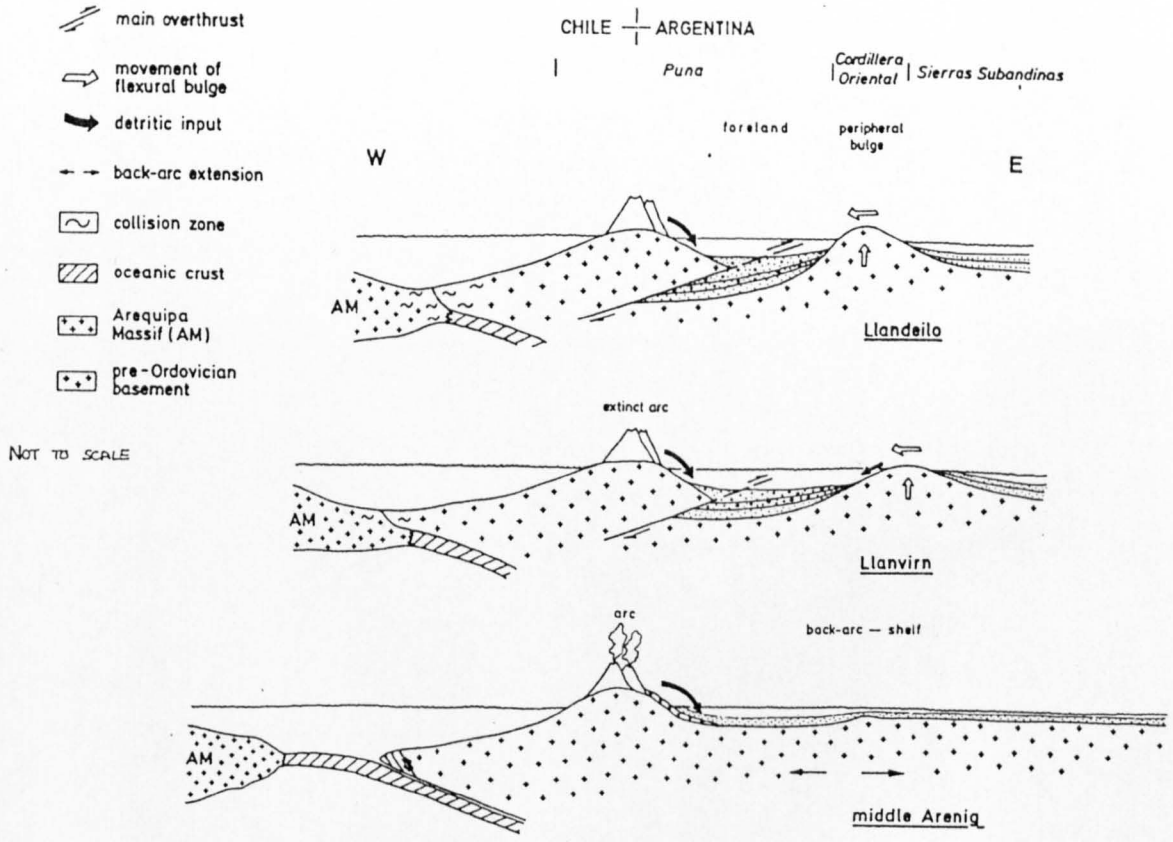

Figure 1.1.3 Hypothetical cross section depicting tectonic evolution of the Gondwanaland margin in Northwestern Argentina and Northern Chile during the Ordivician (Bahlberg, 1991)

two basins have been interpreted as representing a quiescent phase in tectonic activity. The sediments of both basins are considered autochthonous in position (Bahlberg and Breitkreuz, 1993).

During the early Late Carboniferous I and S type granitoids were emplaced in different segments of the Pre, High and Coastal Cordilleras. These granitoids have been dated as mid Permian (for example, the Cifuncho Complex 278 +/- 11 Ma, Brook et al 1986; granitoids in study at ~S25° have ages of 240- 290 Ma, Hervé et al 1991). Bahlberg et al (1987) identified a north-south chain of volcanic islands in the Pre-and High Cordilleras. The significance of the granitoids is disputed. The granitoids are calc-alkaline, tonalitic to granodioritic in composition. They are interpreted as either crustally contaminated mantle derived melts (Brown, 1991) and used to infer a subduction zone to the west (Bell 1982, 1987; Brown 1991); or as evidence of anatexis during crustal extension (Zeil, 1979).

A general westward migration of orogenic zones identified by Bahlberg (1987) corresponds with westward migration of magmatism (Andriessen and Reutter, 1994). Assuming a subduction origin for the magmas, Breitkreutz and Zeil (1994) offer an explanation as to why the subduction zone shifted westward. They suggest the continental insulation of the supercontinent caused an enhanced mantle convection which as well as initiating intracontinental rifting, was able to deflect the angle of dip of the downgoing slab, increasing it. This resulted in propagation of the magmatic arc westward.

Several phases of late Palaeozoic deformation are recognised, the most significant is the mid Permian San Rafael compressional phase, associated with the accretion of the Patagonian Massif, which caused unconformities in sedimentary basins of Chile.

A radically different Palaeozoic history has been concluded by Damm et al (1994). Isotopic and geochemical analyses on basement areas of northern Chile from 580 - 270 Ma identified only anorogenic and synorogenic intrusives. The absence of I-type intrusives is taken to indicate a history of an ensialic, autochthonous passive margin for western South America, with repeated opening and closing of intracontinental basins with a north-south trend.

For the purposes of this study, the relative merits of the different models are not assessed as all models produce a proto-Andean margin with a north-south structural grain. Ramos (1994) concludes that for latitudes south of the study area at 30° - 33°S, the present morphotectonic units of the Andes are divided as dictated by the Pre-Andean structural grain. All models also concur that the Pre-Andean history involved extension and compression occurring cyclically, which was manifest in opening and closing of north-south striking basins. To distinguish whether this occurred as a result of plate collision or simply a change in the stress regime prompted by plate motions without collision is not necessary here.

1.2 The Andean Cycle

The Andean history of the Southern and Central Andes is better defined and generally less controversial than the Pre-Andean history. Numerous review papers are in existence (for example, Mpodozis and Ramos, 1990; Coira et al, 1982; Scheuber et al, 1994). Coira et al divided the Andean cycle into an Early Period, from Triassic to mid-Cretaceous, and a Later Period, from Late Cretaceous to Recent. The Early Period is characterised by an arc - back-arc basin pair, whilst the Later Period is characterised by a single eastward migrating arc.

Early Period (Triassic to Mid Cretaceous)

By the Late Palaeozoic, accretion had ended in Northern Chile. By the earliest Mesozoic the magmatic arc had shifted westward to the present Coastal Cordillera (Mpodozis and Ramos, 1990). Brown (1991) proposed that the Coastal and Altiplano Permo-Triassic intrusives could have been part of the same magmatic arc. Continued extension between Triassic and Early Cretaceous resulted in the separation observed. Triassic coastal intrusives however, are not emplaced at extensional jogs but dilate low angle metasedimentary layering (Grocott and Wilson, 1997). Figure 1.2.1 gives a summary of the Andean cycle.

The Mid Jurassic magmatic arc was sited in the present Coastal Cordillera, Figure 1.2. The La Negra Formation extends over 1000 km from Arica to Chañaral (~ latitude S20° - S26°). The La Negra Fm is made up of subsaturated andesites, andesites and olivine basalts (Garcia, 1967) and overlies lower Lias marine sediments. McNutt et al (1975) concluded that these magmas were the product of an early stage in subduction, where the down-going slab is still at shallow levels. The ages of associated intrusions in the magmatic arc define a general trend of younging towards the east (Quirt, 1972; Zentilli, 1974; Ulriksen, 1979; Wilson, 1996). Distinct phases of volcanic and magmatic activity have been identified by Grocott et al (1994) and Dallmeyer et al (1996). They suggest that activity of the magmatic arc fault system was contemporaneous with plutonism, while volcanics were deposited in periods of quiescence. Maksaev (1978) constrained the activity of La Negra arc to between 190 - 115 Ma, Scheuber et al (1994) cite the activity to have occurred between 200 - 90 Ma.

The magmatic arc fault system, the Atacama Fault Zone extends for over 1000 km between Iquique and La Serena (20°S - 30°S) and accommodated sinistral deformation during the Cretaceous (Arabasz, 1971; Naranjo and Puig, 1984; Brown et al, 1993; Dallmeyer et al, 1996). In the El Salado segment north-south mylonites bounding Upper Jurassic plutons (for example, Las Animas) indicate the pluton was emplaced while extensional, east side down, faulting occurred (Dallmeyer et al 1996). Early Cretaceous plutons (Las Tazas, Remolino and La Barracha) record the switch from extensional to transtensional tectonics at 130 Ma

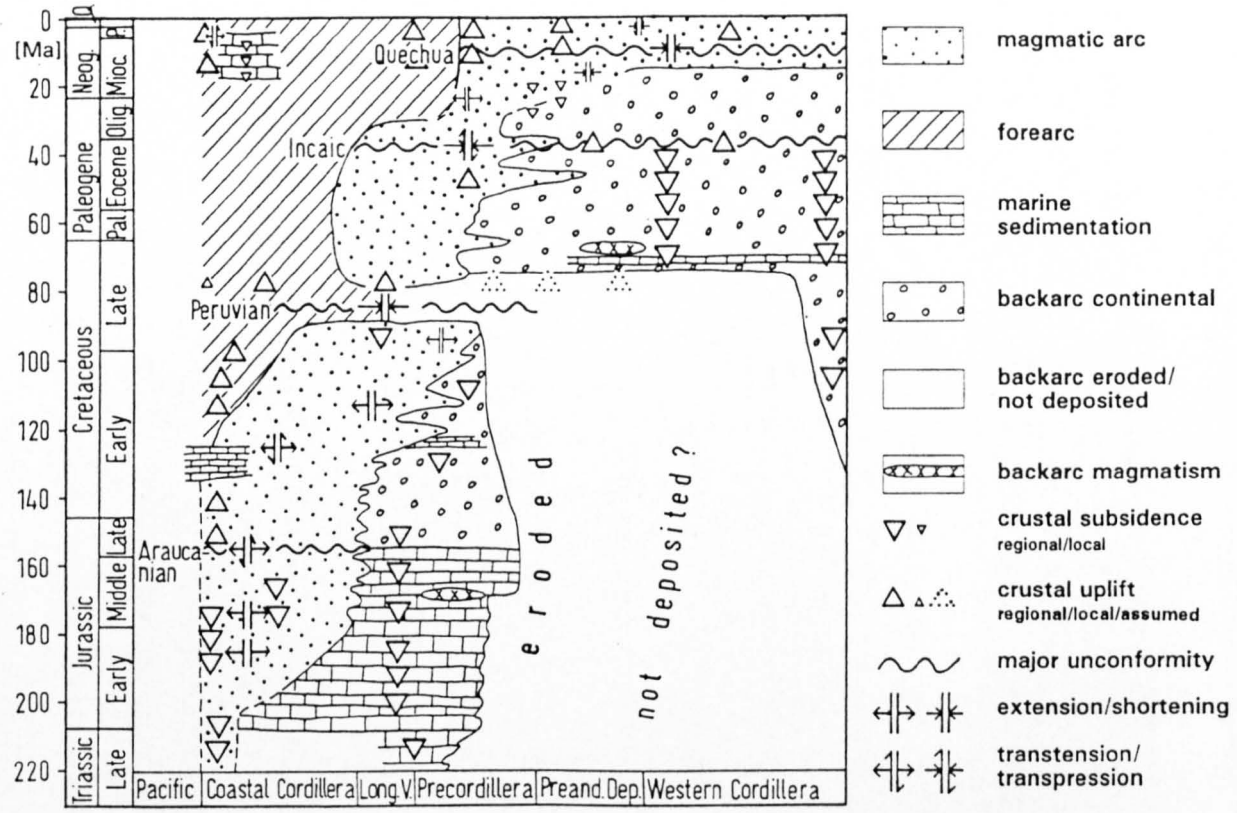

Figure 1.2.1 Major aspects of the geological and structural development of the North Chilean Andes since early Jurassic (Reutter et al, 1994).

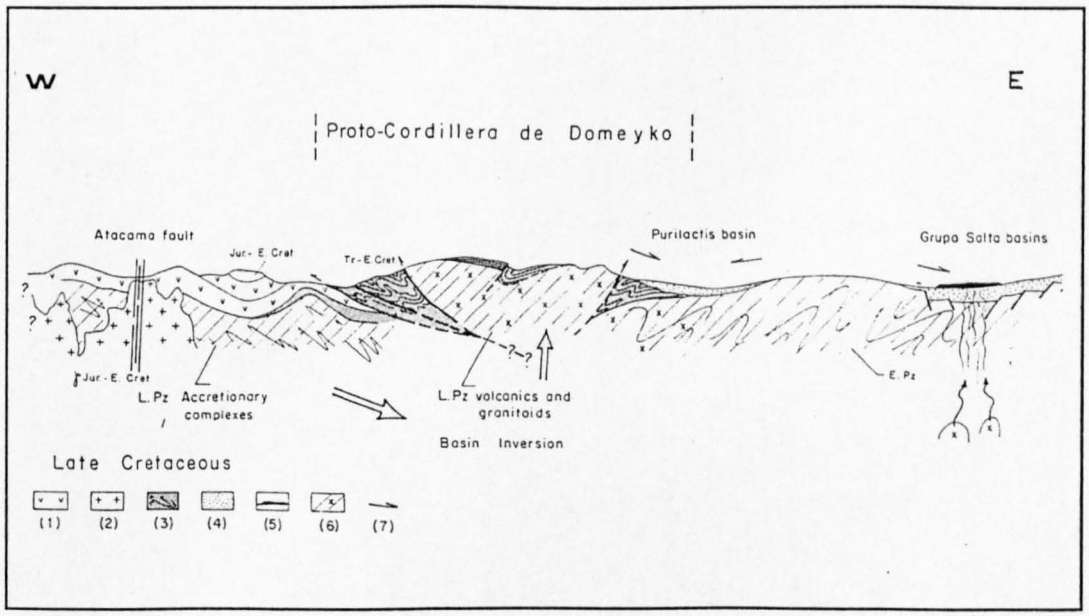

Figure 1.2.2 Cross section at latitude 25°S immediately after middle Cretaceous deformation: (1) lavas from the extinct La Negra arc; (2) Jurassic-Early Cretaceous granitoids; (3) deformed sediments of the Tarapaca back-arc basin; (4) Late Cretaceous red beds; (5) alkaline basalts; (6) uplifted sialic floor of the Tarapaca basin to form the Proto Cordillera Domeyko (PCD); and (7) provenance directions of the Late Cretaceous sediments. Large arrows indicate direction of middle Cretaceous uplift in the PCD and the east directed underthrust of the La Negra arc below

(Dallmeyer et al, 1996; Wilson, 1996). In the Antofagasta segment (further north) the AFZ has undergone sinistral movements since 144 Ma (Scheuber et al, 1995). Significant uplift and cooling of the magmatic arc occurred between 144 and 138 Ma (Maksaev, 1990; Scheuber et al, 1995). Extension continued at this time, as evidenced by the Sierra Fraga extensional detachment complex (Mpodozis and Allmendinger, 1993).

The back arc had developed into a broad marine basin, bound to the west by the active arc and extending to the Palaeozoic foreland in the east, Figure 1.2.1. Thick calcareous Jurassic sequences (Profeta Formation in the study area, Chong 1977) were deposited across the Longitudinal Valley and the Precordillera in the Tarapaca basin. The north-south basin opened from the south in the Hettangian (Ardill, 1996) and extended from at least S26° to S21° at its peak in the Bajocian (Prinz et al 1994). From isopach maps, Prinz et al (1994) identified tectonic activity to cause sudden deepening of the basin above the proto-Domeyko Range. Resolution is not high enough to determine the strike of the faults. In Oxfordian times the sea began a southward retreat from the north and by the end of Tithonian times had retreated from the south also. Ardill (1996) identified the oceanic basin as forming in response to a global sea level rise coupled with regional tectonics. Ardill distinguished tectonically driven sea level falls in the Bajocian, Late Oxfordian and Valanginian times. These sea level falls are related to rifting of Gondwana, not simply local subduction dynamics (although a change in subduction dynamics may have been prompted by the Gondwana tectonism). By the early Cretaceous continental red beds were deposited in the back arc region interbedded with occasional lava flows (Ardill, 1996).

Foreland magmatism east of the back-arc basin (in the Puna) occurred in the uppermost Jurassic and early Cretaceous. High $^{87}Sr/^{86}Sr$ ratios have been cited to suggest crustal anatexis (McNutt et al, 1975 Coira et al, 1982).

Later Period (Mid Cretaceous to Recent)

Mid Cretaceous orogenesis saw the end of the arc - back-arc basin pair, as the Andean margin of Chile became contractional. Magmatic activity in the La Negra arc ceased. A tectonic event, the Peruvain Phase (Larson and Pitman, 1972; Ramos and Ramos, 1979) occurred along the length of the Andean domain. The Peruvian Phase coincided with an increased spreading rate between the South American and African plates at circa 100 Ma.

Inversion of the back arc basin resulted in uplift of the ensialic floor of the Tarapaca basin onto a Proto-Cordillera de Domeyko (PCD) (Mpodozis and Ramos, 1990). This provided the main topographic high between the coast and the present day Puna, Figure 1.2.2. To the east of the PCD, deposition of red beds,

the Tonel Formation of the Purilactis Group, (Marinovic and Lahsen, 1984) formed from erosion of the PCD high. The AFZ was reactivated as a transpressive structure in its southern segment (Thiele and Pincheira, 1987). Salfity (1980) has recognised three phases of alkaline volcanics interbedded with synrift sediments of the Argentine foreland; 130 - 100 Ma, 80 - 75Ma and 60 - 65Ma. $^{87}Sr/^{86}Sr$ ratios again indicate crustal anatexis. Back arc extension is thought to have occurred from the Maastrichtian to Lower Palaeocene (Marquillas and Salfity, 1988).

After the Peruvian Phase, the magmatic arc was centred in the present day Longitudinal Valley, Figure 1.2.3. Sporadic outcrops south of S21° of the Icanche Fm, Chile - Alemania Fm (Chong, 1977) and Augusta Victoria Fm (Garcia, 1967) record this magmatism as calc-alkaline volcanics interfingered with continental sediments. K/Ar dating yields ages of 72 - 39.9 Ma (Boric, Diaz and Maksaev, 1985). Extensional tectonics as evidenced by caldera complexes occurred between 58 - 53 Ma (Mpodozis and Allmendinger, 1989; Cornejo et al, 1997).

The Late Eocene, Incaic event (Steinmann, 1929) occurred as the magmatism in the Longitudinal Valley ended. Arc-normal shortening and arc-parallel transcurrent motions characterise this event, both of which are present in the Domeyko Range. En echelon folding of Mesozoic sediments (Profeta Fm in study area) and transcurrent motions along the DFS are evident (Scheuber et al 1994). Back arc regions were also subject to strong folding and reverse faulting (Scheuber et al 1994), which must have contributed to an important crustal thickening of the area (Reutter et al, 1988). Coarse deposits of the synchronous Purilactis Formation of the Purilactis Group, eastwards of the PCD, indicate substantial uplift of the Domeyko Range (Charrier and Reutter, 1994). Oblique subduction to the northeast is thought to have caused the transcurrent deformation in the Andean margin (Noblet et al, 1996). The detailed history of the DFS is discussed in section 1.3.

The Late Eocene to Early Oligocene magmatic arc was located in the Chilean Precordillera (Scheuber et al, 1994). This arc was relatively quiescent when compared with preceding arcs. The magmatic activity was associated with the emplacement of large copper porphyry copper deposits towards the end of a period of rapid convergence (Davidson and Mpodozis, 1991).

The interarc stage saw relaxation of thickened crust. Formation of the Pre Andean depression, (the Salar de Atacama, Punta Negra and Rio Loa depression, for example, Reutter et al, 1991) are evidenced as crustal thinning (Scheuber et al, 1994). Oligocene uplift of Eocene-Oligocene and older plutons (Maksaev, 1990) are consistent with this, if uplift is caused by active erosion. An Andean-wide period of peneplain formation occurred (the exact timing is poorly constrained, Chong 1977).

In the Late Oligocene - Early Miocene the magmatic arc moved to its present location, Figure 1.2.3. North of S22° explosive caldera-type rhyolitic volcanism is dominant, while south of S24° andesitic stratovolcanoes dominate. Isotope ages indicate igneous activity since 28 Ma, with an increase in activity at 17 Ma and a further increase at 10 Ma (Scheuber et al, 1994). The Quechua Phase (Charrier and Vicente, 1970) caused folding of Eocene and Oligocene strata in the Puna. There is evidence of the event in the Western Cordillera, but the compressional deformation front had migrated eastward of the arc and there is significant folding and east vergent thrusting of sediments in the Puna. The first Quechua phase caused an estimated 35 - 70 km of horizontal shortening in the High Cordillera, during waning volcanic activity: the two later Quechuan Phases involved 90 - 130 km of horizontal shortening (Allmendinger et al, 1990). Along the continental margin major uplift occurred (Coira et al, 1982) The Quechua diastrophism is though to relate to the termination of sea floor spreading in the Galapagos Ridge and initiation of spreading along the East Pacific Rise. This resulted in an increased convergence rate and a change from margin-oblique to margin-normal relative plate motions (Jordan and Gardeweg, 1989).

The easternmost flanks of the SubAndean ranges are an active fold and thrust belt.

The distance between La Negra arc and the present day trench is perceived to have been greater in the Jurassic. Either subduction erosion or lateral transport are invoked to account for this discrepancy (Mpodozis and Ramos, 1990).

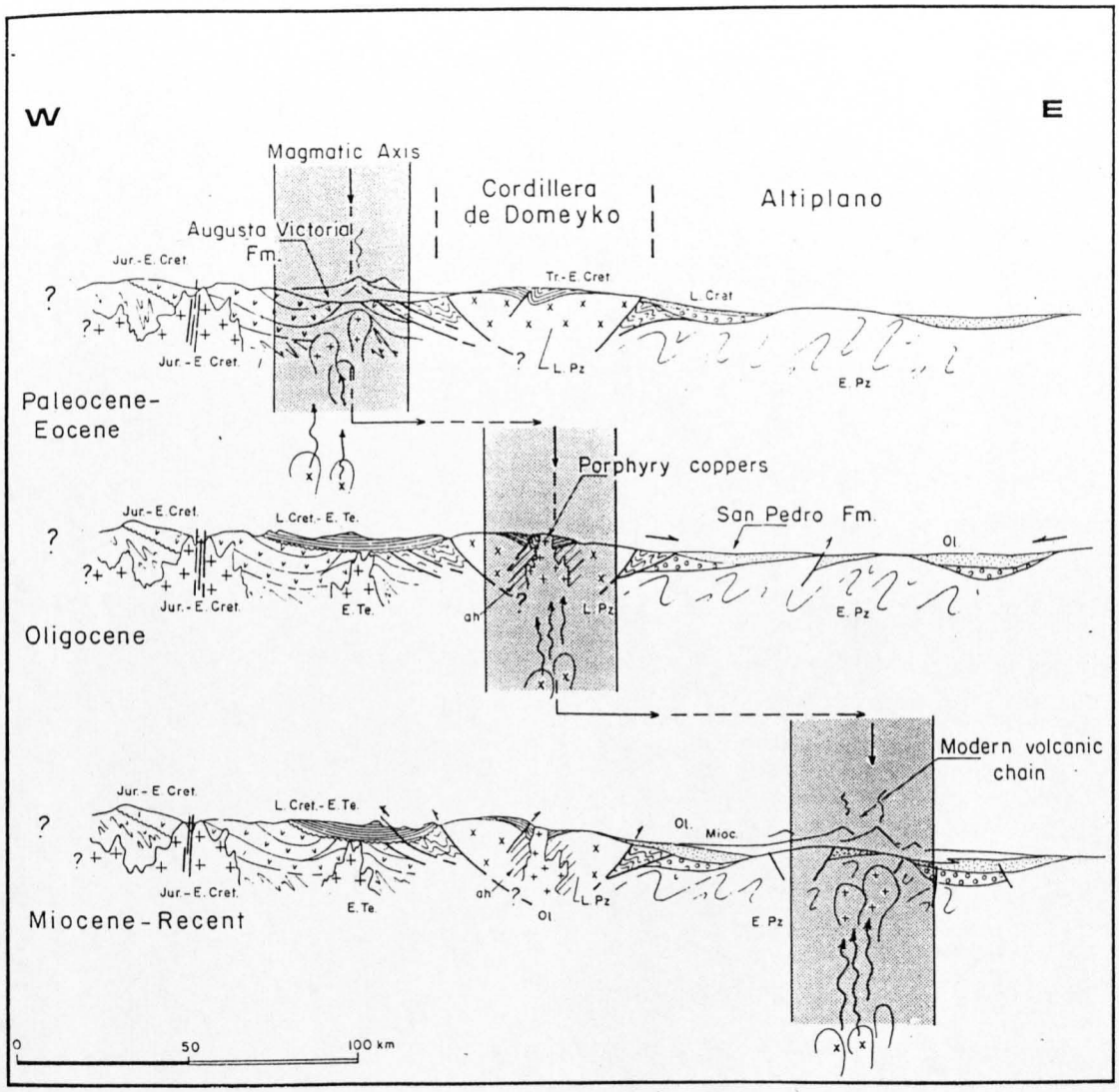

Figure 1.2.3 The discontinuous eastward migration of the magmatic foci in Northern Chile during the Cenozoic, Mpodozis and Ramos, 1990.

1.3 History of The Domeyko Fault System

The Domeyko Fault System is known to extend for over 800 km, from 21° to 28°, Figure 1.1. It can be divided into segments based on fault patterns and continuity. In between each segment is an area of no exposure. The northernmost segment extends for 200 km, from Quebrada Blanca to south of Chuquicamata mine. The Calama Basin hides any exposure immediately south of the Chuquicamata hills. At Limon Verde the central segment begins and extends for 300 km to Vaquillas mine. 50 km of no exposure separates the central and southern segments. The southern segment, 200 km long, passes through El Salvador to Quebrada Carazalillo, where it terminates. Each segment comprises one master strike slip fault, which is the same length as the segment and numerous shorter dip slip faults.

The movement history of the DFS is summarised in Table 1.3.1 and the references with the evidence cited summarised in Table 1.3.2. The southern and central segments have comparable histories. Both have sinistral displacements and shortening across the Domeyko Range. The timing of the sinistral displacement in the central segment is poorly constrained and could be contemporaneous with that in the southern segment. This deformation can be correlated with the Eocene Incaic Event. Later dextral movements occur in both segments. In the Miocene, reactivation of faults in the Domeyko in a reverse sense is followed by extension to the east of the Domeyko Range to form the Salar de Punta Negra. Normal faulting is the final deformation recorded along the central segment of the DFS. Mpodozis et al (1993) largely based their Incaic chronology on geometries of large scale faults and regions of extension and compression along the edges of curved faults: meso scale data are sparse.

The Northern segment has more evidence of reactivation of the DFS. Direct evidence indicates a small dextral displacement occurred syn- and post-mineralisation. This was post-dated by a large sinistral displacement in the Oligo-Miocene. Final activity includes dextral and dip slip faulting. Tomlinson (1997) infers the occurrence of a sinistral event preceding the detailed events on the basis of similarities between this segment and the central segment.

A broadly compatible history for the segments of the DFS can be defined involving sinistral deformation and shortening across the arc during the Incaic event (44 - 40 Ma) followed by a less significant dextral offset along the system in the mid - Late Oligocene. The 36 km of postulated sinistral offset along the northern segment is not evident in the central and southern segments. The majority of the deformation along the DFS is brittle, at Chuquicamata mine there is evidence for ductile shear that was contemporaneous with pluton emplacement (Lindsay et al, 1995).

Epoch	Ma	Northern segment	Ma	Central segment	Ma	Southern segment
Miocene - Pliocene	<3	dextral, reverse and normal significant uplift [1]		normal faulting [10]		shortening [19]
	17		24	Punta Negra depression formed [11]		
Early Miocene-End Oligocene		sinistral ~ 36 or 25 km displacement post mineralisation [2,3,4]		reactivation of reverse fault [12]		
	31		30	dextral (Oligocene) [13]	32	
Upper Eocene		dextral ~ 2km displacement + shortening [5]		La Escondida mineralisation [14]	35	dextral [20]
	34	syn-mineralisation dextral [6,7]	34		36	
			40			sinistral and shortening [21]
Incaic Event	37			uplift [15, 16]		
		shortening [8]			42	
		Limon Verde + Chuquicamata hills rotated clockwise, translated N-wards [9]		sinistral ~30 km displacement timing poorly constrained [17]		
	44					
				dextral history throughout [18]		
Palaeocene						
			45			

Table 1.3.1 Chronology of deformation in the Domeyko Fault System, Northern Chile.
Numbers in square brackets refer to references in Table 1.3.2.

Northern segment	Central segment	Southern segment
[1] Tomlinson & Blanco (1997) Relative timing — cross cutting relationships Timing — fault scarps within gravels Sense — offset of gravels Amt. displ. — gravel provenance from both sides of fault [2] Tomlinson & Blanco (1997) Timing — cross cutting dated sericitization (31Ma) syntectonic deposition of Papajoy Fm (24Ma) cross cutting 19-15 ma mineralisation Sense — s-c fabric, porphyroclast rotations Amt disp — ~36 km correlation units and faults across fault [3] Reutter et al (1996) Timing — age mineralisation and cut gravels Sense — sidewall rip-outs, overprints in Chuqui. pit Amt disp — ~25 km correlation of units [4] Maksaev (1990) Timing — $^{40}Ar/^{39}Ar$ dating of porphyries [5] Tomlinson & Blanco (1997) Timing — deformation style indicates contemp. with intrusion and sericitization Sense — mylonitic assymetries Amt disp — structural restoration across fault zone [6] Lindsay et al (1995) Timing — fabric associated with hot intrusion Sense — kinematic indicators, mapping, sampling [7] Reutter et al (1996) Timing — cf folding, intrusion of granodiorite Sense — s-c fabric, ecc, fault patterns mylonite assymetries [8] Tomlinson & Blanco (1997) Timing — K/Ar dating fault rock $^{40}Ar/^{39}Ar$ dating unconformity Amt disp — structural restoration across fault zone [9] Tomlinson & Blanco (1997) Timing — cf central DFS segment Sense — rotation of foliation parallel to curved fault correlation with curved faults in central segment	[10] Mpodozis et al (1993) Timing — recent fault scarps Sense — apparent in field [11] Mpodozis et al (1993) Timing — constrained by age of sediments Sense — apparent in the field [12] Mpodozis et al (1993) Timing — Oligocene porphyry not displaced above fault trace Sense — fracture patterns and extension direction of interfingering diorites [13] Mpodozis et al (1993) Timing — cf northern and southern segments and reutter et al (1991) [14] Ojeda (1986) Timing — mineralisation K/Ar dated [15] Maksaev (1990) Timing — fission track dating [16] Ramirez & Gardeweg (1982) Timing — stratigraphic and structural relationships (uplift to Purilactis Group deposition) [17] Mpodozis et al (1993) Timing — age basins, tectonic juxtapositions Sense — side wall rip-out, geometries of faults [18] Reutter et al (1991) Timing — unconstrained Sense — vertical folds, fault patterns shortening,	[19] Cornejo et al (1997) Timing — post-dated earlier deformation [20] Cornejo & Mpodozis (1996) text not seen, results reported in Tomlinson and Blanco (1997) [21] Tomlinson et al (1990) Timing — dating rocks cut by fault 40Ma (upper age limit) syntectonic intrusion 39Ma Sense — kinematic indicators on fault fault patterns.

Table 1.3.2 Sources and basis for structural history of DFS as described in Table 1.3.1.

The deformation history cited by Reutter et al (1991) is not directly compatible with the above deformation history. Vertical folds and fault patterns provided evidence of dextral faulting in the northern, central and southern segments. To determine a sense of lateral movement from vertical folds the orientation of layering prior to deformation must be known, as rotations can be counter-intuitive (Lamb, 1987), these data are not available for all of the areas analysed. Analysis of fault patterns can be a powerful tool in determining the sense of faulting, however if multiple fault events have occurred, the fault pattern may become distorted or only reflect one of the events.

A model for the deformation in the central segment of the DFS has been proposed by Mpodozis et al (1993). The master strike slip fault in the central segment is the Sierra de Varas fault which is present over the length of the segment. Another strike slip fault has been identified by Mpodozis et al (1993), which lies to the east of the Domeyko, the La Escondida Fault. These two faults are assumed to have been active contemporaneously and define a shear lens (the La Escondida Shear Lens, LE), Figure 1.3.1. Deformation to the east of this shear lens occurred via rotation of basement blocks along curved faults, to produce basins at the trailing edges of the blocks. Deformation was distibuted across this zone. To the north, the strike slip province is bound by a rigid buttress, Sierra Limon Verde. Tomlinson (1997) relocated the rigid buttress to Sierra Moreno, north of Chuquicamata as the structural style across the region remains identical. According to the model, northward motion of the Domeyko Range during the Eocene resulted in the formation of an extensional basin , the Salar de Punta Negra, at the southern termination of the displaced block. The rigid buttress prompted the displacement to be transferred east along curved faults.

Comparison with plate tectonic reconstructions shows the sinistral deformation is opposite to transcurrent motions expected from the oblique direction of subduction. Transcurrent motions further south along the Chilean margin are consistent with those predicted from plate reconstructions, indicating the fault system is not responding directly to the relative plate motion. Yañez et al (1994) have proposed a model involving a rigid rotating upper crust floating on a ductile decoupled lower crust.

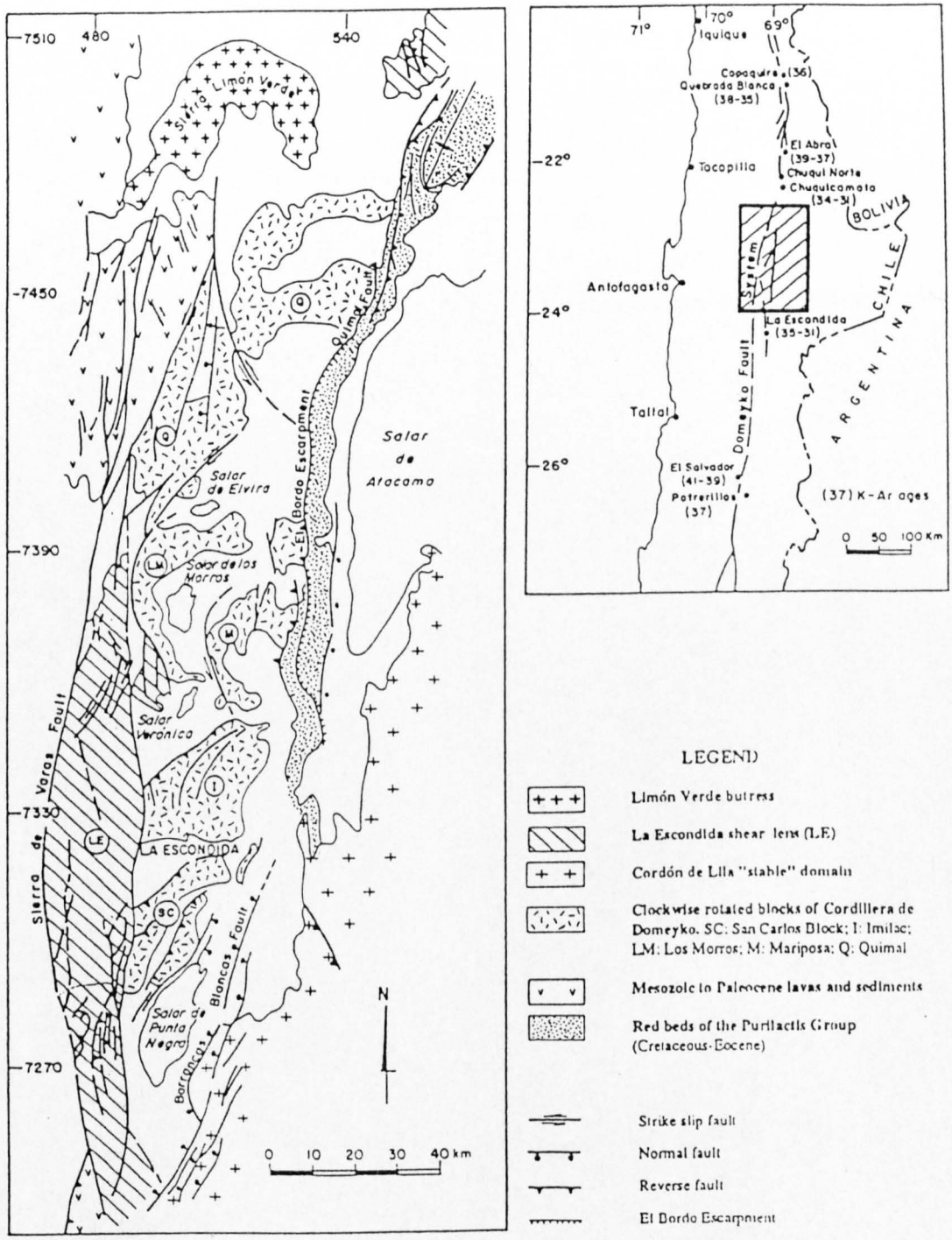

Figure 1.3.1 Structural domains and major faults in Cordillera de Domeyko between sierra Limon Verde and Salar de Punta Negra (Mpodozis et al, 1993).

1.4. Aims of this study

Directly determined kinematics of deformation along the central segment of the DFS are sparse, so areas have been targeted with a view to unraveling the temporal relationship of faults with different orientations and senses, relating these faults to timing of folding and determining the kinematics of faulting wherever possible.

The geometry of the central segment of the DFS has been ascribed to predominantly sinistral shear by Mpodozis et al (1993) and dextral shear by Reutter et al (1991). Palaeomagnetic quantification of the directions and amounts of rotations suffered by rocks beside the Sierra de Varas fault aimed to clarify the divergent histories assigned to the DFS.

One reason that kinematic data is so elusive within the central segment of the DFS is that the majority of faulting was at shallow levels in the crust, so fault data often consists of numerous fracture sets, sometimes with slickenline data and sometimes with cataclasite or fault gouge. Time has been invested to define a method to identify kinematics of brittle fault zones from fracture orientations within a zone where the kinematics were well constrained.

Chapter 2

Structural Analysis of Folds and Faults

CHAPTER 2 STRUCTURAL ANALYSIS OF FOLDS AND FAULTS

The core of the Domeyko is comprised of igneous bodies and volcanogenic sediments, Figure 2.1.1 and Foldout 2.1. Tectonic surfaces with kinematic indicators are rare. Attempts were made to map primary structures (fiammé), breccia bands and slip surfaces within an andesite from La Table Formation in Q. Las Mulas. Considerable structural analyses did not yield any consistent strain axes or deformation history. The original orientation of the eutaxitic fabric was either disturbed by more than one episode of deformation or the fabric was not originally planar. Without palaeomagnetic analysis, it is not possible to recognise rotation within the intrusive bodies, as jointing orientation and density varies locally within the units and fabrics are not pervasive enough to allow mapping. Kinematic data was not forthcoming from most of the Domeyko core. To constrain the deformation history, folds within Jurassic sediments on the western flanks of the Domeyko range between latitudes S24° 50' and S25° 08' and slip surfaces along the Sierra de Varas fault have been targeted.

2.1 Deformation within Jurassic sediments

Structural sections were constructed in four locations, from north to south, Quebrada Profeta (section 1), Quebrada del Viento (2) and Quebrada Las Mulas (3) with a fourth section taken to the west of section 3 in Q. Las Mulas, see Figure 2.1.2 and Foldout 2.1. The well defined biostratigraphy (Hillebrandt et al, 1992) and lithostratigraphy (Ardill, 1996) has allowed resolution of ages within Jurassic stages along cross sections. The longer sections will be discussed first.

Quebrada Profeta

The folded Jurassic sediments of Q. Profeta have a common hinge line of 18/025. Individual small scale folds (up to 100m) possess sub-parallel hinge lines. Site H is the one exception to this pattern. The distribution of data points at this site do not provide a well defined great circle. If the pole at 30/175 is ignored, a computer generated best fit great circle of poles to bedding indicates a fold axis of 01/184, more consistent with the trend observed along the rest of the section. East of the bend in the profile (Figure 2.1.2), the cross section is approximately perpendicular to the fold hinges, so the section provides a profile plane view. Across this part of the section all fold axial traces are seen to dip to the east. The western part of the section is oblique to the profile plane and the dips of axial traces are not so clearly defined. The folding near the thrust which marks the western limit of the Jurassic has a steeper easterly dipping axial trace, than the folds further east. This is corroborated by the axial planes measured and calculated at sites A and B, which dip to the east.

Despite minimal direct evidence for younging direction, the repetition of Oxfordian around a fold core of Kimmeridgian evaporites indicates a large scale syncline. Whilst locally variable, the average dip direction of the sediments is consistent with a synform. The only small scale fold offering any

W69º 15'
480km
490km
N
7280km
7270km
7260km
7250km
7240km
525º
7230km
7220km
7210km
7200km
10km
470km
268+/-7
278+/-10
260+/-17
280+/-10
269+/-6
268+/-6
270+/-6
269+/-6
355+/-23
AGUA EL ORO
284+/-7
241+/-12
Co de PROFETA
SIERRA de ARCOMEDO
274+/-8
273+/-13
278+/-7
Alto de Varas
50+/-2.9
Aguada de Varas
288+/-7
FALLA SIERRA DE VARAS
SIERRA DE VARAS
Section 1
Quebrada Profeta
FALLA PROFETA
Portezuelo de la sal
Río Frío
Section 2
Quebrada Punta del Viento
Section 4
Quebrada Las Animas
Section 3
Co Pastos Largos
Quebrada Sierpe
SIERRA VOLCANICA
Saline Deposits

Formacion Pampa de Mulas / Gravas de Atacama
Oligo-Miocene.
Poorly consolidated polymictic gravels with occasional intercalations of ignimbrite sheets.
Unconformably overlying Fm Chile-Alemania .

Formacion Augusta Victoria / Chile Alemania
Palaeocene - Mid Eocene
Lavas and pyroclastics of andesitic-dacitic composition with subordinate basalts and rhyolites.
Unconformably overlying Fm Santa Ana

Formacion Santa Ana
Upper Jurassic - Neocomian
Clastics and shallow marine deposits with intercalations of volcanic andesites.
Conformably overlying Fm Profeta.

Formacion Profeta
Upper Triassic - Upper Jurassic
Marine sediments with occasional continental influences.
Conglomerates, shales , evaporites, limestones with fossiliferous concretionary horizons.
Conformably overlying Fm Q.del Salitre

Formacion Quebrada del Salitre
Upper Triassic
Fossiliferous marine and continental sediments with volcanic horizons; composition of lavas and breccias ranges from andesitic- basaltic.
Unconformably overlying Fm La Tabla and Grupo Plutinco Punto del Viento

Estratos Sierra de Varas
Permian - Triassic??
Continental and volcanic sediments including chert, pelite, arenite with intercalations of lavas and breccias

Formacion La Tabla
Carboniferous - Permian
Rhyolites, dacites and subordinate andesites.
In places a gradual contact with Gp Plutonico Punta del Viento is visible.

Permian - Carboniferous undifferentiated units including
rhyolite-dacite porphyry
lavas and breccias (Co Guanaco)
monzogranite intrusives, some foliated
Grupo Plutonico Punto del Viento (S of 7240km)

Ignimbrite sheets within Gravas de Atacama
Miocene
Río Frío Ignimbrite
Ignimbrite in Pampa de Mulas

Intrusives Permian - Carboniferous

Rhyolite Porphyry, occasionally with biotite

Tonalite with biotite and fine grained amphibole

Foliated tonalite with hornblende and biotite

Fault trace (undifferentiated sense)

Inferred fault trace

Normal fault

Reverse fault

Non-tectonic contact

K/Ar date, biotite

K/Ar date, amphibole

K/Ar , muscovite

K/Ar , whole rock

Detail in Figure 2.1.2

This map is taken from Naranjo and Puig, 1984 and Herve et al 1991.

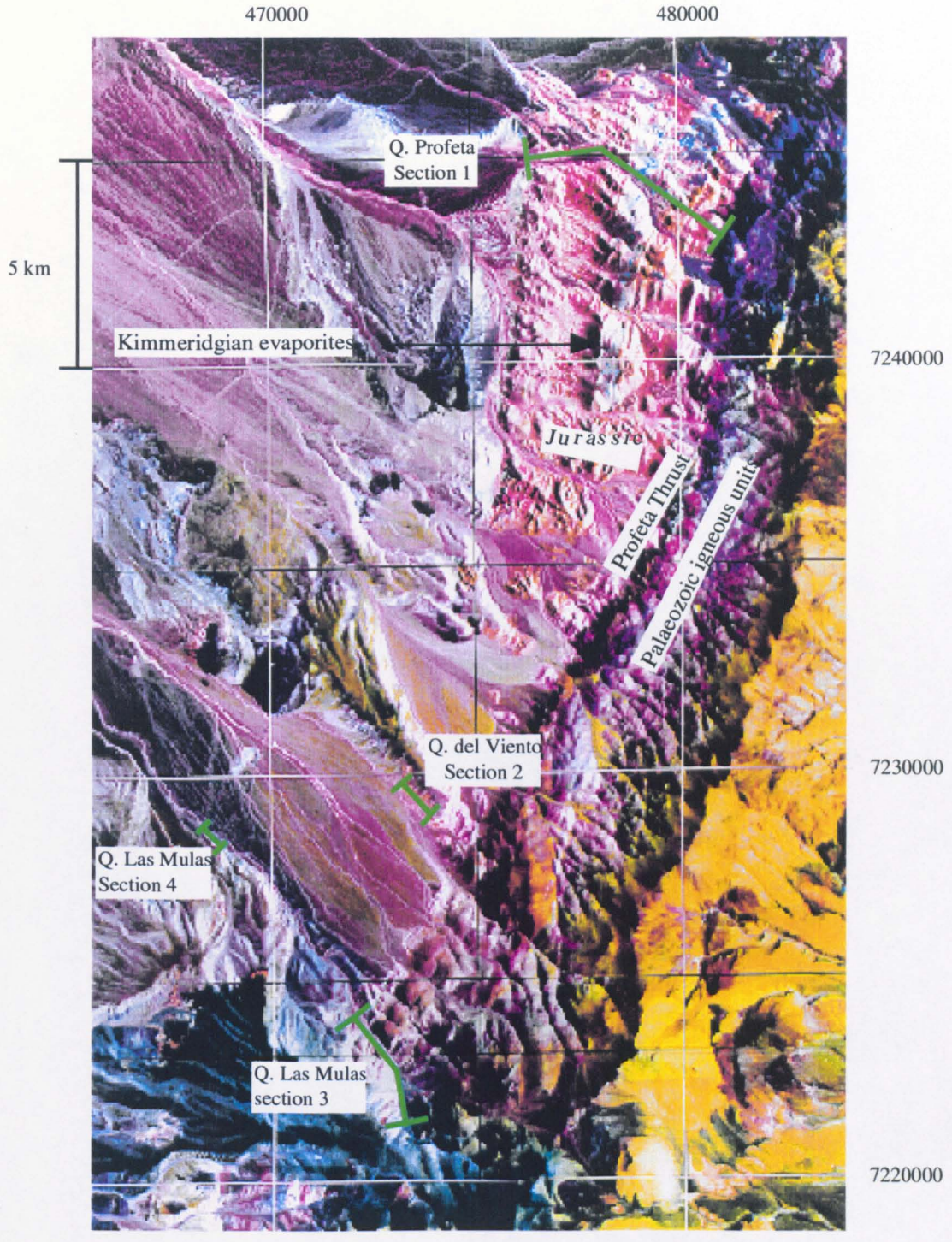

Figure 2.1.2 Satellite image showing the location of the cross sections within the folded Jurassic sediments. The different lithologies have different reflectivities, resulting in colour changes. See Figure 2.1.1 for location within the fault system.

Denotes line of section.

unequivocal indication of vergence lies between sites I and J and indicates an antiform to the west. This is not consistent with the suggested synformal syncline hinge line to the west of site H, unless, as seems likely, the vergence relates to the smaller scale antiform with site I as its core, Figure 2.1.3.

Normal faults with their sense inferred from tilting of blocks and drag structures also occur along the section. The orientation of the faults is not known. From the geometry of the section, the faults within the Jurassic sediments are inferred to have small displacements; they occur either in the core of folds (for example site I) or bedding parallel (for example, site K) the faults are inferred to accommodate the folding. The exception is the fault which bounds the western margin of the Kimmeridgian evaporites (to the east of site F) which may accommodate significant bedding parallel slip. The western margin of the evaporites is sharp at this fault, whilst in the east a gradational change to more silty beds occurs, indicating a loss of strata along this fault. This is supported by the satellite image, Figure 2.1.2, which reveals a blue band of Kimmeridgian evaporite layer at the core of the syncline. The contact between the Kimmeridgian evaporites and older Oxfordian silts and sands is sharper along the western margin than the eastern margin, in the satellite image. This fault has not been folded.

The sense of movement on the Profeta Thrust and the thrust placing Jurassic above Tertiary sediments are inferred from stratigraphic constraints (Naranjo y Puig, 1984). A normal fault has displaced the Triassic - Jurassic contact. Assuming that normal faults with similar orientations formed during the same stress regime, a relative chronology of folding and faulting, can be constructed.

Chronology determined from section 1

The deformation sequence began with large scale folding. Smaller folds with consistent geometries, possibly parasitic, to the larger folds may have formed contemporaneous to the larger folds, or afterwards. Reverse faulting then placed the Triassic above Jurassic and Jurassic above Tertiary units. The compatible geometries of the thrusts and folds suggest they may have formed during one E-W compressional event. The thrusting transported sediments towards the west. A final episode of normal faulting occurred, demonstrated by the offset Profeta thrust at the eastern end of the section with downthrow to the west.

Quebrada Las Mulas -East

Between the two cross sections in Q. Las Mulas, a massive-bedded Upper Jurassic, Lower Cretaceous conglomerate occurs. The conglomerate has not been folded:

The folded sediments in Q. Las Mulas, section 3, have a common hinge line of 08/209. Individual small scale folds (up to 20m) and regions bound by parallel faults possess sub-parallel hinge lines. Sections 4 and 5 within this cross section provide exceptions to this pattern. Section 5 has been cut by faults which are antithetic to the most common faults, which may have rotated the bedding sufficiently

to distort the hinge line. Section 4 is almost planar bedded so will not produce a well defined hinge line. In both cases the exceptions are not taken to negate the trend of a common hinge line observed elsewhere along the section. The section was taken across the southern side of the quebrada. Comparison of the orientation of the section line and the hinge lines shows the section to be representative of the profile plane for the folds. The axial trace of the folds viewed in the cross section approximates to a horizontal line.

Fault number 3, can be seen on aerial photographs to have a north-south strike and displace the earlier faults in a dextral sense, with ~ 30m offset. The dip-slip component of motion is inferred to be reverse. The other faults have a NNE-SSW strike. Approximately 50m away from the line of section, the fault beside the Bajocian units and cutting through the rhyolite (fault number 7, Fold-out 2.1) can be seen to displace a pink evaporite horizon along which the Jurassic is thrust. The two faults strike obliquely to one another. Neither fault trace cuts the mid Miocene pediment surface or younger extrusives along strike.

Chronology determined from section 2

A schematic summary section is shown in Figure 2.1.3. The folds are considered to have formed during the same event and been disturbed by later faulting. A chronology of deformation deduced from this cross section is folding either contemporaneous with or closely followed by kinematically consistent reverse faulting. The thrusting appears to be to both the east and west. An episode of oblique faulting on north-south faults with a dextral component of strike-slip movement and a reverse component of dip slip movement occurred; and an episode of normal faulting on NNE-SSW faults. Both post date the thrust activity, however their relative timing is unknown.

Quebrada del Viento

The folded sediments from section 2, Q. del Viento, have a common hinge line of 24/040. The axial traces of the folds in the plane of the section are horizontal. One fault, with a northeastern strike puts the upper Triassic in contact with the Palaeozoic La Tabla Formation. From stratigraphic constraints and the low angle of the fault observed from Foldout 2.1, this is assumed to be a reverse fault. Relative timing of events is not evident at this locality. A schematic cross section is shown in Figure 2.1.3.

Quebrada Las Mulas -West

The folded sediments from section 4, at the western end of Q Las Mulas, have a common hinge line of 27/003. Axial trace orientations are not consistent in the section. Two cross cutting faults both appear to be axial planar to folds and are not assumed to have significant offset. There are two boundary faults, visible on the aerial photos with northeast and north strikes at the west and east ends of the

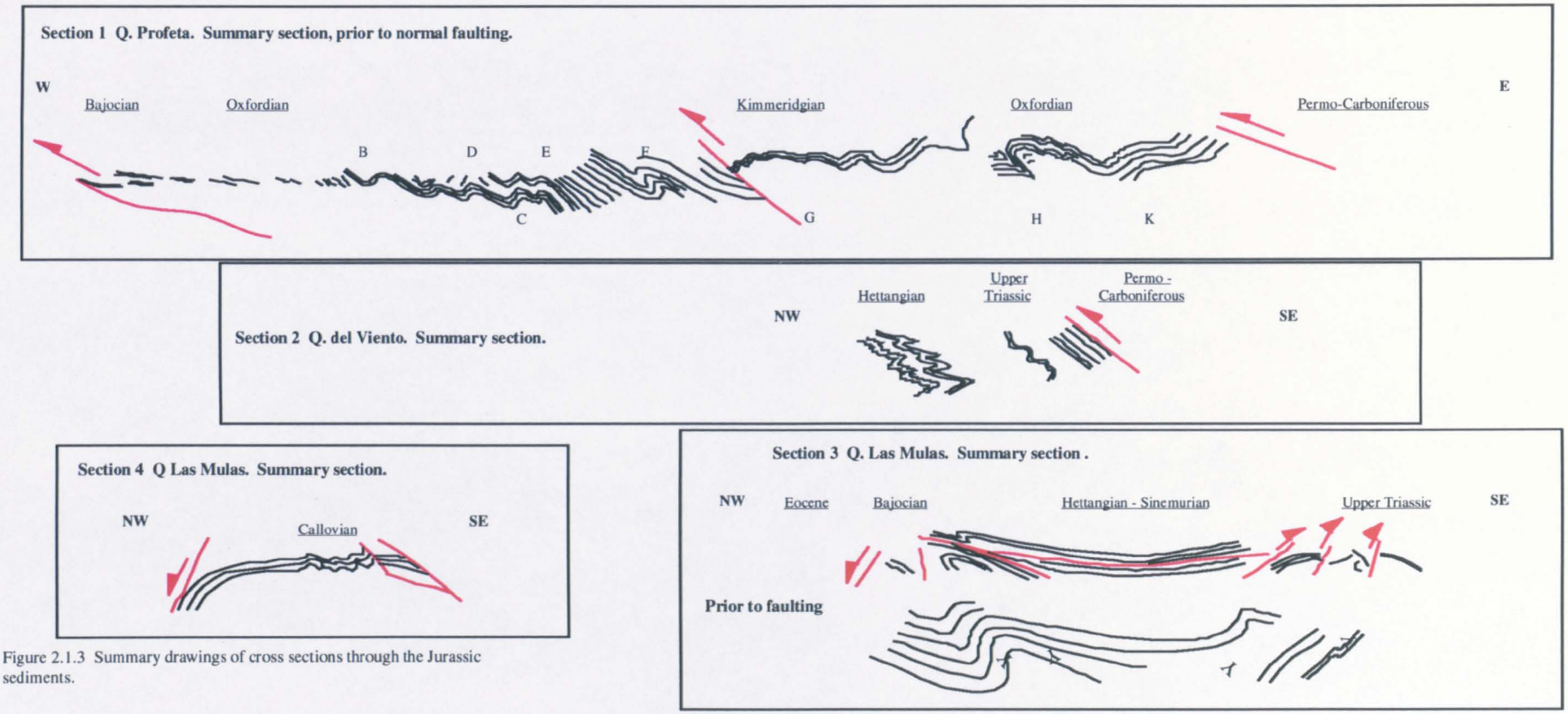

Figure 2.1.3 Summary drawings of cross sections through the Jurassic sediments.

section, respectively. The faults themselves are not exposed however, discolouration of the sediments occurs towards the gullies, indicating fluid transport has been localised. The dip of the fault surfaces has been determined using interactions of the fault with topography on aerial photos. A schematic summary section is shown in Figure 2.1.3. The sense of movement on each fault has been deduced from stratigraphic relationships across them.

Comparison of cross sections

Comparison of the cross sections shows a good correlation of hinge lines for all of the folds. The common hinge line has a shallow plunge and plunging towards either 030° or 200°. Whilst the common hinge line for Q. Profeta plunges to the south, and that from Q. Las Mulas plunges to the north, both sections have one small scale fold with a hinge line plunging in the opposite direction to the trend for that section. The hinge lines from sections 2 and 4, at similar latitudes to section 3, both plunge to the north. The variation in plunge direction of hinge lines along different sections is not therefore taken to reflect a significant difference in fold geometry. All hinge lines have a shallow plunge and are not mis-oriented much relative to each other. The common hinge line for the sections suggests a common geometry prior to faulting and it seems probable that they formed during a single episode of folding.

Comparison of the schematic diagrams, Figure 2.1.3, highlights the differences between the sections. The northern-most section, in Q. Profeta is widest and has fewer faults, with both limbs of a large scale syncline present. In contrast the southern sections are older and thinner. Only the cross sections of Q. Las Mulas and Q. Profeta include Triassic sediments, through all the Jurassic present to juxtaposed younger sediments. As such they provide the main constraints for any model. Age and hinge line orientations are also taken into account from sections 2 and 4. It is possible to correlate faults between sections.

Interpretation of sections

Figure 2.1.4 shows models of the structural setting of sections 1 to 3. All folds are interpreted as part of the same folding event. It is not known whether the folds along the western flank of the Domeyko formed coevally or whether the folding was diachronous.

The consistency of the hinge line orientation calculated throughout the sections is inferred to reflect parallelism of the large scale syncline and smaller scale folds seen in the Jurassic. Minor differences of the hinge line orientation between the two observed scales of folding are beyond the resolution of this technique however. It is not known whether the small scale folds are parasitic to the larger folds or whether they formed after and oblique to the larger folds. In zones of transpression, as suggested by Sanderson and Marchini (1984) early formed larger folds can be rotated around with continued deformation and smaller scale folds form at low angles to the older folds. The two possibilities cannot be distinguished in this instance.

The model of the structural setting of each cross section, with the trace of reverse fault prior to activation, Figure 2.1.4, shows the northern section to be at a higher structural level within the fold to those at the south. Evidence from the satellite image indicates the large scale syncline plunges northwards, Figure 2.1.2. This is shown by the Kimmeridgian evaporites (the blue reflectivity band) at the core of the syncline, which gradually thin to the south. This is consistent with the majority of hinge line orientations determined from bedding readings. The southerly plunging hinge line in Q. Las Mulas may reflect a local disturbance.

Projecting along the strike of the Hettangian sediments from Q. del Viento to Q. Profeta, places the Hettangian sediments at a distance from the exposed Jurassic sediments that is consistent with the expected thicknesses (Prinz et al, 1994) and the fold model. The same process cannot be successfully applied between Q. Las Mulas and any sections further north. Examination of the satellite image (Figure 2.1.5 which highlights the location and Figure 2.1.2 at larger scale) reveals a consistent deflection of features at the latitude of Q del Viento. The main Domeyko range is bent around an s-shaped block of La Tabla Formation; the Jurassic sediments on the other side of the block are offset by an equivalent amount. This fold deflects both the folds and faults chronicled from the cross sections. Bedding measurements from Upper Triassic sediments in Q del Viento that are clearly bent around this fold yield a hinge line of 11/182. This later folding is inferred to be responsible for the southerly plunging hinge line in Q. Las Mulas.

The cross sections can be used in conjunction with the sedimentary thicknesses reported by Prinz et al (1994) to provide an estimate of the horizontal shortening. This method assumes no lateral variation in sediment thickness, other than that which is structurally controlled. This technique is intended to provide a rough estimate of the amount of shortening; the assumptions made are probably an over-simplification hence the result needs to be viewed with caution.

Western limb of the syncline in Q. Profeta:

Bajocian - Oxfordian, horizontal distance = 3.32 km.

Average dip = 35° East.

Thickness orthogonal to bedding = 3.32 x cos 35°

= 2.7 km

Maximum thickness expected from Prinz et al (1994) = 0.72 km (assuming all Lower Bajocian to Upper Oxfordian present).

i.e. a minimum of 3.8 times thicker orthogonal to bedding.

Eastern limb of syncline in Q. Profeta

Callovian - Oxfordian, horizontal distance = 1.7 km.

Average dip = 60° West

Thickness orthogonal to bedding = 0.85 km

Expected maximum thickness = 0.3 km

i.e. a minimum of 2.8 times thicker orthogonal to bedding.

Averaging these values yields a vertical extension of 3.4 times the original thickness.
To conserve area, vertical extension to 3.4 must be accompanied by horizontal shortening of 1/3.4.
% horizontal shortening, across a line striking 115° = (1-1/3.4)/1 x 100 = 70.5%

Any folding with an intermediate principal strain axis oblique to the profile plane will result in an erroneous estimate of shortening.

This estimate of shortening only includes that accommodated by the smaller scale folds.

The absence of cleavage in the majority of folds, especially in the light of the shortening estimates, may imply a thin skinned deformation. The majority of shortening could have been accommodated by faulting, resulting in the intervening sediments becoming distorted (folded). The faulted margins of the Jurassic sediments support this hypothesis.

In between the two sections of Q. Las Mulas is a massive bedded Neocomian-Tithonian conglomerate, Figure 2.1.6(a). There is no evidence of folding within the conglomerate. A faulted angular discontinuity exists between the Cretaceous and Callovian sediments. Whether this is a normal fault that lowered the Cretaceous or a low angle thrust that transported the Cretaceous units laterally is unknown. Either way, a later normal fault is required to lower both the Cretaceous and Callovian sediments to the level observed in Q. Las Mulas, Figure 2.1.6(b).

Summary of chronology inferred from sections

After folding reverse faulting occurred with the main transport direction from the east to the west. Later normal faulting along NNE-SSW faults with downthrow to the west displaced the thrust surfaces and folded sediments. The relative timing of the normal faulting and dextral faulting observed in Q. Las Mulas is unknown.

Age of folding

The discontinuity observed between the Jurassic and Cretaceous units in Q. Las Mulas provide the most important constraint on timing. Two possible interpretations are that folding occurred before deposition of the conglomerate or, the conglomerate was present but was not folded as it is more competent than the Jurassic sediments. The youngest Jurassic units that are folded are Kimmeridgian. The presence of cleavage and brittle fractures and occasional slickenlines within the evaporites suggest

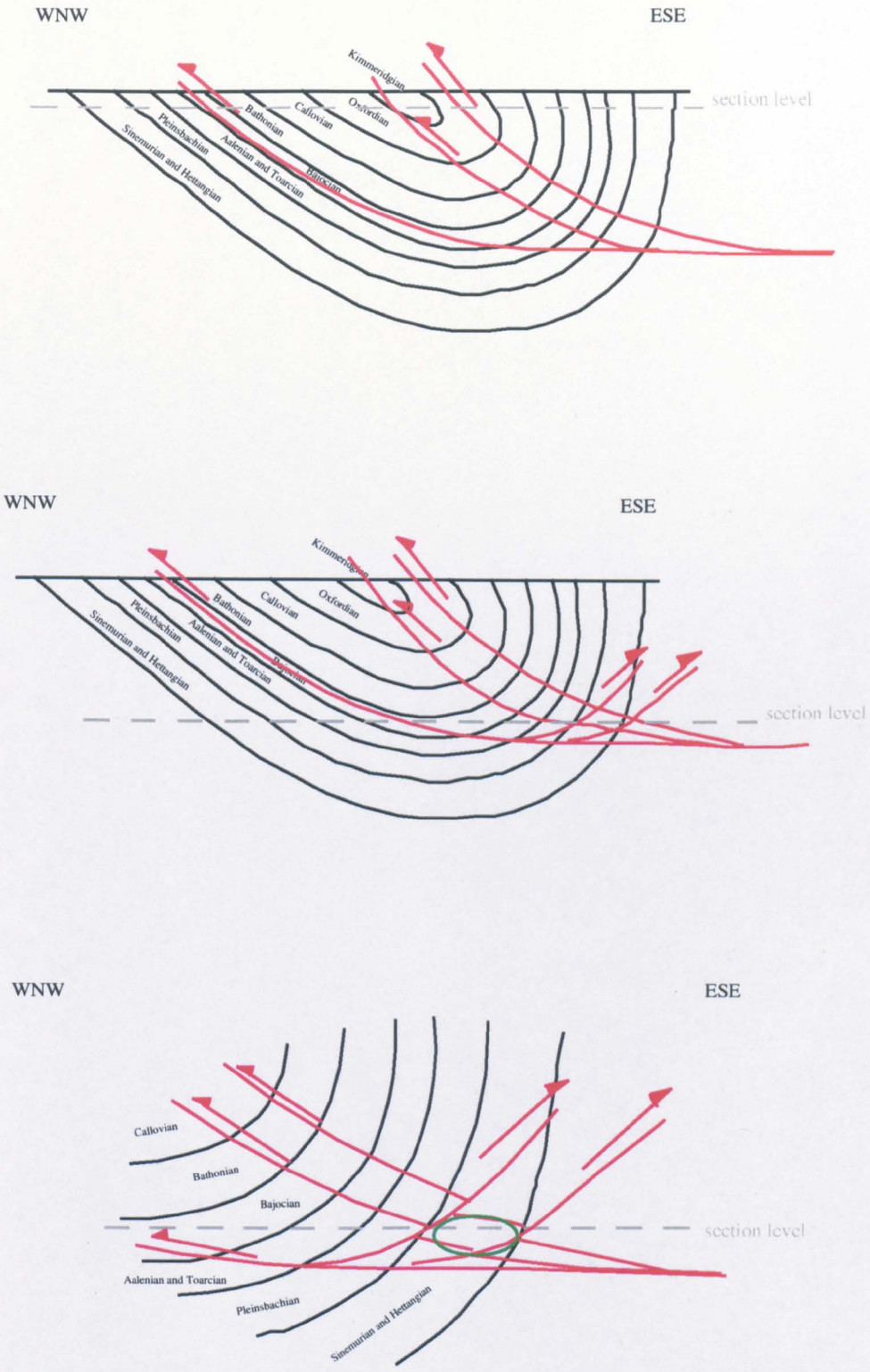

Figure 2.1.4 (a) Traces of faults through the syncline prior to faulting as observed in Q. Profeta. Small scale folds have been omitted for clarity. (b) Traces of faults prior to faulting, through the syncline as observed in Q. Las Mulas. The Toarcian and Aalenian strata have been faulted out. (c) Detail of (b). The green ellipse shows the region exposed in Q. del Viento.

Figure 2.1.5 Satellite image showing Jurassic outcrops along the western flank of the Domeyko. QP, QdV and QLM indicate Q. Profeta, Q. del Viento and Q. Las Mulas respectively. The deflection of the main ridge and s-shaped body of La Tabla Formation have been outline in blue to aid their location. Closer inspection of this deflection is visible in Figure 2.1.2. The outcrop limits are drawn in for Agua el Oro and Aguada Varas.

that the folds are post-depositional. The evaporites are interpreted to have been deposited in a sabkha type environment, whilst the conglomerates represent a marginal marine fan delta system (Ardill, 1996). Comparison of the relative sea level curves for the Jurassic of Northern Chile with the global Jurassic sea level curves indicates this facies change is in response to regional tectonics, such as uplift prompting increased erosion. Folding could have played a role in the uplift. Alternatively, the age of the sediments do not allow much time for lithification and folding between deposition of the Kimmeridgian evaporites and Tithonian conglomerates. Another potentially valid explanation would invoke folding after deposition of the conglomerate, however as the conglomerate is more competent than the Jurassic sediments (which have evaporites occurring to varying degrees throughout at this latitude) a discontinuity developed between the conglomerates and the Jurassic sediments as they buckled. Tilting or faulting of the conglomerate may have occurred to take up the shortening at this level.

The thrust faults lie sub parallel to the axial planes of the folds. This does not necessarily indicate a temporal link as the thrusts may simply have targeted the weaker sedimentary horizons. However, the thrusts and folds have compatible geometries and kinematics.

Comparison with Z-fold observed by Reutter et al (1991) in Q. Profeta

The vertical z-fold cited as evidence of dextral displacement in Q. Profeta is located on section 1 at site G, Foldout 2.1. Comparison with the stereonet of the hinge line shows the fold hinge line has a shallow plunge so is not useful as an indicator of dextral shear.

S-shaped folding in Q. del Viento

The s-shaped folding in Q. del Viento is clearly visible in Figure 2.1.5. Immediately to the west of the Jurassic exposures is a rectangular area that is topographically lower than the surroundings. The Jurassic marks the eastern boundary of this unit, with the s-shaped fold in Q. del Viento at the north-eastern corner of this rectangle. The north and south boundaries both strike NW-SE and en echelon fractures delimit the western boundary (these are not visible on the satellite image). The fractures are visible on aerial photographs because they cause a sudden deepening of a segment of the ephemeral rivers running off the Domeyko range. The surface cut by the fractures is the Mid Miocene pediment (Chong, 1977) present throughout northern Chile.

The fractures indicate a NE-SW extension direction. The northern and southern boundaries have geometries suggestive of normal faults. As Miocene sediments are down-thrown, the faulting must have occurred post-Miocene. It is suggested that the s-shaped fold in Q. del Viento is associated with the lowering of this block. Thus the folding is either late Miocene or more recent. The sense of movement on the faults bounding La Tabla Formation is not backed by field evidence. The shape of

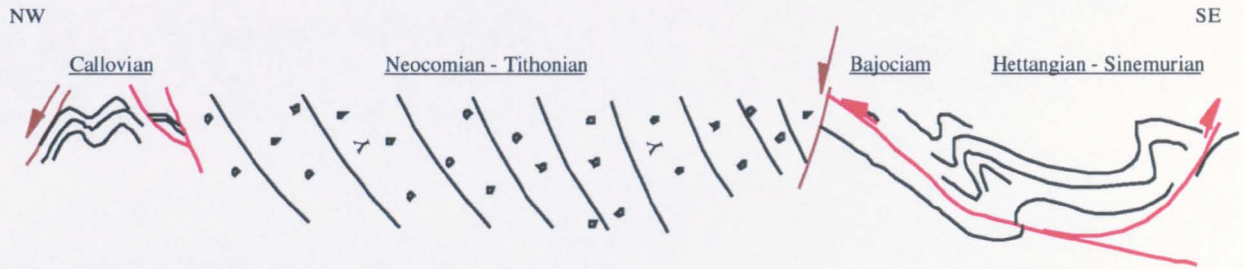

Figure 2.1.6 (a) A schematic cross section of Q. Las Mulas. The sense of movement on the fault juxtaposing Bajocian and Neocomian sediments is inferred from stratigraphy. A small rhyolite intrusion occurs along this fault and is cut by the normal fault, as shown on Fold out 2.1, but has been omitted here for clarity. The sense of movement between the Neocomian and Callovian sediments is unknown.

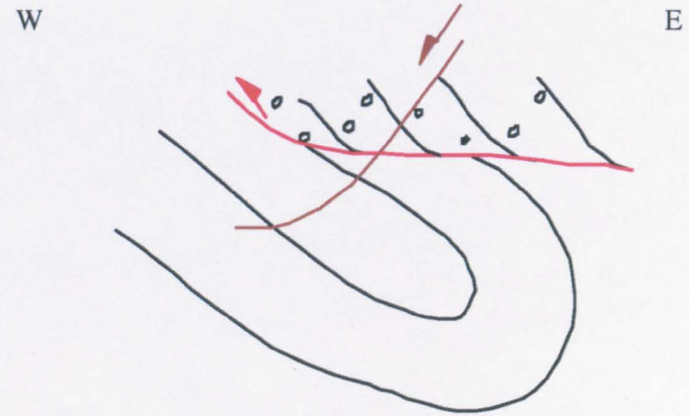

Figure 2.1.6 (b) A model to account for the structures and juxtaposition of stratigraphy observed in Q. Las Mulas. The sense of movement along the thrust isnot certain. It has been drawn as a thrust here, to exemplify lateral transport of the conglomerate; it is equally likely to be a normal fault.

the outcrop is typical of overlapping faults with a significant component of strike slip movement. The s-shaped fold itself is made up of La Tabla Formation, which is not significantly older than the tonalites to the east. This indicates that the s-shaped block has not been uplifted with respect to the juxtaposed units. Dextral motion along the boundary faults would cause uplift at a jog in the fault trace, hence sinistral motion seems more likely.

The siting of the folding at the corner of the block suggests a genetic association between the folding and the lowering of the block. One model that can explain these later structures is transpression (Sanderson and Marchini, 1984). Figures 2.1.7 and 2.1.8 show a schematic diagram of these structures and the structures associated with sinistral transpression. A sinistral deformation along the western side of the Domeyko after the peneplain formation (mid Miocene) can account for the observed structures. The hinge line from folds in Q. del Viento of 11/182 is not directly concurrent with the model. It could either be related to accommodation of the block of La Tabla Fm or directly to the transpression, but as the sediments have been folded previously, the new hinge line is obscured. A bounding fault further west of the block is necessary to establish the necessary conditions across the zone. Linear volcanic fissures striking 030° are suitable candidates and one has been mapped as a fault by Hervé et al, 1984..

Correlation with other Jurassic exposures to the west of the Domeyko

The abrupt termination of a continuous Jurassic sequence at the north of Q. Profeta is likely to have a structural origin. A Miocene pediment surface is apparent above the Jurassic to the north. There may be a minor structure that caused the downthrow of the Jurassic in the south, alternatively preferential uplift of the Jurassic in the south may have resulted in slower erosion rates. The structure does not displace the Palaeozoic core of the Domeyko, so is not considered to have significant displacement.

South of Q. Las Mulas, Jurassic folded sediments of similar ages to those seen in Q. Las Mulas are exposed, until Q. Vaquillas, which marks the end of the central segment of the fault system. To the south west the western limb of the syncline is exposed. North of Q. Profeta there are two outcrops of Jurassic sediments, at Aguada de Varas and Agua el Oro, Figure 2.1.5. The stages represented by these sediments have been determined by Prinz et al (1994), to be Sinemurian - Pleinsbachian and Bajocian - Oxfordian , respectively. Both exposures are fault bounded. With no information relating to the younging direction of these sediments and no further kinematic constraints, the structural model cannot be refined.

Hinge lines throughout the Jurassic exposures

Mapping carried out by Naranjo and Puig (1984), Herve et al (1991), Chong (1977) and Mpodozis et al (1993) along the central segment of the Domeyko Fault System, either side of the Domeyko range, has

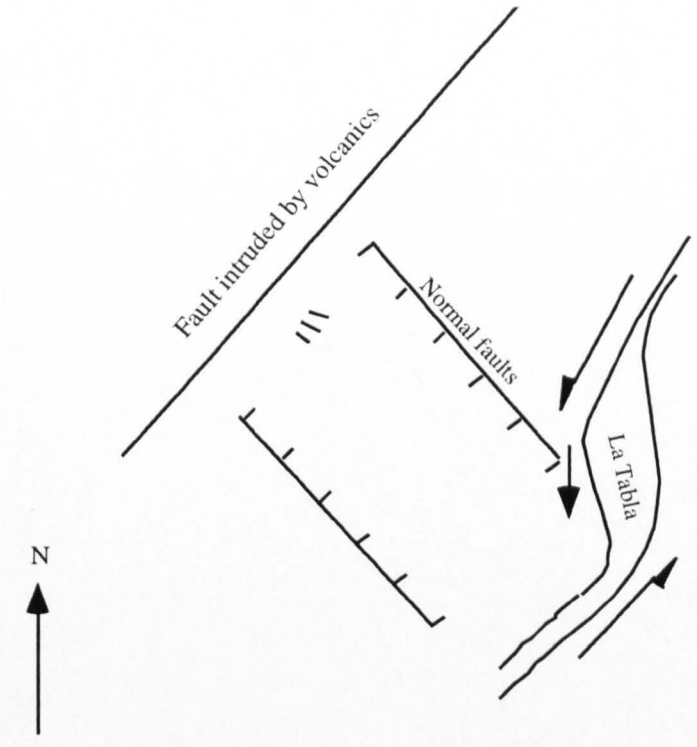

Figure 2.1.7 A schematic diagram of associated structures in the vicinity of Q. del Viento. Interpretive movement sense are added to the trace of structures to aid comparison with Figure 2.1.8.

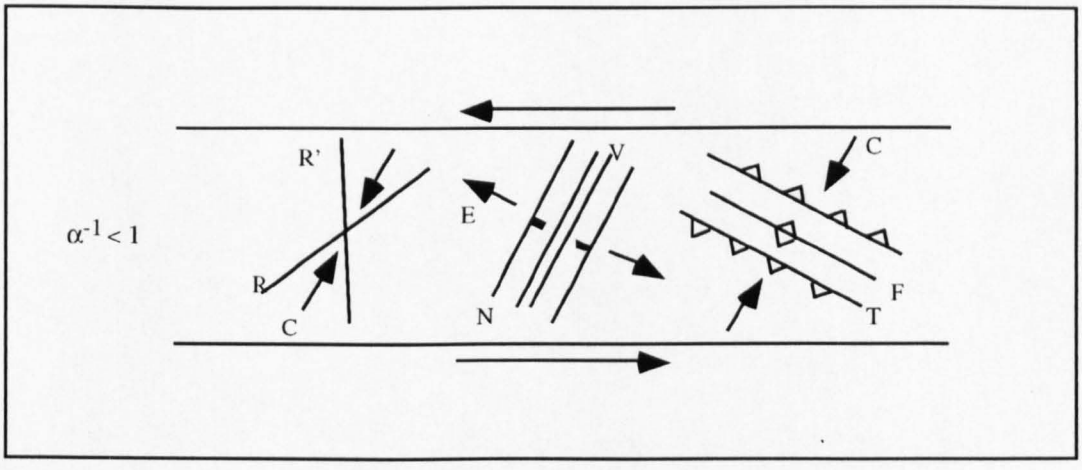

Figure 2.1.8 Orientations of fractures in the transpression model. C, compression axis; E, extension axis; N, normal faults; T, thrust faults; R, R'. Reidel shears or wrench faults; V, veins, dykes or extension fractures; F, fold axes. As the shortening across the zone increases an anticlockwise rotation of fractures occurs and as extension across the zone increases a clockwise rotation occurs.

shown the Jurassic sediments to have hinge lines oscillating about a north - south orientation. Local variations occur beside faults. Some Cretaceous units also share this fold axis orientation. Regional folding of the Jurassic and Cretaceous sediments may have occurred.

Folds in Agua el Oro

Figure 2.1.9 shows the variation in hinge line with distance from the Sierra de Varas fault. The hinge line changes from a shallow plunge to the NE to a steeper plunge to the SE as the Sierra de Varas fault is approached. The spatial variation in hinge line with proximity to the fault suggests the variation in hinge line is prompted by activity along the fault. The consistency of hinge line orientation and well constrained great circles of the profile planes indicate the Jurassic sediments have been rotated, not simply fractured. Transpression with sufficient convergence to orient the longest axis of the strain ellipse vertically, could have been prompted by strike-slip movements along the Sierra de Varas fault. Rotation of lines towards the longest axis of the strain ellipse could cause the reorientation of fold hinge as observed in Agua el Oro. The faulting along the Sierra de Varas fault which rotated the Jurassic sediments is later than the regional folding event with N - S hinge lines.

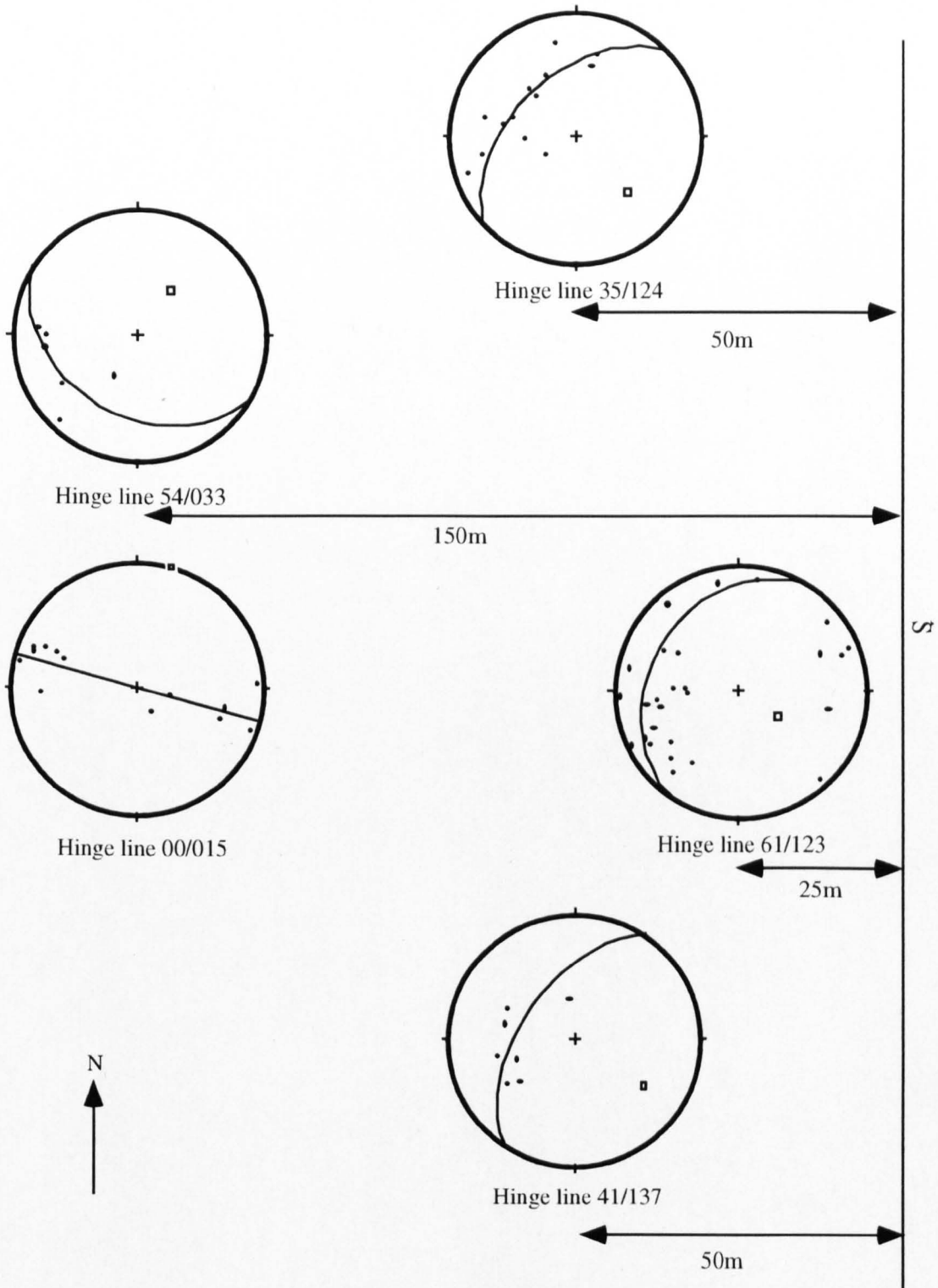

Figure 2.1.9 Plan view of the variation in hinge line orientation with distance away from the fault. The stereonets show poles to bedding from separate localities of folded Jurassic units. The distances are not drawn to scale.

2.2 Analysis of Brittle Fault Data

Throughout this study a "brittle" fault is taken to be a discontinuity across which a strain is accommodated, without a progressive increase in deformation towards the contact. Faults may show variations in discontinuous displacement along their length: a feature which often requires ductile deformation. However, as the scale of observation increases beyond the width of the discontinuity, some faults can approximate brittle behaviour. Single slip surfaces are uncommon for brittle faults. A single fault trace visible on an aerial photo or satellite image may actually be made up of many individual slip surfaces. The data available for the analysis of such faults includes the fault plane orientation, the slickenlines, the sense of movement along the fault and the displacement. Unfortunately not all of these data are available from outcrop studies. Techniques to maximise the information derived from the data are necessary.

Techniques for Analysing Fault Data

Angelier (1979, 1982 and 1989) and Marret and Allmendinger (1990) both converted fault data into fault plane solutions to identify the incremental strain axes, Figure 2.2.1. The extension and shortening axes bisect the pole to the fault and the slickenline and at 90° to this, kinematic data from the fault are necessary to distinguish between the two. The intermediate axis is always perpendicular to the plane containing the fault pole, slickenline and extension and shortening axes, that is the M-plane. This process is not interpretive, but simply provides another means of illustrating the data. Analysis of incremental strain axes allows comparison of non-parallel slip surfaces. For plane strains, the orientation of the intermediate incremental strain axis is coincident with the intermediate finite strain axis. A finite strain substantially larger than the incremental strain can produce a girdle of individually determined incremental strain axes across the plane defined by the maximum and minimum strain axes. Non-plane strain will produce a diffuse distribution of incremental strain axes. Data outliers are not easily recognised.

Hoeppener diagrams can be used to display fault data, (Hoeppener 1955). This is equivalent to the tangent lineation diagram of Twiss and Moores (1992, p206). A small segment of the plane defined by the pole to the fault plane and the lineation on the fault plane is drawn, at the location of the pole to the fault plane, Figure 2.2.2(a). This plane contains the minimum and maximum incremental strain axes. If the displacement sense of the fault is known an arrow can be used to represent the relative movement of the footwall (for a tangent lineation diagram) or the hanging wall (for a Hoeppener plot). The shear plane is tangential to the plotting hemisphere at the point where the pole to the fault plane penetrates the hemisphere, the arrow (or tangent line) is parallel to the lineation on the fault, figure 2.2.2(b). A consistent pattern indicates compatible slip data, that is, the slip surfaces could have been active during the same event. Tangent lineation diagrams are useful for recognising inconsistent data which may be from another source.

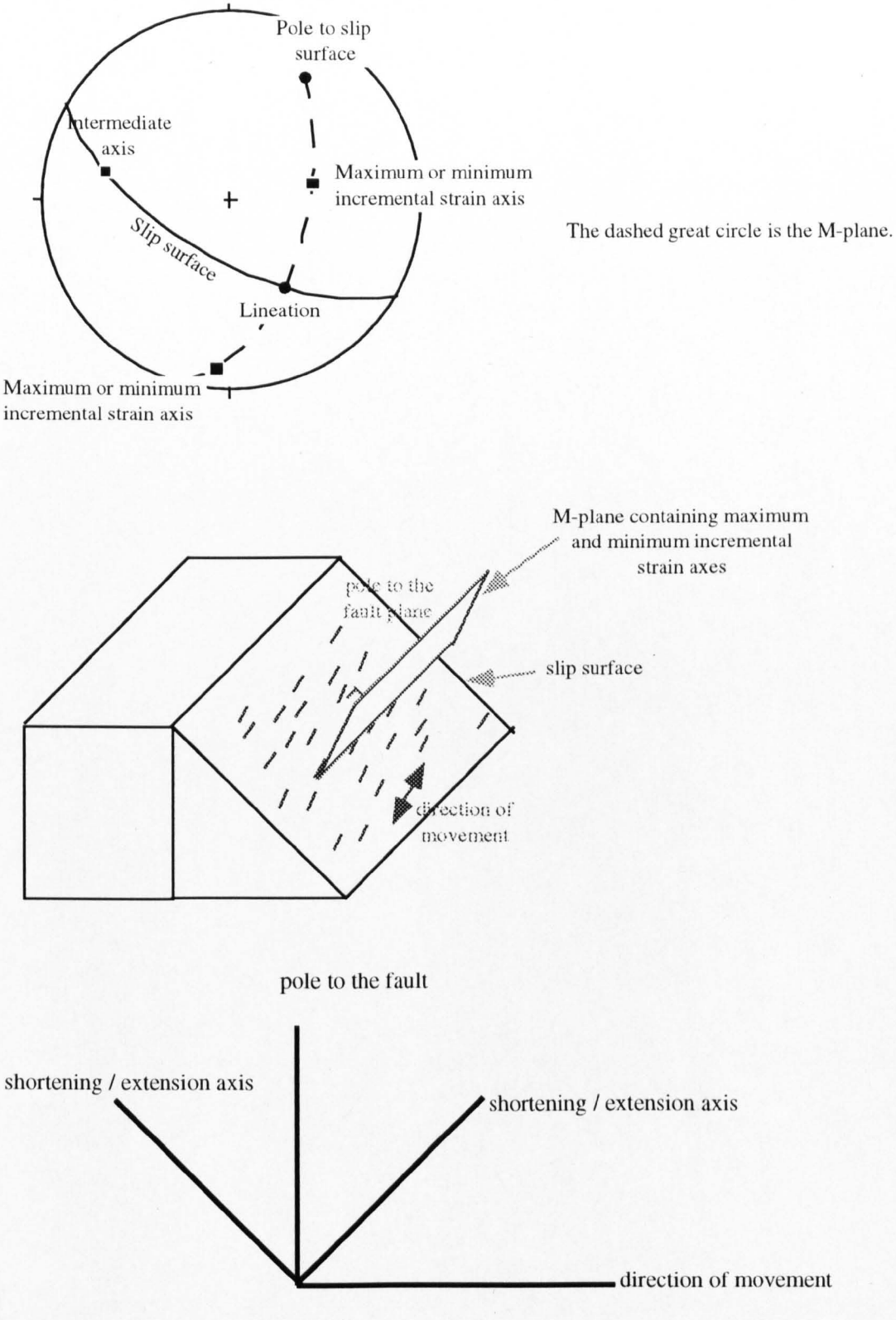

Figure 2.2.1 Determination of incremental strain axes using the slip surface orientation, slip direction and, if available, the sense of movement.

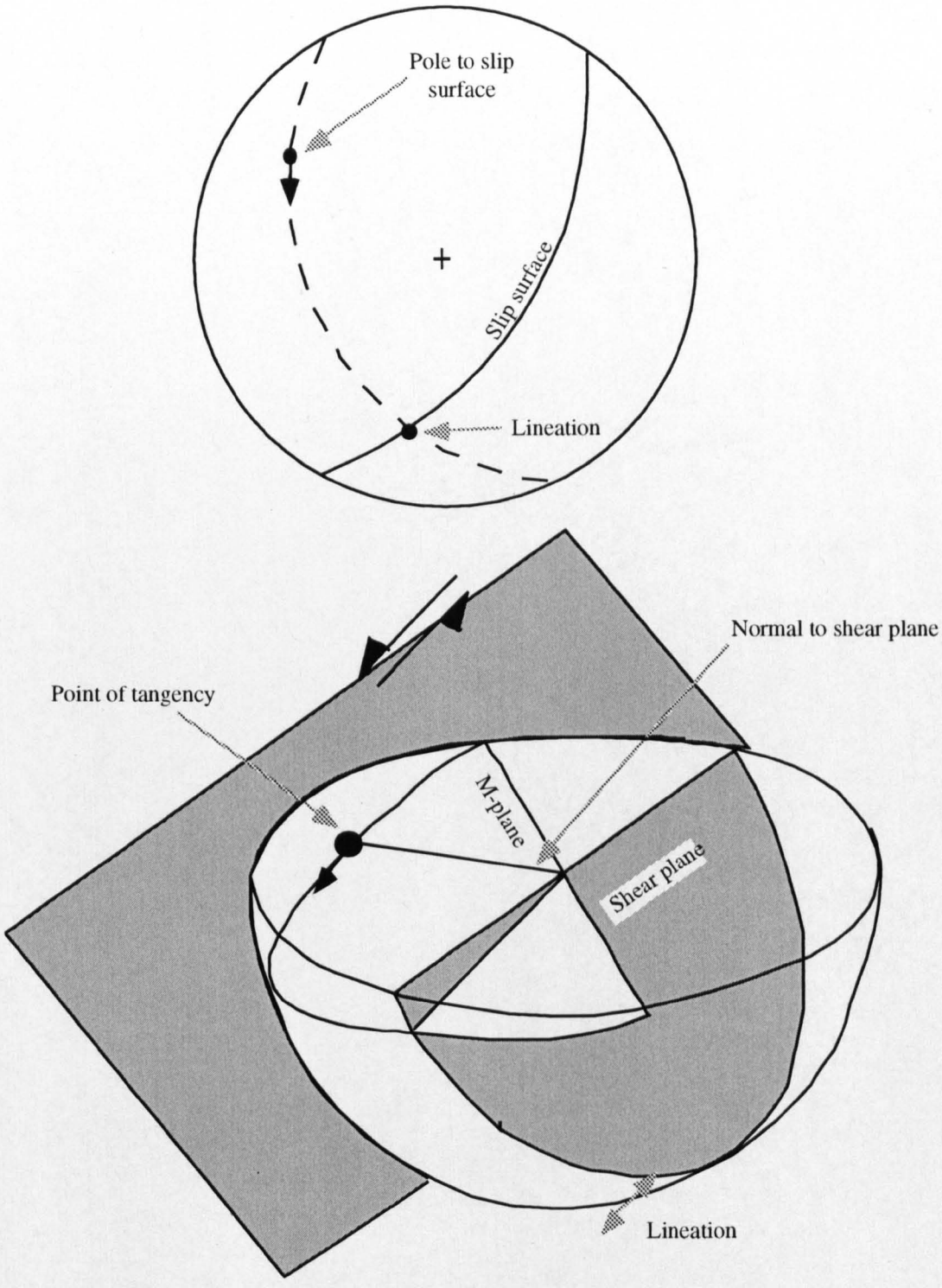

Figure 2.2.2 (a) Construction of a tangent lineation diagram for slickenside lineations. The arrow points in the direction of shear of the footwall. The arrow points from the pole to the slip surface, towards the lineation on the slip surface. (b) Physical representation of a tangent lineation diagram. Diagram after Twiss and Moores (1992).

The significance of the pattern observed on tangent lineation diagrams has been studied indirectly by Arthaud, (1969). Arthaud introduced the concept of movement planes (M-planes) which are the planes containing the pole to the fault plane and the slickenline direction, a segment of which is drawn on tangent lineation diagrams. He suggested that when plotted on a stereonet the M-planes should intersect at one, two or three points, equivalent to the orientation of the principal deformation axes. These deformation axes are indirectly related to the principal stresses. Carey (1976) showed that this relationship is over simplified and is only valid for a radial stress field, as the ratio of principal stresses and orientation of fault plane modify the orientation of the M-plane. Aleksandrowski (1985) modified Arthaud's method to allow application to a triaxial stress field, however this is a time consuming operation that does not guarantee a result.

Wallbrecher et al (1996) computed the M plane orientation for a uniform distribution of fault planes, Figure 2.2.3. The mathematics is based upon Bott's equation (1959, for oblique slip faulting) which assumed that the direction of slip on a shear plane is parallel to the maximum resolved shear stress (MRSS) on that plane. Bott showed the MRSS from a triaxial stress is dependent on both the orientation of the plane with respect to the principal axes of the stress and the linear ratio of the stress axes.

$$\tan q = n/lm \{ m^2 - (1-n^2) (s_Z - s_X) / (s_Y - s_X)\}$$

where q is the pitch of the maximum shearing stress, l, m and n are directional cosines of the fault plane, and s denotes a principal stress axis taken parallel to the coordinate axes x, y and z. The direction of the MRSS is assumed to coincide with the potential slip direction. The relationship between the direction cosines and the slip direction is a constant (the linear ratio of stresses) for any faults responding to the same stresses. This led to the concept of the shape factor, R. The linear ratio of principal stress axes has been modified from the definition of Bott so that

$$R = \frac{|s_2| - |s_3|}{|s_1| - |s_3|}$$

where $s_1 > s_2 > s_3$ and $0 = R = 1$.

A maximum difference between the three principal stresses occurs at R=0.5,

at R=0, $s_2 = s_3$ and at R=1, $s_1 = s_2$.

The assumptions that this mathematics is based upon are as follows;

(i) Only strain accommodated by slip surfaces is considered.

(ii) On a lineated surface with parallel lineations, the fault undergoes plane strain. The deformation plane is defined by the pole to the fault plane and the slickenline direction.

(iii) Each fault moves independently in response to an external stress.

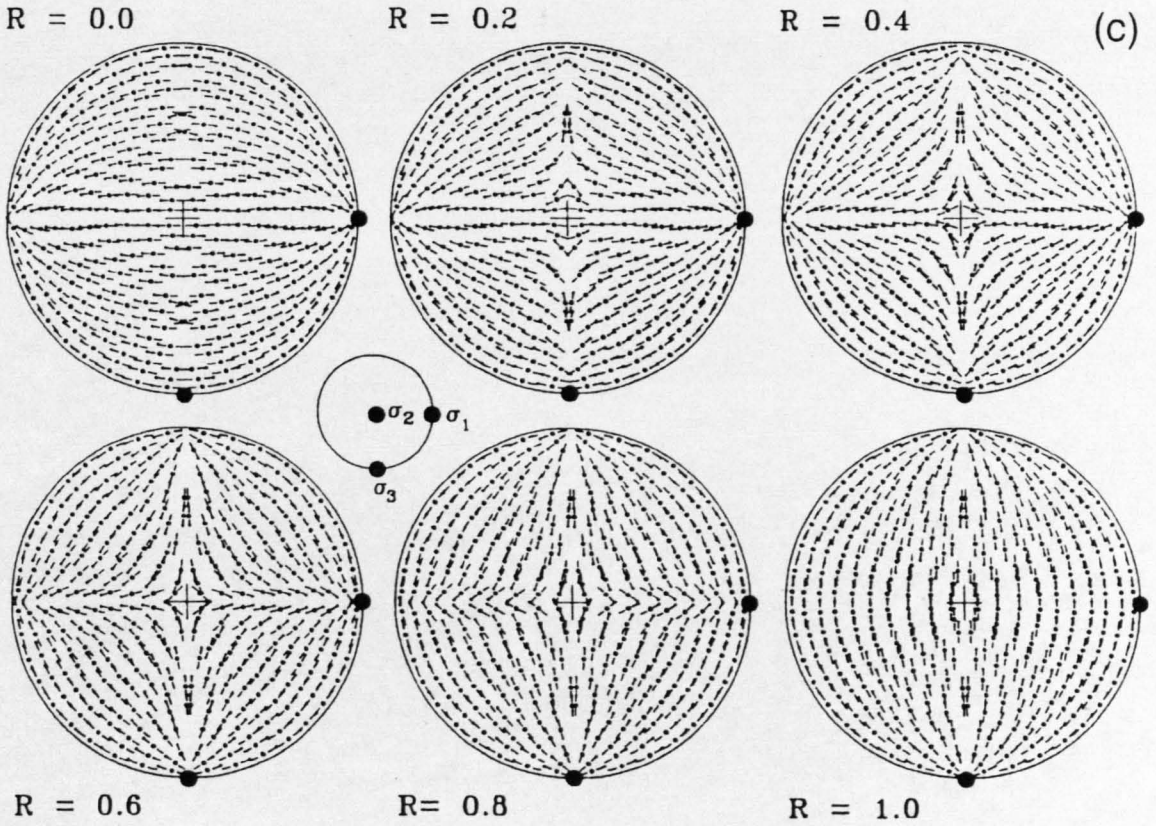

Figure 2.2.3 Hoeppener diagram of slickenlines on 316 uniformly distributed theoretical fault planes undergoing strike slip faulting with different shape factors (as defined in text). After Wallbrecher et al 1996, their Figure 4.

(iv) The deformation is constant volume, the slip is distributed equally among the fault sets and individual faults.
(v) The direction of slip on a shear plane is parallel to the MRSS on that plane.

Wallbrecher et al (1996) have shown that the largest deviations in M-plane orientation occur as the fault orientation approaches the principal stress planes, Figure 2.2.3. Wallbrecher et al have included variations in shape factor to demonstrate the impact on the M-plane distribution. As R reduces, the importance of the intermediate axis increases. For radial stresses the s_1 and s_3 axes are the points of convergence and divergence on a Hoeppener diagram, respectively. Visual comparison of tangent lineation diagrams for "real" data with the computed diagrams of Wallbrecher et al (1996) can be used to estimate the shape factor. The fault data needs to be weighted to compensate for a non-uniform fault distribution.

In conjunction with comparison of the tangent lineation diagram with the acceptable patterns of Wallbrecher et al (1996), an iterative process of removing potential outliers and replotting the incremental strain axes, until the incremental strain axes have the best grouping can also be used to recognise data outliers.

Wallbrecher and Fritz (1989) used eigenvector analysis of the distribution of theoretically determined MRSSes to identify the orientation of the stress axes and the ratio of principal stresses. They discovered the eigenvectors tended to parallel the principal stresses, with the smallest eigenvector parallel to the intermediate axis. The ratio of principal stresses determined which of the remaining two axes coincides with which of the eigenvectors. With information pertaining to sense of slip this distribution could be used to delimit the linear ratio of the stress axes, by comparison with the computed distribution of slip directions.
Many workers have spent time defining methods to reconstruct the palaeostress axes and tensor from fault data using both numerical and graphical techniques (for example Etchecopar, 1981; Angelier et al, 1982; Will and Powell, 1991; Krejci and Richter, 1991; Angelier, 1989; Simon-Gomez, 1986; Twiss et al 1991; Lisle, 1988; Krantz, 1988; Fry 1992; Michael, 1984). Only the techniques mentioned previously are used in this study. The applied techniques are based upon a minimal number of assumptions.

Throughout this study, the principal axes determined from measured fault data are assumed to reflect the strain axes. The only application of a technique with the five listed assumptions occurs when comparison is made between the tangent lineation plot and "consistent" data distribution patterns, as reported by Wallbrecher et al (1991). No attempt is made to translate the principal strains into stresses. Since the rheological properties of the deformed medium are not known. More importantly, the purpose of this research is to constrain the deformation history of the Domeyko Fault System.

Strain axes are used in analysis when they can add detail to the history, but due to local variation are not considered relevant outside of this context.

2.3 **Fault Data from Agua el Oro** (GR S 24° 38' W 69° 12')

The Sierra de Varas fault can be seen on a satellite or aerial photo striking at 330° near Agua el Oro, a deflection from a more typical strike of 352° along the western margin of the Domeyko, Figure 2.1.1 and 2.1.5. Whilst apparent on large scale images of the region, the fault is not detectable on the ground,. At Agua el Oro, Jurassic marine units are exposed immediately to the west of the fault. Some discoloration and disturbance to the sediments are present (Ch 2.1), however there is no exposure of the fault plane. Immediately east of the fault trace, in Palaeozoic igneous units , chloritised and epidotised lineated surfaces are present. The slip surfaces die out eastwards as the distance from the fault increases and their population increases towards the bend in the Sierra de Varas fault. These smaller slip surfaces must reflect either a distribution of deformation towards the fault or accommodation fractures responding to internal stresses caused by the fault motion. None of the surfaces were continuous for more than a few metres. Chloritised and epidotised slip surfaces are not found elsewhere parallel to this fault, however quartz slickenlines are occasionally seen, for example at Aguada de Varas. This may reflect a modification of stresses at the bend in the fault trace, simplistically interpreted as evidence of a dextral movement along the fault.

Measurements of slip plane and slip direction were taken on these surfaces, Appendix 2. It was only possible in a few cases to determine sense of movement. Where determined, sense of shear was recognised using Petit's (1986) shear fracture criterion. Interaction between slip surfaces was not visible in the field. Parallel lineations were observed on slip surfaces. Plots of incremental strain axes and tangent lineation diagrams (without sense marked on as this is unknown in the majority of cases) were used iteratively to separate the data into internally consistent sets, figure 2.3.1 and 2.3.2. Three separate data sets, denoted X, Y and Z have been distinguished using a Hoeppener diagram. Slip surfaces from all three data sets were present throughout the exposure.

Data set X has a shallow southerly plunging intermediate incremental strain axis. This corresponds well with the minimum eigenvector determined for the striae distribution (10/186). The M-plane, defined by the minimum and maximum incremental strain axes is also well defined. The incremental strain axes change through time.

Data set Y has a shallowly plunging south-easterly intermediate strain axis, which also corresponds well with the minimum eigen vector of striae (07/230). The M-plane is well defined with the minimum and maximum axes defining a girdle.

Data set Z has a horizontal intermediate incremental strain axis, which has a similar orientation to the minimum eigenvector. The M-plane is loosely defined. This may reflect non-plane strain or rotation of the slip surfaces since activity.

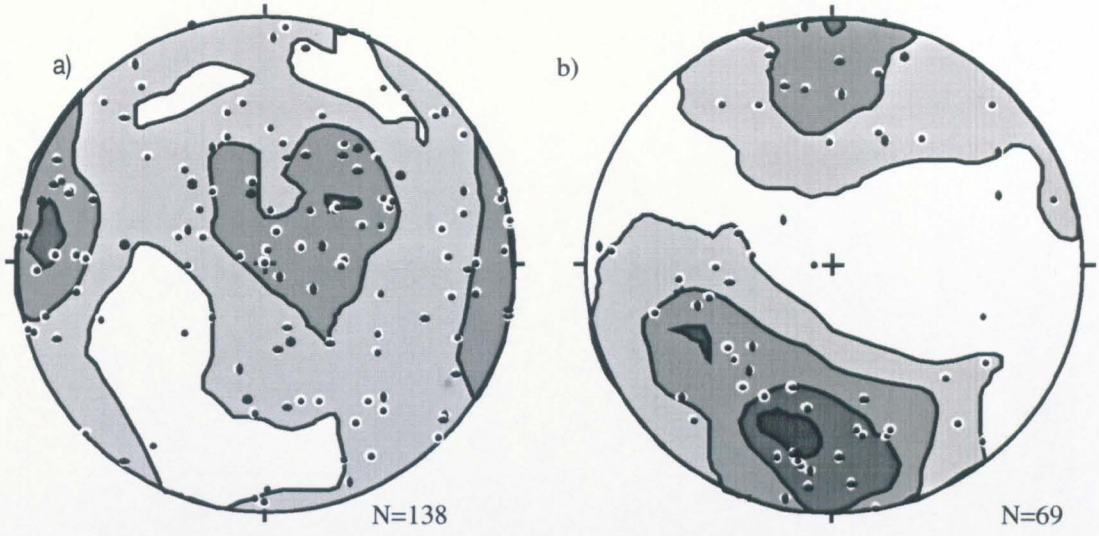

Figure 2.3.1 Kinematic axes (incremental strain axes) determined for all slip surfaces measured at Agua el Oro. a) Contoured plot of maximum and minimum axes. b) Countoured plot of intermediate axes. c) Hoeppener diagram without sense of movement marked. Numbers refer to fault numbers in data . Blue denotes data set X: red denotes data set Y: purple denotes data set Z :and green denotes odd data points.

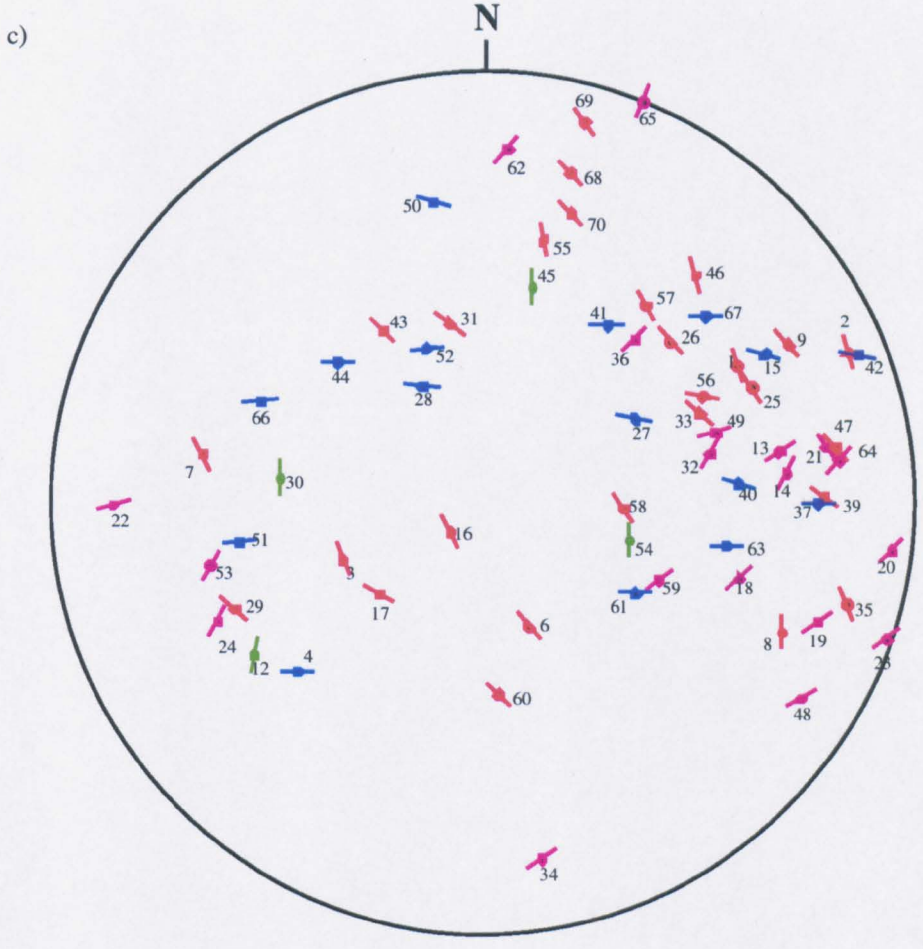

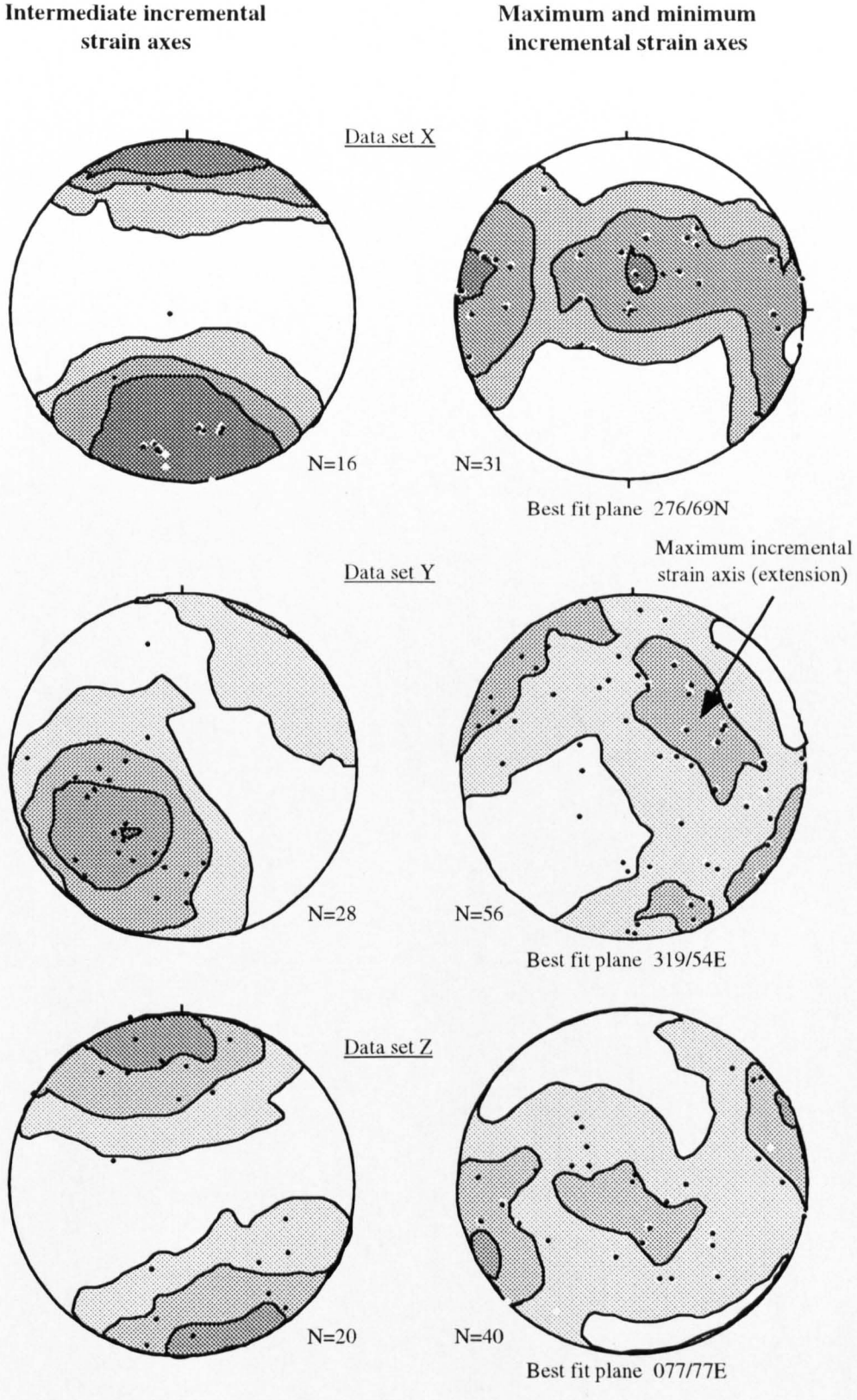

Figure 2.3.2 Incremental strain axes for slip surfaces measured immediately to the east of the Sierra de Varas fault, at Agua el Oro.

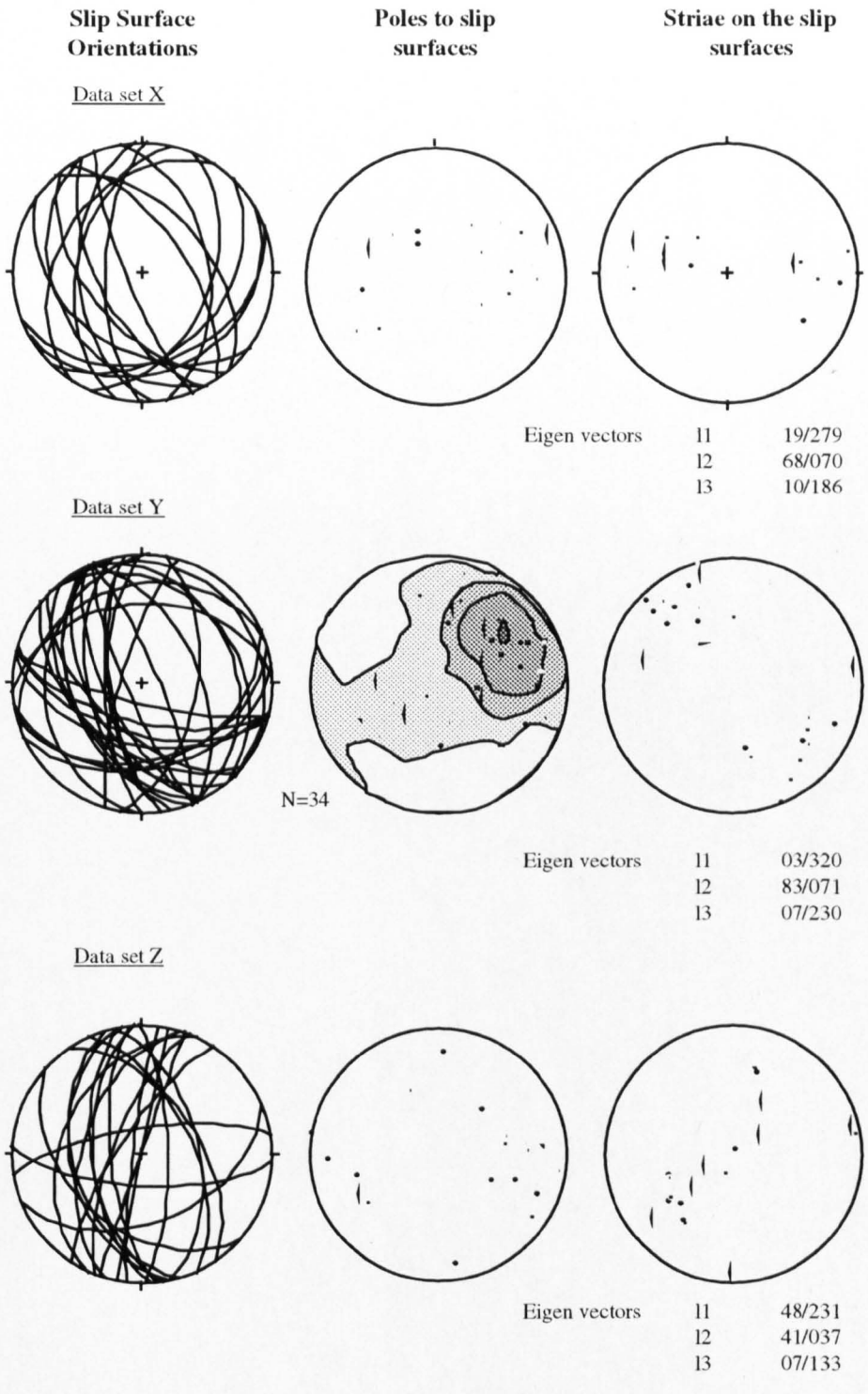

Figure 2.3.3 The fault orientations and striae measured for the data sets. The minimum eigenvector is equivalent in orientation to the intermediate principal strain axis (Wallbrecher and Fritz, 1986)

From the Hoeppener plot, regions where the tangent lineations cross cut each other lie near to the great circles joining the contour centres of the three incremental strain axes calculated for the undivided data. The exceptions to this lie in the eastern quadrant of the stereo net, where the region of cross cutting is diffuse. This suggests that the strain axes for the data sets are similar, but a rotation of strain axes or slip surfaces formed at the onset of deformation has occurred.

An order of activity of the slip surfaces from the data sets can be speculated upon, based upon the orientation of the intermediate strain axes and definition of the M-plane. The intermediate strain axes swing around between the data sets. A gradual change in orientation seems more likely than a switch from 07/230 to 07/133 and finally 10/186. Based upon this, the suggested order of activity is Z - X - Y or Y - X - Z. The less well defined M-plane from data set Z may imply these are the slip surfaces that were active first and rotation as deformation continued has caused the geometrical relationship between the M-planes to break down.

A sub-horizontal intermediate incremental strain axis in all data sets suggests the finite intermediate strain axis is also horizontal. Assuming an Andersonian model of faulting and coincidence of stress and strain axes, this would imply dip slip faulting. Data set Y, the only data set with kinematic information indicates reverse faulting. The location of these slip surfaces at bends in the Sierra de Varas fault suggest the slip surfaces are associated with the extra strain caused by bends in the fault surface. Reverse faulting along the eastern side of a right-stepping bend (Figure 2.1.5) indicates dextral movement along the main fault.

2.4 Summary of Chapter 2

1) Chronology determined from Jurassic folds along the western side of the Domeyko

i) Folding of Jurassic sediments on two scales and there may have been a time lag between the two phases. The folding could have occurred between Kimmeridgian and Tithonian stages. However, geometrically compatible folding of Cretaceous units with the underlying Jurassic sediments along the central segment of the DFS suggest the folding occurred after the Cretaceous.

ii) Thrusting with main transport direction towards the west.

iii) Normal faulting with downthrow towards the west and a small amount of dextral and reverse faulting. The relative timing of the two faulting events is unknown.

iv) Sinistral transpression to the west of the Domeyko with NE-SW extension, occurring in the mid Miocene or later. Only localised effects are seen of this deformation.

2) Chronology determined from Agua el Oro

i) Regional folding of Jurassic sediments, after Cretaceous times.

ii) Refolding of folds beside the Sierra de Varas fault. The new hinge line is indicative of strike slip faulting (transpression). Hence an episode of activity along the Sierra de Varas fault post-dates the regional folding.

iii) Dextral strike slip motion occurred along the Sierra de Varas fault. Indirect evidence of dextral strike slip is found from analysis of slip surfaces at bends in the fault trace.

Chapter 3

Palaeomagnetism

CHAPTER 3 PALAEOMAGNETISM

A general problem with structural studies along the DFS is that kinematic evidence is sparse. The main strike slip fault in the central fault segment, the Sierra de Varas Fault, has not been subjected to the rigorous study that the equivalent faults in the northern and southern segments have been subjected to (see for example, El-Salvador-Potrerillos, Tomlinson et al, 1994; Falla Oeste, Chuquicamata, Lindsay and Zentilli, 1995). In this study samples have been taken from beside the Sierra de Varas fault and the dip slip fault in Quebrada Las Mulas with the aim of using palaeomagnetism to constrain the kinematics of the faults. The study follows on from investigations within this project aimed at identifying suitable techniques to determine as much information as possible about the brittle faults of the DFS. Palaeomagnetic study cannot provide a final tectonic model, but can help to identify the relevant questions for ongoing research in this region.

Objectives of Palaeomagnetic Analysis

Samples were collected from ten sites along the Sierra de Varas Fault with at least two sites from the same unit at different localities to allow direct comparison. Comparison of the Natural Remanent Magnetisation (NRM) direction with that predicted by the apparent polar wander path (APWP) yields an estimate for the tectonic rotation. A discrepancy between units of the same age but at different positions along the fault would indicate a displacement gradient along the fault. A common ellipsoid orientation for the anisotropy of magnetic susceptibility (AMS) can be used to indicate a tectonic origin for the anisotropy, indicative of pervasive deformation. Samples from three sites were collected from Q. Las Mulas, two of which were from a fault that has been the subject of a detailed study. These samples underwent the same treatment and analysis as those described here, but the results are discussed in Chapter 4.

Appendix 3 gives a brief summary of magnetic theory, to provide an understanding of the techniques used, if necessary.

3.1 Sampling, Treatment and Analytical Procedures

Two block samples were taken from each of 13 sites (Map 3.1, Foldout 2.1) and oriented using sun and magnetic compasses. Azimuthal differences between these two readings were typically less than 3°, although for sample AO50, block B, the discrepancy was 9°. Three 2.54 cm cores were drilled perpendicular to each surface, the surface orientation was measured in the field. Each sample was then cut perpendicular to the first surface to produce a second oriented surface which was then drilled, Figure 3.1.1. This yielded an average of 12 cores per site. The cores were marked with 3 perpendicular axes and all measurements carried out relative to these axes. The specimens were treated using standard thermal demagnetisation techniques (e.g. Tarling 1983). Magnetic susceptibility was monitored during thermal cleaning, to check for alteration during heating. Remanence directions for individual cores was determined using principal component analysis (Kirschvink, 1980), to calculate the least squares best fitting line (Figure 3.1.2). Remanence directions per core are based on a minimum of three demagnetisation steps. No single step heatings or bulk demagnetisations have been used in the analysis. Mean directions for each site were calculated by combining core remanence directions, using the method of Fisher, 1953.

Virtual geographic poles (VGPs) are calculated using the geocentric dipole model, (see Butler 1992, pp157 - 159). All laboratory measurements were taken in the Geomagnetism Laboratory at Liverpool University, using specific computer software written by Alan McCormack, Dr John Share, Dr T. Rolf or Dr S. Openshaw. Stereo nets are equal area, lower hemisphere plots and all inclination readings are positive downwards.

Cores with higher magnetic intensities were measured on a Molspin Fluxgate Spinner Magnetometer with parallel data interface, while weaker cores were measured using a FIT liquid nitrogen SQUID Magnetometer model HSM. The lavas and rhyolite dyke possessed the highest intensities of magnetisation (7800000×10^{-9} Am^2kg^{-1}), while the granitoids were weakest (5×10^{-9} Am^2kg^{-1}). Rotation of results to geographical coordinates was performed prior to principal component analysis. Tilt adjustments were not performed because the lavas were horizontal and a lack of structural features in the intrusive bodies precluded recognition of a palaeohorizontal. Any tilting of these igneous bodies would need to be recognised within a chronology relative to fault activity.

In addition to the palaeomagnetic measurements, a series of rock magnetic experiment and magnetic fabric studies were performed on material from the palaeomagnetic sites. A translation bar Curie balance, designed and built by Dr J Share, was used to analyse a small sample from each block and aid in identification of the main magnetic carriers. Anisotropy of magnetic susceptibility (AMS) was measured at

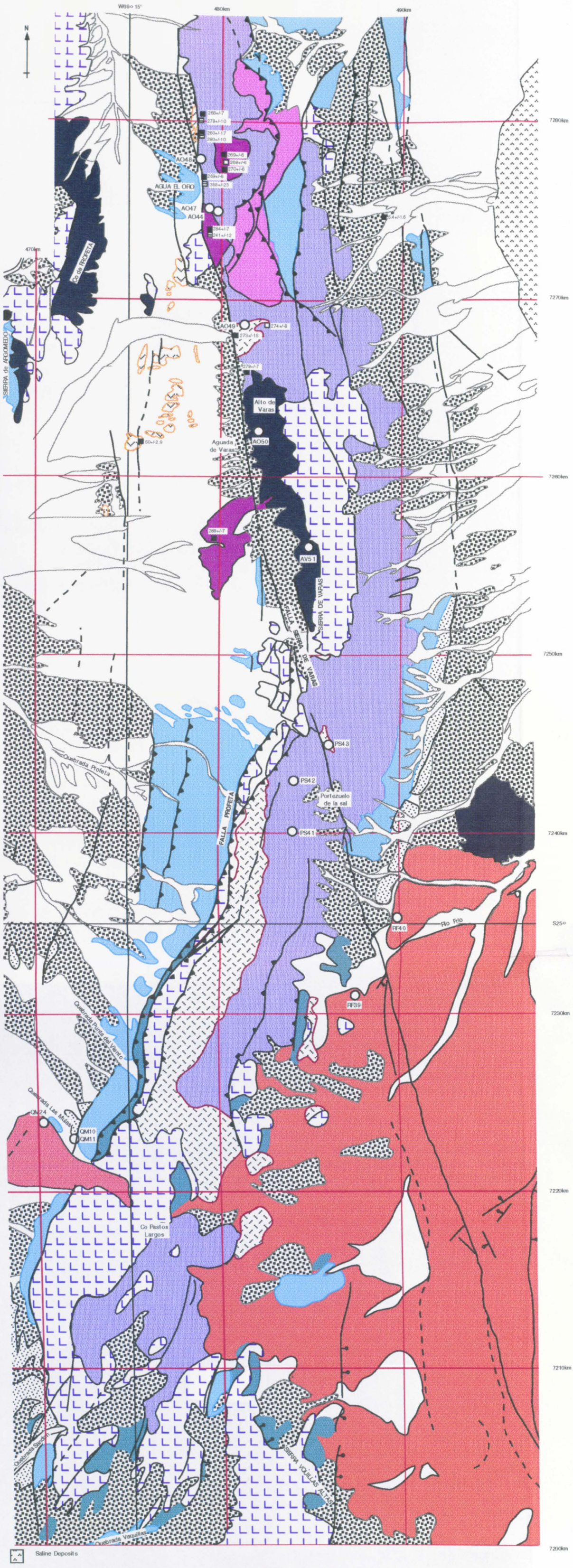

This map is taken from Naranjo and Puig, 1984 and Herve et al 1991.

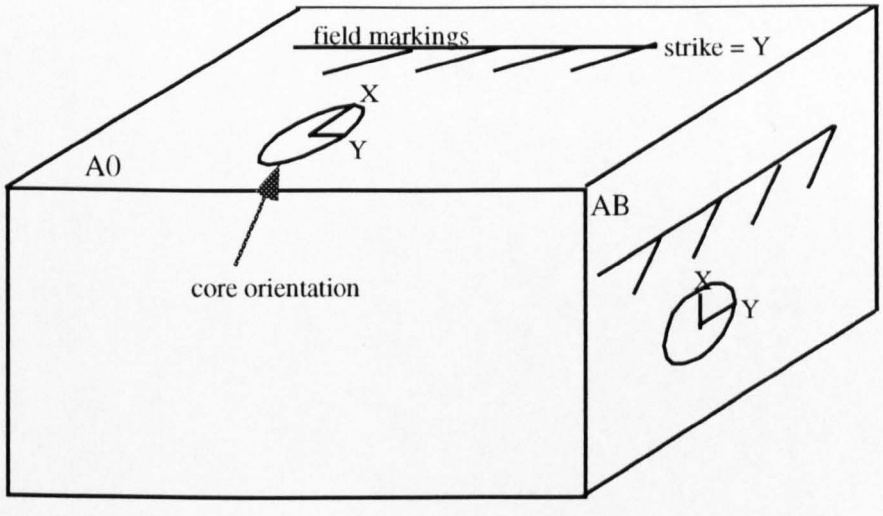

Figure 3.1.1 The surface A0 (or B0) is oriented in the field using sun and magnetic compasses. Surface AB (or BB) is oriented using a magnetic compass. The purpose in having two almost perpendicular surfaces from one block is to check for remagnetisation during drilling.

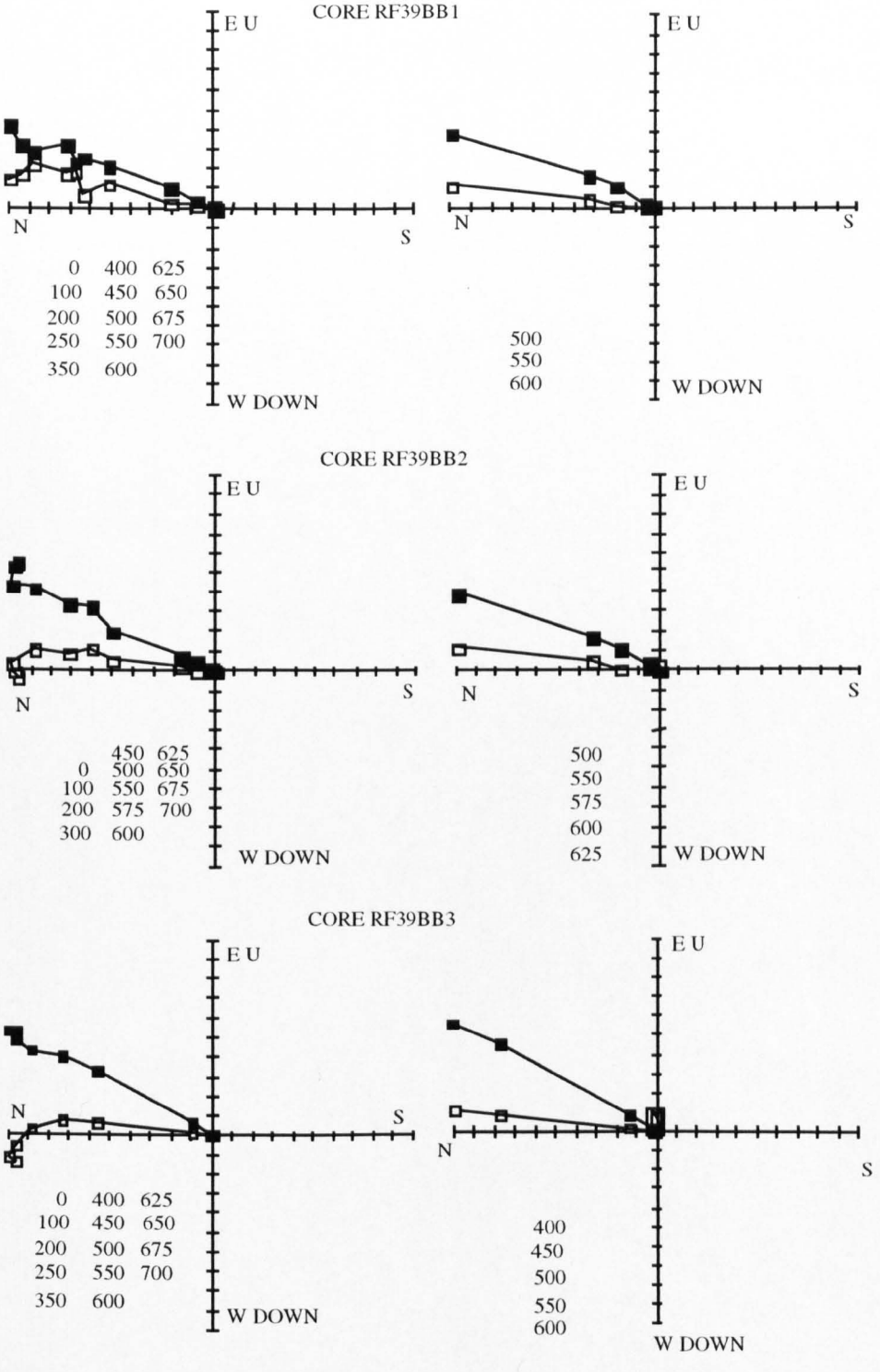

Figure 3.1.2. Examples of orthogonal plots of thermal demagnetisation results from three cores of this study. The left hand figures show the full data set whilst the right hand figures show separated high temperature vectors. The figures are temperatures in C.

0°C and after demagnetisation at 350°C using a Molspin AMS delineator with PC IEEE interface. For each core, the AMS reading was repeated until consecutive results were within 2° of each other.

3.2 Results

Samples at six out of the eleven sites to be discussed in Chapter 3 were successful in yielding discrete components from which characteristic remanence directions (ChRM) could be calculated using principal component analysis. These ChRM directions are either in the northeast quadrant with a negative inclination or in the north west quadrant with positive inclination. The ChRM's were recognised as linear segments in the demagnetisation trajectory and isolated within the temperature range 450° - 675 ° C for all samples except AO49 and AO50. Table 3.2.1 shows the individual core results for each site. The sites were deemed unsuccessful if;

a) the magnetic signal was too weak to be measured accurately; this was manifested by the demagnetising trajectory orbiting the origin in a haphazard fashion accompanied by variations in intensity: or

b) if there was no common magnetic component isolated from the majority of cores from one site.

Samples from PS41 could not be used as a result of an ambiguity in the orientation of the cores.

A low temperature component of magnetisation was present in 58 samples between 0° and 150° C, an example of which is shown in Figure 3.2.1. A viscous remanent magnetisation (VRM) is expected to align to the present geomagnetic field (inclined at ~43° up to the north at this latitude). From Figure 3.2.2, a corresponding concentration of lower temperature components, oriented approximately -43/000 and its antipode, can be seen amongst a wider distribution. Low temperature magnetic components have variations in orientation between cores drilled from the same oriented block, but the clustering around the present day magnetic field direction provides evidence that there has been no systematic mis-orientation of the rock material during sampling or coring. The components not aligned to present day field orientation are likely to be short term viscous magnetisations acquired in the laboratory prior to treatment.

A relatively rapid intensity reduction over the temperature interval 100° - 300° C was observed in fourteen cores (Figures 3.2 .3 and 3.2.4). All cores gave low temperature components similar to the ChRM's identified at higher temperatures. These are evidently the same component with a broad unblocking temperature spectrum.

All the results are summarised in Table 3.2.1.

Sample No	T range °C	Component I/D	M.A.D. a_{95}		T range °C	Component I/D	M.A.D a_{95}	VRM
11A01	200 - 300	35.3 / 298.3	0.9		550 - 650	32.4 / 299.1	0.5	
11A02	200 - 250	25.7 / 296.7	3.3		575 - 650	27.1 / 292.2	1	
11A03	0 - 300	26.4 / 289.2	1.5		550 - 600	23.3 / 295.7	1.9	
11AB1	100 - 300	26.7 / 298.4	1.9		550 - 650	23.4 / 296.8	1.6	
11AB2	100 - 300	15.8 / 300.5	1.5		575 - 650	21.1 / 297.6	0.9	
11AB3	0 - 300	20.9 / 293.9	1.5		575 - 650	24.0 / 294.3	1.8	
11B01					500 - 575	27.5 / 293.2	1.6	
11B02	0 - 450	31.0 / 293.9	1.2		500 - 575	28.9 / 296.7	2.9	
11B03	250 - 300	26.1 / 298.2	2.9		550 - 600	23.5 / 302.9	3	
11B04	250 - 400	27.8 / 295.6	2.8		550 - 650	27.5 / 302.2	0.8	
11B05					575 - 650	26.0 / 300.7	0.5	
11B06	LOST!							
					fish aver'ge	**alpha 95 K**		
			0 - 450		26.2 / 296.1	4.0 164.5		
			500 - 650		25.9 / 297.4	2.6 321.6		
10A01	0 - 350	16.1 / 302.5	2.6		550 - 675	17.8 / 301.5	1.6	
10A02	200 - 350	15.4 / 311.1	1.9		600 - 675	14.4 / 314.0	0.1	
10A03	200 - 300	18.0 / 313.3	1.6		550 - 600	19.8 / 300.1	4.5	07 / 110
10AB1	200 - 350	18.8 / 310.8	1.2		600 - 675	19.9 / 311.9	0.3	- 24 / 194
10AB2	200 - 300	20.1 / 316.1	1.8		600. - 675	20.1 / 315.3	0.3	
10AB3					600 - 675	20.1 / 315.3	0.3	
10B01	200 - 300	29.8 / 311.6	1.2		575 - 650	29.8 / 313.8	1	- 68 /007
10B02	100 - 250	28.6 / 310.6	1.9		600 - 650	30.2 / 312.1	0.9	24 147
10B03	350 - 450	29.7 / 313.0	2.3		575 - 650	29.3 / 312.7	1	
10BB1	200 - 300	38.2 / 310.9	1		450 - 550	41.4 / 291.7	4.3	
					575 - 650	32.7 / 309.2	0.2	
10BB2					400 - 650	34.0 / 303.5	1.1	
10BB3	200 - 300	- 04.2 / 310.2	2.9		575 - 650	- 04.0 / 310.8	0.1	
					fish aver'ge	**alpha 95 K**		
			0 - 450		21.1 / 311.0	7.2 45.6		
			550 - 675		22.1 / 310.0	6.2 49.3		
AV51A01	**100 - 300**	**36.9 / 353.4**	2		**400 - 675**	**7.2 / 036.1**	1.9	
AV51A02	**100 - 300**	**29.3 / 345.1**	2.6					39 /100
	40 - 550	**34.5 / 351.6**	2.2		**575 - 675**	**38.4 / 355.3**	0.9	
AV51A03	**200 - 500**	**40.3 / 349.4**	2.6		**550 - 650**	**46.0 / 353.8**	0.6	39 / 100
AV51AB1	**200 - 400**	**35.8 / 313.9**	4.8		**600 - 675**	**33.5 / 313.9**	0.7	05 / 006
AV51AB2	**100 - 300**	**48.3 / 337.5**	8.3		**500 - 675**	**30.2 / 215.4**	1.3	71 / 056
AV51AB3	**200 - 500**	**44.2 / 338.9**	4.9		**550 - 675**	**38.4 / 335.5**	3.8	
AV51B01	**200 - 350**	**39.0 /355.0**	1.7					
	350 - 500	**32.5 / 357.7**	0.2		**550 - 650**	**37.3 / 350.2**	1.9	
AV51B02	**200 - 350**	**23.9 / 351.5**	5.1					
	400 - 500	**37.3 / 341.6**	3.4		**575 - 650**	**34.8 / 339.6**	0.6	
AV51B03	**300 - 400**	**49.1 / 002.5**	3		**550 - 650**	**36.4 / 352.4**	3.5	
					fish aver'ge	**alpha 95 K**		
			0 - 500		36.5 / 345.3	11.8 20.0		
			300 - 500		34.9 / 350.1	10.8 131.5		
			550 - 675		42.2 / 343.8	26.2 4.8		
24A01	100 - 400	- 28.1 / 010.4	4.7		400 - 600	-35.4 / 014.3	0.9	- 12 / 307
24A02					450 - 650	- 30.1 / 358.2	2.1	- 41 / 222
24A03					500 - 600	- 26.7 / 001.9	1.6	- 03 / 046
24A04	200 - 300	- 23.5 / 002.1	2.2		500 - 600	- 34.0 / 004.5	0.4	- 29 / 016
24A05	200 - 500	- 27.7 / 002.3	2.2					- 16 / 042
24A06	100 - 300	- 21.7 / 354.2	3		500 - 650	-26.4 / 3.9	1.6	
24B01	0 - 400	- 26.4 / 004.1	2.9		500 - 650	- 31.0 / 012.9	0.7	
24B02	100 - 500	- 29.4 / 012.3	3.9					
24B03	200 - 400	- 32.5 / 011.0	4.5		450 - 575	- 35.3 / 022.1	4.6	- 34 / 309
24BB1	*100 - 300*	*01.8 / 183.1*	*2.5*		*550 - 600*	*00.5 / 194.5*	*0.2*	*59.1 / 164.7*
24BB2	*200 - 500*	*- 00.5 / 184.5*	*3*		*550 - 600*	*- 03.6 / 193.1*	*2.5*	
24BB3					*0 - 500*	*01.9 / 185.5*	*2.9*	
					fish aver'ge	**alpha 95 k**		
			0 - 500		- 27.2 / 005.1	5.1 141.2		
			450 - 650		- 31.5 / 008.0	6.0 100.9		

Table 3.2.1

39A01	100 - 300	07.9 / 163.6	2.5		450 - 600	28.8 / 192.5	3	-35 / 267
39A02	100 - 300	13.7 / 198.4	3.5		450 - 600	30.0 / 191.3	4.6	05 / 322
39A03					450 - 600	25.0 / 198.8	6.1	-02 / 119
39AB1	100 - 250	37.3 / 186.1	3.3		450 - 600	7.5 / 188.0	2.2	35 / 283
39AB2					400 - 600	17.8 / 195.4	0.8	- 49 / 187
39AB3					400 - 600	13.8 / 188.8	2.8	-47 / 168
39B01					450 - 600	- 09.9 / 008.8	2.8	- 41 / 284
39B02					500 - 600	- 07 / 005.9	2.6	- 09 / 282
39B03					500 - 600	- 15.3 / 346.9	1.5	- 70 / 338
39BB1					500 - 600	- 25.5 / 006.8	2.8	- 57 / 336
39BB2					500 - 625	- 20.8 / 006.5	2.9	- 29 / 230
39BB3					400 - 600	- 29.3 / 006.4	1.2	01 / 212
						fish aver'ge	**alpha 95**	**k**
					400 - 600	- 19.4 / 007.9	6.1 52	
					100 - 300	20.2 / 182.4	36.5 12.5	
40A01					550 - 650	- 30.8 / 08.4	3.4	
40A02					575 - 650	- 33.5 / 015.0	3.6	
40A03					550 - 650	- 34.6 / 013.3	3.1	58 / 044
40AB1	350 - 450	01.4 / 352.4	3.1		550 - 650	- 28.7 / 001.6	2.2	
40AB2	200 - 400	05.0 / 334.3	4.1		550 - 650	- 31.5 / 007.8	2.5	- 38 / 264
40AB3	300 - 400	05.2 / 336.6	1.2		550 - 650	- 25.8 / 010.8	2.5	30 / 256
						fish aver'ge	**alpha 95**	**k**
					550 - 650	- 30.9 / 009.4	4.3 243.8	
40B01					500 - 600	- 18.8 / 153.7	0.1	
40B02	200 - 450	03.2 / 129.4	4.9					- 23 / 059
40B03	300 - 500	01.3 / 136.5	2.2		550 - 700	-34.9 / 067.9	3.6	47 / 239
40BB1	400 - 500	- 00.4 / 133.3	4.9		550 - 625	- 44.1 / 063.3	3.2	19 / 118
40BB2	200 - 500	02.6 / 137.8	4.5		550 - 700	-45.6 / 062.4	1.9	- 78 / 143
40BB3	100 - 400	08.4 / 138.7	1.1		550 - 625	- 43.5 / 058.5	5.6	- 43 / 248
						fish aver'ge	**alpha 95**	**k**
					500 - 700	- 44 / 081	34.8 5.8	
41A01	100 - 250	20.3 / 178.3	1.9		600 - 700	06.3 / 172.9	2.7	-48 / 267
41A02	300 - 550	- 10.6 / 183.3	3		575 - 675	- 07.6 / 174.6	3.3	-42 / 097
41A03	300 - 550	- 08.9 / 197.0	3		500 - 675	-3.2 / 185.9	3.2	34.4 / 320.5
41AB1					500 - 675	- 22.9 / 155.2	1.1	- 25 / 247
41AB2					625 - 675	- 001.0 / 156.4	1	- 43 / 033
41AB3	300 - 500	- 14.4 / 162.9	1.6		600 - 650	- 10.4 / 154.1	0.8	39 / 266
41B01	250 - 400	- 41.7 / 223.5	0.5		550 - 650	- 16.1 / 208.4	2.7	- 15 / 225
41B02					500 - 675	- 16.5 / 216.4	1.9	- 40 / 024
41B03	100 - 250	- 39.2 / 219.3	2.4		550 - 675	- 20.4 / 216.7	1.6	30 / 150
	350- 450	- 41.0 / 222.6	2.1					
41BB1	100 - 350	- 04.4 / 207.2	5.2		500 - 675	00.6 / 220.4	2.6	-80 / 255
41BB2	100 - 550	- 21.6 / 220.9	2.5		575 - 700	- 06.1 / 239.2	7.9	29 /031
41BB3	100 - 400	- 25.0 / 222.0	3.9		550 - 700	- 12.6 / 240.9	9.7	-54 / 025
49ZB1								
49A01	noise							
49AB1	noise							
49AB2	0 - 200	09.6 / 331.6	9.1					
49B01	0 - 200	19.8 / 337.6	26.6					
49B02	0 - 200	42.7 / 343.1	5.6					
49B03	0 - 300	27.2 / 336.3	5.6					
49BB1	0 - 250	8.8 / 320.1	7.1		100 - 550	-21.1 / 318.1	6.7	
49BB2	*0 - 300*	*- 1.9 / 324.1*	*7*					
49BB3	0 - 350	21.9 / 331.2	15.4					
						fish aver'ge	**alpha 95**	**k**
					0 - 350	18.4 / 331.5	12.3	25.1
47002	8.3							
47AB2		**REJECTED**						
47AB1								

Table 3.2.1

48bz1, 48az1, 48az2, 48az3.								
48A01	350 - 550	31.6 / 117.1	4.3					44 / 132
48A02	0 - 300	- 66.4 / 009.0	3.6					
48A03	350 - 500	36.0 / 113.0	4.6		575	63.0 / 099.2		41 / 217
48AB1	noise							
48B01	noise							
48B02	0 - 300	10.9 / 025.9	6		REJECTED			
50A01	100 - 300	05.7 / 355.3	3.1		400 - 500	08.4 / 335.0	2.8	
50A02	200 - 400	27.4 / 338.5	1.8					18 / 039
50AB1		unstable						25 / 185
50AB2	0 - 350	- 24.9 / 162.6	16.1					
50B01					300 - 500	56.1 / 315.6	3.3	41 / 170
50B02					0 - 550	57.8 / 320.2	3.2	41 / 165
50B03					0 - 300	69.9 / 334.6	7.5	22 / 165
50BB1	0 - 200	13.8 / 336.2	6.1		350 - 450	56.4 / 344.0	3.5	15 / 001
50BB2	200 - 300	19.6 / 005.0	2.9		350 - 550	12.5 / 351.4	5.9	
						fish aver'ge	alpha 95	k
					0 - 400	18.6 / 347.6	13.9	31.2
					-550	44.7 / 335.6	24.1	8.7
44A01	100 - 200	34.1 / 069.3	1.1		200 - 350	38.4 / 055.7	2.2	68 / 002
44A02	noise							
44AB1					300 - 500	41.5 / 291.9	8.1	
44AB2	noise							
44B01	noise							
44B03	noise							
44AB3	100 - 300	48.9 / 238.6	3.9		400 - 575	20.6 / 209.3	12.6	
44BB1								
44BB2					150 - 500	- 01.9 / 013.3	15.2	
44BB3					100 - 500	- 12.4 / 004.0	12.8	
					REJECTED			
43AB1	350 - 550	- 07.0 / 181.9	15.3					
43AB2	400 - 550	01.5 / 208.0	3.5					27 / 213
43B01	noise							
43B02	400 - 600	- 14.6 / 045.6	9		550	31.5 / 044.5		- 03 / 083
43B03	100 - 400	21.8 / 021.7	5.6					
43BB1	noise							
					REJECTED			

Table 3.2.1

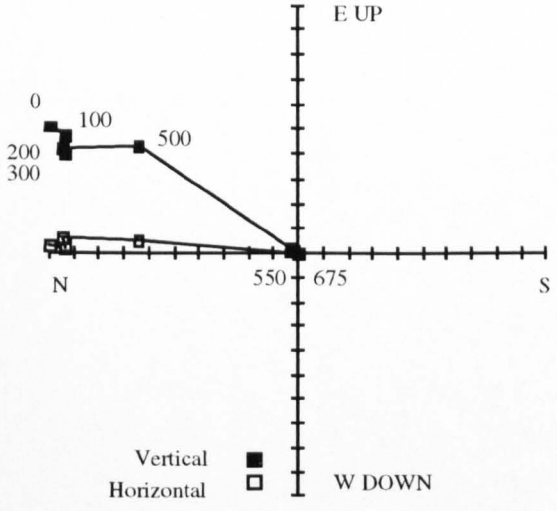

Figure 3.2.1 Orthogonal plot for core QM24A04. The numbers refer to the demagnetising temperatures.

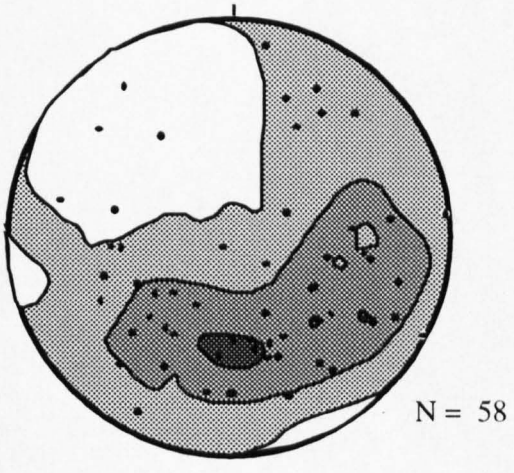

Figure 3.2.2 Contoured lower hemisphere stereo net of subtracted low temperature components (0 - 150^{o} C) from 58 cores throughout the sampled region. Darker shading indicates higher density of data points.

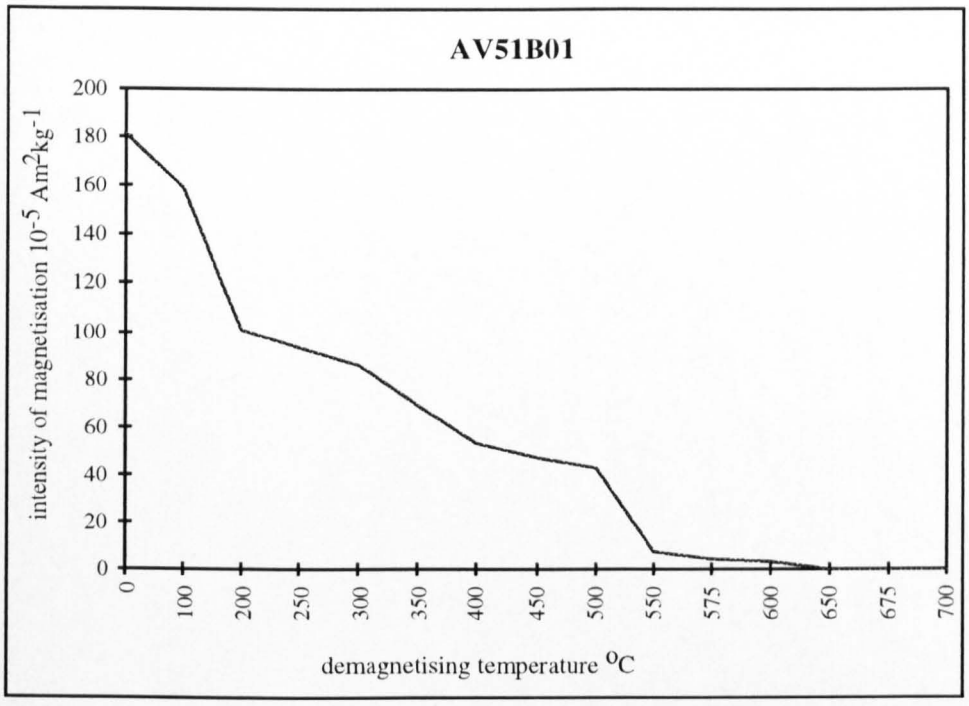

Figure 3.2.3 Variation in magnetic intensity during thermal demagnetising of core AV51B01.

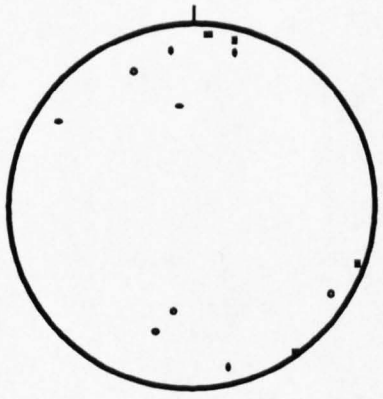

Figure 3.2.4 Stereo plot of 14 data points from cores at sites RF39 RF40, PS41 and AV51. Data points are magnetic directions determined from thermal cleaning over the temperature interval 100 - 300^o C.

3.3 Individual Site Results

Sites along the Sierra de Varas fault

Palaeozoic Units (Sites PS41, PS43, AO44, AO47, AO48, AO49, AO50 and AV51)

Samples were taken from Palaeozoic intrusive bodies (with ages shown on Map 3.1). Those without isotopically determined ages have both tectonic and stratigraphic contacts with dated units and a similar mineralogy. The units have been assigned to the Upper Palaeozoic to Lower Triassic magmatic belt extending from southern central Argentina to northern Chile (Niemeyer et al, 1985, Davidson et al, 1983, reported in Jesinkey et al, 1987). Regional correlations (Hervé et al 1991) have constrained the units without isotopically determined ages (AO50, AV51, PS41 and PS43) to the Early Permian to Late Carboniferous.

Sites AO48 and AO47 have weak magnetic intensities and no stable magnetic signal following thermal cleaning. The low ferromagnetic content also prohibited any successful identification of AMS.

The other Palaeozoic units sampled along the Sierra de Varas fault are analysed comparatively. Table 3.3.1 shows a summary of results in order of location from north to south along the fault. Within site PS41 there were inconsistent results from separately oriented blocks, Table 3.2.1. Whether this is the result of inhomogeneous magnetisation or remagnetisation whilst drilling, is unclear and the sample data remain statistically non-significant. Samples PS43 and AO44 failed. Figure 3.3.1 shows the ChRM determined from samples AO49, AO50 and AV51. Whilst all three samples have large 95% confidence circles, they yield approximately consistent ChRM directions. The lower temperature components (0° - 500° C, Table 3.3.1) have a lower inclination, but higher azimuth than the higher temperature components. The lower temperature component directions are inferred to reflect a secondary magnetisation.

From the anisotropy data it is apparent that there is no common shape fabric in the different units beside the fault, Figures 3.3.1 and 3.3.3. The degree of anisotropy is less than 2, for all samples and more typical of fabrics generated during flow of magmas, than during deformation (Hrouda, 1982). Therefore it is inferred that the anisotropy probably does not reflect the strain axes at the time of faulting. Comparison of primary magnetic anisotropy along the faults, would only be valid if the units have the same age-common initial axes of anisotropy; it cannot be realistically attempted to evaluate this here because the fabric of an intrusive body may well vary over the km scale of sampling. Comparison of like units AV51 and AO50 is also not possible as AO51 exhibits isotropy of magnetic susceptibility. Comparison of the orientations of anisotropy axes from sites AO49 and PS43, both samples of Permo-Carboniferous tonalites with similar igneous

Site No	AO44	AO49	AO50	AV51	PS41	PS43
GR	S 24^{o} 38'20" W69^{o} 12'24.6"	S 24^{o} 42'5.8" W 69^{o} 11'28.2"	S 24^{o} 40' 12.9" W 69^{o} 10'30.3"	S 24^{o} 48' 30.4" W69^{o} 09'32.9"	S 24^{o} 57'15.5" W 69^{o} 8'34.56"	S 24^{o} 54'40.4" W 69^{o} 8'36.7"
Unit	tonalite	tonallite	rhyolite porphyry	porphyritic rhyolite	tonalite - dacite	
Age	284+/-7 (bt) 241+/-12(amph)	273+/-15 (bt)	Permo-Carboniferous		Permo-Carboniferous	
dating technique	K / Ar	K / Ar				
equivalent units?	AO48	AO44	AV51	AO50		AO49
0 - 500^{o} CRM	failed	18/ 331	18 / 347.	36 / 345	-10 / 190	failed
α_{95}		12.3	13.9	11.8	18.7	
550 - 675^{o} C ChRM		unstable	44.7 / 335.6	42.2 / 343.8		
α_{95}			24.1	26.2		
magnetic carrier			magnetite	magnetite and haematite	magnetite	
intensity ($Am^{2}kg^{-1}$)		1.5×10^{-8}	0.4×10^{-5}	100×10^{-5}	200×10^{-5}	
No components		1	2	2		
AMS P	1.076	1.023	1.05	none	1.08	1.02
oblate / prolate inconclusive	oblate	oblate	prolate	equant	oblate	
k1	21 / 340	32 / 158	78 / 076	N/A	65 / 308	24 / 020
α_{95}	0.0	9.6	15.9		0.0	0.0
k2	35 / 049	62 / 008	8 / 289		55 / 215	75 / 248
α_{95}	19.6	18.7	41.4		0.0	41.4
k3	65 / 219	40 / 274	48 / 137		67 / 120	48 / 137
α_{95}	8.5	0.0	40.9		0.0	40.9

Table 3.3.1 Results of palaeomagnetic and magnetic fabric analysis of sites along the Sierra de Varas Fault. Samples are in order of occurrance, from north to south, along the fault. AO48, AO47 and PS42 were too weak to produce a consistent ChRM or AMS.

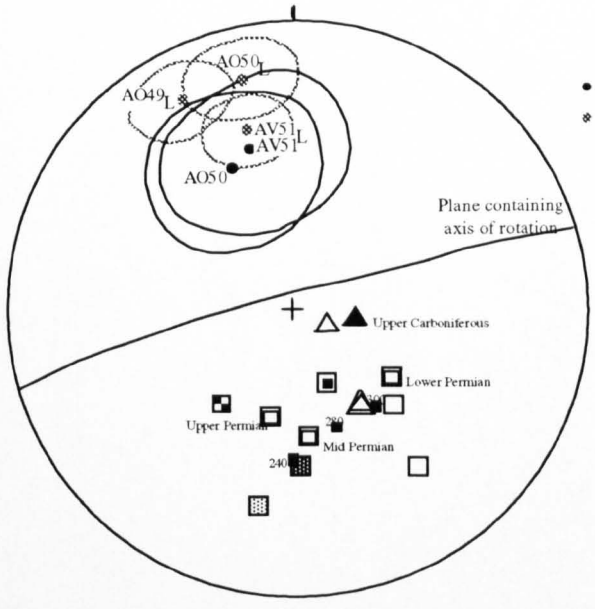

Valencio and Mitchell, 1972	263 +/-5 Ma	Beck et al, 1991	299 +/-5 Ma
Rapalini 1991	Permian	Vilas, 1981	Carboniferous - Early Permian
Vilas and Valencio, 1982	276+/-5 Ma	Creer 1965	Mid Upper Carboniferous
Rapalini and Tarling, 1993	Early Permian	Rapalini et al, 1994	Mid Carboniferous
Truco and Rapalini, 1996	Early Permian	Irving and Irving, 1982	Ages written beside

Figure 3.3.2 The ChRM and 95 % confidence circles for Palaeozoic samples along the Sierra de Varas fault contrasted with palaeofield magnetism calculated from the APWP of South America, for the same location. Sources of the APWP data are given above. Lower hemisphere plot. The great circle contains the likely axis of rotation that mapped the Permian palaeofield magnetisation onto the ChRM determined in this study.

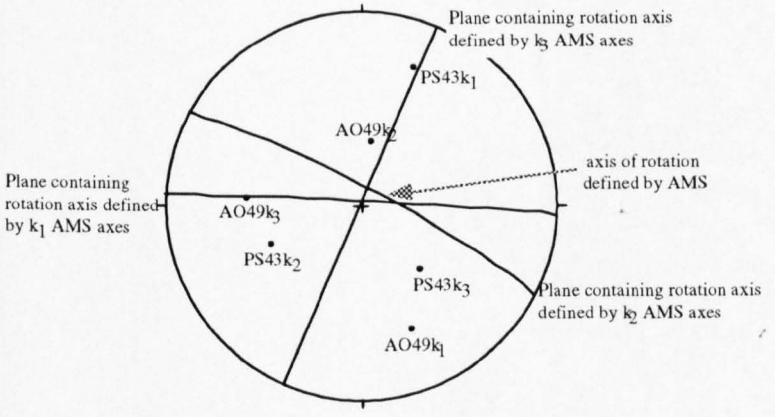

Figure 3.3.2 Axes of rotation as defined using the axes of AMS from samples 43 and 49 (equivalent units). Lower hemisphere plot. The axis of rotation can map the two AMS axes onto eachother.

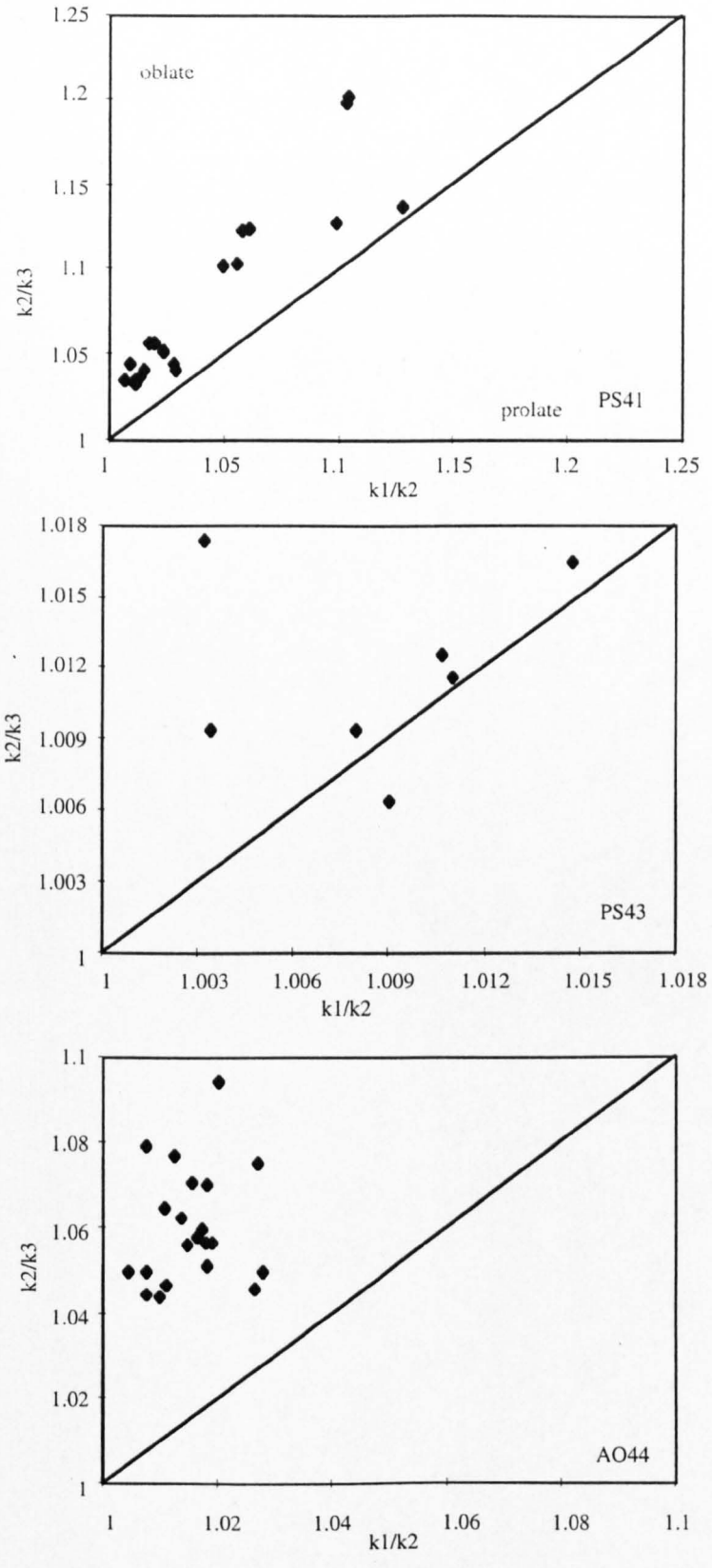

Figure 3.3.3a) Flinn diagrams illustrating the degrees of anisotropy for Palaeozoic sites along the Sierra de Varas fault

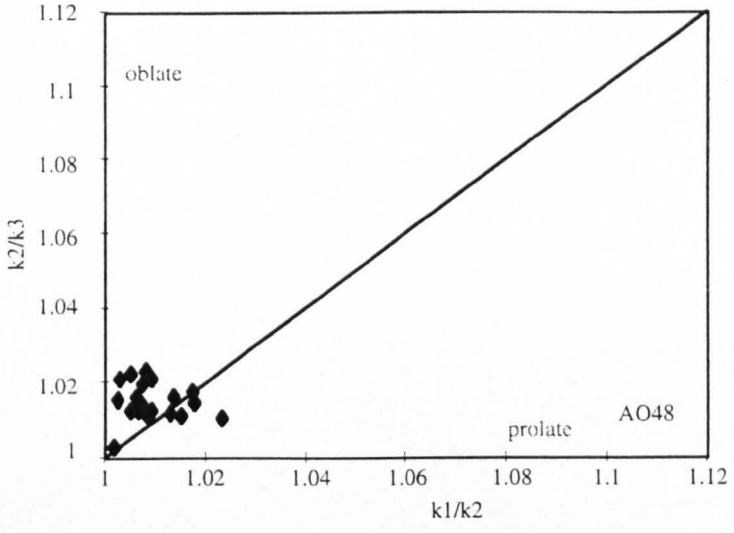
1.12
1.1
1.08
1.06
1.04
1.02
1
k2/k3
oblate
prolate
AO48
1
1.02
1.04
1.06
1.08
1.1
1.12
k1/k2

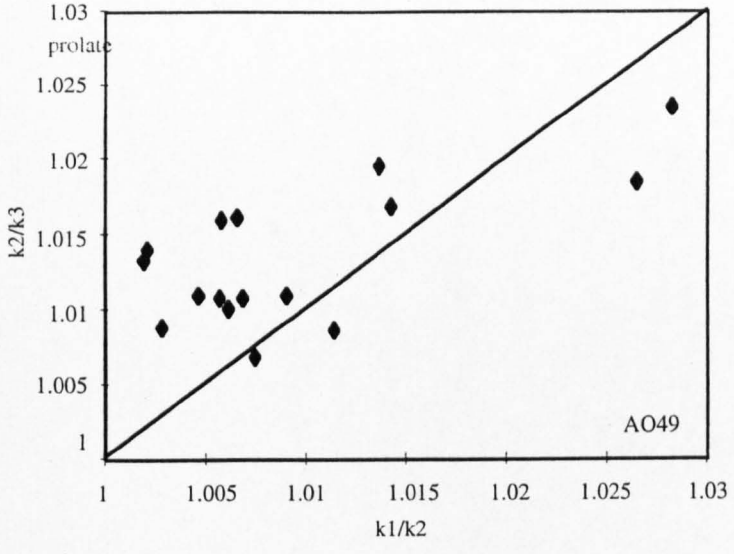
1.03
prolate
1.025
1.02
1.015
1.01
1.005
1
k2/k3
AO49
1
1.005
1.01
1.015
1.02
1.025
1.03
k1/k2

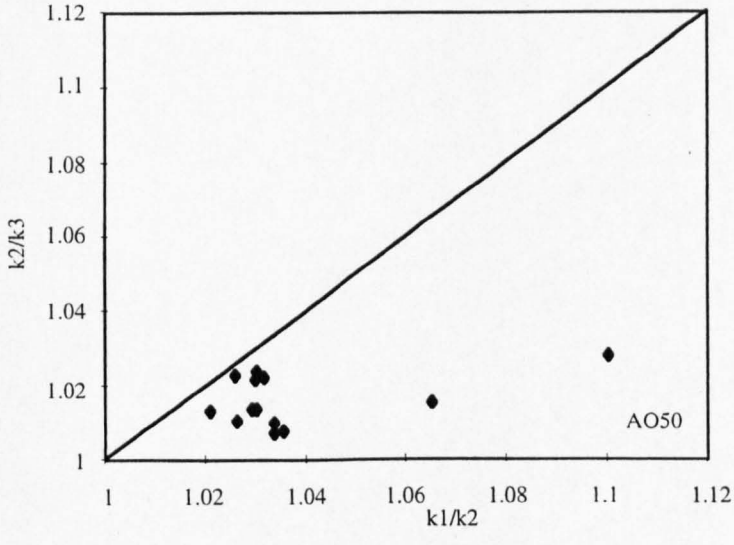
1.12
1.1
1.08
1.06
1.04
1.02
1
k2/k3
AO50
1
1.02
1.04
1.06
1.08
1.1
1.12
k1/k2

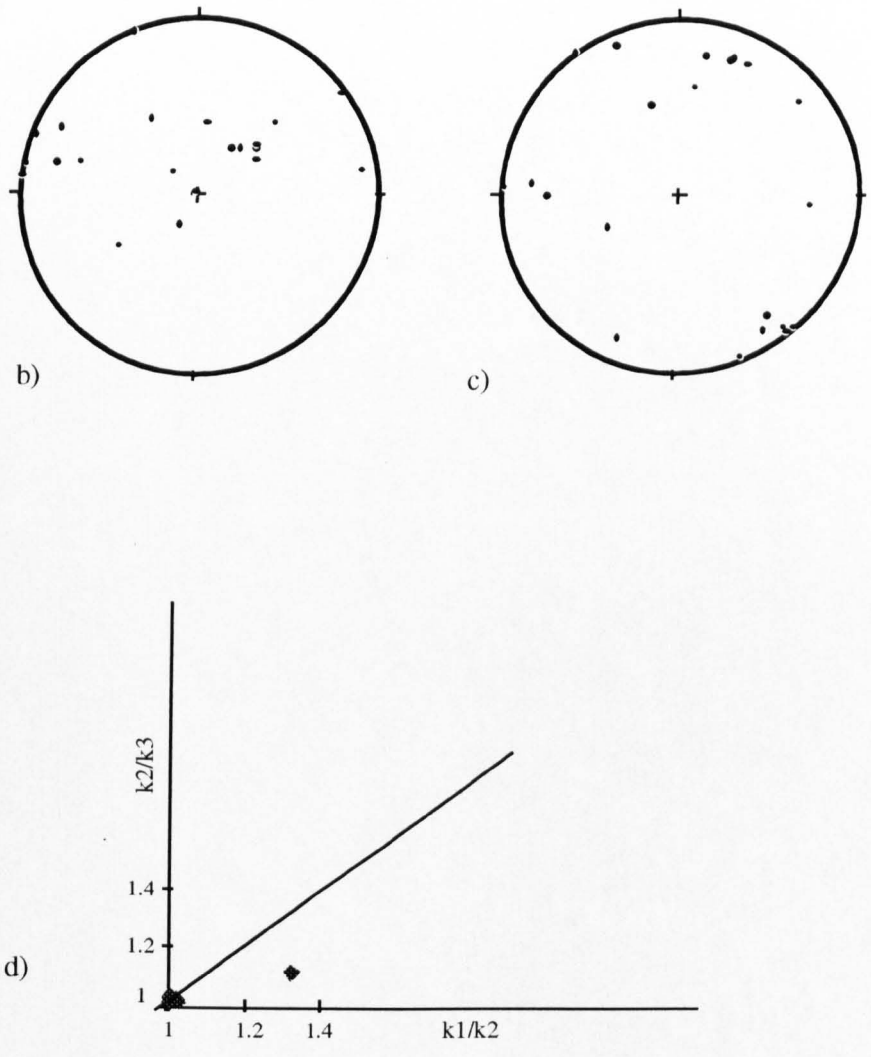

Figure 3.3.3 b), c) and d). Stereonets and Flinn plot, showing anisotropy of magnetic susceptibility for site AO48. (b) The orientation of the maximum axis (k_1) of magnetic susceptibility. (c) Orientation of the minimum axis (k_3). (d) Flinn diagram. (The line of a gradient 1 represents isotropy.) Since the distribution of data points falls along this line, sample AO48 is essentially isotropic.

textures, identifies a subvertical axis of rotation, with approximately 130° of rotation, Figure 3.3.1. This would correspond to a subvertical intermediate strain axis obeying the Andersonian model for strike slip faulting, however this would be a large variation in rotation produced by a displacement gradient and is not supported by the directions of magnetisation.

Comparative palaeofield directions in the study area computed from the APWP for stable South America are listed in Table 3.3.2. Since 300 Ma there has been little change in the predicted geomagnetic field directions in South America. The scatter of the computed palaeofield directions at 240 - 300 Ma is equivalent in magnitude to the 95% confidence intervals around the ChRM's measured at these sites. Determining the exact age of the samples , within 10 Ma is irrelevant as the APWP is more precisely defined than the palaeomagnetic results from single site means. Recognition of the unit as Early Permian in age is sufficient for the purposes of this study.

In general the lower blocking temperature components removed over the temperature interval 0°- 500°C are unlikely to be primary and may have resulted in part from hydrothermal alteration. The higher temperature components (the ChRM's) are most readily interpreted as primary acquisitions. There is some uncertainty as to the age of the magnetic remanence within the samples. Thin sections of AO49 show it to be a brecciated igneous porphyry, with cracked and strained anhedral quartz phenocrysts, chlorite veins and occasional chlorite alteration surrounding the opaques. Samples AO50 and AV51 are less altered and sample AV51 displays a pristine igneous texture. York (1978) showed that the forms of the equations governing isotopic and magnetic blocking temperature are identical, so that the Ar/Ar and K/Ar ages can give reliable estimates of the magnetic age provided that low temperature alteration has not occurred. The deformation that influenced these rocks has occurred at low temperatures, well below the blocking temperature of the magnetic minerals. The magnetic remanences could however, have been partially reset by low temperature hydrothermal activity. There is no visual evidence of hydrothermal fluid alteration in samples AO50 and AV51 and no apparent fracturing of opaques. The only evidence for hydrothermal alteration is indirect and comes from a unit to the east of AO49. The K/Ar age of 274 Ma (Mpodozis et al, 1993) is similar to unaltered units in the Domeyko. The K/Ar system has clearly remained closed since Permian times.

Virtual geomagnetic poles (VGPs) calculated for the ChRM from sites AO49, AO50 and AV51 are listed in Table 3.3.3. These results are not coincident with the APWP, Figure 3.3.1. Since instantaneous resetting of the magnetic direction during a geomagnetic excursion could only be a very occasional explanation for this discordance, it would appear that tectonic rotation, of these sites in the proximity of the Sierra de Varas fault is the most likely reason for differences between the observed and predicted palaeomagnetic directions. The inclination of the ChRM indicates reverse polarity at time of acquisition. This would be

Age / Ma	Predicted Direction	
10	-49 / -003	
30	-339 / 001	
50	-55 / -004	
60	-50 / -008	
80	-46 / -012	
100	-45 / -006	
130	-40 / 002	
150	-53 / 005	
170	-59 / 017	
200	-53 / 019 (53 / -161)	58 / -173
240		48 / -178
280		56 / 161
300		54 / 140

Table 3.3.2 Predicted declination and inclination of the ambient magnetic field in the study area at 24.5^{O}S, 291^{O}W. Negative inclination is in the upper hemisphere and negative declination is measured from N anticlockwise. Directions from 10 - 200Ma are calculated from Roperch and Carleir (1992); directions from 200 - 300Ma are calculated from Irving and Irving (1982).

Site	VGP (lat, long)	dp/dm
AO49	15.5^{O}N, 143.4^{O}W	8.9^{O}, 17.4^{O}
AO50	7.5^{O}N, 129.136^{O}W	13.6^{O}, 22.5^{O}
AV51	6.8^{O}N, 127.9^{O}W	20.0^{O}, 32.3^{O}

Table 3.3.3 VGPs calculated from ChRM directions determined from sites along the Sierra de Varas fault. The procedure for pole determination can be found in Butler (1992). Dp and dm are the semi axes of the confidence ellipse about the pole positions.

compatible with a primary magnetic remanence acquired between 250 - 320 Ma, an interval during which uniform reverse polarity characterised the Kiaman Reverse Superchron (Harland et al 1989). The internal consistency of the samples, maintained closure of the K/Ar system and polarity all suggest a primary NRM.

Work by Jesinkey et al (1987) in an Early Permian igneous unit, La Tabla Formation (GR 51°S, 347°E) sited 14 km to the west of the study region, showed that the ChRM concurs with the APW path of Irving and Irving, 1982. This indicates that rotations observed in the vicinity of the fault zone are distributed over a restricted zone about the fault and do not apply to a belt wider than ~10 km.
The orientation of the remanent magnetism calculated from the Carboniferous to Triassic APW path for the location of the Palaeozoic sites is shown in Figure 3.3.1. The fault has caused clockwise rotation of units immediately to its east. There are two possible models for this rotation:

1) the rigid block bound by the fault has undergone a clockwise rotation during sinistral motion, or

2) the deformation is not discrete at the fault surface and smaller blocks have taken up the deformation nearer the fault margin, this is compatible with a dextral offset.

The slip surfaces found to the East of the fault have only been observed near a bend in the fault trace (for example at Agua el Oro, Ch 2.3). Few slip surfaces have been found beside straight segments of the fault The kinematic analysis of the slip surfaces showed they were linked to dip slip faulting. There is no evidence that lateral motion along the Sierra de Varas Fault was accommodated anywhere other than along the discontinuity of the main fault surface. The clockwise rotation observed in the palaeomagnetic data can therefore be explained in terms of a sinistral offset along the fault.

During the observed rotation of ~160°, the shape of the rotating body is likely to have changed (Lamb, 1987); although to discuss the initial shape is highly speculative. Mpodozis et al (1993) divided the Domeyko at this latitude into the La Escondida Shear Lens bound by the Sierra de Varas and La Escondida Faults. To the east, ~50° of clockwise rotation was recognised. These observations can be explained by invoking a zone of distributed deformation (McKenzie and Jackson, 1986) across the Domeyko range. This model is discussed further in the final chapter when the constraints from other chapters are added.

Reverse faulting on the slip surfaces at Agua el Oro is linked to dextral faulting (Ch 2.3). The slip surfaces occur a similar distance away from the bend in the fault trace as site AO49. The compression experienced at the bend in the fault is transmitted away from the bend. It can be supposed that a sinistral motion causing ~160° of rotation of a body up to 4 km across, will have sizable displacement (a minimum of 4 km). A sinistral motion is expected to cause an extension at the bend in the fault. The extension is anticipated to be transmitted through the rocks, to be accommodated across a distance near to the fault bend. The vertical component of displacement due to the extension is expected to cause a rotation of the rocks about a

horizontal axis. This would result in differing inclination of NRM when compared with sites further away from the bend in the fault, where no vertical motion, is believed to have occurred. In fact all the ChRM's are oriented within 95% confidence limits of each other. Since the rotation about a horizontal axis is not observed, the kinks in the fault trace are inferred to have formed after the large sinistral offset was complete. A tentative chronology of deformation starts with a large sinistral displacement along the Sierra de Varas fault, followed by an event causing the fault to bend, then a minor dextral displacement. The dextral displacement must be smaller than the sinistral displacement as the net rotation of the units is attributed to sinistral offset. A thrust fault can be seen to terminate near the bend in the fault, Map 3.1. Activity on the thrust could prompt the bending of the fault trace. In summary, a large sinistral displacement along the Sierra de Varas fault was followed by thrusting on the eastern side of the fault, which was in turn followed by a relatively minor dextral movement of the Sierra de Varas fault.

Miocene Units

RF39 and RF40

Samples from these two sites in porphyritic, acidic extrusive units are taken from the Rio Frio ignimbrite on either side of the Sierra de Varas fault. The fault lineament is clearly visible on the satellite image, Figure 3.3.4, and some workers (Naranjo and Puig, 1984) have reported horizontal lineations on the fault plane at Rio Frio itself although there is little offset of the ignimbrite sheet. The Rio Frio ignimbrite is Miocene in age (18 Ma, Hervé et al, 1991). RF40 lies to the east of the fault and RF39 lies to the west. RF39 is marginally more fine grained than RF40, but both have a primary flow texture, including a weak eutaxitic texture parallel to layering, visible in thin section.

The Curie curves indicate that the dominant magnetic carrier is magnetite with some haematite, Fig 3.3.5. Two contrasting magnetic components are present in Sample RF39. The remanence from block A is antipodal to the remanence from block B and therefore of opposite polarity. The components from block B have therefore been included in the mean site remanence, by rotating them through 180° and changing the sign of the inclination.

At RF40 both blocks have normal polarity magnetic directions, although block B has a higher azimuth. Since cores from both block samples are internally consistent, it is possible that the discrepancy arises from the misorientation of one of the blocks or a recording of a transitional direction of the geomagnetic field. Eigenvector analysis of AMS results also highlight an increase in azimuth of 40B compared with 40A, Figure 3.3.6. However there is little distinction in distribution of these axes when plotted together. As there are just 12 data points from each block, the average directions for each block are not tightly defined and it

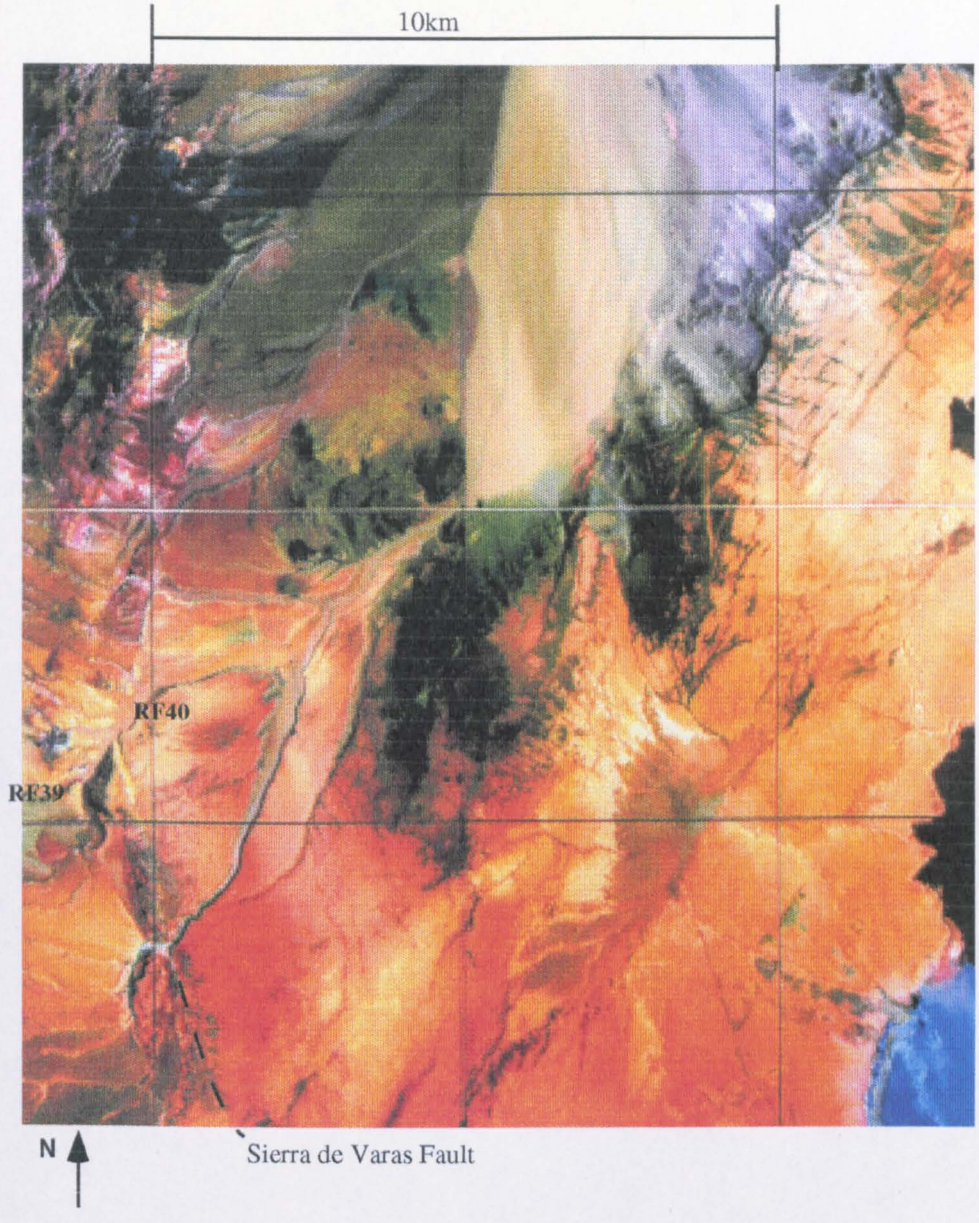

Figure 3.3.4 Satellite image of the Rio Frio ignimbrite. The Rio Frio ignimbrite can be seen as the orange sheet covering thelower portionsof the image. The Sierra de Varas Fault can be seen to the west, however no offset is visible across it. Fractures further east cut the ignimbrite and displace it. Either the latter faults moved in response to local stresses or the Sierra de Varas Fault has locked up and deformation has migrated eastward.

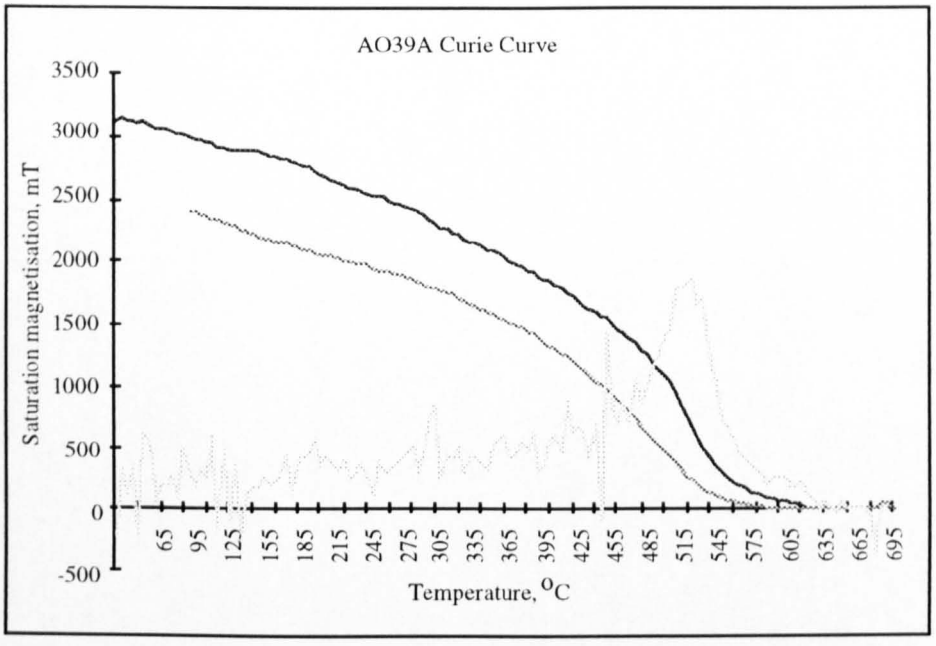

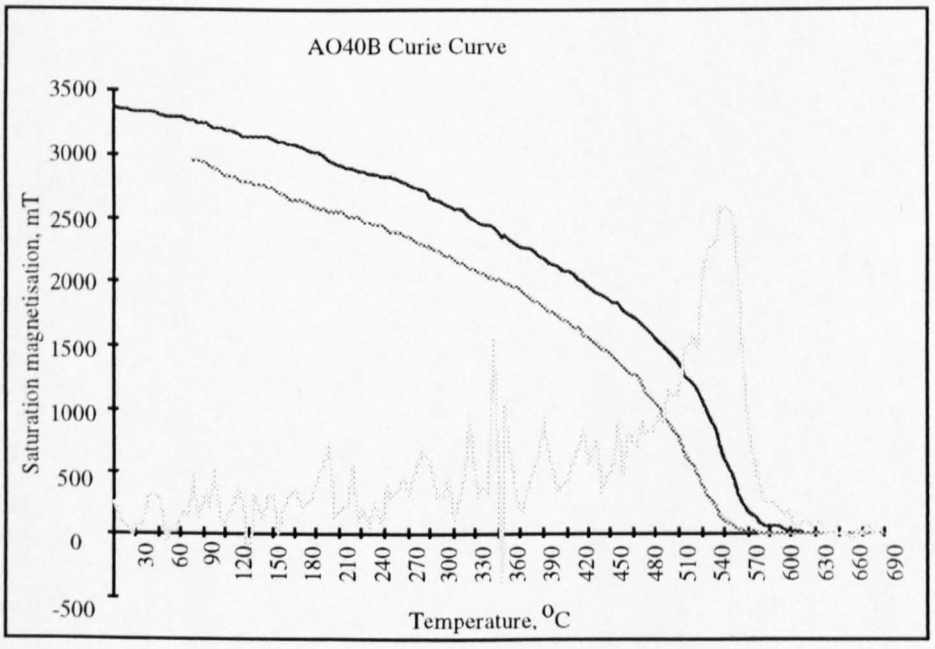

Figure 3.3.5 a) Thermomagnetic curve for RF39, block A during heating (black) and cooling (dark grey). The gradient of the heating curve is shown in pale grey, so peaks of this mark the Curie points.
b) Thermomagnetic curve for RF40, block B.

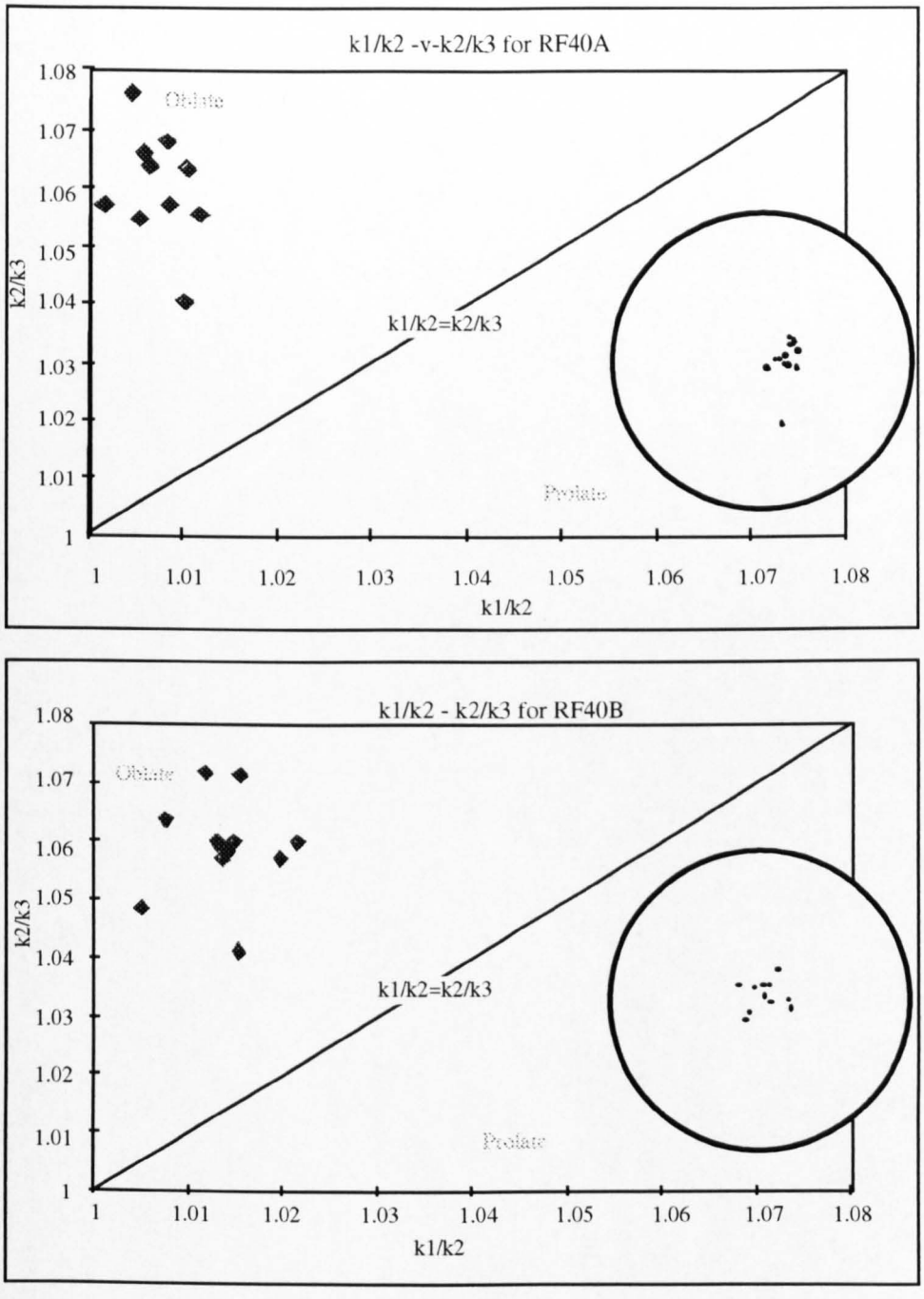

Figure 3.3.6 Flinn diagram for sample fabrics for RF40A and RF40B. Both are oblate. The k1 axes are poorly grouped, possibly reflecting local flow direction variations , whilst flattening, reflected by the drawn k3 axes (shown in inset), was a more homogeneous process.

becomes necessary to consider the ChRM's of each block. If block A (ChRM -31 / 009) is representative, a small rotation is apparent between RF39 and RF40. This would be consistent with the ignimbrite fracture pattern observed on the satellite image. If, however RF40B is representative (-44 / 081), a rotation of 60° is identified across the fault. The satellite image shows no evidence of this magnitude of rotation either from the numerous fractures associated with the Sierra de Varas fault, or as a massive rigid rotation of the ignimbrite sheet, Figure 3.3.4. Block RF40B is therefore believed to be unrepresentative; it could record a transitional direction of the geomagnetic field and has been excluded from consideration.

AMS measurements on samples RF39 and RF40 both yield oblate fabrics. The orientation of the flattening axis is typically homogeneous across a horizontal ignimbrite and parallel to the k_3 axis of anisotropy . Hence this unit appears to have a primary shape anisotropy (Fig 3.3.7) with the k_3 axis perpendicular to flow. The degree of anisotropy before thermal cleaning is 1.067 and 1.068 for RF39 and RF40 respectively. RF40 has both magnetite and haematite carriers and it is unlikely that any deflection of the remanence has occurred (Irving and Park, 1973). Core RF39BB2 however, exhibits a much higher degree of anisotropy of 1.33 and to compensate for this, the calculated actual angle between the ambient magnetic field and the NRM (calculated as 7.6° using modified equation [A3.2]) has been added to the ChRM. Application of equation [A3.2] highlights a 3.0° increase between the observed NRM and the palaeofield direction of RF39, Table 3.3.4.

Figure 3.3.8 shows the ChRM determined from RF39 and RF40 and the minimum axes of magnetic susceptibility. There is some overlap of the 95% confidence circles of the ChRM directions, implying that little or no rotation has occurred across the fault since deposition of the ignimbrite. The axis required to translate the ChRM and AMS data of the two samples onto each other is not in the plane of the fault. Since the fault strikes 341°, with a possible easterly dip (as a scarp is observed cutting the ignimbrite) and the axis of rotation does not lie within this plane, it is concluded that either no rotation is has occurred or that the fault was merely accommodating external deformation. Either result implies that no significant displacement has taken place along the fault since deposition of the ignimbrites in the Miocene.

Site QM24

Two independently oriented block samples were taken within 1m of each other, from different levels in the flow layering of the rhyolitic Liparitic Formation. The unit has been assigned an age of 14 Ma (Chong, 1977) and overlies the Miocene pediment surface. No fault traces can be seen to cut through the ignimbrite, hence any rotation determined palaeomagnetically would appear to involve a rigid block rotation.

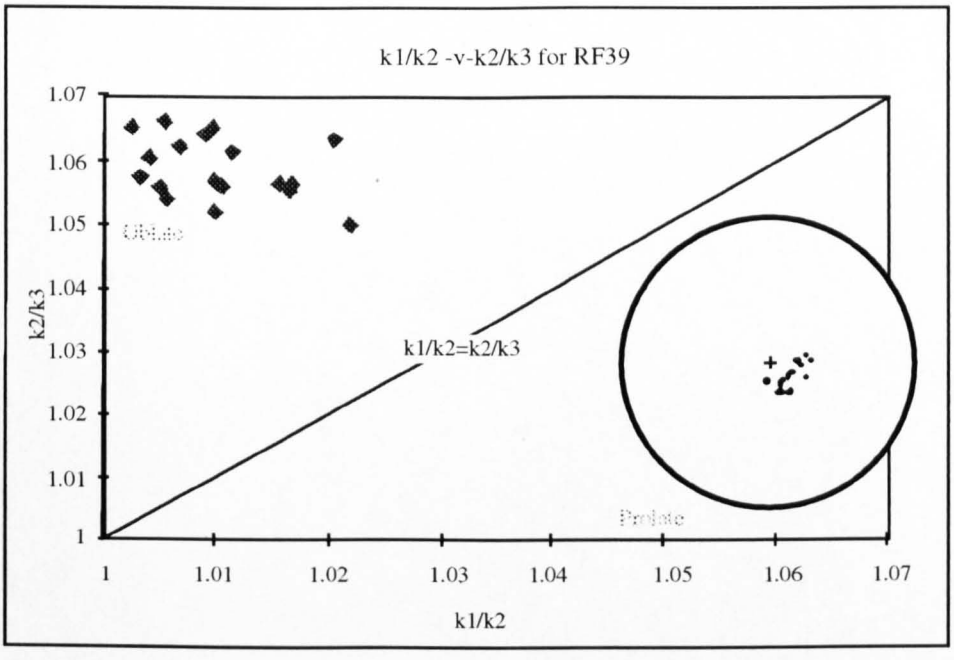

Figure 3.3.7 Flinn diagram of the AMS at site RF39. The inset stereo net shows the grouping of the k_3 axes in the lower hemisphere.

Sample	**RF39BB2**	**RF39**
Uncorrected RM	-21 / 007	-120 / 009
k1-k2 plane	160 / 28W	218 / 14W
orientation mag cpt in k_1-k_2 plane	33^o from south	28^o from north
$(\text{dimensions mag cpt})_0$	250.35	1014
alpha	7°	152°
[k3/k1-k2]cpt (ie P_0)	1.422	1.065
$(\text{dimensions mag cpt})_B$	245.77	836
P_B	1.387	1.073
beta	6.6°	3°
Corrected RM	-27 / 004	-25 / 007

Table3.3.4 Corrections to account for modifications to RM by AMS, based on a modified equation A7.2. (Uyeda et al, 1963, modified by the author).

AMS analyses were not carried out on these samples. Most of the cores yielded multi component results, again with a magnetically "soft" component removed between 0 and 100° C (only in core QM24A04 is this component aligned with the present day field). The thermal demagnetisation shows magnetic carriers to be both magnetite and haematite. However since the saturation remanence of magnetite is much higher than that of haematite, the latter is masked in the Curie curve, Figure 3.3.9; it becomes apparent by demagnetisation above 550° C when a resident haematite ChRM is resolved. Assuming the high temperature component is representative of the ancient magnetic field without no significant deflection by anisotropy of remanence, the ChRM is -32 / 009 (Table 3.2.1). The directions from QM24BB are antipodal and the dispersion of results (k = 101) is indicative of a well defined ChRM of possible primary origin. The orientation of the ChRM lies within the direction predicted from the APWP for 30 - 10 Ma (Roperch and Carlier, 1992), Figure 3.3.10. Hence it is concluded that no rigid block rotations of the region containing the Pampa Las Mulas ignimbrite have occurred since 14 my BP.

Significance of the Sites along the Sierra de Varas Fault

Mpodozis et al (1993) recognised two periods of activity along this fault: a major sinistral event in the Eocene and a minor dextral offset in the Miocene. The ChRM's determined from the Permian units are compatible with this chronology. The kinematic data are consistent with a minor dextral offset (Ch 2.3). The absence of discrepancy of inclination of ChRM from the Permian units is consistent with this order of activity, as the concurrence of inclination of ChRM's is taken to indicate the bends in the fault trace formed after the sinistral event. The Miocene ignimbrites have not been offset nor rotated by activation of the Sierra de Varas fault, so the lesser dextral event must have occurred before deposition of these units 18 Ma ago, or been transmitted along the western side of the Domeyko Fault System.

Significance of RF39, RF40 and QM24 (Miocene) results

Palaeomagnetically-determined rotations from North and South of the Arica bend at a latitude of 19°S show anticlockwise and clockwise deflections respectively (summarised in Randall et al 1996). This has been explained by two deformation models. The oroclinal model, based upon Carey (1955) and more recently cited by Isacks (1988) invokes passive rotation of two rigid crustal blocks either side of the deflection. An initially straight South American western margin is considered to have developed into two separately rotating blocks. The thickened Andean chain across the deflection could then be explained in terms of a compressive stress in the hinge area of rotation. Extension behind the hinge area is not observed however. Two phases of oroclinal bending have been inferred from the palaeomagnetic data (Beck, 1988), one pre-Late Jurassic and the other Post Miocene. From concordance of the Miocene palaeomagnetic directions with those predicted from the APWP at 24.5°S observed in this study, it is clear that there is no case for

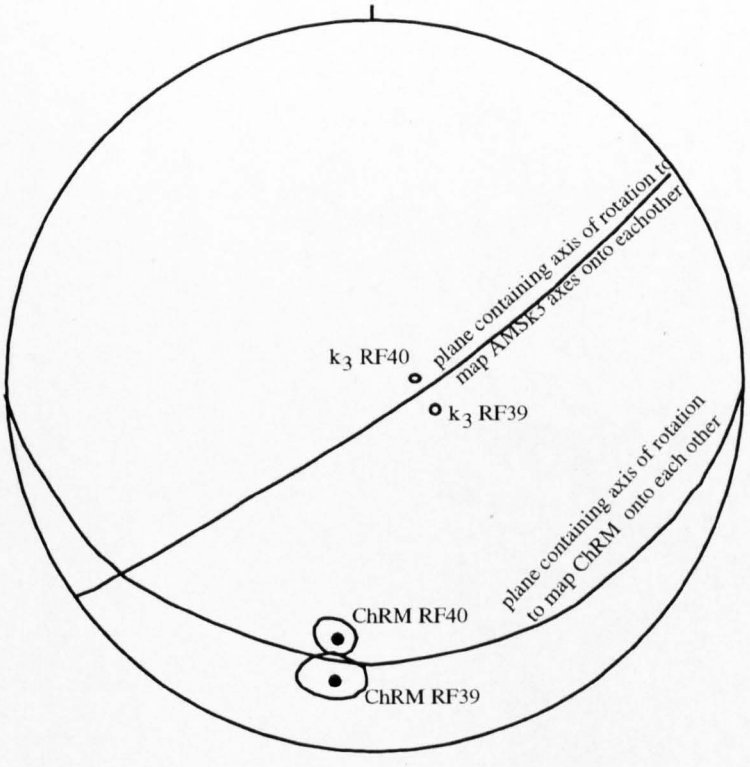

Figure 3.3.8 Stereo net showing ChRM directions for samples RF39 and RF40, sited on either side of the Sierra de Varas Fault. The ChRM's are plotted in the lower hemisphere to allow comparison of the planes containing the axis of rotation determined from AMS data, however have a negative plunge. The error circles (alpha-95) are shown around the ChRM results. The fault strikes 341^{o} with moderate to steep dip.

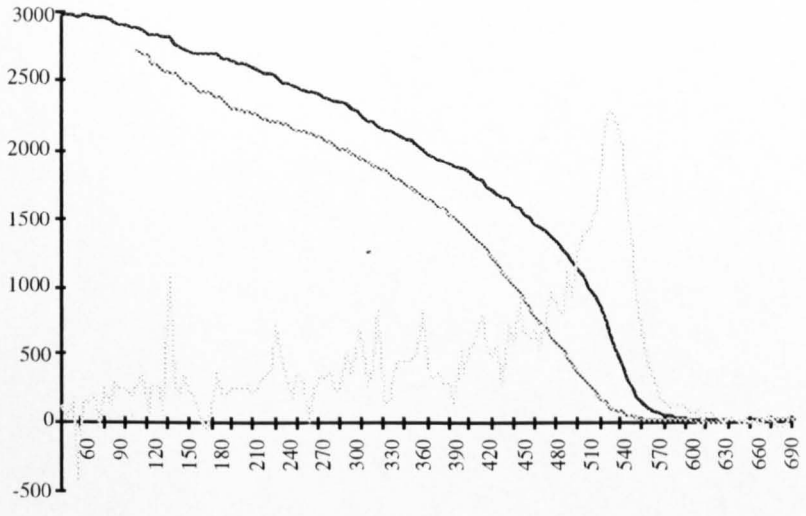

Figure 3.3.9 Thermomagnetic curve for site QM24A and representative of block B.

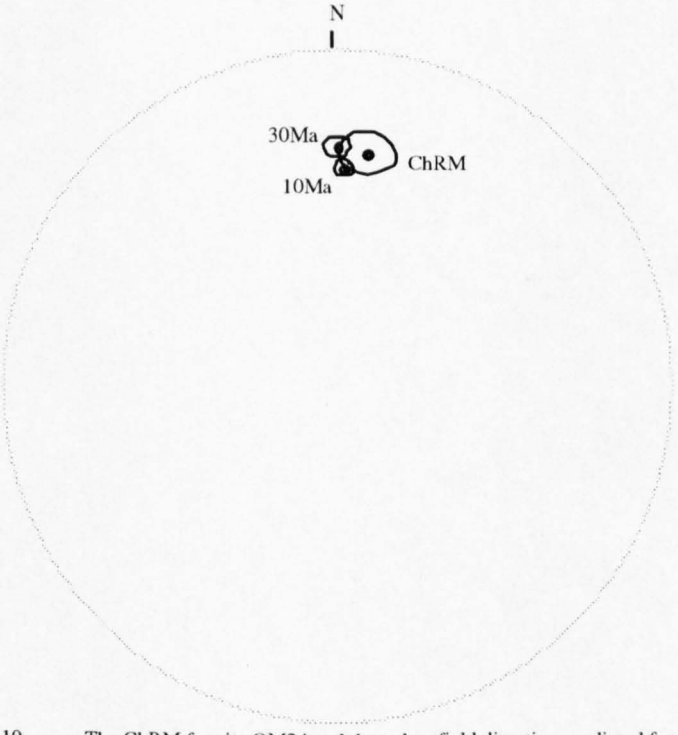

Figure 3.3.10 The ChRM for site QM24 and the palaeofield direction predicted from the APWP, at 10 and 30 Ma with 95% confidence intervals. The overlap of confidence intervals is interpretted to be due to a lack of tectonic rotation at site QM24.

passive rotation of the orogen at this latitude. Passive rotation would require either that any rotation is older than Miocene or that the timing of rotation was earlier than predicted. The second model involves domino style rotations bound by major fault systems to explain the palaeomagnetically-determined rotations. Designation of the bounding faults is still open to dispute: Forsyth and Chisholm (1994) advocate the Atacama Fault Zone and the northwest faults whilst Randall et al (1996) assign the Atacama Fault Zone and a Central Valley Shear Zone to the bounding fault systems. Whilst the results from this study cannot distinguish between the bounding faults, the 3 sites from six independently oriented blocks appear to rule out any Post Miocene passive rotations along this sector of the Andes.

Summary of Significance of Palaeomagnetic Investigations

1) The large clockwise rotation of Palaeozoic igneous units immediately to the east of the Sierra de Varas Fault can either be interpreted as evidence of dextral or sinistral motion along the fault, depending upon the model of deformation adjacent to the fault. No evidence is seen to suggest the deformation was accommodated in small blocks. The large clockwise rotation is therefore attributed to a sinistral event along the fault. A rotation of this magnitude has inherent geometrical problems. Future palaeomagnetic sampling along transects perpendicular to the fault should better constrain the model of deformation.

2) Combining this with the evidence of dextral motion along the Sierra de Varas Fault, from structural analysis of dip-slip fault surfaces in Ch 2, it becomes apparent that a reactivation of the fault with an opposite sense of displacement has occurred. The sinistral displacement is inferred to have been greater than the dextral displacement, as the net rotation of the primary palaeomagnetic signal is from a sinistral event. The dip-slip surfaces analysed in Ch2 are only present at a bend in the fault trace. No dip-slip surfaces are seen to be associated with sinistral faulting which would be anticipated if the fault surface was bent during sinistral faulting. It is inferred the sinistral faulting occurred first, then the fault surface became bent and finally a minor dextral faulting episode occurred. The bend in the fault occurs at the intersection between thrust faults with the Sierra de Varas Fault. Activity on these thrust faults in between the sinistral and dextral strike slip activity could have caused the bent fault trace.

3) No significant displacement occurred along the Sierra de Varas fault east of the Domeyko Range since deposition of the Rio Frio ignimbrite 18Ma.

4) No passive rotation of the region containing Pampa Las Mulas Ignimbrite has occurred since 14Ma.

5) There is evidence against post-Miocene passive rotation of the Domeyko Range.

Chapter 4

Detailed Fault Analysis

CHAPTER 4 DETAILED FAULT ANALYSIS

Objectives of Chapter

Resolution of the kinematics of the Domeyko Fault System (DFS) in areas that have undergone brittle deformation has been hindered by a lack of appropriate techniques for analysis of the structures. Where fault orientation, slickenline data and sense of shear are apparent, application of, for example, Marret and Allmendinger's graphic technique (1990) or Angelier's inverse technique (1989) can identify the strain axes of the system. Unfortunately a typical exposure in this and other study areas does not always provide such useful data. More commonly, a fault will include a complex system of fractures, some fracture surfaces with slickenlines and few, if any, kinematic indicators. This chapter describes the detailed analysis of a brittle fault. The outcrop studied reveals both slickenlined surfaces and a localised shear zone of intensely fractured rock. The two deformation styles are assumed to be complementary. Orthodox analysis of slip surfaces involves application of Marret and Allmendinger's (1990) technique to identify the incremental strain axes. The intermediate incremental strain axis is then used to determine the profile plane of the fault. The fracture distribution within this plane is compared with Reidel's model, to determine the sense of movement along the fault. The results are used to outline a novel analysis of the intensely fractured shear zone in Chapter 5, to define a technique for recognition of kinematics in zones of intense fracturing.

Characterisation of faulting style, including fracture geometries, conditions of faulting and distribution of fractures along the fault will allow a better understanding of faulting mechanics in this region of brittle faulting. Kinematic analysis, even without an ideal data set will have implications for the regional geological history. The timing of fault activity is also important for understanding the regional geological history.

Throughout this chapter displacement, strain and strain direction are measured and studied. The link between stress and strain is understood to be complex, dependent on rheology (Edelman, 1989). The rheology of the material has not been studied, so reference is made to principal strain axes, not stress axes. When citing work by other authors, where inferences have been made between stress and strain then the terminology of the original authors is used.

4.1 Description of the Fault Zone

At the western margin of the Domeyko Range, between S 24° 53' 36" and S 25° 11' 29.2" the contact between marine Jurassic units in the east which are thrust over Tertiary continental sediments to the west, can be observed, Map 3.1. In Q. Las Mulas, the marine Jurassic units are in tectonic contact with Neocomian - Tithonian conglomerates across a normal fault which cuts through a rhyolite dyke (Ch 2.1). The timing of normal faulting post dates the major folding and thrusting episodes experienced at this latitude (see Ch 2). The fault marks the western limit of the Jurassic exposure in the north and the eastern margin of the Punta del Viento - Las Mulas lowered block at the southern end of the fault (Ch 2.1). The lowering of the block (see Ch 2 for location) may have been contemporaneous with the main fault activity. The fault which thrust Jurassic over Tertiary strata, typically occurs along a pink coloured, silty evaporite layer of Bajocian age, with a moderate dip to the east. In Quebrada Las Mulas a sub-vertical rhyolite dyke lies oblique to the Bajocian evaporite horizon. Faults within the dyke have apparently displaced the evaporite, Figure 4.1.1. The rhyolite is cut by numerous slip surfaces of varying degrees of complexity. The juxtaposition of Bajocian and Neocomian sediments requires displacement of the order of kilometres across the strike of the fault.

The dyke strikes approximately N 040° E. Over the 150m exposure the rhyolite dyke maintains a constant strike. Throughout the conduit, numerous lineated slip surfaces are present (Figure 4.1.2), one of which was sampled in hand specimen QM42. During this study, the structures in the dyke have been mapped at a scale of 1:100 for a length of 140m, Fold out 4.1. Two palaeomagnetic sampling sites 80m apart along the fault were been established (samples QM10 and QM11). The exposure perpendicular to the fault is limited to 3-4m. The strike, dip and pitch of the slip-surfaces (sense could not be determined in the majority of cases) were recorded. There are two rhyolite units, distinguished by their colour, yellow and purple, Figure 4.1.1. The boundary between these units is generally gradational (over 1.5m) but occurs across a narrow fault zone for 4m parallel to the strike of the dyke, Figure 4.1.3. Two hand samples of the purple rhyolite were taken for Ar^{39}/Ar^{40} dating (QM56 and QM57). Paired slip surfaces bound a complex fracture network to form a localised fault zone ~60m from the reference point in Foldout 4.1. Three samples were taken of this zone, QM43, QM63 and QM65. One of the slip surfaces is the contact between the yellow rhyolite and fault zone, with purple rhyolite forming the majority of the fault rock between the slip surfaces. The bounding slip surface between the yellow rhyolite

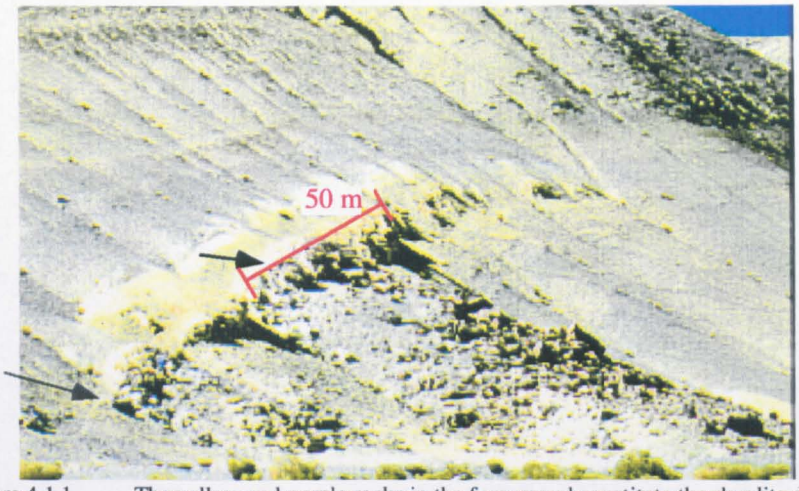

Figure 4.1.1 The yellow and purple rocks in the foreground constitute the rhyolite dyke with slip surfaces distributed throughout. The black arrow points to the localised intensely fractured fault zone. The grey arrow points to the zero reference point, from which the position of all readings are located. The distance from this point was measured along the top of the exposure. Overlying units are folded Jurassic marine sediments. In the top right a Miocene pediment surface can be seen. Facing south.

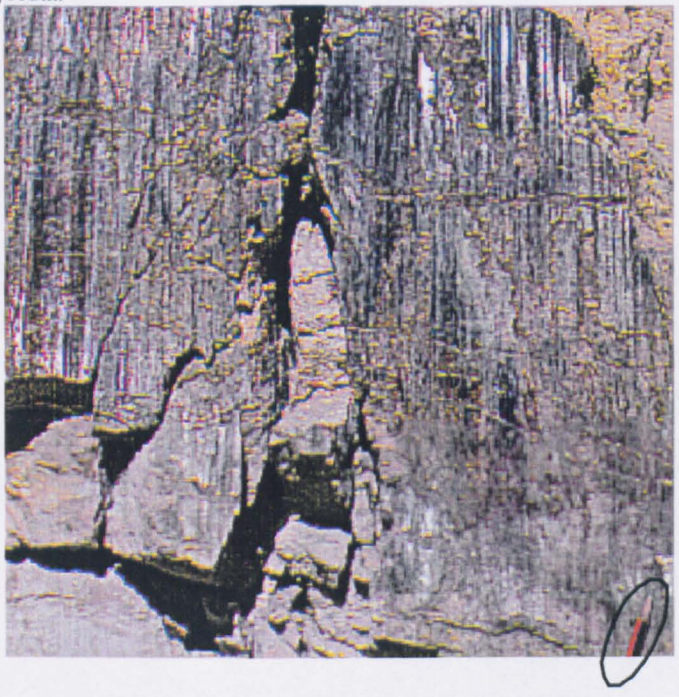

Figure 4.1.2 A slip surface in Quebrada Las Mulas, looking to SSE. Pencil, bottom right, for scale.

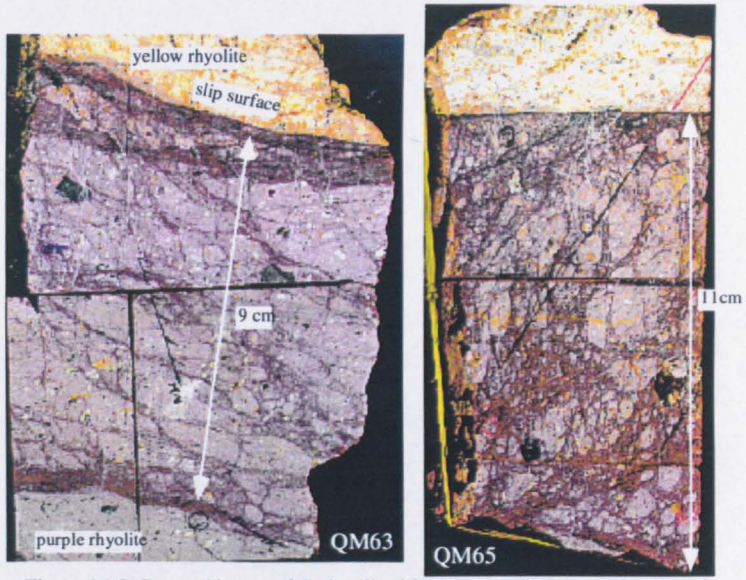

Figure 4.1.3 Scanned image of the localised fault zone. The contact between the yellow (to top) and purple rhyolites can be seen marking the upper boundary of the fracture network, with a sub-parallel surface 10cm below. Immediately outside of the localised zone, the fracture population is greatly reduced.

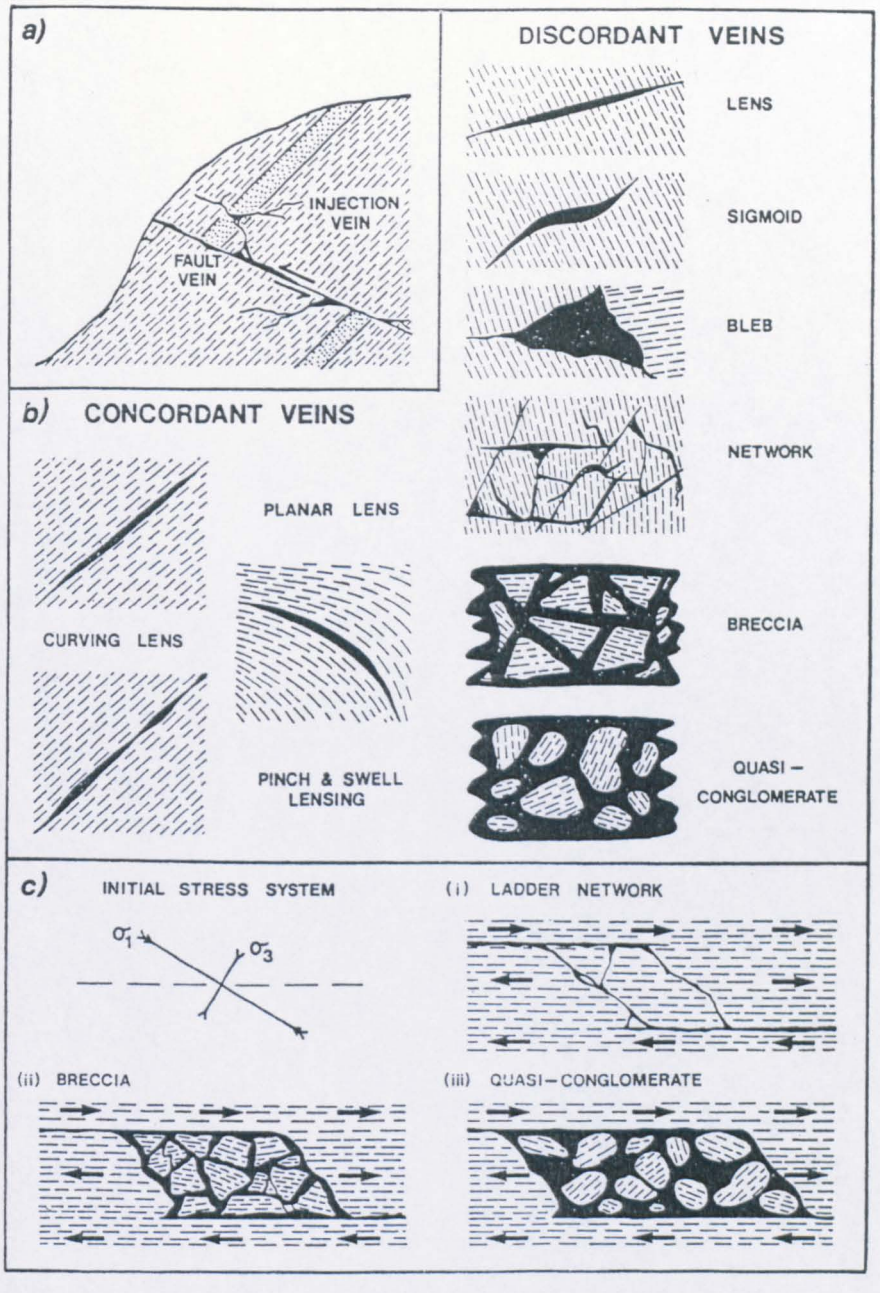

Figure 4.1.4 After Sibson, 1975. (a) Fault and injection vein relationships. (b) Geometric classification of pseudotachylyte veining. (c) Mechanism for quasi-conglomerate formation.

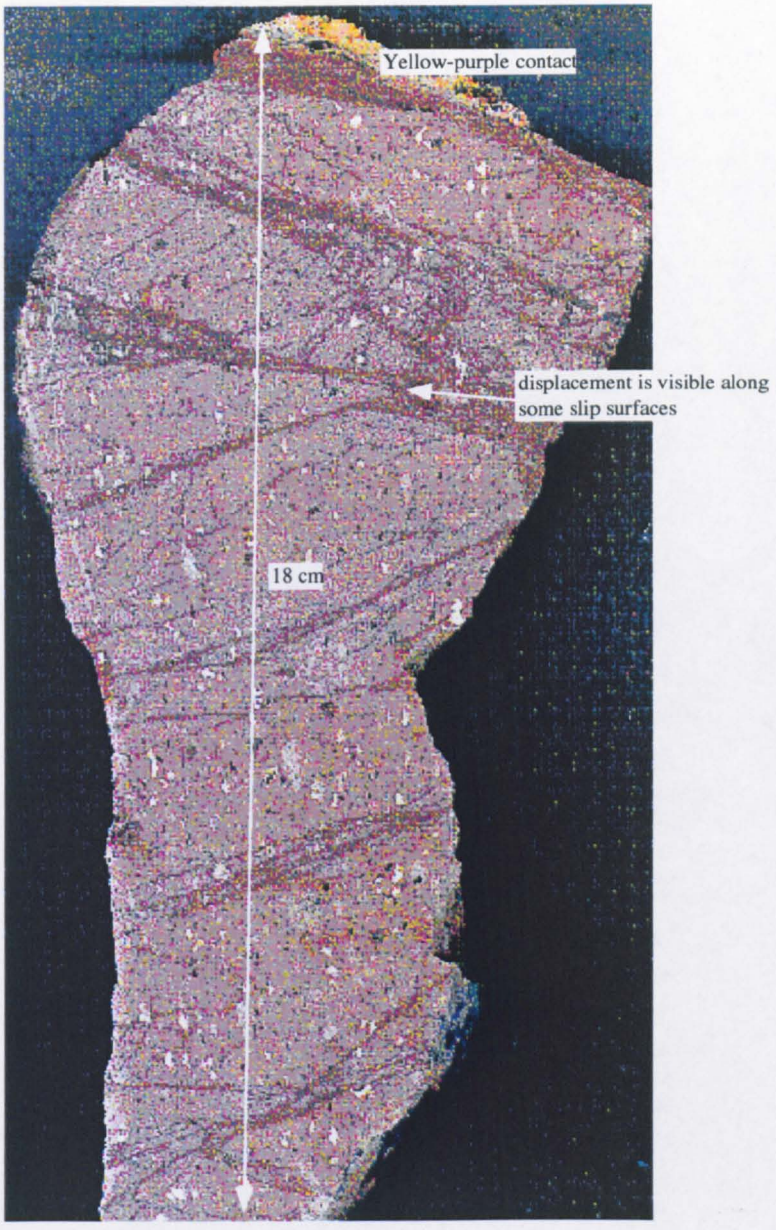

Figure 4.1.5 Sample QM43, situated at one end of the localised fault zone, as the distance between slip surfaces increases and interaction is reduced.

and the fault rock is parallel to the gradational yellow-purple boundary and has an irregular trace for 2m. At the point of overlap and parallelism with another slip surface in the purple rhyolite, both bounding surfaces become planar and parallel, ~ 10 cm apart. Two samples QM63 and QM65 of the localised fault zone are comparable with the breccia and quasi conglomerate, respectively, of Sibson (1975, Figures 4.1.3 and 4.1.4) formed between overlapping slip surfaces. Within the fracture network between the paired slip surfaces, angular rock fragments are suspended in a fine grained dark matrix. The localised fault zone dies out at the northern end into a suite of slip surfaces, Figure 4.1.5. The slip surfaces can be seen to sole into the localised fault zone and appear to contain the same fine grained, dark material within the fractures. Lineated slip surfaces also occur alongside the localised fault zone.

The lineated fault rock has a thickness of ~1 mm. The surface appears polished, the lineations are formed by a consistently oriented indentation of this surface. There is no evidence of crystal formation or variation in grain size defining the lineation. The lineations are interpreted to reflect relative movement directions across the slip surface.

Figure 4.1.6 shows a vein in the yellow rhyolite. The vein can be traced to a slip surface. Angular clasts of rhyolite occur within the vein, some oriented in a manner suggesting the vein has brecciated and incorporated the wall rock. The vein is finely laminated and a fabric can be seen around the larger breccia clasts. The breccia is predominantly yellow rhyolite, with some purple rhyolite.

Description of yellow and purple rhyolite units

The yellow rhyolite is predominantly composed of glassy shards in a quartzo-feldspathic cryptocrystalline groundmass. Euhedral feldspar phenocrysts up to 3 mm are present, Figure 4.1.7. Occasional anhedral, altered biotite crystals (>2 mm) are observed. Iron staining around some shards is visible. No fabric is apparent. The purple rhyolite is also predominantly composed of glassy shards in a microcrystalline quartzo-feldspathic groundmass, Figure 4.1.8. Phenocrysts of biotite, quartz and occasional feldspars are more plentiful than the phenocrysts in the yellow unit. The quartz crystals are subhedral, up to 2 mm with inclusions in larger phenocrysts. Two generations of biotite are present, the larger (>2 mm) crystals are anhedral, altered and occasionally completely replaced Figure 4.1.9.

Figure 4.1.6 Injection vein , cutting through yellow rhyolite. Clasts of host rock are seen detached from the vein wall (A). Note the asymmetry and disruption of the laminations around the clasts (B). A zone of cataclasite occurs 2/3 of the way along the lower contact (C). Clasts of purple rhyolite can be found within the breccia .

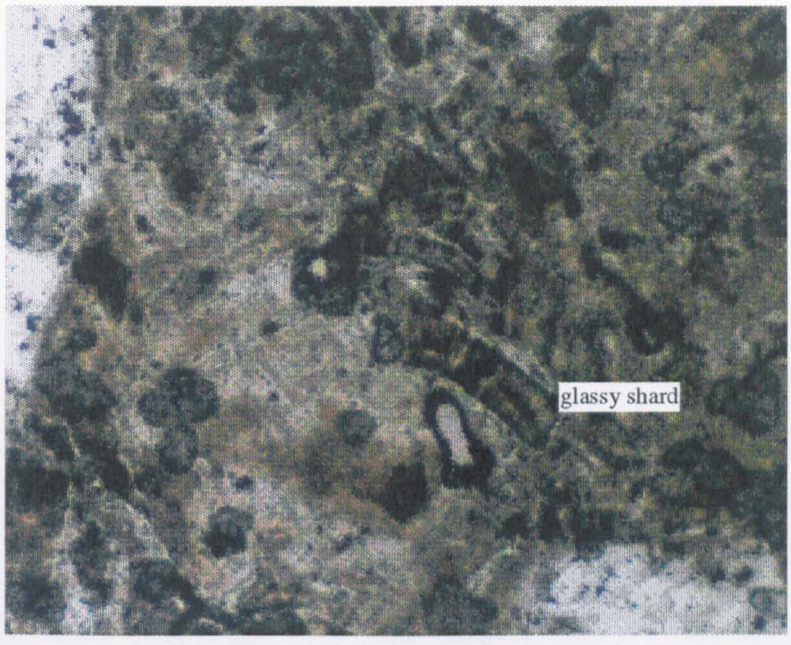

Figure 4.1.7 Photomicrograph of QM42, a sample of yellow rhyolite under plane polarised light. The edge of a large plagioclase phenocryst can be seen in the top left corner. Glassy shards are visible in the quartzofeldspathic groundmass. Scale x 64.

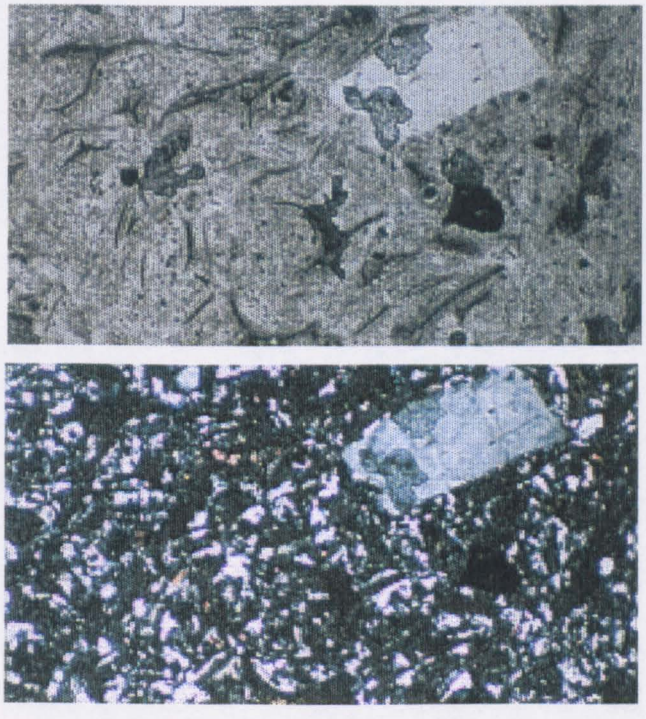

Figure 4.1.8 Photomicrograoh of sample QM57, purple rhyolite under plane polarised light and crossed polars. A subhedral quartz pheoncryst, glassy shards, quartzofeldspathic groundmass and small biotite crystals are visible. Scale x 16.

(a)

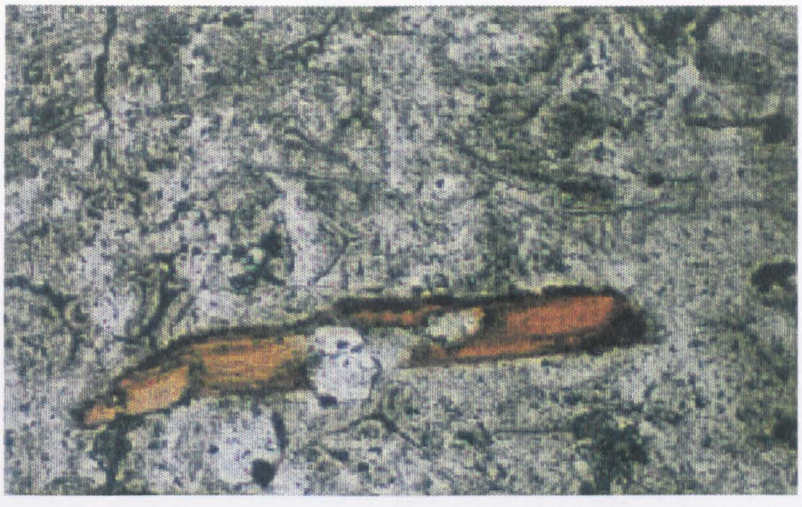

(b)

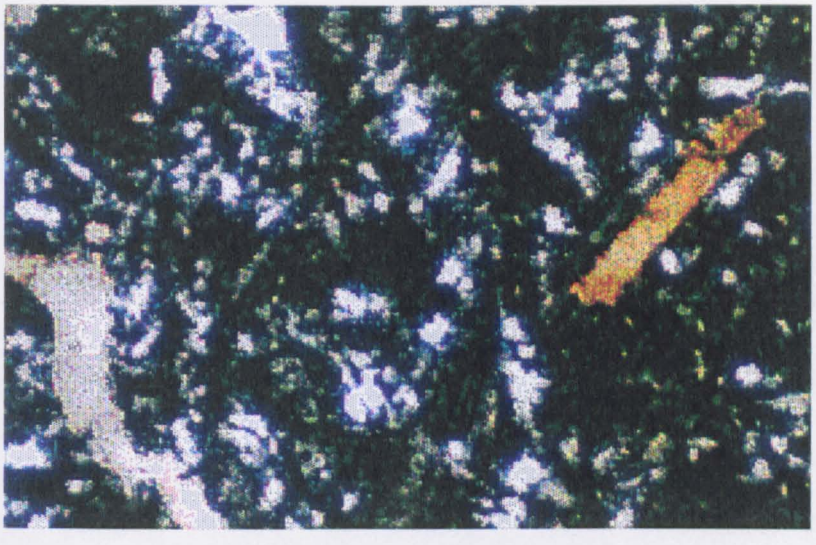

Figure 4.1.9 (a) Older generation biotite, replaced and altered. Note the apatite replacing the biotite to centre.
(b) Younger generation pristine biotite, note calcite vein to bottom left of slide. Scale x 64.

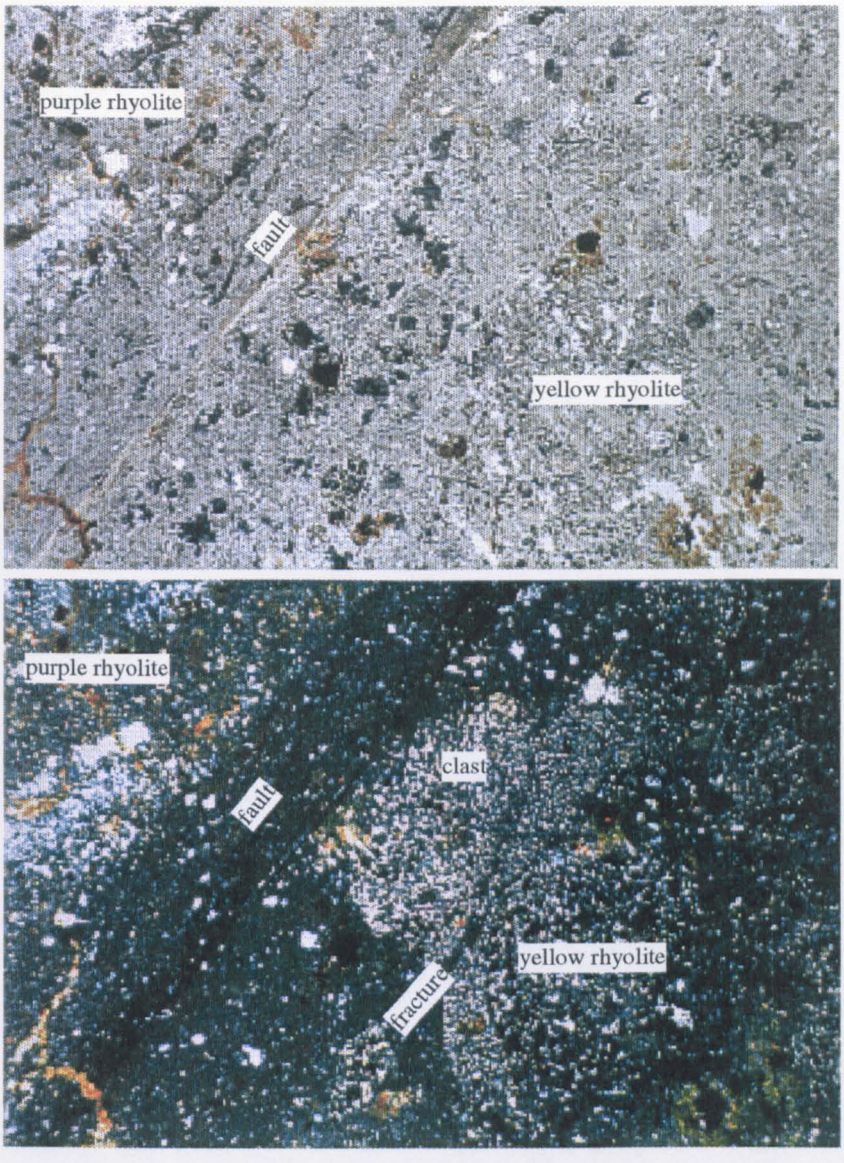

Figure 4.1.10 The tectonic contact between the yellow (bottom right of slide) and purple rhyolites(top left), from sample QM65 under plane polarised light and crossed polars. The actual boundary between the units is straight, isotropic and believed to be a generation surface for either ultracataclasite or pseudotachylyte. Both the yellow and purple units have a reduced grain size towards the fault. Fine grained fractures are seen to cut a brecciated clast within the yellow unit. Later iron-rich veining crosscutiing the fault shows it to be later than fault activity. Scale x 13.

The smaller biotites are up to 1.5 mm, euhedral and unaltered. Iron staining is not observed in samples situated away from the localised fault zone.

The similarity of the two units and gradational boundary between implies the temporal separation between their emplacement was small. Evolution of the magma chamber could account for the variation in phenocryst mineralogy. The rhyolite dyke is interpreted as a conduit. The glassy shards within the matrix imply rapid cooling presumably at shallow crustal levels (epibyssal).

Thin sections of the tectonic contact between the yellow and purple rhyolites reveal a clear, sharp contact between the rhyolites and the bounding faults of the localised fault zone, Figure 4.1.10. A well defined hyaline line marks the contact, yellow stained in plane polarised light and isotropic under crossed polars. The thickness of the layer varies along this contact ranging from 1 - 3 mm, sometimes with a curved margin towards the fault zone. Both the yellow and purple units become finer grained and disrupted towards the bounding slip surfaces. The fault zone is composed of angular quartzo-feldspathic clasts and fragments of yellow and purple rhyolite, cut by fractures with fault rock associated. The large fractures bend into parallelism with the bounding structures. The thickest fractures (~2 mm) occur at 3-4 cm intervals, at a low angle to the bounding surfaces and cut across the breccia. When viewed under crossed polars, the centre of each fracture is isotropic and much finer grained than the surroundings. Towards the edges coarser material can be seen containing angular clasts of host rock, Figure 4.1.10. Occasional rounded clasts of quartz occur within the fractures and slightly larger angular clasts occur in the cryptocrystalline regions beside the fractures. Both the purple and yellow rhyolites are cut by the glassy network. The fragments are smaller towards the boundaries of the fault zone. The fragments still recognisable as large quartz or feldspar crystals are brecciated and if still optically aligned, show undulose extinction. Fragments cut by hyaline fractures are deformed towards this fracture, with cataclasites formed around the margins, Figure 4.1.11. The fragments bound by fractures have undergone only brittle deformation. As the disturbance decreases away from the edge of the localised shear zone, and the grain size increases, the clasts are assumed to be less rotated. Iron staining is visible around some fragments closer to the networks of glassy material. An iron rich vein that cuts across and not displaced by the bounding structures, indicates the iron rich fluid passed through the rock after deformation.

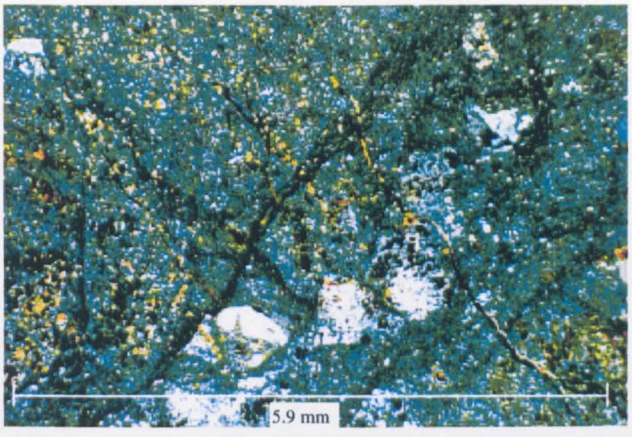

Figure 4.1.11 Thin section under crossed polars of the detailed fault zone in sample QM65, zone 1. Fault veins (fractures with isotropic fill) cut through clasts, however generally there is a region of reduced grain size between clasts and fault veins.

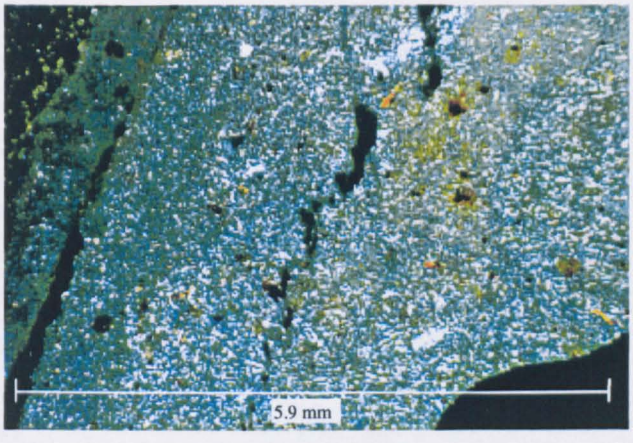

Figure 4.1.12 Thins section of QM42, yellow rhyolite, under crossed polars. A slip surface occurs to the left of the slide. Note the reduction in grain size towards the slip surface. At higher magnification it can be seen that the slip surface contains clasts of host rock and isotropic fractures. Scale x 13.

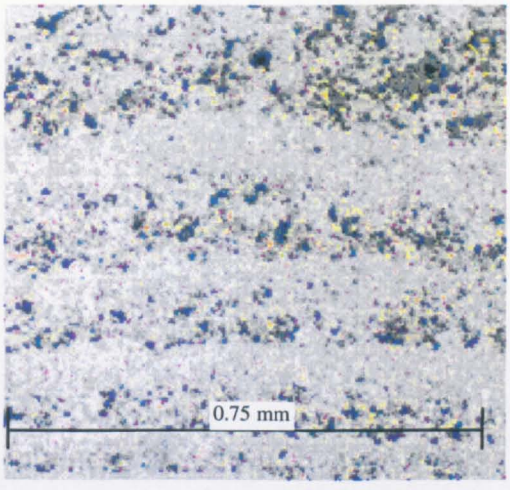

Figure 4.1.13 (a) The laminations in sample QM43 are brecciated opaques.

Figure 4.1.13(b) The prevalent fabric defined by the lamination is parallel to the top of the photomicrograph. An irregular swirl is just visible in the centre of this slide. The laminations either side have not been disturbed.

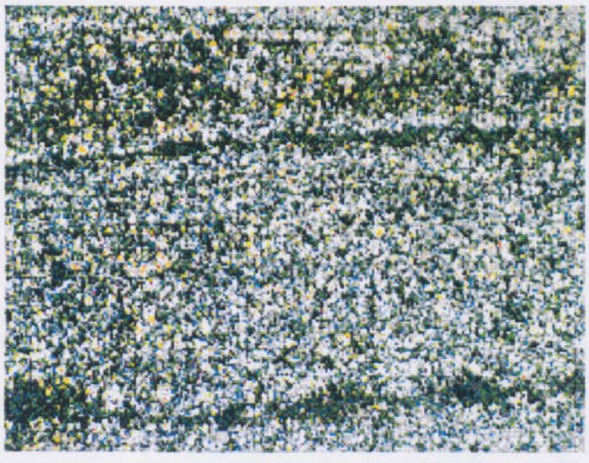

Figure 4.1.13(c) Under crossed polars the swirl in (b) cannot be seen. Scale as in (b).

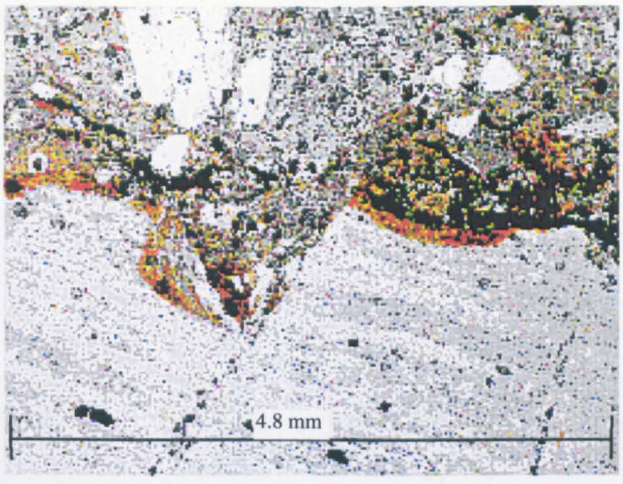

Figure 4.1.14 Contact between the vein material and the rhyolite. The brown areas beside the rhyolite is glass along the chilled margin of the vein.

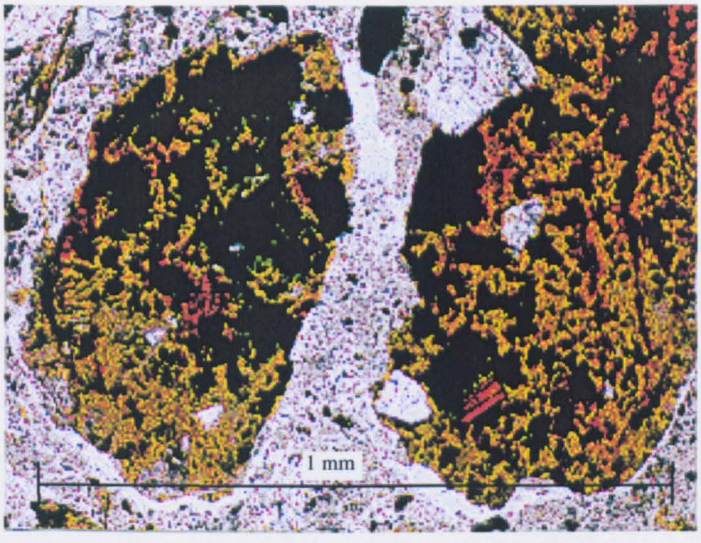

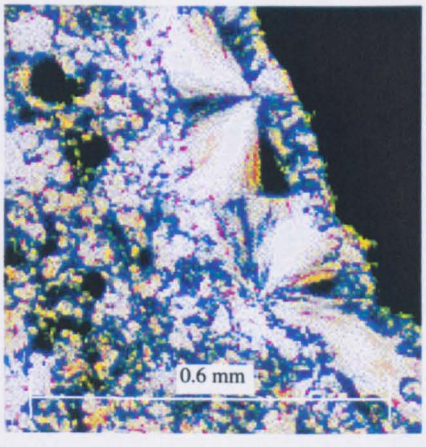

Figure 4.1.15(a) Vein fill surrounding clasts of rhyolite plucked from the wall rock. A transparent chilled margin occurs around the larger clasts.
(b) A clast of rhyolite can be seen in the top right, spherulites occur beside the clast, in the transparent region in (a).

The lineated fault rock on slip surfaces is optically identical to the material found within the fractures in the localised fault zone. The disturbance to the rock beside an individual slip surface is substantially less than that observed approaching the localised fault zone. Over 5 mm beside the lineated surface, the grain size decreases towards the surface (Figure 4.1.12). The phenocrysts less than 2 cm away from the slip surfaces are unstrained.

Thin sections of the fine grained, laminated vein in sample QM43 show the lamination to be caused by a variation in the size of opaques within the vein fill. The vein material itself is microcrystalline with a quartzofeldspathic composition, Figure 4.1.14. Approaching the vein margins and the larger breccia clasts, the texture of the vein is modified and some reduction in grain size occurs, spherulites can be seen, Figure 4.1.15. The fabric of the vein has been disturbed by flow around clasts, Figure 4.1.15. As the vein margin is approached from the host rock intense quartz and calcite veining is observed. The quartz and calcite fill have strained and twinned extinctions, respectively. Smaller shear veins with displacement along the veins offset the larger vein margins, Figure 4.1.14. The smaller shear veins post dated the injections of the quartzofeldspathic melt.

A polished block and thin section of a slip surface (sample QM42) were scrutinised under a scanning electron microscope (SEM). The fault rock consists of a matrix with grain size beyond the resolution of the SEM (2μm) and angular clasts. The matrix is either very fine grained or glass, Figure 4.1.16. Comparison of the fault rock with the rhyolite, Figure 4.1.17, shows the fault rock to be finer grained than the rhyolite. X-ray chemical analysis of the lineated material reveals similar chemistry to the host rock, with a variable iron content. Within the ultra fine grained lineated material, clasts of host rock are visible of a continuous size range up to 5μm are present. The clasts are highly angular.

The picture produced by the SEM of the lineated surface highlights an unusual feature, Figure 4.1.19. A lineation is defined by a trail of coarser grains oblique to the main lineation viewed in hand sample. The lineations are curved and inconsistent in orientation. The origins of these lineations are unknown and may even be the result of an imperfect coating in sample preparation for the SEM.

Classification of the Fault Rock : Ultracataclasite or pseudotachylyte?

The texture in the localised fault zone could conceivably be the product of either cataclasis

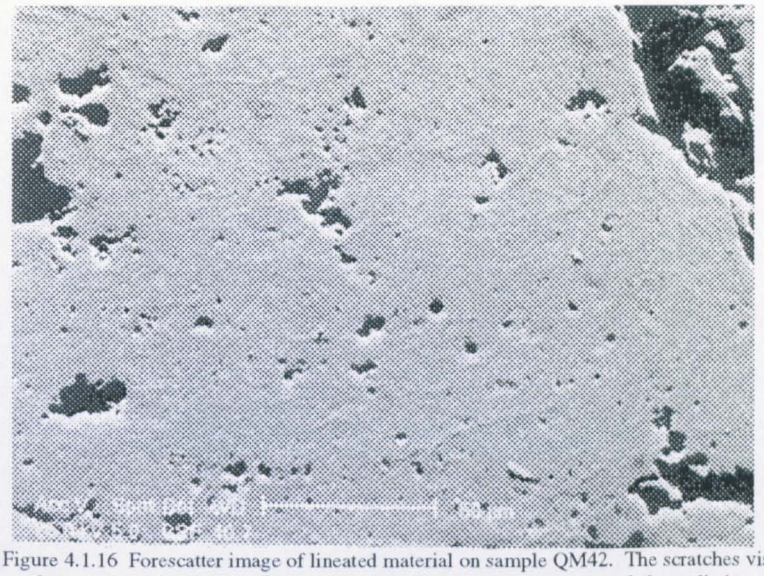

Figure 4.1.16 Forescatter image of lineated material on sample QM42. The scratches visible are from an imperfect polish. Using fore scatter imaging, separate crystals have distinct shading. The image presented here has no variation in shading (apart from the black holes in the specimen).

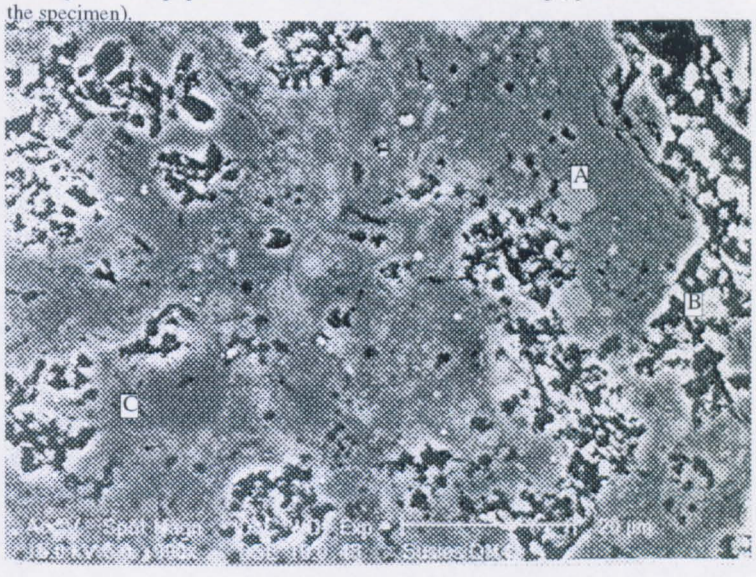

Figure 4.1.17 Back scatter image of the lineated fault rock. Irregular fragments (A) and holes (B) are seen amongst a very fine grained or glassy matrix (C).

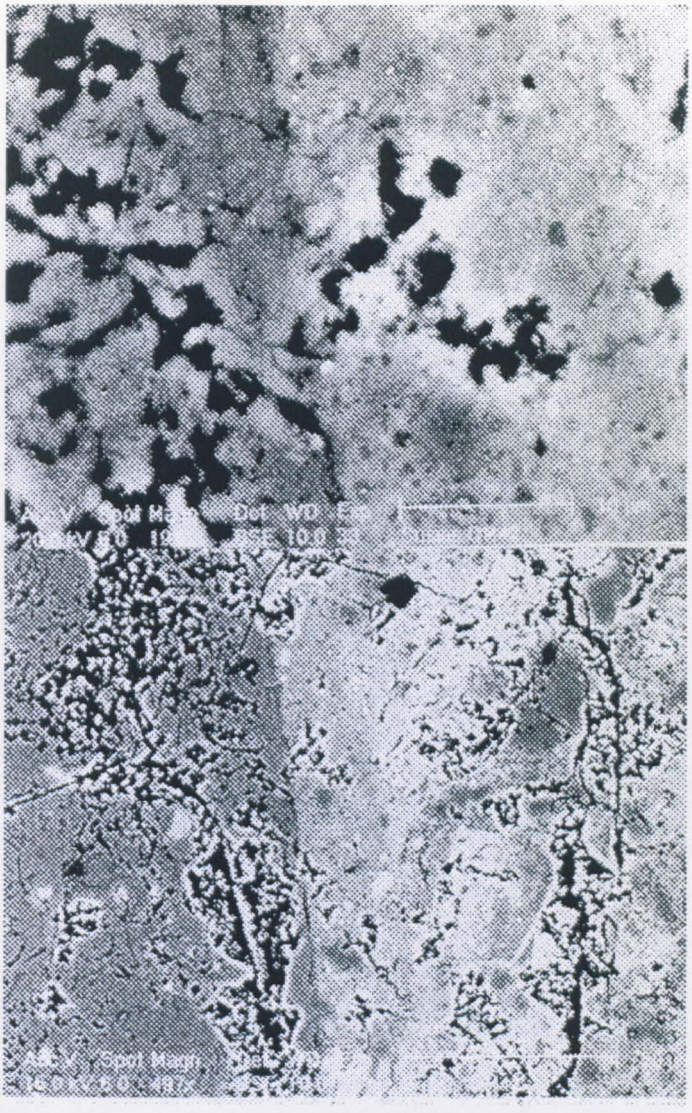

Figure 4.1.18 Back scatter image of the lineated fault rock and yellow rhyolite immediately beside, from sample QM42. The fault rock is on the left. The fault rock is too fine grained for distinction of individual crystals or clasts.

Figure 4.1.19 A trail of coarser grains defines a lineation oblique to the main lineation on the slip surfaces. The white arrow (bottom right of diagram) shows the direction of the lineation visible in hand specimen, that is, the lineation is east-west with respect to the diagram.

or pseudotachylyte generation.
The sample shown in Figure 4.1.6, QM43, resembles a reservoir zone for pseudotachylyte. The presence of yellow and purple rhyolite clasts in Figure 4.1.6 indicates the fluid forming the veins has passed through both units.

Ultracataclasites commonly have dominant feldspar porphyroclast composition (Sibson, 1975) whilst pseudotachylytes tend towards quartz and feldspar (obviously dependent upon original mineralogy). Mafic minerals are rarely preserved near the generation zone of pseudotachylyte, as they are melted preferentially to the felsic components (Spray 1992). The quartz and feldspar porphyroclasts and the lack of biotite observed in the samples from the localised fault zone suggest melting of the host rock, not just frictional comminution. The irregular distribution of iron in the fault rock could reflect the incorporation of biotite to the melt and little mixing of the melt before freezing. The check list produced by Magloughlin and Spray (1992) to indicate a melt origin to the fault rock has been applied to the samples to clarify the mechanism of fault rock production.
A variation in texture and size with respect to position in the vein is observed in sample QM43, the possible pseudotachylyte injection vein. This is anticipated for a hot melt in contact with a cool body, where cooling rates vary across the melt. The spherulitic texture is also indicative of rapid cooling of a melt (Cox et al, 1979).

Many clasts within the fault veins are angular, however a significant number of porphyroclasts (or remains of) have smooth edges, and embayment of clasts is seen: both suggest melting.

The equivalent chemistry of the slip surfaces and the host rock is compatible with the melt having formed from the host rock.

It is concluded that the fault rock is a mixture of associated cataclasite, ultracataclasite and pseudotachylyte. Magloughlin (1992) found evidence that pseudotachylyte was generated along pre-existing cataclasite zones, melting some cataclasite in the process. This sequence fits with observations here, however in this instance not so much of the cataclasite has melted.

The localised fault zone is interpreted to have formed in response to the overlap of two independent slip surfaces. Interaction between the slip surfaces has caused a failure zone, the localised fault zone.

4.2 Kinematic Analysis of the Slip Surfaces

The data collected from the slip surfaces along the rhyolite dyke can be seen in Appendix 4.1. The majority of the slip surfaces, when plotted on a stereonet have a westerly dip, Figure 4.2.1. The strike of the rhyolite dyke is approximately 042°. The cross cutting relationships of slip surfaces visible in the field indicate a cyclicity of deformation, between variously oriented slip surfaces, Figure 4.2.2. Calcite extension veins up to 4 mm thick are also found to exhibit cross-cutting relationships with slip surfaces which indicate a cyclic deformation history.

Application of Marret and Allmendinger's (1990) technique, explained in Ch 2.2, to the slip surfaces distributed throughout the rhyolite, to determine the intermediate incremental strain axes produces two areas of high density, Figure 4.2.3. It is not possible for one strain ellipse to produce two intermediate strain axes. Use of a tangent lineation diagram (see Ch 2.3 for explanation) to distinguish inconsistent data, highlights two valid data sets Figure 4.2.4. They are referred to assystem Aand B (orsystem Aand B).

Data sets A and B both possess sub-horizontal intermediate strain axes, so both relate to dip-slip faulting but the senses are unknown, Figure 4.2.5. system Ahas a well defined intermediate incremental strain axis and a well defined M-plane (using Arthaud's (1969) definition, that is, the plane containing the maximum and minimum incremental strain axes); this suggestssystem Awas a plane strain event. The intermediate incremental strain axes forsystem Bslip surfaces are less well clustered, however, they still form a concentration on the stereonet. system Beither represents non-plane strain or the slip surfaces have undergone relative rotation since activity.

Orientation of system A and system B slip surfaces

Figure 4.2.6 shows the orientation of slip surfaces in deformations A and B. The majority of slip surfaces in both data sets dip to the west. A number of slip surfaces in deformation A, strike parallel to the rhyolite dyke. Slip surfaces involved insystem B have no dominant orientation and commonly intersect near the orientation of thesystem Bintermediate strain axis.

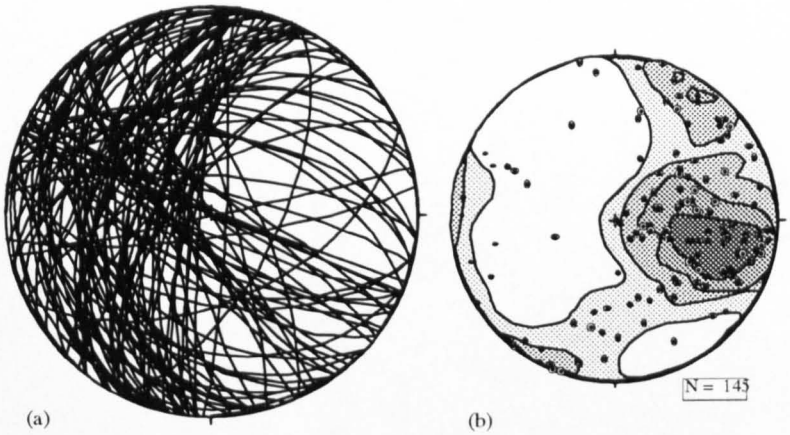

Figure 4.2.1 (a) Orientations of slip planes measured in the Quebrada Las Mulas rhyolite dyke. (b) Poles to slip planes.

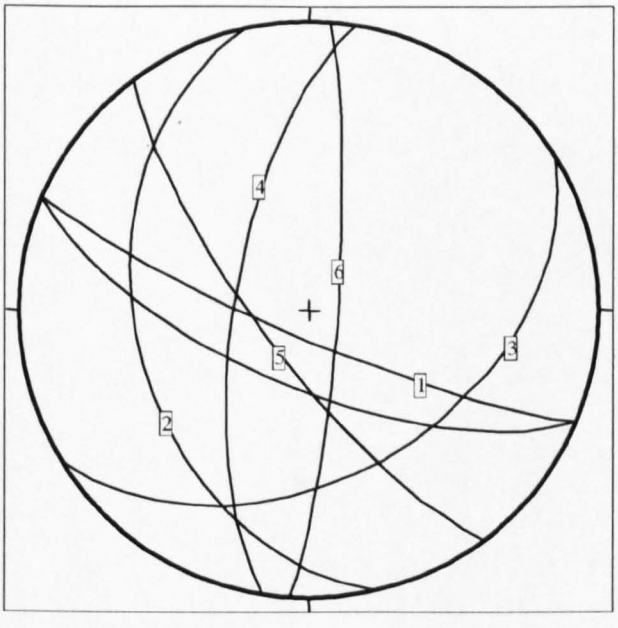

Figure 4.2.2 The relative timing of slip surfaces measured at 25 m from the reference point, Appendix 4, has been assessed using cross cutting relationships. There does not appear to be a correlation between slip surface orientation and order of activity.

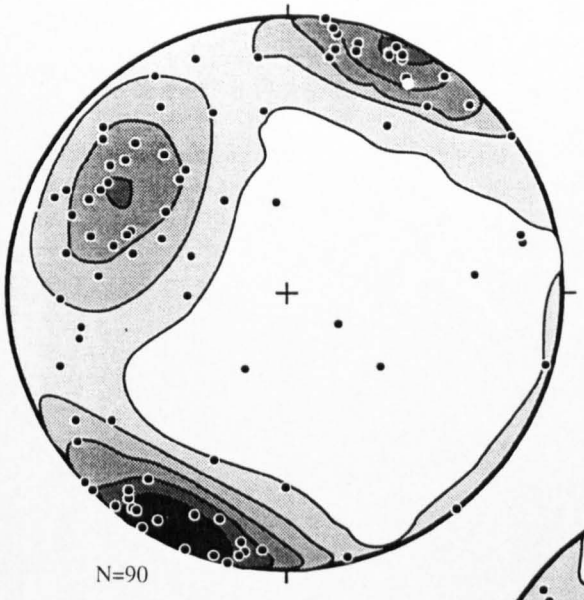

Figure 4.2.3(a) Contoured stereo net of the intermediate incremental strain axes for all of the slip planes occurring in the QLM rhyolite dyke, calculated using Marret and Allmendinger, 1990.

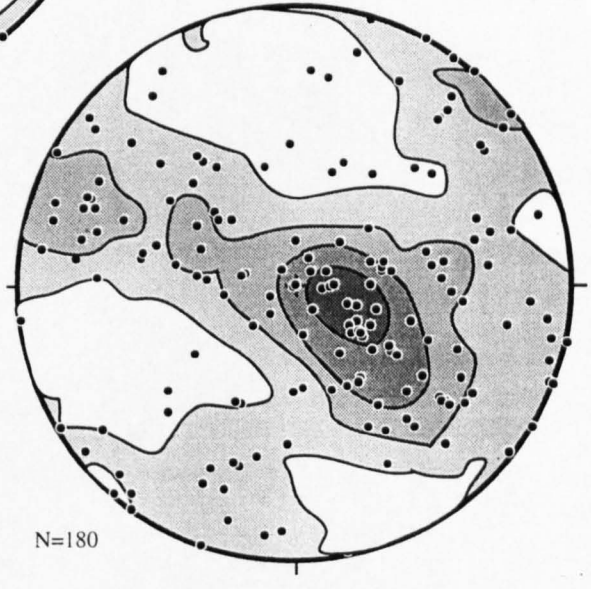

Figure 4.2.3 (b) Contoured stereo net of the maximum and minimum incremental strain axes for all the measured slip planes in the QLM rhyolite dyke. Maximum and minimum axes have not been distinguished.

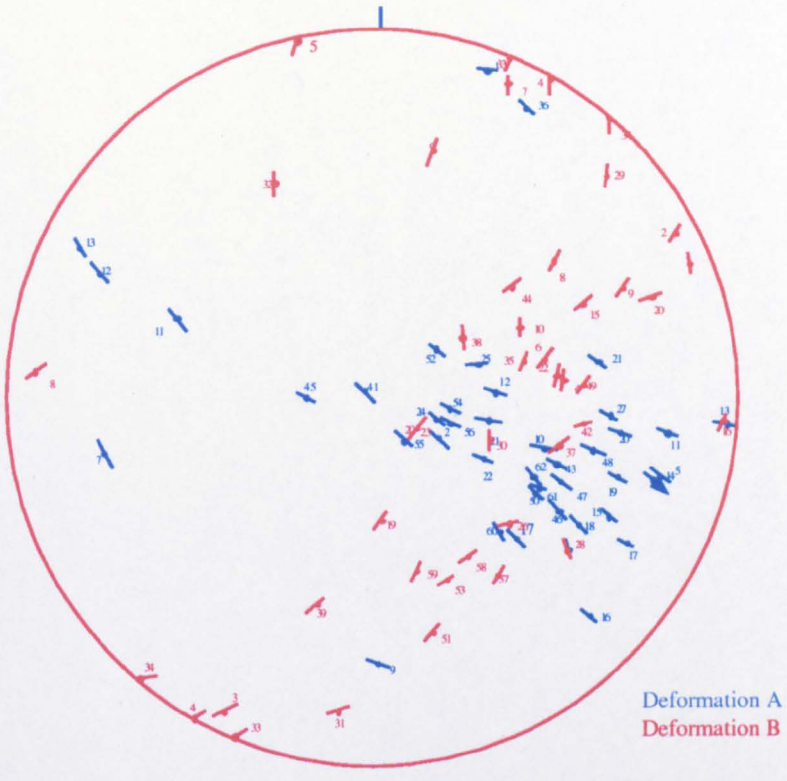

Figure 4.2.4 Tangent lineation diagram for the slip surfaces cutting through the rhyolite dyke. Where shown, the arrow indicates the movement of the footwall. Two separate concordant patterns can be distinguished, deformations A and B.

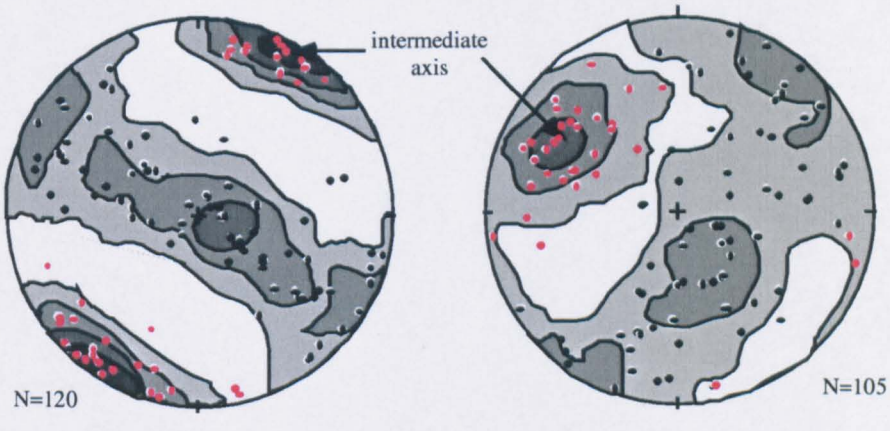

Fig 4.2.5.(a) Incremental strain axes for deformation A. The close grouping of the intermediate strain axis indicates plane strain. The maximum and minimum axes define a NW-SE subvertical plane. The intermediate axes are shown in red for both diagrams. Fig 4.2.5(b) Incremental strain axes for deformation B. The orientation of areas of high density approximate to those of deformation A. The intermediate axes are well grouped. The maximum and minimum axes loosely define a NE-SW plane, the kinematic axes are not as clustered as for deformation A. The maximum and minimum axes cannot be distinguished without sense information from the fractures.

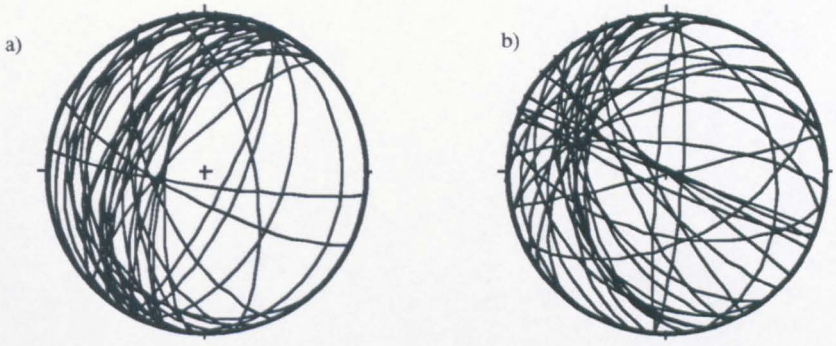

Figure 4.2.6 The distribution of slip surfaces in data sets A and B (diagrams (a) and (b) respectively) has also sub-divided the slip surfaces in terms of their orientations. Data set A commonly have slip surfaces parallel to the strike of the dyke. The slip surfaces associated in data set A all intersect at the orientation of the intermediate strain axis for data set A. Data set B has the same relationship with the strain axes. The common intersection point of data set A is 04/202(c): the common intersection point for data set B is 36/296 (d).

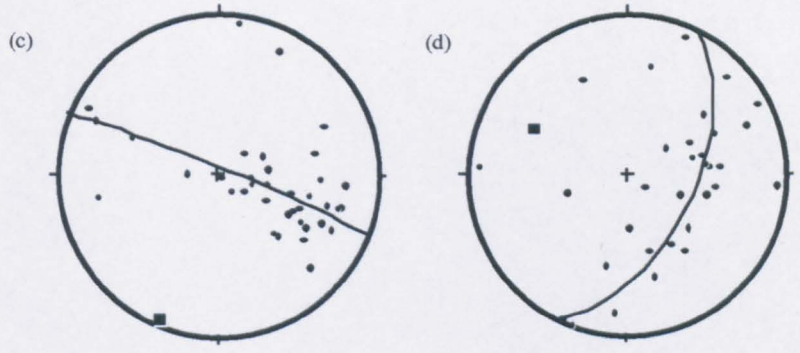

Figure 4.2.7 The striae from the slip surfaces for deformations A and B as (a) and (b) respectively. Striae are shown in blue and eigenvectors are shown in red. The relative magnitude of the eigenvectors is denoted by λ_i , where 1>2>3.

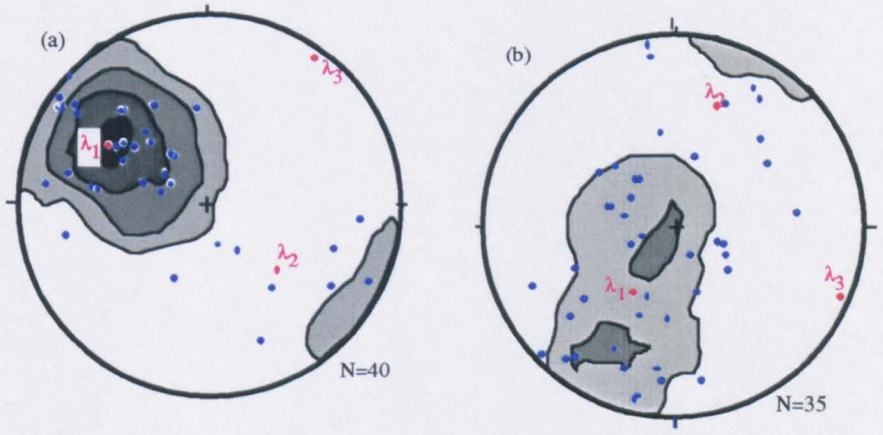

Relative timing of the two slip systems

Appendix 4 contains relative timing information of cross cutting slip surfaces, deduced from offsets. Those surfaces which have been categorised as system A or B can be used to infer the chronology of the two slip systems. At 8.7 m from the reference point there is evidence of activity on ansystem A slip surface preceding activity on a B slip surface. At 10 m from the reference point the opposite relationship is observed. At 25m there are three generations ofsystem B slip surfaces followed by activity on ansystem A slip surface. At 68m there is evidence for activity on ansystem A slip surface, followed by asystem B slip surface and followed by ansystem A slip surface. Finally at 98m slip surface activity is noted as B - A - B. A minimum sequence of B- A - B - A must have occurred to be compatible with the observations. The three generations of slip system B surfaces measured at 25m probably reflect a cyclicity between both slip systems during fault activity. The fault activity probably occurred over a geologically short period of time, so the two slip systems can be considered as contemporaneous.

The two systems were active contemporaneously and system A slip surfaces show no evidence of having undergone relative rotation since activity. This suggests that system B slip surfaces facilitated a non-plane strain. The two types of slip surfaces cannot be separated objectively and may represent changes in the geometries of the bounding faults. Depending upon the distribution of slip surfaces from each system, this might have prompted thickening and thinning of the fault zone, without volume change, along the length of the dyke.

Striation analysis

Wallbrecher and Fritz's (1989) method of analysing the striation distribution of a fault system to determine the orientations of the principal strain axes has been applied to both fault systems. Using this analysis the orientation of the smallest eigenvector corresponds to the orientation of the intermediate strain axis.

The smallest eigenvector for system A lies within the centre of the cluster of orientations for the intermediate strain axis, Figures 4.2.5 and 4.2.7. The incremental and finite intermediate strain axes are coincident for plane strain: this results in a close grouping of incremental intermediate strain axes. System A has undergone a strain that approximated to

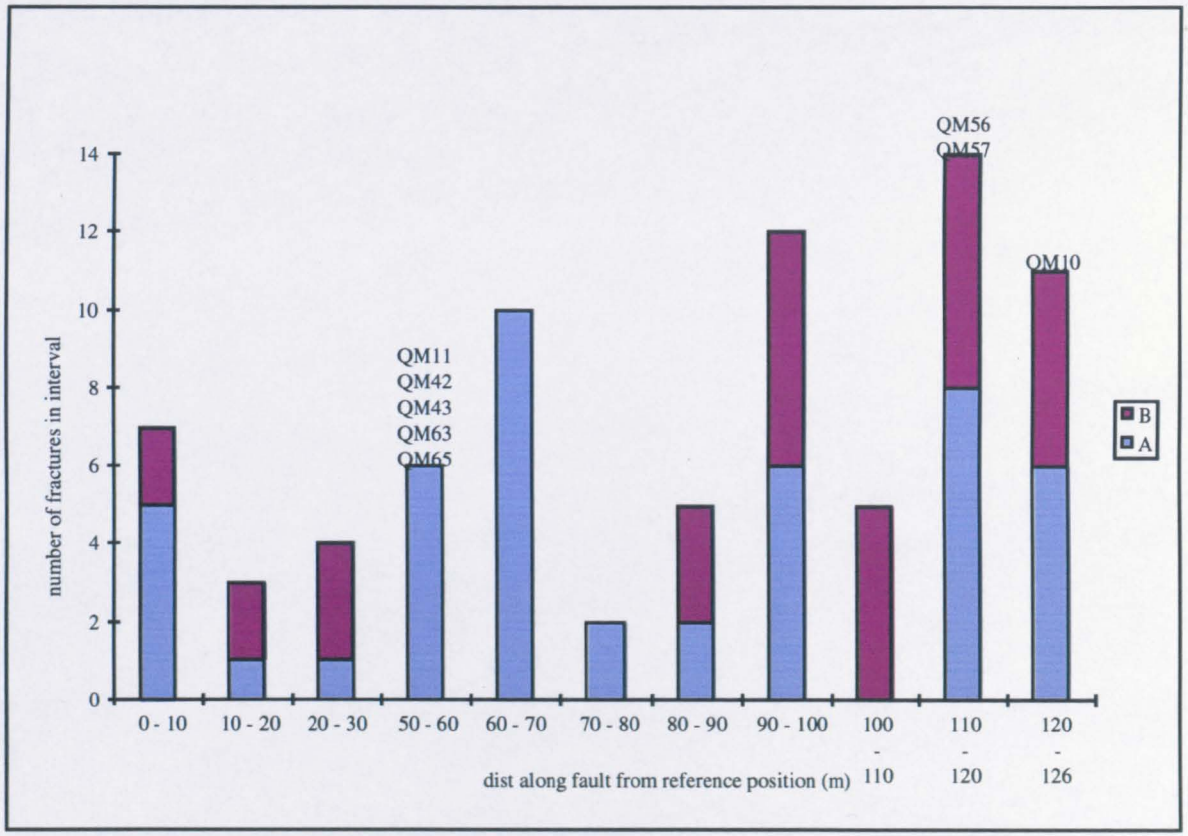

Fig ure 4.3.7 Distribution of type A - V- type B slip surfaces along the Q Las Mulas fault. Distances are measured from the reference point at the NE end of the detailed mapping. The sample numbers above the histogram show the location of the sampling sites. There is no exposure between 30 and 40 m. The higher number of fractures in an interval increases above 90m from the reference point as the exposure is continuous.

a plane strain. The smallest eigen vector for system B lies at the edge of the cluster of intermediate incremental strain axes. System B has been recognised to have undergone a non-plane strain. Hence the scatter of incremental strain axes is high. The calculation of incremental strain axis based on striae orientation, does not take the orientation of the fault surface into account, as with Marrett and Allmendinger's technique. The incremental intermediate strain axis calculated using Marret and Allmendinger's technique for system B is used in this analysis.

Distribution of slip surfaces within the fault zone

Observations from a histogram showing the distribution of slip surfaces along the fault, Figure 4.2.8 are;

(1) there is a length of dyke with exclusively system A slip surfaces;

(2) there is a length of dyke with exclusively system B slip surfaces;

(3) there are lengths of dyke with both system A and B slip surfaces.

The distribution of slip surfaces into sections of dominantly system A then system B along the fault could be explained by block faulting. The maximum width of the fault zone and hence of the fault blocks is constrained by the exposure to be 30m, as compared with a block length of ~40m. The length of fault zone with both A and system B surfaces is as long as the length of fault zone with only system A surfaces; hence interpreted as fault blocks, deformation zones as long as the blocks themselves are present between the blocks. Whilst this is not impossible, it seems more likely that the distribution of slip surfaces is controlled by a heterogeneity within the dyke.

The different orientations of the intermediate strain axes for systems A and B indicate the systems are not sets of secondary fractures in the style of the Reidel model, Figure 4.2.9(c). The secondary fractures within the Reidel model share the same orientation of intermediate strain axis as each other and as the boundary structures, which is parallel to the intersection lineation of the fractures. Reidels within Reidels will also have the same intersection lineation. The systems are active over the same time period, so are assumed to have complementary activity to produce a net strain in accord with the stress regime. The variation in slip surface type with distribution along the dyke suggests strain partitioning based upon a heterogeneity within the dyke, such as a change in the orientation of the dyke.

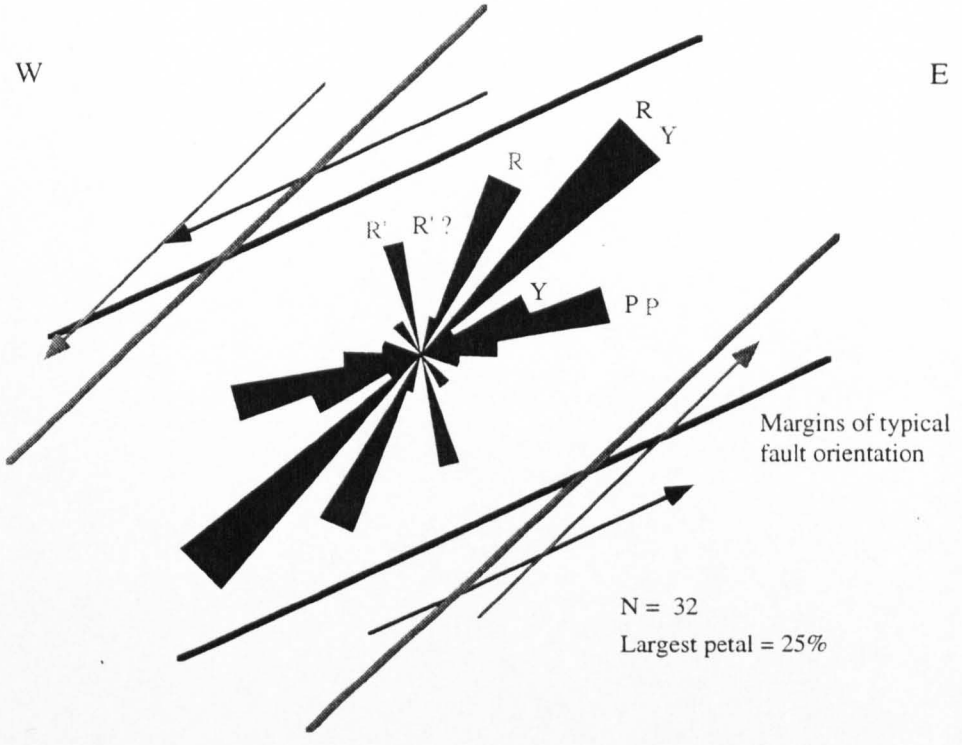

Figure 4.2.9 (a) Deformation A profile plane with the pattern of associated fractures. Correlations with the Reidel model are noted. The sense can be determined from comparison with the Reidel model. The two possible interpretations of the fracture distribution are shwon in grey and black. Uplift to the east is confirmed by the stratigraphic relationship. Profile plane orientation 118/90.

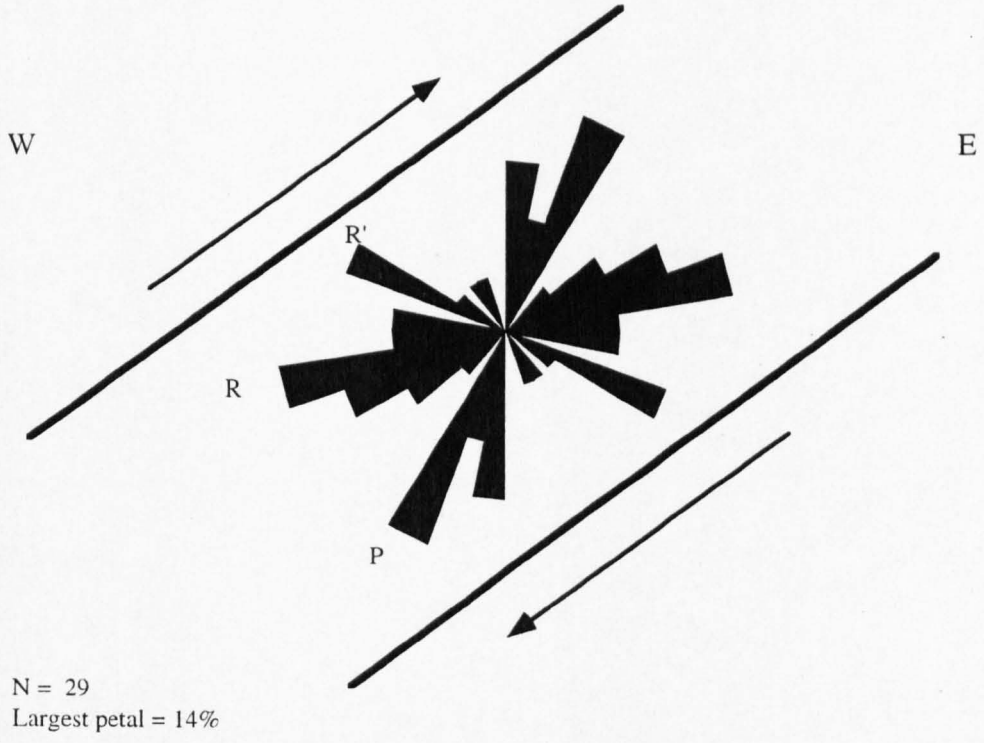

Figure 4.2.9 (b) As above for deformation B. The majority of type B slip surfaces dip to the west. Profile plane orientation 030/62S.

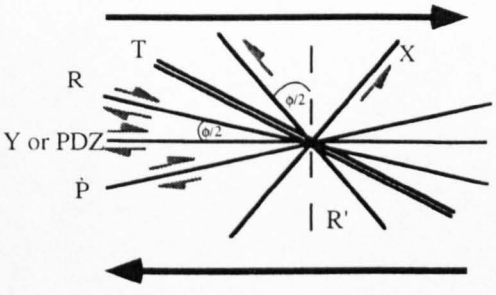

Figure 4.2.9 (d) The Reidel model distribution of fractures in the profile plane of a fault. The R and P shears are symmetrical about the Y or Principal Displacement Zone, which is parallel to the bounding faults. The angle between the R and P shears varies between 30° and 40°, depending upon the angle pf internal friction. The intersection lineation of all the fractures is parallel to the intermediate strain axis; the plane bisecting the R and P shears is parallel to the bounding faults.

The distribution of slip surfaces may indicate that faulting prompted thickening and thinning across the fault zone, however with no overall volume change.

The relative displacements of systems A and B are not known. Either A could be the dominant system and B is merely accommodating A, or vice versa, or both A and B are secondary structures associated with a discontinuity surface between the rhyolite and sediments. The latter model would invoke a distributed deformation model for the fault, with the structures in the rhyolite antithetic or synthetic to the main deformation.

Sense of Slip

The profile plane is the plane which has the intermediate axis as its pole, that is, the M-plane. The distribution of fractures formed during the deformation, on this surface, can be compared with the Reidel model of secondary fractures, Figure 4.2.9(c). From physical modeling experiments (for example, Bartlett et al 1981, or Tchalenko, 1970) the X fractures are seen to have a much smaller population than the R' fractures and the R fractures form the mode of the distribution, with P fractures symmetrical about the orientation of the boundary structure. It is necessary to determine the pitch of the boundary structures within the profile plane. The asymmetry of the fracture distribution with respect to the boundary structures can then be used to determine sense of slip.

The pitch of the boundary structures on the profile plane, for system A is inferred to pitch at an acute angle from the west (see Figure 4.2.6). The exact pitch is not known. Recognition of the R and Y fractures from the distribution in Figure 4.2.9 (a) can be used to determine this. There are two possible interpretations of the distribution of fractures. If R is recognised as the modal fracture type the boundary structures are at a lower angle than if R and P are recognised as symmetrical about the Y fractures. In both situations, the sense of slip on system A is compatible with the overall motion of the fault, with uplift to the east and normal motion across the fault.

The pitch of the boundary structures of the B slip system on the profile plane is not known. Using the distribution of fractures on the profile plane the R and P fractures can be identified, the boundary surfaces will bisect the angle between the R and P fractures, Figure 4.2.9(b). Hence the B boundary surface dips to the west. The distribution of fractures produce an ambiguous conclusion. The modal fracture orientation is not distinct, hence

either large petal could be R or P fractures; there appear to be R' and X fractures. A sense of movement can be inferred assuming the R' fractures are more abundant than the X. In this case system B is a reverse fault in the profile plane. System B underwent non-plane strain, so the significance of the profile plane is not the same as for system A. System B is clearly more complex than system A.

Symmetry

The slip surfaces from system A have a monoclinic symmetry in the profile plane, with respect to the bounding faults. The degree of symmetry of the fractures in the reference frame of the bounding structures can be used to qualify the type of strain. Monoclinic and triclinic symmetries are indicative of simple shear (Choukronne et al, 1987), whilst higher orders of symmetry reflect pure shear (Reches and Dieterich, 1983). Hence system A has undergone simple shear. System B is almost symmetrical, however as system B did not undergo plane strain, the significance of the profile plane as determined from the incremental stain axes is limited. Hence in 4.2.9, system B might not be in the correct reference frame to interpret the symmetry of the fracture distribution in terms of deformation history.

Using the fault orientation and lineation, any strike components of slip can be determined, Figure 4.2.10. system Bhas a greater component of strike slip than system A. Slip system A has a normal and a small dextral component of motion. Slip system B has a dextral and reverse components of motion. The designation of the sense of movement along the B slip system is not rigorously determined however.

Calcite extension veins are noted to have formed during the deformation cycle (A4.1). They are observed to cut the nearby evaporite, when the rhyolite dyke has terminated. Figure 4.2.11 shows the orientation of the veins. Along the fault the orientation of the veins vary, but not in any systematic fashion as the type of slip surface varies. Extension direction is assumed to be perpendicular to the vein orientation, however any shear along the vein will modify the orientation (Bussell, 1989). Without direct evidence for the extension direction, the veins cannot be analysed within this study.

(a)

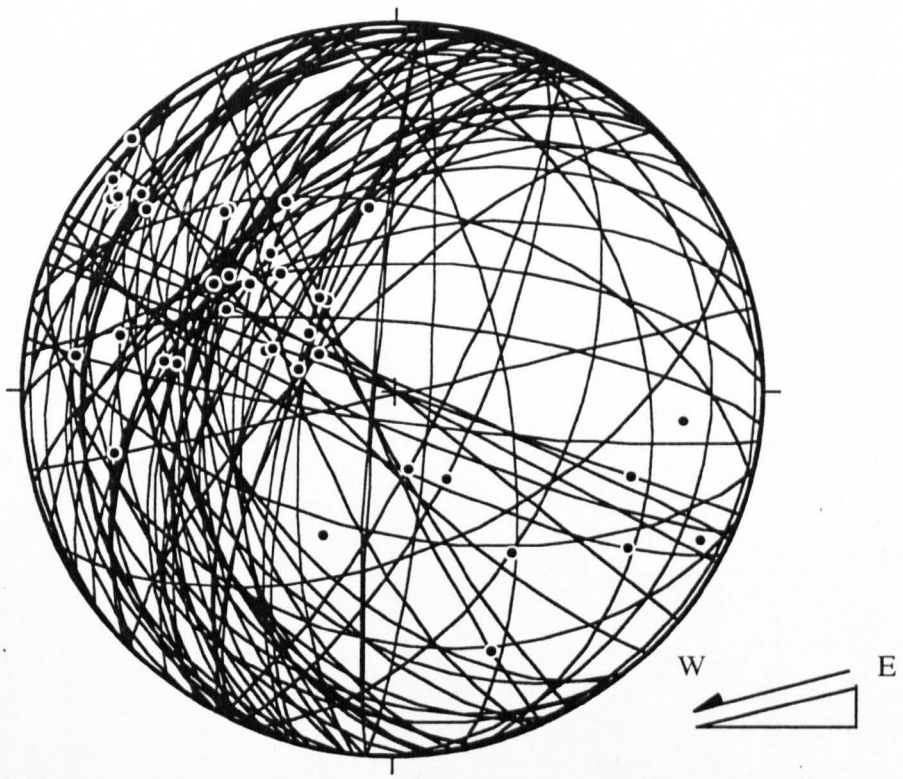

Figure 4.2.10 (a) Slip surfaces and lineations for data set A. The majority of type A slip surfaces have displacements of a predominantly dip slip nature, with a small component of oblique slip. The main sense of movement has already been shown to be normal, so the strike slip component is dextral. The kinematic interpretation in the vertical plane is shown in the inset.

(b) Slip surfaces and lineations for data set B. Most motion is oblique slip, assuming the faults are synthetic to data set A and the dip slip component of motion is in a normal sense, the strike slip component of motion is in a sinistral sense in slip surfaces dipping to the southwest and dextral in the vertical p

(b)

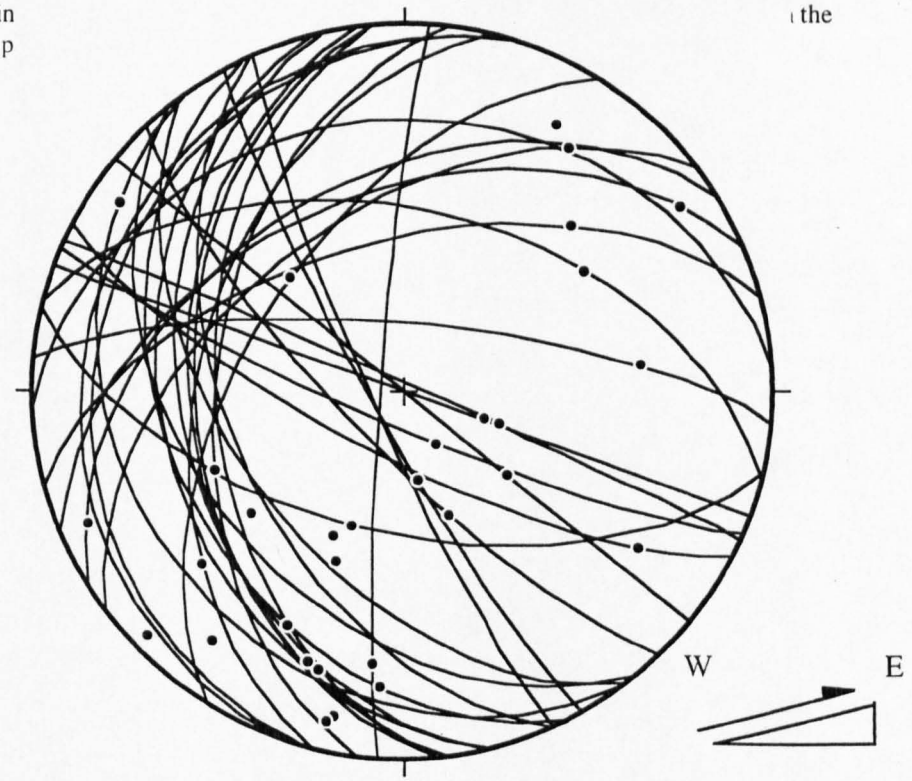

Boundary structures

Sibson (1975) and Scholz (1987) both present empirical evidence for a relationship between the thickness of pseudotachylyte and fault gouge respectively, and the amount of displacement cross a fault. Sibson defines the relationship

$d = 436.a^2$

where d is the slip and a is the thickness of the pseudotachylyte layer. Since this is dependent upon the mineralogy of the host rock, the equation will not be applied other than to suggest the modest amount of pseudotachylyte (a maximum of 6 cm width at any point across the fault) and cataclasite seen nearby the slip surfaces and localised fault zone of the rhyolite dyke are not enough to have accommodated all the necessary displacement to juxtapose Bajocian and Cretaceous sediments. Hence it is concluded that there is at least one major discontinuity surface. Whether there are two or only one bounding faults does not affect the interpretation and cannot be determined unless observed in the field. It is probable that there are two bounding surfaces as the rhyolite dyke will naturally provide two surfaces at the contacts with the country rock.

A model for the fault is shown in Figure 4.2.12. Palaeomagnetic sampling and analysis was undertaken to constrain the model of fault activity, to clarify the relative significance of the two systems, amount of rotation and sense of movement and any differential rotations along the length of the fault.

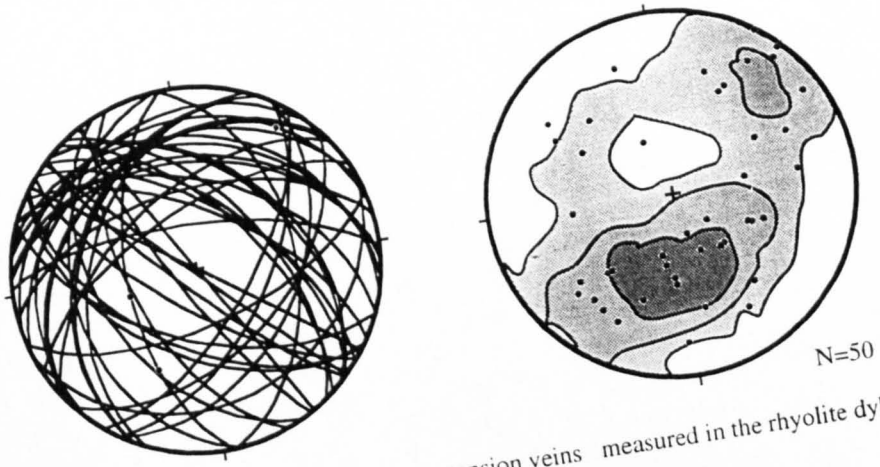

Figure 4.2.11 The orientation of, and poles to, extension veins measured in the rhyolite dyke.

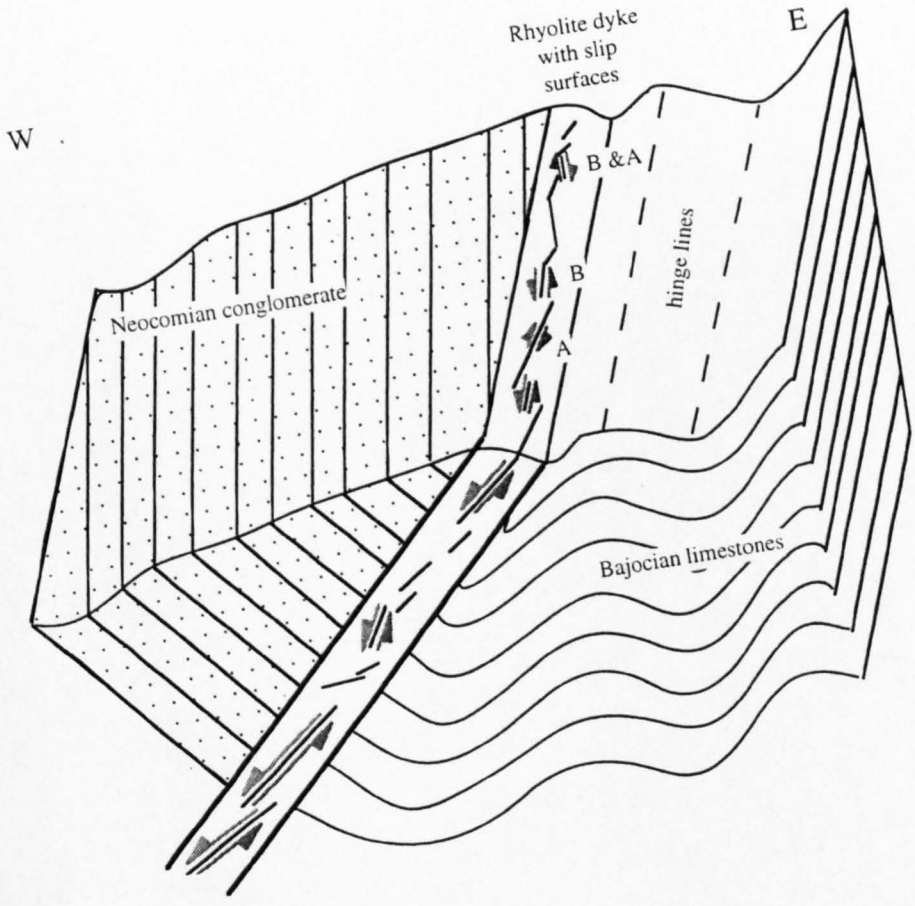

Figure 4.2.12 Schematic model of the fault in Quebrada Las Mulas, with associated slip surfaces cutting through the rhyolite dyke. The slip sense has been shown for a few type A and type B slip surfaces.

4.3 Ar^{39}/Ar^{40} Dating

Objectives of this study

The age of the ignimbrite which the fault passes through will provide an upper age limit on the fault activity as the textural analysis of the fault rock indicates the activity was post cooling. Any consistent age determined from the lower temperature steps when step heating the samples may reflect the actual age of the faulting. Constraints on the timing of fault activity will aid the regional geochronology.

Radioactive Decay

In radioactive decay an unstable parent atom decays to a daughter product. The process occurs at random intervals. The number of remaining parent atoms, N is dependent upon the initial number of parent atoms, N_0, time since initial conditions, t and the decay constant for that isotope, λ.

$N = N_0 e^{-\lambda t}$ This is known as the decay equation. [4.3.1]

Assuming the system remains closed, the total number of daughter atoms, $D_{tot.}$ can be defined in terms of the radiogenic daughter atoms produced since t=0, D*, and the original number of daughter atoms, D_0.

Combining this relationship with the decay equation

$D_{tot} = D^* + D_0 = N(e^{\lambda t} - 1) + D_0$ [4.3.2]

This is the basic equation on which radioactive dating is based.

The K/Ar System

When unstable potassium-40 decays, it forms calcium-40 and argon-40, with a half life of 1250×10^6 years.

$$^{40}K \rightarrow \begin{matrix} ^{40}Ca \\ \\ ^{40}Ar \end{matrix}$$

The amount of radiogenic ^{40}Ar in the minerals can be measured more easily than ^{40}Ca. The ^{40}K and ^{40}Ar are measured separately, so equipment accuracy is paramount. Excess argon can cause serious errors in the age calculations and can neither be detected nor corrected for.

Excess argon can be carried in fluids generated in metamorphic terranes (from any potassic minerals); extraneous argon can be trapped within a viscous silica rich melt, so can occur in rhyolites.

Assumptions in K/Ar dating

The decay rate of K^{40} is unaffected by physical state, pressure and temperature.

The $^{40}K / ^{39}K$ ratio is constant in nature.

The radiogenic argon measured in the sample was produced in-situ.

The sample has remained a closed system since the event being dated.

$^{39}Ar / ^{40}Ar$ dating

This is also based upon the radioactive decay of $^{40}K \rightarrow ^{40}Ar$. The technique was developed by Merrihue and Turner, 1966. The essential difference between K/Ar and $^{39}Ar/^{40}Ar$ dating methods is the technique by which the ratios of parent to daughter isotopes are measured. In $^{39}Ar /^{40}Ar$ dating, the sample is irradiated with thermal and fast electrons in a nuclear reactor to promote the reaction

$^{39}K (n,p) \rightarrow ^{39}Ar$

The amount of ^{39}Ar is used to calculate the amount of parent ^{40}K, using the $^{39}K/^{40}K$ ratio. The irradiated sample is heated in a furnace or by a laser, releasing the argon held within its lattice. The gas isotope ratios are then analysed in a mass spectrometer.

The dating technique measures the $^{40}Ar / ^{39}Ar$ ratio released from one sample in a mass spectrometer. The ^{40}Ar is the radiogenic daughter product. From this data, the age of the sample or event is calculated.

Mitchell, 1968, calculated the number of ^{39}Ar atoms produced during irradiation:

$$t = \frac{1}{\lambda} \ln \left(1 + J \frac{^{40}Ar^*}{^{39}Ar}\right) \qquad [4.3.3].$$

where t is the age of the sample, λ is the total decay constant for ^{40}K, $^{40}Ar^*$ is the radiogenic argon and ^{39}Ar is the argon converted during irradiation. J can be solved using mineral standards.

Advantages of ^{39}Ar / ^{40}Ar over K / Ar dating

Both measurements are made from one sample at the same time, in the same machine, reducing the equipment related errors and removing the problem of sample heterogeneity.

The Ar / Ar technique enables analysis of small samples as the sensitivity of the mass spectrometer is orders of magnitude higher than the equipment used in K / Ar dating.

The Ar / Ar technique allows tests and compensation for ^{40} Ar derived externally.

For a fuller explanation of this technique see Kelly (1997), Faure (1986), or McDougall and Harrison (1971). The error given after an age is representative of the precision of the equipment.

Sample Location

The samples were taken from the purple rhyolite immediately beside the fault in Quebrada Las Mulas. The samples were both at 118.5m from the reference point along the dyke in Quebrada Las Mulas. Care was taken not to sample across a fracture or vein.

The rhyolite has quartz and biotite phenocrysts. The quartz phenocrysts are 1-2 mm, subhedral and show no signs of deformation. Some of the larger crystals have inclusions and some anhedral crystal margins show evidence of re-equilibration with the melt. Two generations of biotite are distinguishable. The larger grains (>2 mm) are highly altered. Clusters of opaques, anhedral quartz and glassy shards are arranged in biotite shaped groups: the fabric within these clusters is discontinuous with that outside the ghost biotites. The smaller biotites range in size from 0.5 - 1.5 mm and are pristine. In sample QM56, occasional thin calcite veins cut across the igneous fabric. These range in thickness from 0.3 mm - 3 mm, with fragments of angular rhyolite enclosed in the larger veins. A microcrystalline quartzofeldspathic groundmass with glassy shards exhibits a poorly defined planar fabric.

The Chile-Alemania formation is a sequence of volcanics, most commonly consisting of andesites and basalts with subordinate rhyolites and dacites (Chong, 1977, Naranjo and Puig, 1984). K/Ar ages for the Chile-Alemania Formation range from 66 +/- 5 My to 47 +/- 2 My (Naranjo and Puig, 1984). The similar lithology of the rhyolite dyke suggests an

association with the emplacement of the Chile-Alemania formation (pers. commun. G Chong 1996). The Chile -Alemania Formation outcrops in Longitudinal Valley and rarely occurs east of the Domeyko. A dyke in this location signifies either a pre-existing high ground, so the lavas drained to the west or, the favoured interpretation is that of subsequent uplift and erosion of the exposure from this location. There is little constraint as to when the fault activity began in this locality. Isopach maps for deposition during the Jurassic show activity on a North-South oriented fault, to the southwest of this location (25°30' - 26°20'S and 69°10'W), however there is little evidence of pre-Cretaceous fault activity here.

Methodology

Euhedral biotite crystals of approximately 1mm diameter, were hand picked after crushing two hand samples of the purple rhyolitic unit. Pristine crystals were chosen to avoid altered samples and to prevent xenocrysts being chosen (they would be sub or anhedral as they may have been partially re-equilibrated with the later melt). The biotite crystals were then irradiated. The samples received 10^{18} fast neutrons per cm^2.
A Nd-YAG (Nd doped yttrium aluminium garnet laser) with a wavelength of 1.06μm (i.e. an infra red beam) was focused at the sample surface through a standard petrological microscope with the sample in a vacuum laser port, figure 4.3.1. The biotite crystals were then either spot heated or step heated.

Laser Spot Analysis In this technique the laser is fired into the sample for 5 - 10 minutes, until enough gas is released for the analysis or the crystal fused. The argon is released from all sites and a single age calculated. Gases were "cleaned" in the extraction system, where getters removed any active gas species, and after 10 minutes equilibrated via automatic valves into a static mass spectrometer, which was then isolated from the extraction system. Standard isotope analysis began as the gas entered the spectrometer. The mass spectrometer used is a single collector machine (i.e. each isotope is measured individually, alteration of the strength of the electromagnet allows a different mass number to be deflected on to the detector). The electron multiplier has a gain of ~10 000. Peaks between 35 and 41 were scanned 9 times (cyclically) for each analysis. These peaks were then used to calculate the amount of radiogenic ^{40}Ar and irradiated ^{39}Ar, figure 4.3.2. The sample was then pumped out and the process begun again (either for another sample or for a blank). Blanks were run before, between and after the sample analyses.

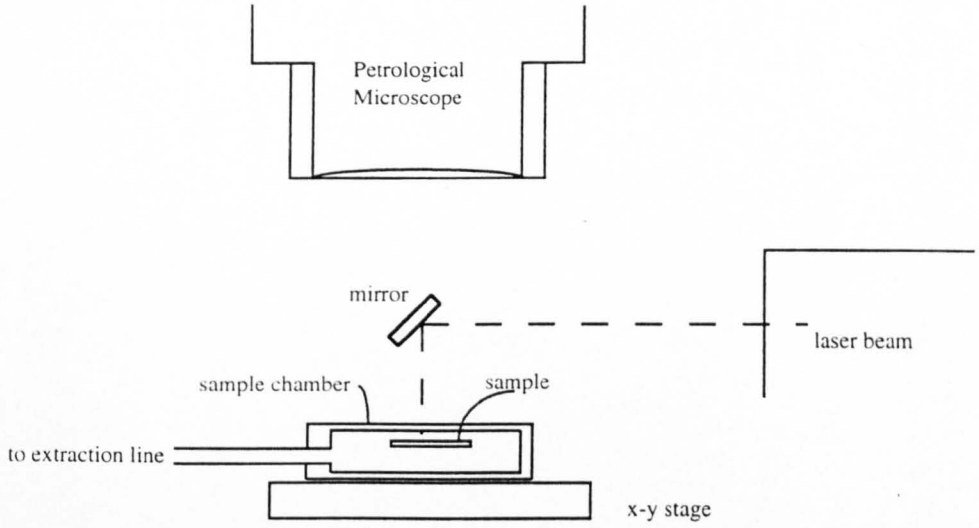

Figure 4.3.1 Schematic design of instuments to choose site and heat the sample used in this study.

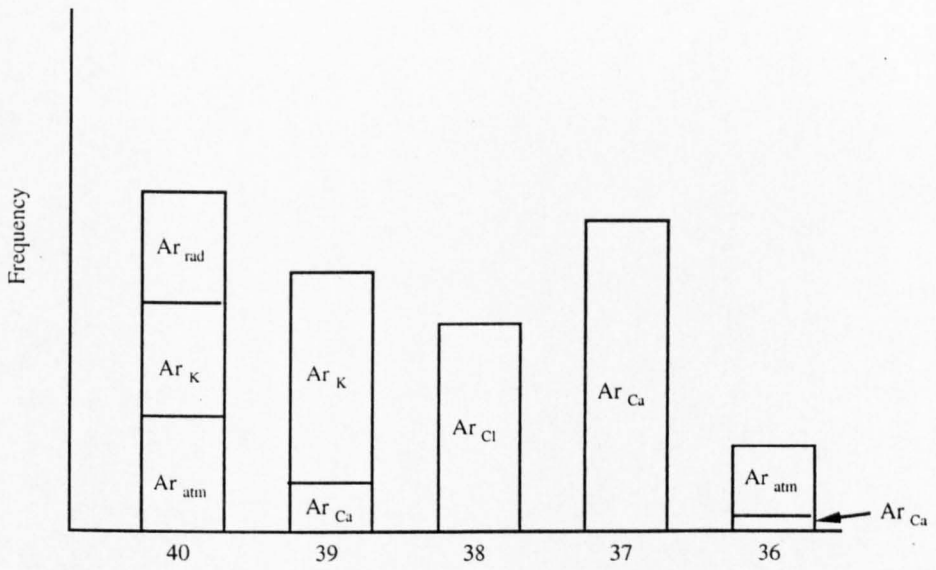

Figure 4.3.2 Schematic diagram of decreasing mass number versus abundance of isotopes measured in the mass spectrometer. To apply the age equation, the ratio $^{40}Ar_{rad}$ / $^{39}Ar_{K}$ is required, the amount of these isotopes from other sources must be excluded from the calculations. The isotopes are used to correct for reactions in the reactor. In the reactor more than just the desired ^{39}K (n,p) ^{39}Ar reaction occurs. Calcium breaks down to ^{37}Ar and ^{36}Ar, ^{39}K breaks down to ^{39}Ar. Atmospheric argon can also become encorporated with the sample. Likewise, the ^{39}Ar needs to be divided between that which was formed from ^{39}K in the reactor and that from calcium. Measuring all the isotope peaks allows this distinction.
All the ^{37}Ar is from calcium. The ratio ^{37}Ar / ^{36}Ar from the breakdown of calcium is known and is used to determine the amount of ^{36}Ar produced from calcium. This is then deducted from the ^{36}Ar peak, the remaining value of ^{36}Ar is used (using the ^{40}Ar/ ^{36}Ar ratio of 295.5, as in air) to remove the $^{40}Ar_{atm}$ from the ^{40}Ar peak. The $^{37}Ar_{Ca}$ peak can also be used to remove the effects of the $^{39}Ar_{Ca}$ from the ^{39}Ar peak. There is a similar correction for any ^{40}Ar that formed in the reactor also. The subscripts are the atoms degrading to the Ar isotope.

Blank analyses were run for the same amount of time, however without using the laser, to provide a measure of the continuity of accuracy of the equipment while used.

Laser Stepped Heating This technique involves incrementally increasing the intensity of the laser beam, until total fusion of the sample. As a consequence, argon is released from the sample in a series of steps, with more strongly held argon released as the power increases. An age can be calculated for each step (in the same way as a laser spot heating age). If the $^{40}Ar^{*} / ^{39}Ar$ system has remained undisturbed the ratio, and hence ages, should be the same for each step. However if radiogenic 40 Argon has been gained or lost, the ratios of gas released at different stages should vary to reflect this. A graph of apparent age against temperature of the step heating stages will show the lower temperature results with lower ages, and an older age from the higher temperature analyses, figure 4.3.3. A plateau is defined by the higher temperature analyses and this is taken as the age of the sample. Errors are included in the averaging process, producing a Mean Standard Weighted Deviation (MSWD), which is indicative of the quality of the data. An MSWD>>1 indicates a geological problem with the sample.

The laser beam was diffused to ~1 mm diameter. The biotite crystals were heated slowly to avoid any flaking. The initial analyses were carried out at intensities well below those of total fusion. The procedure followed for gas analysis and blank analysis was as described above. The biotite crystals have different shapes, sizes and have top surfaces lying at differing angles to the beam. Transmission of the heat right through the sample cannot be guaranteed, so the crystals do not have the same heat absorption, so the temperature associated with each step cannot be calculated accurately.. Because of this, the results of analyses can only be used to determine if there has been any disturbance since cooling and the age of cooling without attaching any quantitative significance to the energy of the laser at different stages.

Unfortunately, as a result of sample confusion whilst in the reactor, the samples were not analysed at the same time, but 9710156 was analysed a number of weeks after the rest. This has resulted in slightly differing data, for example, % radiogenic ^{40}Ar is only known for 9719156 analyses.

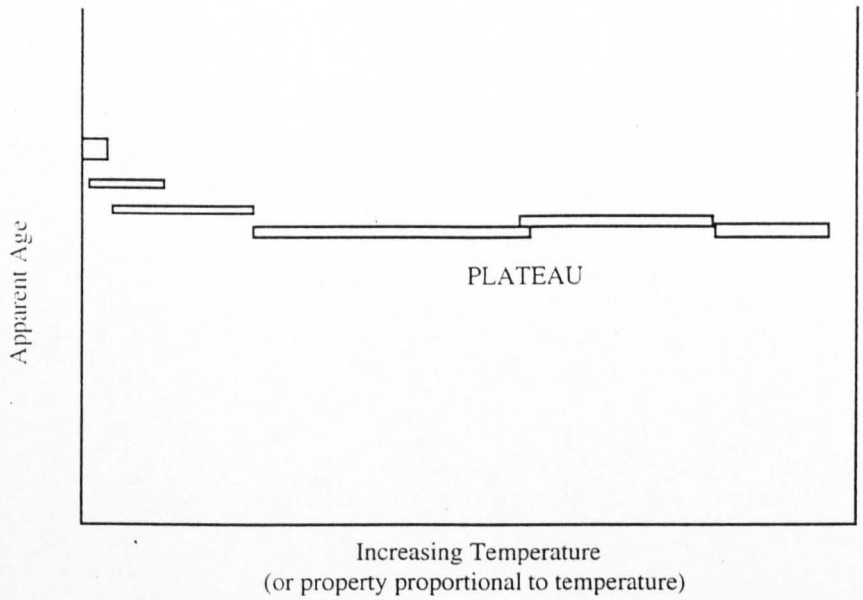

Figure 4.3.3 Interpretation of step heating results. The lower temperature components can give a lower apparent age, whilst the higher temperature componentsdefine a plateau which is taken as the age of the sample. The errors are shown by the height of the rectangle, these are also averaged to produce the MSWD, see text.

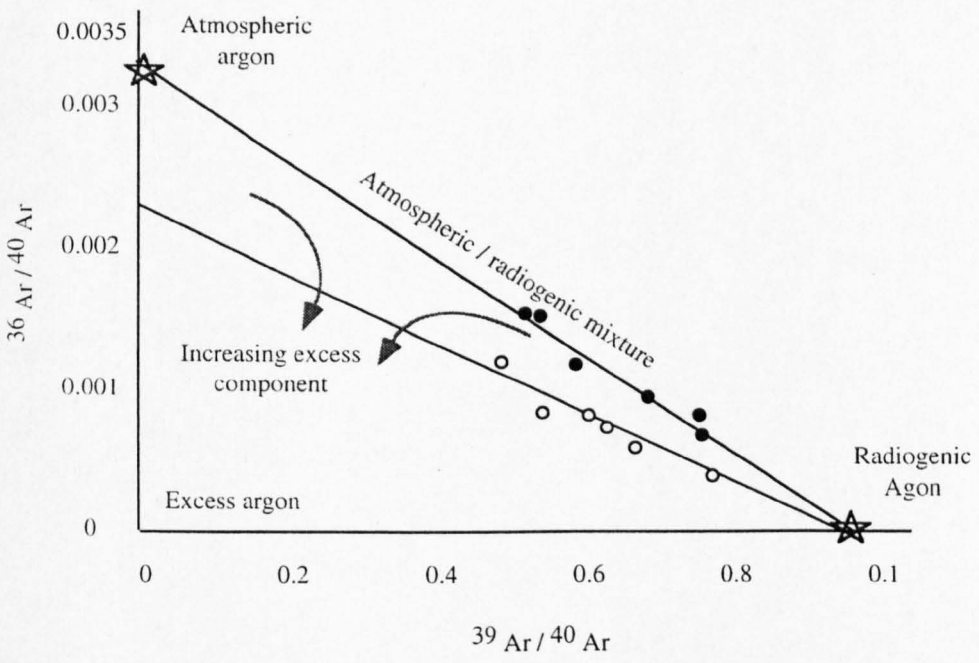

Figure 4.3.4 A plot of $^{36}Ar^{40}Ar$ - v- $^{39}Ar/^{40}Ar$, used to distinguish excess argon and the true age of the sample. See text for explanation.

Results

Argon isotope data are presented in Table 4.3.1. All errors are quoted at the 2σ level, that is, the 95% confidence interval. Samples with K/Ca ratios of less than 10 were not included in the correlation diagrams. Biotite (formula $K_2(Mg,Fe^{2+})_{6.4}(Fe^{3+},Al,Ti)_{0.2}[Si_{6.5}Al_{2.3}O_{20}](O,H,F)_4$ with occasional substitutions of Ca for K in interlayer sites) should have a higher K/Ca ratio than 10. Analysis of samples 9710083 at step 340 and 710057 at spot heating 1a, were not included because only a low percentage of argon was released, presumably from the loosely held sites and so not representative. Sample 710156F is also not included in age calculations as the % radiogenic ^{40}Ar is anomalously low.

The ages calculated from the individual step or spot heatings range from 49.8 to 54.7 My. Laser step heated samples have a weighted mean plateau age, Table 4.3.2, which give an age of 53.3 My. Neither of these calculations test for extraneous argon, or mixing with air's $^{36}Ar/^{40}Ar$ ratio. An isotope correlation diagram (Merrihue and Turner, 1966) can account for all of these factors, Figure 4.3.5. Plotting $^{40}Ar / ^{36}Ar$ against $^{40}Ar/^{39}Ar$ the ratios for each fusion or step heating event will ideally define a straight line with end points of the $^{36}Ar/^{40}Ar$ ratio (y intercept) and the $^{39}Ar/^{40}Ar$ ratio (x intercept) used to calculate the "real" age. The $^{36}Ar / ^{40}Ar$ ratio in nature is assumed constant over geological time (1/295.5, as in air), however extraneous ^{40}Ar can alter this ratio and hence affect the age calculation. The data points lie along the mixing of these two end member positions (as the results still contain data with a mixture of radiogenic and non-radiogenic argon). Unless the non-radiogenic value of the $^{36}Ar/^{40}Ar$ is known, (the y-intercept) more than one analysis is necessary to define the slope of the line. The projection of this line onto the x-axis is used to calculate the absolute ages of the samples. If the data cluster and do not adequately define a gradient for the correlation line, the line can be fixed to pass through the composition of air, thus providing a maximum age of the sample.

Correlation diagrams for this study are shown in Figure 4.3.5. Analyses of QM57 all cluster close to the x-axis, while analyses from QM56 neither define neither a line nor a cluster. The clustering of the data from hand sample QM57 has precluded independent determination of the gradient in the correlation diagram. Correlation diagrams for individual crystal step heating analyses also show clustered data, so are no more informative than one correlation diagram for the whole hand specimen data. The correlation line has been fixed to pass through the $^{36}Ar/^{40}Ar$ ratio of air (1/295.5). The sample will be younger if extraneous argon has entered the system.

Sample No	step/ spot	Jvalue	+/ -	Total39/moles	%Ar-39	% 40-Ar rad	39/4 0	+/ -	36 / 40	+/ -	K/ Ca	age	+/ -
QM5 7													
9710081	330	0.0028 45	0.0000 085		23.26		0.08912 307	0.000506 464	0.0004 014	0.0000 166	41.2229	50.0561	0.4196
	339	0.0028 45	0.0000 085		37.44		0.09141 669	0.000519 925	0.0001 240	0.0000 067	30.1437	53.2906	0.3308
	348	0.0028 45	0.0000 085		30.76		0.09255 238	0.000525 966	0.0000 886	0.0000 199	5.2168	53.2096	0.4364
	359	0.0028 45	0.0000 085	3.41E-13	8.53		0.09245 009	0.000525 418	0.0000 973	0.0000 476	2.207	53.1286	0.8006
9710083	340	0.0028 45	0.0000 085		2.67		0.1127 826	0.001133 904	0.0009 963	0.0003 241	20.6295	31.882	4.1888
	347	0.0028 45	0.0000 085		20.62		0.0910 736	0.000517 552	0.0005 321	0.0000 407	21.2269	46.9605	0.7158
	357	0.0028 45	0.0000 085		66.92		0.0873 449	0.000496 366	0.0002 599	0.0000 146	12.0102	53.5392	0.4064
	364	0.0028 45	0.0000 085		5.22		0.08915 823	0.000506 716	0.0002 732	0.0001 050	20.1337	52.2472	1.717
	fused	0.0028 45	0.0000 085	2.30E-13	4.57		0.08788 074	0.000790 825	0.0004 376	0.0001 183	20.1247	50.2323	1.999
9710057	spot 1a	0.0028 45	0.0000 085		3.23		0.08906 805	0.000506 918	0.0004 335	0.0000 940	18.3575	49.5551	1.548
	spot 1z	0.0028 45	0.0000 085		15.38		0.08836 109	0.000502 122	0.0004 279	0.0000 230	14.9914	50.0394	0.496
	spot 2	0.0028 45	0.0000 085		17.19		0.08845 652	0.0005 027	0.0002 534	0.0000 173	10.7473	52.8932	0.4292
	spot 3	0.0028 45	0.0000 085		40.3		0.08670 634	0.004927 204	0.0006 360	0.0000 083	8.6037	47.4386	0.3608
	spot 4	0.0028 45	0.0000 085	4.33E-14	23.9		0.09095 543	0.005168 602	0.0002 479	0.0000 149	101.7086	51.5502	0.3932
9710080	350	0.0028 45	0.0000 085		81.24						40.2075	49.7667	0.3784
	400	0.0028 45	0.0000 085		18.76						5.745	54.0197	0.7896
QM5 6													
9710156 A	spot	0.0028 44	0.0000 085	4.93E-15		70	0.092456 468	0.000578 578	0.0014 373	0.0000 183	44.045 16	54.655 44	0.35552 604
971056C	spot	0.0028 44	0.0000 085	9.98E-15		70	0.097934 909	0.000287 516	0.0007 116	0.0000 039	55.675 48	51.641 38	0.182783 632
9710 56D	spot	0.0028 44	0.0000 085	1.23E-14		75	0.097803 911	0.00031 952	0.0011 147	0.0000 089	66.769 33	51.709 56	0.198377 124
97I0156E	spot	0.0028 44	0.0000 085	1.00E-14		87	0.098220 924	0.000590 694	0.0005 048	0.0000 017	18.937 25	51.4931	0.3235 384
97I0156F	spot	0.0028 44	0.0000 085	4.44E-15		61	0.108822 726	0.001069 665	0.0021 535	0.0000 334	3.2201 62	46.540 64	0.4619 024
air							0		0.003384 095				

Table 4.3.1 Argon data from biotites from two samples, QM56 and QM57, along the fault in Quebrada Las Mulas. J values calculated from calibrated sanidine samples in reactor at known heights; the number in step/spot column refers to an arbitrary scale on the laser reflecting its power. A number after 'spot' is to distinguish individual spot heating from a batch of analyses.

Table 4.3.2 Results of age calculations.

Sample No	step / spot laser heating	mean weighted plateau age My	error My	MSWD	average age	error My	correlation diagram age	error
9710081	step	53.25	0.2	0.0859			51.83	1.7
9710083	step	53.35	0.5	6.121			51.11	0.8
9710057	spot				51.57	0.4	50.91	0.4
9710080	spot				51.89	0.8		
QM57 - all					53.3	0.4	52.1	0.15
9710156A	spot				54.65	0.4	31.89	0.4
9710156C	spot				51.64	0.2	43.89	0.2
9710156D	spot				51.71	0.2	34.67	0.2
9710156E	spot				51.49	0.3	41.25	0.3
9710156F	spot				46.54	0.5		
QM56 - all					53.3	0.2	39.16	3.0

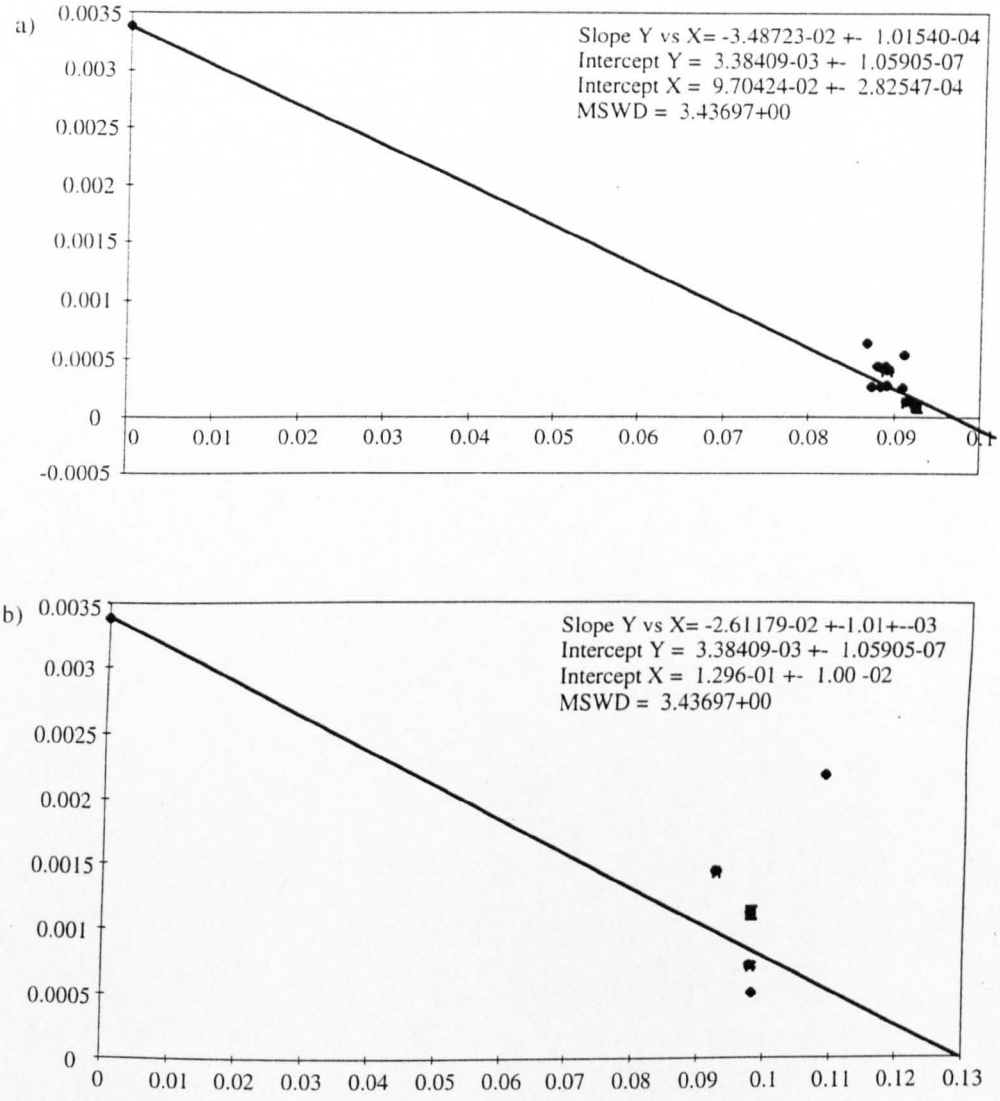

Figure 4.3.5 Correlation diagrams for (a)hand sample QM57 and (b) QM56. As neither data define the gradient of the correlation line, this has been fixed to pass through the $^{36}Ar/^{40}Ar$ composition of air. The x axis intercept is used in age calculation. Where they are not visible the error bars are smaller than the data points. The data points represent both spot and step heating results. The decay constant used in calculations is that of Steiger and Jager (1977).

Fixing the $^{39}Ar/^{40}Ar$ to pass through the atmospheric ratio, the age range of the hand sample QM56 is from 45.3 to 39.4 My. This is significantly lower than the ages calculated from hand sample QM57. It seems likely that hand sample QM56 has undergone alteration associated with the calcite veining seen in thin section. Loss of argon in hand sample QM56 would cause an increase in both $^{39}Ar/^{40}Ar$ and $^{36}Ar/^{40}Ar$ ratios. Extraneous ^{36}Ar would simply cause an increase in $^{36}Ar/^{40}Ar$ ratio. Either effect would prompt a younger apparent age for the sample. Extraneous ^{36}Ar can be produced from $^{39}K(n,\alpha)^{36}Cl$, with subsequent decay of ^{36}Cl to ^{36}Ar with a half life of $3x10^5$ years (Dalrymple and Lanphere, 1971). Recalling the consistent stratigraphic age assignation with results from QM57, the maximum age of the rhyolite will be taken as **52.1 +/-0.15 My**. The lower age calculated for hand sample QM56 could be the age of the alteration, however the extent of the disruption to the argon system is unknown so these ages are not attributed any significance here.

Significance in Regional Geological Chronology

The age of a mineral calculated from the accumulated radioactive decay products corresponds to the time when a mobile daughter product became trapped within the lattice. For shallow igneous rocks, provided the extrusion temperature is high enough to have re-equilibrated the isotope proportions with the environment, cooling is rapid and the age produced should correspond accurately with the age of extrusion. Any later heating of the unit can cause whole or partial resetting of the argon ratios within the system.

The maximum age of the rhyolite dyke is 52.1 +/-0.1 My. This is consistent with the model of the rhyolite dyke as a conduit for the Chile-Alemania Fm (Chong, pers.comm. 1995). Disturbances in the $^{39}Ar/^{40}Ar$ system in QM56 associated with the $CaCO_3$ veining, which, in turn, is probably associated with faulting. The faulting is thus younger than the dyke, which is consistent with the inference that the dyke had cooled prior to faulting. The Ar^{39}/Ar^{40} system has remained undisturbed away from the $CaCO_3$ veins.

This work was carried out at the Scottish Universities Research and Reactor Centre in East Kilbride, under the guiding hand of Malcolm Pringle.

4.4 Palaeomagnetic Analysis

Palaeomagnetic Sampling

Sites QM10 (GR S25° 06' 18.1" W 069° 16' 41.0": 4054m) and QM11

The two sites are 80m away from the rhyolite which is cut by the NNE striking fault in Quebrada Las Mulas, Figure 4.2.8. Both samples are taken from the purple rhyolite. Care was taken not to sample iron stained units, since thin section evidence suggests this was later than fault activity. The iron staining is restricted to fracture and slip surfaces, so this proved possible. QM10 is at the southern end of the mapped fault, where fault motion has produced discrete slip surfaces; QM11 is east of a localised fault zone of intense fracturing. Neither site contains a fracture surface. The sites are assumed to be of the same age as they have identical mineralogy and textures (Ar^{39}/Ar^{40} dated at 52.1+/-0.1 Ma, Ch 4.3). The methodology of sampling, laboratory preparation and analysis is the same as that described in chapter 2.

Both sites exhibit a multicomponent natural remanent magnetisation (NRM); however only 4 cores from QM11 exhibit a discrete low blocking temperature component (Table 3.2.1). One of these components is aligned with the present day field but there is no apparent concordance of directions between the other three cores and they were probably acquired in the laboratory. Similar thermomagnetic curves at each site indicate that magnetite is the dominant ferromagnetic constituent with haematite present as a subordinate saturating mineral. The thermomagnetic curves also show a Curie point at ~370 °C, Figure 4.4.1, indicating the possible presence of maghemite, although this is not apparent in the intensity plots of individual cores during thermal demagnetisation, when it may be progressively converted to haematite.

As noted in chapter 3, equations governing closure temperature of Argon diffusion and the blocking of magnetic remanence have the same form (York, 1978). The radioisotopic data presented earlier (Ch 4.3) indicate a relatively simple thermal history, with veins, and probably slip surfaces, resetting the system locally . It is therefore concluded that the remanence in these samples is primary, given that veins and slip surfaces were avoided when sampling.

Measurements of AMS highlight a weakly oblate anisotropy ellipsoid (Figure 4.4.2). Both

a)

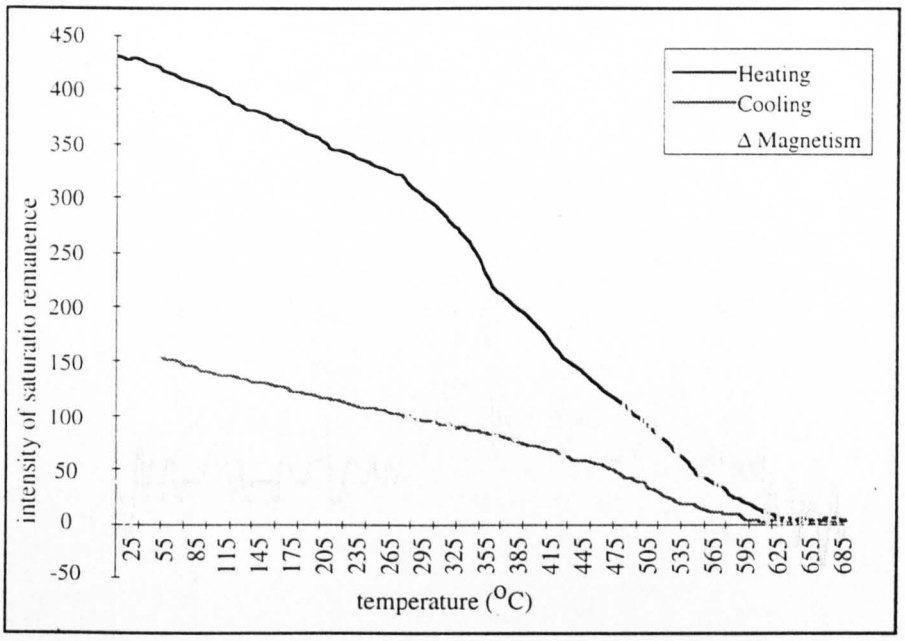

b)

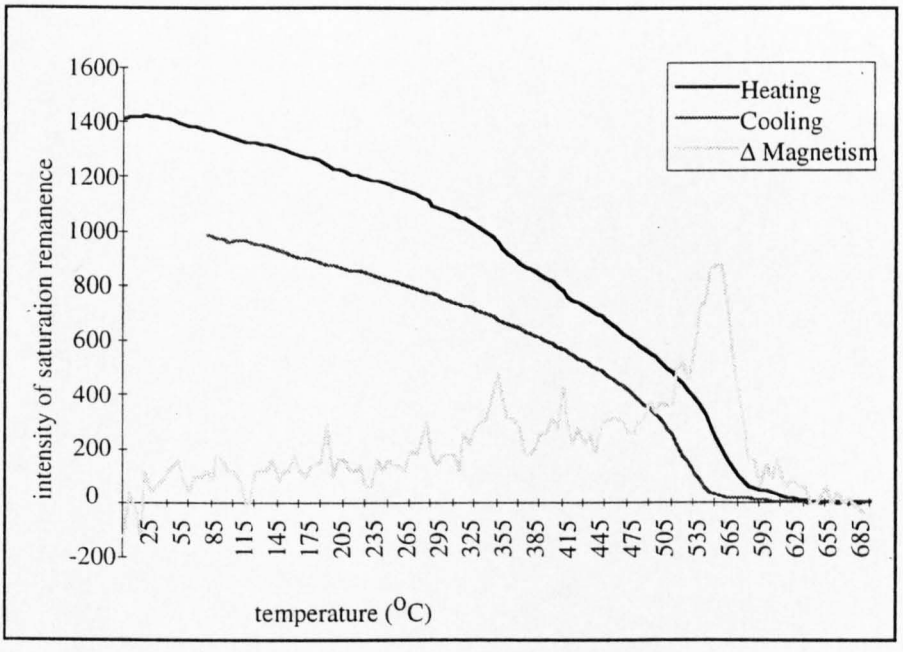

Figure 4.4.1 a) Thermomagnetic curve for QM11 block A. The darker curve is the heating curve and indicates Curie points at 370° C , 550° C and 650°C. The light grey curve is the gradient of the heating curve and is used to determine inflection points more accurately. the vertical axis is measured in mT.

b) Thermomagnetic curve for QM10 block B. A minor inflection at 380° C hints at the presence of maghemite. The dominant magnetic carrier is again magnetite with some haematite, indicated by the 580°C and 635°C inflection points, respectively.

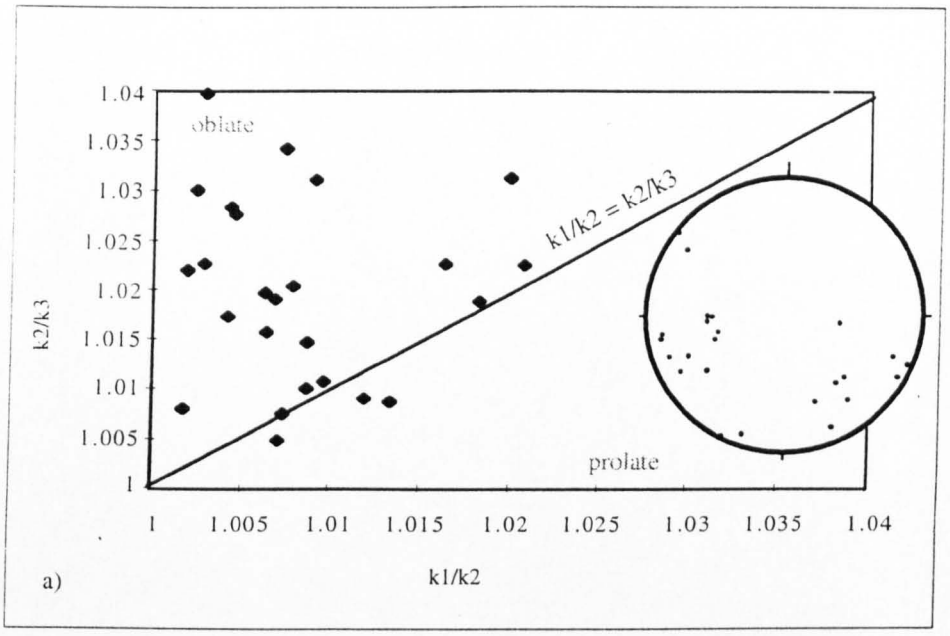

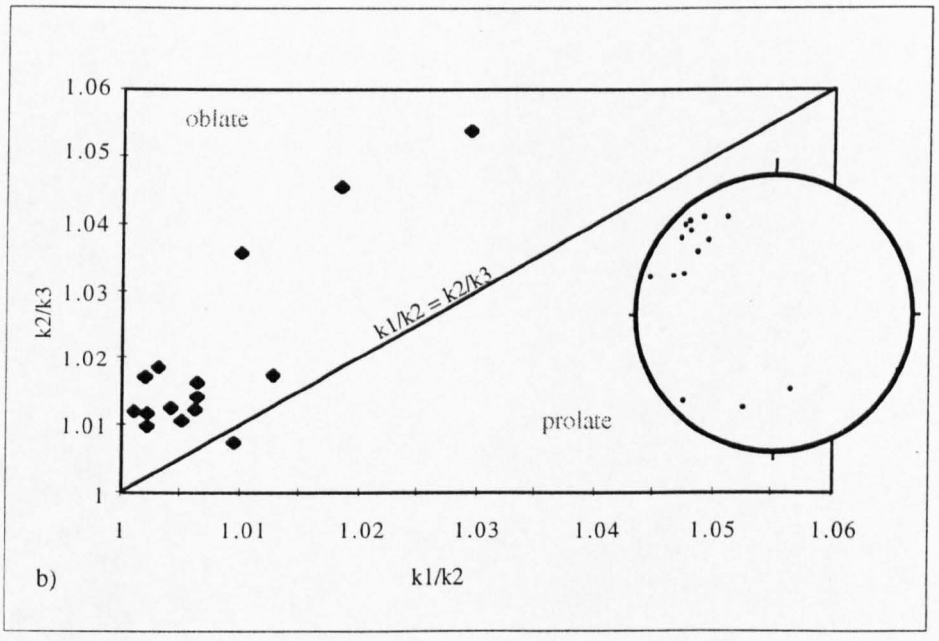

Figure 4.4.2 a)Flinn diagram for site QM10. The line of gradient =1, indicates isotropy. Inset stereonet shows k_3 directions. This is the best grouped axis, although grouping is deemed insufficient to define the axis precisely. b) Flinn diagram and k_3 distribution for site QM11. The k3 axes both lie approximately perpendiculr to the strike of the rhyolite dyke.

QM10 and QM11 have poorly grouped axes of anisotropy with the k_3 axes showing most concurrence. The degree of anisotropy (P_0) prior to thermal cleaning of both QM10 and QM11 is 1.03 and implementing equation [A3.2] yields a modification of the ambient magnetic direction of less than 1° for both samples. Comparison of Figure 4.2.5 with 4.4.2 shows the AMS is not unambiguously related to the incremental strain axes. The degree of anisotropy is more commonly associated with magmatic flow than deformation (Hrouda, 1982) The AMS is therefore inferred to be a primary fabric reflecting flow during emplacement, rather than deformation fabrics. The variation in AMS along the dyke indicates the primary fabric anisotropy is not pronounced. The flow fabric is perpendicular to k_3 and steeper than the slip surfaces contained within the dyke. Assuming the flow is parallel to the dyke margins, the slip surfaces are steeper than the dyke boundaries.

Figure 4.4.3 shows the two magnetic components at QM11 and QM10 and the planes containing the axis of net rotation between these two sites. These planes have been defined by the line bisecting the two temperature components and the pole to the plane containing these components. Ideally the intersection point of two planes should yield the unique axis of rotation. However since these planes are sub parallel, a small error in one could result in a large error in the intersection point. However from the preceding detailed kinematic analysis of this fault, the axes of rotation from two slip systems active along the fault are already known, the intermediate strain axes.

There are few palaeomagnetic results available for cratonic South America during these times, as most Mesozoic - Recent palaeomagnetic studies in South America have focused on either tectonically active regions or regions that have undergone tectonism since acquiring magnetism. To surmount this deficiency Roperch and Carlier (1992) calculated an APWP for South America from 0 - 200Ma based upon the African APWP (Besse and Courtillot, 1991) after incorporating the progressive closure of the South Atlantic, using rotations determined by Cande et al (1988) and culminating in the total fit of Lawyer and Scotese (1987), Figure 4.4.1. The resultant curve fits well with other available South American data (e.g. Ernesto and Pacca, 1988, Butler et al, 1991) and the APWP is summarised in Table 3.3.2. For the age and location of the ignimbrite dyke, the APWP predicts a magnetic direction of - 27 / 004 at 50Ma and - 34 / 008 at 60Ma. For the age of the ignimbrite dyke of 52.1Ma, this gives an expected magnetic inclination and declination of - 30 / 006 with an α_{95} of 4.3°. Figure 4.4.4 displays this information.

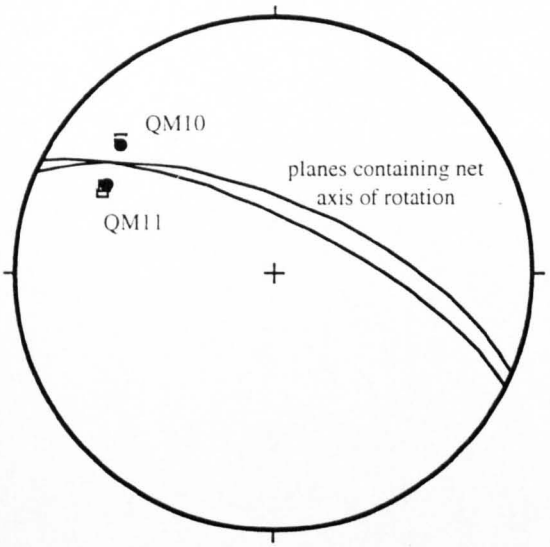

Fig 4.4.3 Location of the net axis of rotation between sites QM10 and QM11, along fault at Quebrada Las Mulas. Circles show magnetic components calculated at 550° - 675°C and obscured squares show components calculated at 0° - 450°C components. The high and low temperature directions seem to represent the same component. The averaged plane containing the net axis of rotation is oriented 114 / 70 N. 95% confidence circles of 4 for QM10 and 6.5 for Qm11 have not been shown, they do not put the two readings within error of eachother.

Age Ma	VGP/Afr lat	long	rotations Afr/SA lat	long	Angle	VGP SA lat	long	α_{95}
10	84.3	159.0	59.7	−38.5	3.6	84.5	137.4	2.3
30	82.0	155.2	57.0	−35.0	3.6	80.5	107.3	2.7
50	76.9	191.1	59.0	−31.5	19.5	78.9	127.0	4.3
60	73.1	216.1	61.5	−32.5	22.7	80.5	160.7	4.2
80	66.4	232.2	63.0	−34.0	31.0	78.9	183.0	3.5
100	61.6	245.6	53.7	−33.1	41.5	84.4	174.9	7.1
130	51.0	262.4	44.5	−32.2	58.2	87.4	344.9	4.9
150	54.8	245.9	44.5	−32.2	58.2	80.3	87.8	6.4
170	63.5	231.8	44.5	−32.2	58.2	69.6	72.5	2.9
200	66.3	242.9	44.5	−32.2	58.2	71.1	56.8	6.7

Table 4.4.1 Calculated apparent polar wander path for South America, taken from Roperch and Carlier (1992). See text for explanation. VGP is the virtual geomagnetic pole for South America. Specifying latitude and longitude, the VGP can be used to calculate palaeofield directions.

The two rotation axes, A and B, are mutually perpendicular. It can be seen that the rotation from the primary remanence direction to the resolved magnetic components at sites QM10 and QM11 cannot be achieved without appreciable rotation about both axes. This indicates that one set of slip surfaces is not merely accommodating the other, but that both have played a significant role in the fault history. The exact rotation path is not shown and probably involves alternating rotation about each intermediate strain axis.

Sense of movement

A clockwise rotation about axis A (when viewed from the NE) has been recognised from the kinematic analysis. This rotation coupled with a clockwise rotation about axis B (when viewed from the NW) can result in the rotation of the primary remanence onto the measured ChRM directions. A clockwise rotation about intermediate axis B requires rotation through a smaller angle than an anticlockwise rotation, hence this seems more probable. The order of rotation does not affect the orientation of the result. It is assumed that the active axes themselves are not rotated. Neither the intermediate strain axes of system A or B can map the palaeofield primary remanence onto the ChRM's determined at sites QM10 and QM11. Both A and B slip systems must have been active to rotate the ChRM by the observed amount.

Along the length of the fault there is evidence for differential rotation as shown by the contrasting remanence directions at sites QM10 and QM11. This difference could be achieved most simply by rotation about the B axis and is of the order of 40° (see Figure 4.4.4). QM11 lies in a region with nosystem B surfaces, while QM10 lies in a region with both system B and system A surfaces. The rotation along the fault zone is not constant. This reflects the division of the fault zone into regions of different slip surfaces and causes a displacement gradient.

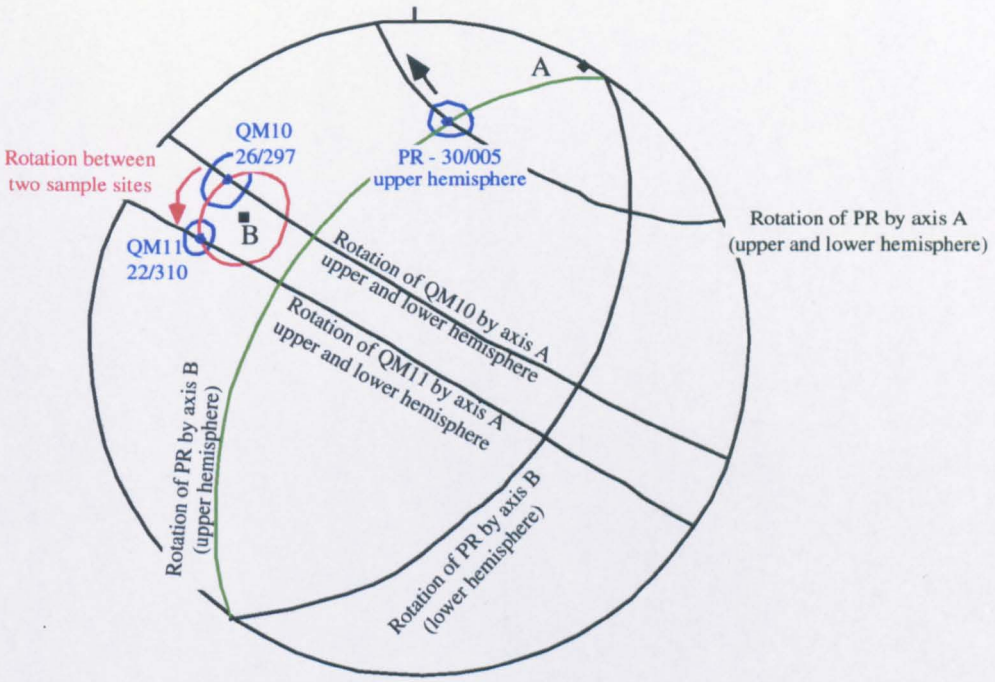

Figure 4.4.4 The primary remanence direction (PR),(as calculated from Roperch and Carlier for 52 Ma, 1992), the ChRM directions determined from samples QM10 and QM11 with the two rotation axes, A and B, equivalent to the intermediate incremental strain axes. The small circles surrounding the ChRM's are the α_{95} radii of the cones of confidence. The rotation paths of the various components rotated by different axes are shown, the sense of rotation about axis A is known from kinematic analysis. QM10 is in an exposure with A slip surfaces , exclusively, whilst QM11 is from an exposure with both A and B slip surfaces. The difference in the ChRM of each sample is clearly due to rotation about the intermediate strain axis from slip system B.

4.5 Model of the Fault Zone

Any model of the fault zone needs to be consistent with the evidence determined previously.

(i) Comparison of the age of the rhyolite with the age of the main fault activity indicates the rhyolite was in place for the main fault event and the rhyolite had cooled.

(ii) From the presence of pseudotachylyte it is evident that the fault was subject to seismic failure. A cyclicity in activity of slip surfaces indicate many separate events.

(iii) The kinematic analysis revealed two contemporaneous slip systems. Slip system A accommodates dip slip faulting with downthrow to the west; slip system B accommodates oblique slip, possibly with a reverse and dextral sense. Boundary structures are inferred to define the edges of the fault zone within the rhyolite.

(iv) The palaeomagnetically determined rotations show activity of both fault systems was necessary to cause the observed rotations. Differential rotation along the fault can be correlated with the presence of system B slip surfaces. The presence of system B slip surfaces has caused an additional rotation of ~40° about the B axis in an anticlockwise direction for sample QM11 as compared with sample QM10. The rotation caused by the presence of system B structures is compatible with the rotation sense along the whole fault.

The composite intermediate strain axis for systems A and B is assumed to lie on a great circle defined by the two incremental intermediate strain axes. As the two slip systems are secondary to larger boundary faults the composite intermediate strain axis should coincide with the intermediate strain axis for the boundary structures. The palaeomagnetic analysis has defined a plane containing the axis of rotation to map the predicted palaeofield primary remanence direction onto the ChRM's determined from sites QM10 and QM11. The axis of rotation is coincident with the intermediate strain axis. The intersection of the plane containing the axis of rotation and plane containing the intermediate strain axis should define the intermediate strain axis of the fault, Figure 4.5.1. This will actually be an approximation as the intermediate strain axis for system B is only the incremental strain axis. The profile plane at 90° to the intermediate strain axis contains the slip direction of the fault. From the majority of slip surfaces in both data sets A and B, it is assumed the boundary fault plane dips to the west. An estimation of the intersection point of the boundary fault and the profile plane defines the slip direction. The slip direction for a westerly dipping boundary fault with a north-south or NNE-SSW strike indicates oblique slip. With the palaeomagnetically determined sense of rotation, this indicates components of sinistral and normal motion. The low plunge of the slip direction indicates the normal

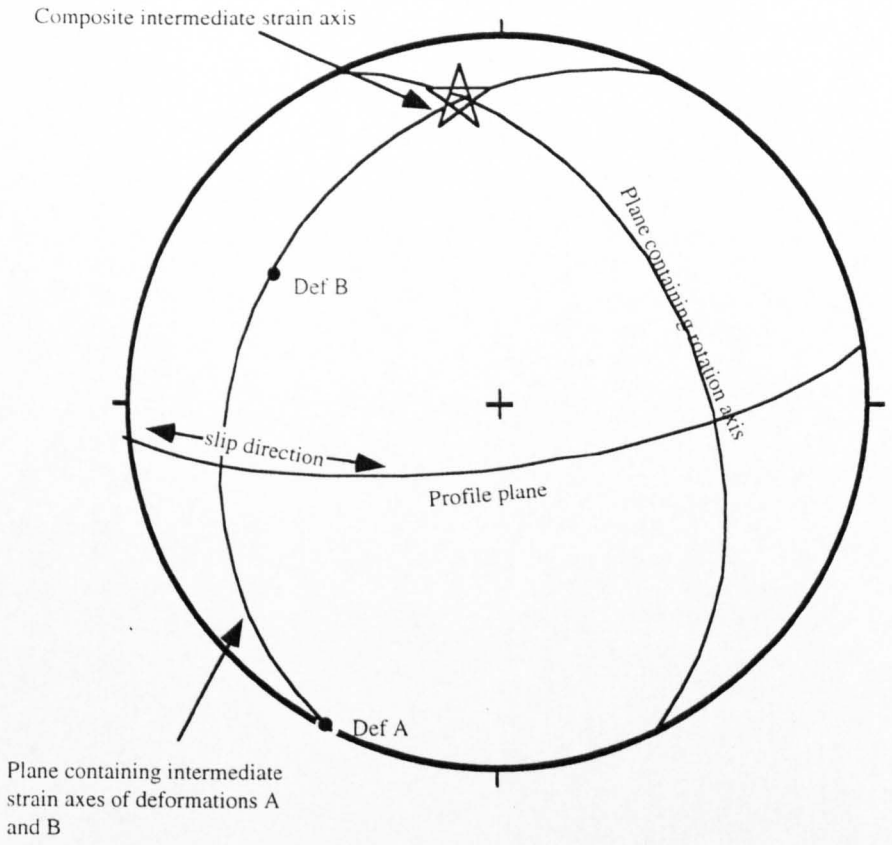

Figure 4.5.1 The composite intermediate strain axis for the fault has been identified at the intersection between the plane containing the axis of rotation, determined from palaeomagnetic analysis and the plane containing both intermediate strain axes of deformations A and B. The slip direction must lie in the plane of the fault and in the profile plane. The fault is inferred to dip to the west, producing a range of slip directions. Fuller explanation in text.

component of motion is much greater than the lateral component.

Comparison of the sense of slip of the overall fault system with the individual senses of slip for systems A and B shows system A to be synthetic. System B is antithetic if the interpretation of the fracture distribution in the profile plane is valid (Figure 4.2.9). It is known from the differential palaeomagnetically determined rotations of sites with B slip surfaces and sites without B surfaces (Ch 4.4) that rotations from B are synthetic to the overall sense of the fault. The errors involved in the estimation of the composite intermediate strain axis cannot be quantified without knowledge of the system B finite strain axis. It is possible the slip direction could plunge towards the NW, not west. This would result in a dextral lateral component of motion. Alternatively, the initial interpretations of system B with a dextral component of motion, and a sinistral offset along the fault could occur. Overlap of the slip surfaces would result in a rotation synthetic to the sinistral offset of the fault. The two cases cannot be distinguished. The majority of displacement was dip slip, which is determined to have been in a normal sense.

The Reidel model of fracture generation within a brittle fault zone has been shown to be valid within the slip systems operating along the rhyolite dyke. The fractures within A and B slip systems have Reidel geometries, without the presence of faults bounding the separate systems. Physical modeling has identified R and P fractures form early in the development of a fault zone, followed by Y fractures, then R' and X fractures (Naylor et al 1986, summarised by Sylvester, 1988). System A has R, Y and P fractures well developed with a small amount of R' fractures. Slip system B has a different kinematic history. It can only be tentatively compared with slip system A as it was a non-plane strain event. There are equally developed R and P fractures, less well developed Y and R' fractures and poorly developed X fractures. This slip direction is more variable in system B than in A. This may have consequence in the development of the secondary fracture system.

Systems A and B do not demonstrate a simple relationship with each other as described in the Reidel model of secondary fracture generation. This may reflect partitioning of strain as a result of a planar heterogeneity within the rhyolite.

Conclusions

Two systems of slip surfaces have been identified along the ignimbrite, using tangent lineation diagrams. Cross cutting relationships have shown them to have been interactive in

achieving the net displacement. The distribution of slip surfaces and their symmetry in the profile plane indicate that slip system A underwent plane strain, while slip system B underwent non-plane strain. The difference between the two attributed to a pre-existing heterogeneity. Palaeomagnetic analysis has shown both were important in producing the resultant displacement along the fault. Combining the kinematic and palaeomagnetic data the overall fault motion is identified as predominantly normal with a minor strike slip component of motion. The strike slip component of motion is tentatively identified as sinistral. The fault activity was after 52.1 +/- 0.15 Ma.

Chapter 5

Analysis of the Localised Fault Zone

CHAPTER 5 ANALYSIS OF THE LOCALISED FAULT ZONE

Objectives of Chapter 5

A detailed study of secondary fracture geometries between two slip surfaces is undertaken. The main objective is to define a technique for identifying kinematics from fracture orientation which will be transferable for use in other brittle fault zones. This is especially important for the DFS as many fault have undetermined kinematics due to a lack of striations. Two samples taken from within 1m of each other are analysed. A novel approach is used; this involves modeling the shapes of rock pieces between secondary fractures. Comparison of the fractures across the localised fault zone with the kinematic features identified in Chapter 4 for the whole fault is then undertaken to understand how the localised fault system reacts to the larger system. Finally, the fracture orientations present in the localised fault system can be divided into groups based on orientation. These are then compared with the order of fracture generation as identified by physical modeling (Bartlett et al, 1981).

5.1 Fracture Analysis

A complex network of fractures can be seen between the two bounding surfaces of the localised fault zone, Figure 4.1.3. No slickenlines are accessible on these surfaces, so analysis is dependent upon the orientation of the fractures between the bounding surfaces.

Within the localised fault zone, the surfaces along which displacement has occurred are referred to as fractures. Outside the localised fault zone, the surfaces are referred to as slip surfaces. The distinction is based upon scale. The slip surfaces are seen to be continuous over at least a few metres. Whilst many of the fractures within the localised fault zone can only be traced for a few centimetres. It is likely that trace length reflects the magnitude of displacement. Within the localised fault zone small offsets of the thicker fractures (up to 4 mm width) by thinner fractures can be seen to be in the order of a few mm to cm displacement. Offsets of the thinner fractures by thicker fractures are harder to distinguish as there are so many thin fractures. The thicker fractures may become separate slip surfaces away from the fault zone, however they shall be referred to as fractures within the fault zone.

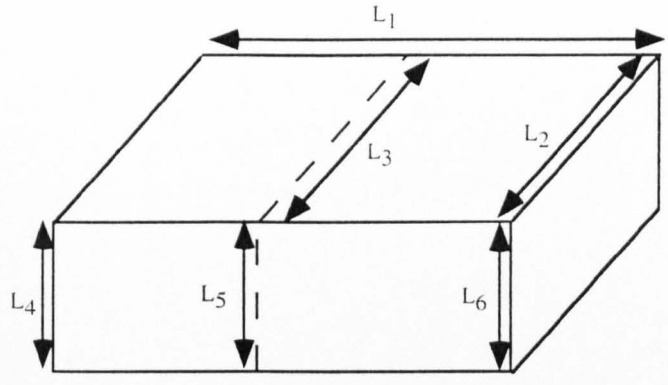

Figure 5.1.1 Sections through the samples were cut so that the total length of intersections between orthogonal sections were the same length. This avoided bias in the data set towards fracture surafces perpendicular to the longest intersection.

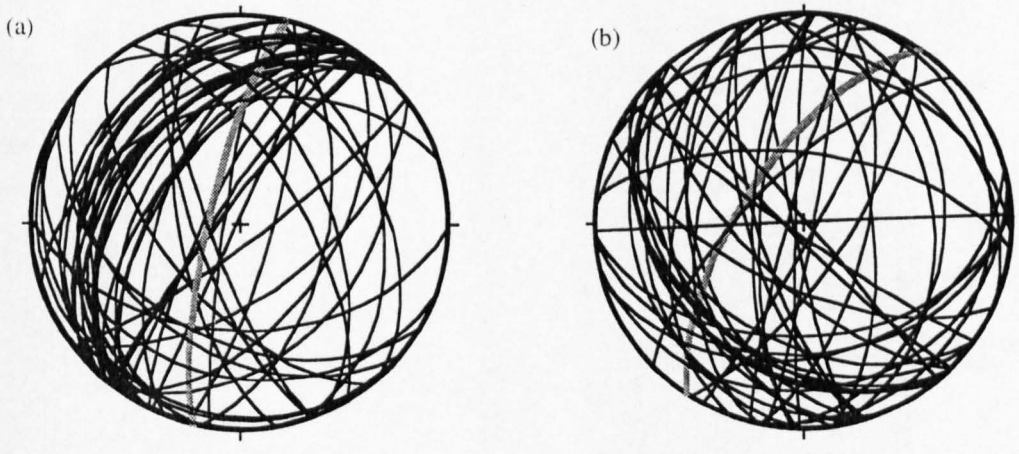

Figure 5.1.2 Orientation of fracture planes measured from samples of the localised fault zone. The orientation of the bounding slip surfaces are shown by a grey thick great circle.
(a) Hand sample QM63, fractures measured inside the fault zone; (b) fractures measured from hand specimen QM65, inside the localised fault zone.

Each sample was oriented in the field. The samples were sliced to produce three orthogonal sections and each section oriented. The errors associated with re-orienting samples is estimated to be up to 4° (2° is the accuracy of a Silva compass clinometer, used on two independent occasions). For each fracture, the pitch was measured on two sections. These data were combined on a stereonet to give the orientation of the slip surface. To avoid biasing the data set against slip surfaces parallel to one of the cut sections, sections were cut into the rock such that their intersections were of the same length and orthogonal, Figure 5.1.1. Initially two samples, QM63 and QM65 were analysed, Appendix 5.

Both samples QM63 and QM65 were taken from 55m to the SSW of the reference point along the rhyolite dyke in a zone of exclusively system A slip surfaces, Chapter 4.3. Both samples contain the localised fault zone. In sample QM63, across the fault zone approximately 15% of the rock is made up of fault rock. In sample QM65 the fault rock makes up 25% of the sample. The fractures within the localised fault zone sole into one another, abut each other and offset each other, with complex relative timing. The fractures are assumed to have formed during the same event, which is inferred to be contemporaneous with activities of slip system A.

The orientation of the bounding fractures of the localised fault zone are 011/79W and 038/70W for samples QM63 and QM65 respectively. The fractures in sample QM63, Figure 5.1.2 (a), have a group of fracture surfaces comparable with the fractures associated in data set A, Figure 4.2.6. The common intersection direction for the fractures is 09/024, Figure 5.1.2(c). Sample QM65 has no dominant fracture orientation, however the common intersection direction is 21/178. Comparison with system A slip surfaces, Figure 4.2.6, shows QM63 to have a fracture set with a distribution similar to system A (striking NE, dipping to the west), however there are also some fractures not represented in the system A slip surfaces. Sample QM65 does not have a fracture distribution representative of system A slip surfaces or system B. Both of the intersection directions of the fracture sets lie within the contoured region for the intermediate incremental strain axes of data set A, Figure 4.2.5, determined using Marrett and Allmendinger's technique (1990). The intersection of fractures in sample QM65 however, lie on the outskirts of this region.

The fractures between the bounding structures in a fault zone interact, so are not independent fractures. They are therefore inferred to have formed in response to the bounding fault imposing simple shear across the fault zone. Application of the Reidel

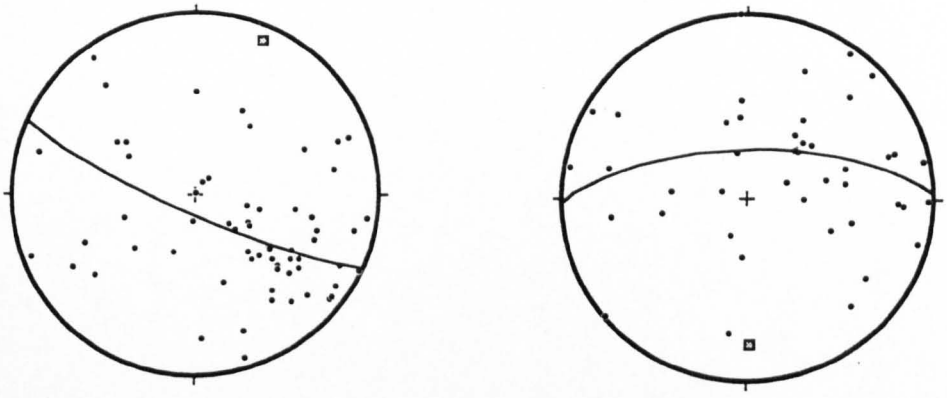

Figure 5.1.2(c) Poles to fracture orientation in samples QM63 and QM65. The pole to the best fit great circle is the average intersection direction of the fractures. For QM63 this is 09/024 and for QM65 this is 21/178.

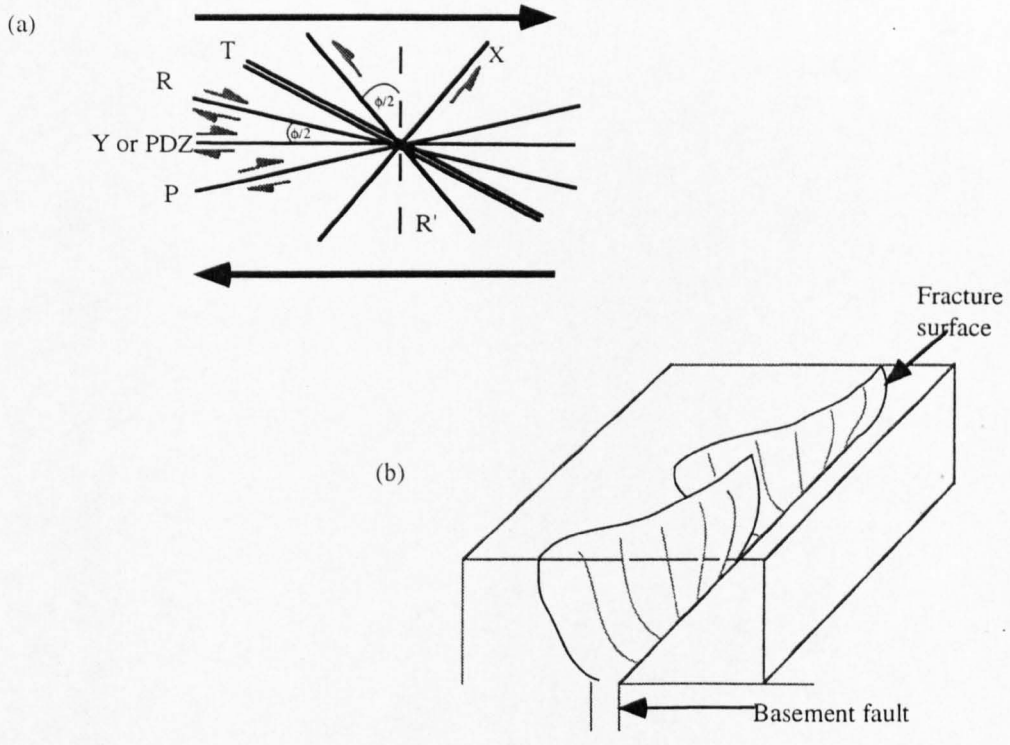

Figure 5.1.3(a) Model of expected fracture patterns from simple shear, in 2 dimensions. Riedel model, (from Sylvester, 1988)

R, P & PDZ	synthetic shears
R' & X	antithetic shears
T	extensional veins

If all the fractures are perpendicular to the plane of section and do not vary in orientation, whole rock pieces between the fractures, would be infinitely long in the direction of the fracture intersection.

Figure 5.1.3(b) Individual Reidel shears in dextral simple shear, reconstructed from sections through a sanbox after physical modelling experiments, after Sylvester, 1988 and Naylor, 1986. The effects of overlapping fractures can be seen to modify the fracture orientation.

model of simple shear, (reported in Sylvester, 1988), Figure 5.1.3(a) can be used to determine sense of movement of the system. The distribution of associated fractures, when viewed in the M-plane, should form an asymmetric array (Ch 4.3). Comparison of the fracture pattern and, if possible, the sense of offsets along these individual fractures with the Reidel model can be used to determine the sense of shear, as in Ch 4.3. From Reidel's model, the fractures generated during the simple shear should intersect in the orientation of the pole to the M-plane, the intermediate strain axis. In reality, the intersection of these fractures is tends to plot near the orientation of the intermediate strain axis, but not necessarily parallel, as can be seen by comparison of Figure 5.1.2 (c) and Figure 4.2.4. Naylor et al (1986) have shown in three dimensions that slip surfaces need not be planar, Figure 5.1.3(b). Overlap of slip surfaces causes modifications of both surface orientation and slip direction. The difference between the intersection lineation of the fractures and the intermediate strain axis may be a result of this, or may reflect local variations in the strain axes. To base any kinematic interpretation on fracture distributions, the effect of variation in the fracture orientations must first be compensated for.

In order to side step this problem, it has been recognised that the intact fragments of rock defined by the fractures and fault rock are a complementary data set. The intact clasts defined by the fractures of fault rock have a common shape on any planar section cut through the fault zone. The clasts share a long axis, and consequently short axis, orientation. There is an elliptical shape fabric defined by the intact clasts of rock, apparent on sections cut through the fault zone. Measurements of the clasts will not only yield a complementary data set to fracture orientation measurements, but will have the effect of averaging out the local deflections in fracture orientations. If defined by a planar fracture set, clasts would be infinitely long in the direction of the intersection. The curvature of fractures as described by Naylor et al (1986) causes termination of clasts. Sections through the localised fault show the intact clasts of rock to be elliptical, as defined by the fracture network. The clasts are assumed to be ellipsoidal in three dimensions. This assumption will be assessed when calculating the ellipsoid axes.

The clast shapes are a function of fracture orientation and slip on the surfaces. As the displacement increases, either the system will lock up as angular extremities of neighbouring clasts come into contact, or the clast shape will be abraded to allow movement. The comminution of the host to form cataclasites, will occur at regions of highest stresses - at touching asperities between clasts. As abrasion continues, the

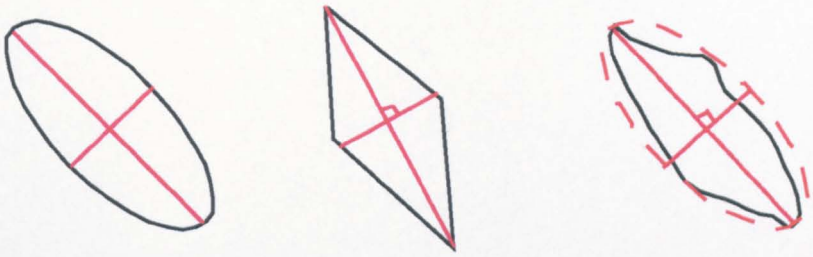

Figure 5.2.1 Measurement of elliptical clasts of rock between the slip surfaces. The aspect ratio of the ellipse was measured (long/short axis), the orientation of the long axis and the orientation of the plane measurements were taken on. If the fragment shape was irregular, as in the final case, and the shape bulged both above and below the half way line on the long axis, then the short axis was extended up to this line.

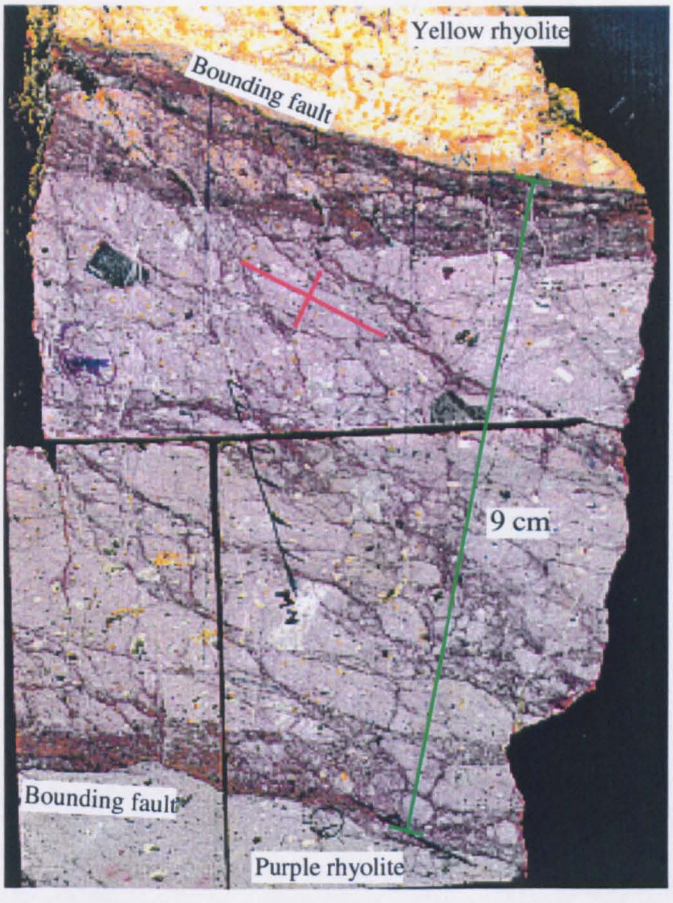

Figure 5.2.2 A scanned image of the localised fault zone occurring along the tectonic contact of the yellow and purple rhyolites, sample QM63. The distance between bounding slip surfaces is 9 cm. The axes of an ellipse is drawn. There is a common orientation of rock clasts with an elongation about this direction.

relationship between clast shape and fracture geometries becomes complex. Thus if cataclasis has occurred beyond a critical level, the clast shape fabric will be obscured within the rock. This can also obscure displacement sense and magnitude along fractures where the edge of a clast has been removed.

5.2 Methodology

The long axis orientation and aspect ratio of ellipses on approximately orthogonal, oriented sections through the localised fault zone were measured on two samples, QM63 and QM65, Figure 5.2.1 and 5.2.2. The fracture orientations were determined from the same sections (Ch 5.1). The measurements were only taken where a clast fabric was apparent.

Calculating a best fit ellipsoid

From measurements of pitch and axial ratio measured on three randomly oriented sections the best fit ellipsoid can be calculated by a program by Owens (1984). The process is divided into two stages, the first program, Tryel, is used to identify 6 initial solutions which are then individually refined using a least squares approach in the second program, Bfel. A successful analysis results in converging answers. That is, while the six solutions for each data set are refined in Bfel, the individual solutions should tend towards each other. The initial ellipsoid is generated using an equation for the trace of an ellipse on a plane. The remaining five solutions are then calculated using this value in three equations. Systematic effects arising from the fact that the initial solutions are tied to the reference frame are avoided by orienting the principal ellipsoid axes randomly with respect to the reference axes. Orthogonal sections are found to produce the most accurate results.

There are three separate quality controls. A rapidly converging result indicates a consistent data set. The program also calculates axial ratio and orientation predicted from the calculated ellipsoid for sections with the same orientation as those input. A scattering about the actual measurements indicates a reasonable result, consistently high or low results indicates some outliers in the data set. The final quality control is a "notional undeformed ellipse", ρ. The ellipsoid is "undeformed" to a sphere; the aspect ratio of which on any surface should be 1.0, the difference provides a measure of the data consistency. The values of the undeformed ellipse are averaged for each ellipsoid calculation (using a weighted log

(a)

	329/29	Section orientation	
	Aspect ratio	Theta	
	5.00	31.00	
	3.50	53.00	
	4.00	62.00	
	2.67	35.00	
	2.57	21.00	
	4.17	49.00	
	3.14	18.00	
	2.83	41.00	
	4.57	50.00	
	3.82	49.00	
	4.33	41.00	
	3.40	45.00	
	3.32	40.00	
	2.40	23.00	
harmonic mean	3.39	39.96	vector mean
	223/82	Section orientation	
	2.19	55.00	
	2.00	15.00	
	1.75	35.00	
	2.50	30.00	
	2.80	32.00	
	2.69	31.00	
	2.80	25.00	
	2.00	18.00	
	1.90	19.00	
	2.92	15.00	
	3.70	7.00	
harmonic mean	2.36	25.31	vector mean
	158/54	Section orientation	
	2.43	116.00	
	2.83	120.00	
	5.00	118.00	
	2.67	132.00	
	2.83	131.00	
	2.07	119.00	
	3.25	131.00	
	2.29	140.00	
	3.33	136.00	
	2.33	112.00	
	2.00	108.00	
	3.82	148.00	
	5.00	137.00	
harmonic mean	2.82	126.75	vector mean

Table 5.2.1 (a) Measurements of aspect ratio and long axis orientation of ellipses taken on orthogonal sections of QM63. The data from each section are averaged using harmonic and vector means (Lisle, 1986), to calculate the representative ellipse for each section.
(b) Data input to Tryel includes the strike and dip of the sections the measurements were taken from; the pitch of the average ellipse long axis on the section (vector mean); the average axial ratio of ellipses (harmonic mean) and each data point is given equal weighting. If two parallel sections are input to Tryel they are each given a reduced weighting.

(b)

Strike	dip	pitch	axial ratio	weight
223	82	25	2.4	1.0
158	54	127	2.8	1.0
329	29	40	3.4	1.0

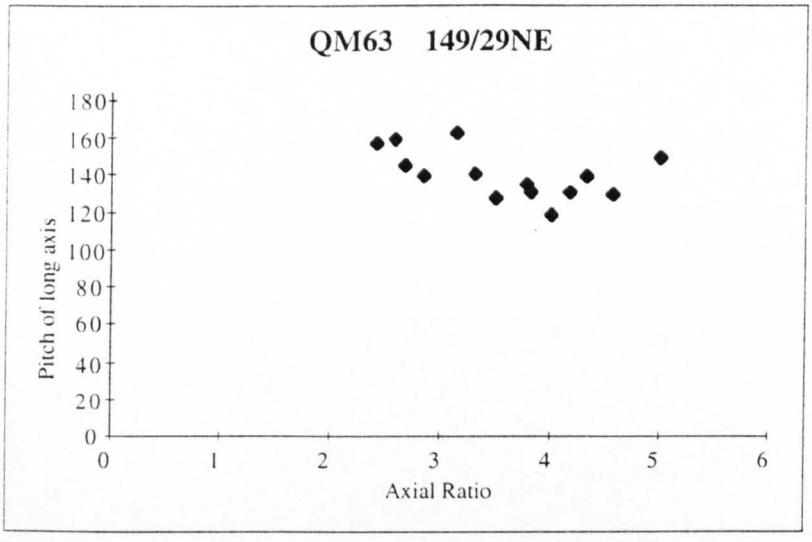

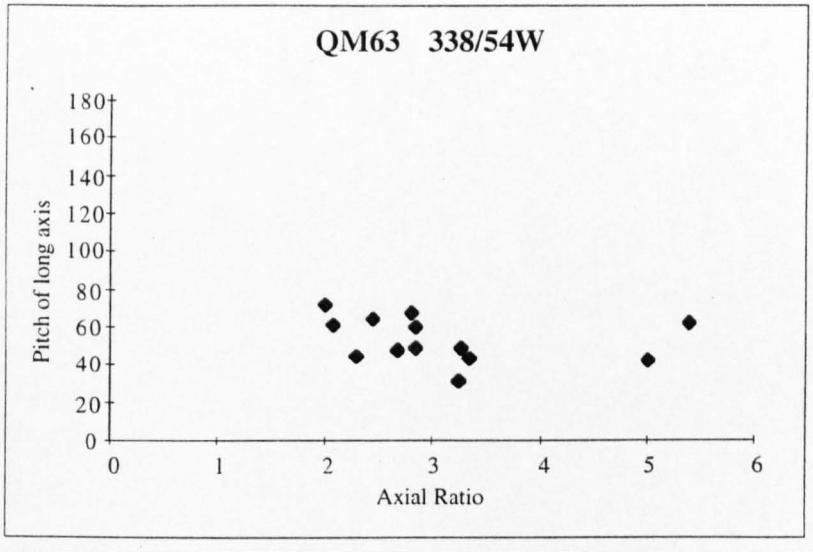

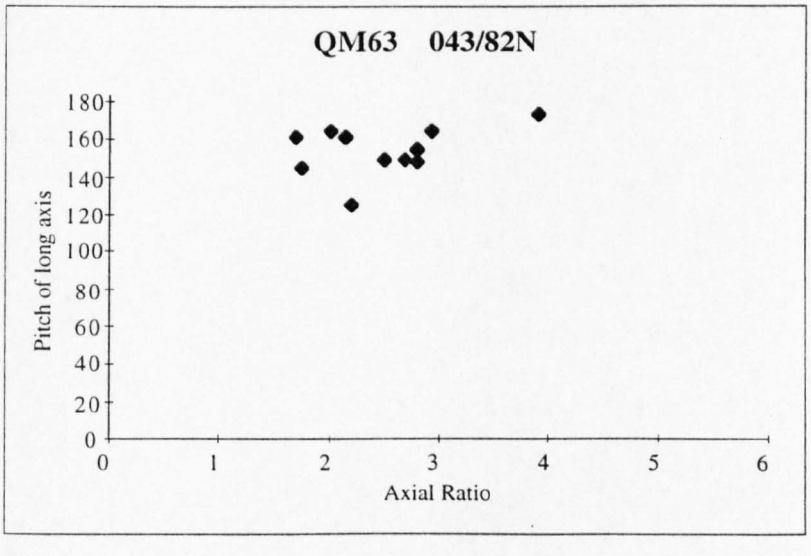

Figure 5.2.3 The pitch and axial ratios of ellipses measured on approximately orthogonal sections on sample QM63.

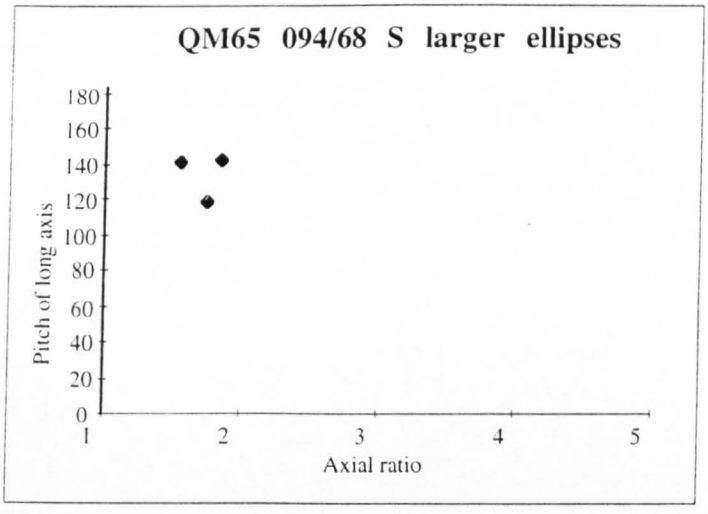

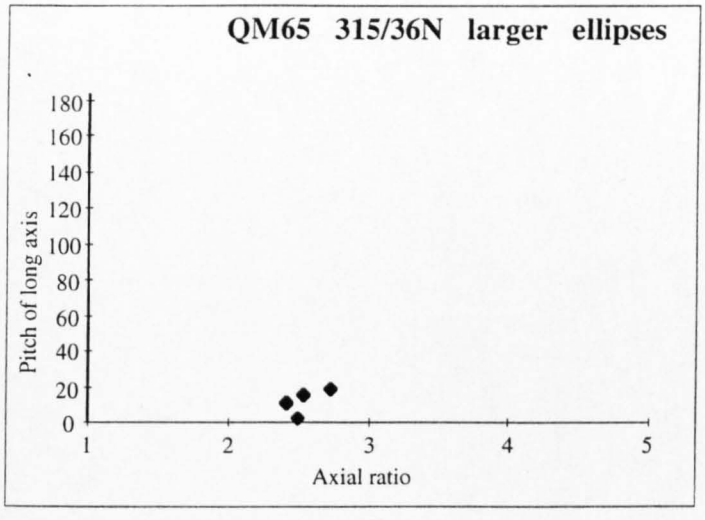

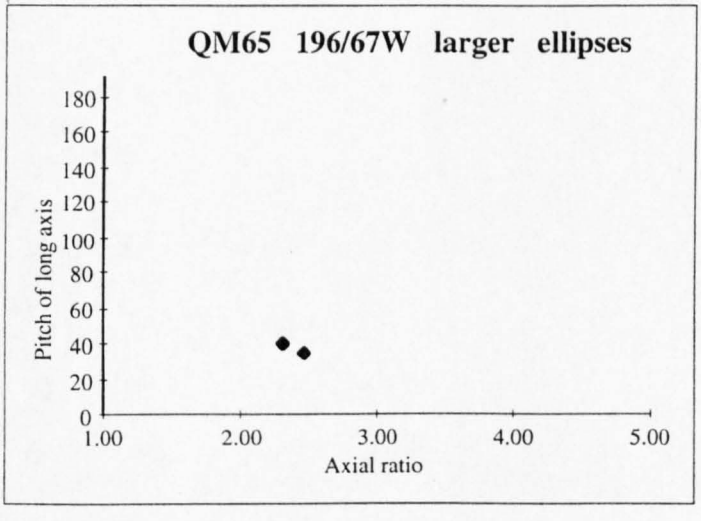

Figure 5.2.2 (b) The pitch and axial ratios of ellipses defined by fractures of at least 1 mm width, measured on approximately orthogonal surfaces on sample QM65.

mean). The undeformed ellipse is also dependent upon the suitability of the orientations of sections used in calculations. As the number of sections increases, so ρ decreases.

QM63

Across the fault zone within QM63 the clasts have a common orientation. The data collected on each section is shown in Table 5.2.1(a) and Figure 5.2.3. Before application of this program, it is necessary to determine a representative ellipse from each section. Although there is variation in the number of readings from different sections, determining representative ellipses gives each section an equal weighting. As the ellipse orientation and aspect ratio are independent, to average the data for each section, the harmonic mean and vector mean are calculated according to the equation of Lisle (1986, p14), Table 5.2.1(b).

Vector mean = $\theta = 0.5 \arctan (\Sigma \sin 2\theta / \Sigma \cos 2\theta)$

Harmonic mean = $N / (R_{f1}^{-1} + R_{f2}^{-1} + R_{f3}^{-1} + ... R_{fN}^{-1})$

The data is now ready to be input to the first program, Tryel.

QM65

Sample QM65 has a complex fabric defined by the clasts. Three sub-zones within the fault zone can be recognised, based upon fault rock : intact clasts, Figure 5.2.2(b). Sub zone 1 is taken immediately beside the bounding fault which is the contact between the yellow and purple rhyolites. The fault rock constitutes 21% of the area of sections through sub-zone. In sub zone 2, the fault rock constitutes 40% of the area of sections through the sub zone and in zone 3 the fault rock constitutes at least 50% of the area of sections through the sub zone. Fractures at a low angle to the bounding faults mark the boundaries of the three zones. The third zone has no discernible fabric defined by the clasts of rock. The clasts are well rounded, not in contact and have been abraded too much to have a simple shape significance. Within the other two sub-zones, there are two scales of ellipses recognisable on each section. The larger scale ellipses have a common orientation across both sub-zones and are limited by fractures>1mm thick. The smaller ellipses are defined by any fractures, hence a thinner set of fractures at a high angle to the bounding faults have an effect on the orientation of the ellipses. The common long axis of the ellipses is effectively rotated by the recognition of this fracture system. The modal long axis orientation of these smaller ellipses is not the same in sub zones 1 and 2. Data collected across subzones 1 and 2, of the larger ellipses are given in Table 5.2.2(a), with the data from each sub-zone in (b) and (c). Plots of axial ratio against the pitch of the long axis are shown in Figure 5.2.3 (b) - (d). The

data were then averaged to determine the representative ellipse from each section. The sample size and scale of ellipses combined with division into sub-zones has reduced the number of readings as compared with QM63. The clarity of the clast fabric is comparable in both samples and variations over the scale of the sample are minimal (once the scale of the ellipses have been defined), so QM63 is not considered a better analysis.

As with any analysis of relative orientation, the surfaces are assumed not to have been re-oriented with respect to each other since cessation of fault activity. This assumption appears valid, given the consistent kinematic interpretation of slip surfaces in chapter 4.

5.3 Results

QM63

Quality Control

The Tryel solutions for QM63 are shown in Table 5.3.1. The solutions have a similar orientation. Table 5.3.2 shows the detailed Tryel results for solution q33 from Table 5.3.1. Comparison of the calculated aspect ratios and pitches with the input data shows a distribution scattered about the input values. This, combined with the low value of the log mean undeformed ellipses, indicates an internally consistent data set.

The results from Bfel are shown in Table 5.3.3. There are six successful solutions (out of a possible six). It is only necessary for Bfel to perform the refining process four times on each solution until it cannot be improved. The almost identical result of each fourth analysis attests to the quality of the data. The final five lines of each solution can be used as an estimate of the internal consistency of the data, as discussed in the Methodology section (5.2). A comparison of input and calculated pitch and axial ratio shows the calculated values to approximate the input values, with a scatter about the input values. Each result has a low log mean undeformed ellipse of 1.17, again indicating a high level of internal consistency. The log mean undeformed ellipse generated by Bfel is lower than that from Tryel. This indicates the resulting ellipsoid from Bfel is more representative of the input data. The orientation and dimensions of the ellipsoid have been improved. The internal consistency of the results is taken as validation of the assumption that the ellipses on sections through the sample are ellipsoidal in three dimensions.

Results

Table 5.2.2(a) Measurements of long axis orientation and aspect ratio of ellipses taken from orthogonal sections of QM65. Ellipses are defined by fractures a minimum of 1mm thick. Caption as for Table 5.2.1 (a).

Section orientation		094/68S	
	Theta	Aspect Ratio	
	141	1.55	
	142	1.85	
	118	1.75	
harmonic mean	136.13	1.70	vector mean
	surface 2	315/36N	
	2	2.5	
	15	2.54	
	11	2.42	
	18	2.73	
harmonic mean	11.53	2.54	vector mean
	surface 8	196/67W	
	40	2.32	
	35	2.46	
harmonic mean	37.50	2.39	vector mean

Table 5.2.2(b) Measurements of ellipses on sections of QM65 taken from the smaller fault zone immediately beside the yellow-purple rhyolite contact (zone 1).

Section orientation		094/68	
	Aspect Ratio	Theta	
	2.25	8	
	3.6	7	
	2.33	23	
	4.25	5	
	4	0	
Harmonic mean	3.05	8.50	vector mean
Section orientation		315/36	
	2.4	162	
	3	148	
	4.67	168	
	4	144	
	2.33	172	
	3	150	
	2.5	162	
	2	176	
	3.33	167	
Harmonic mean	3.15	161.08	vector mean
Section orientation		196/67	
	2.15	6	
	2.69	30	
	2.4	3	
	2.5	36	
Harmonic mean	2.42	18.72	vector mean

Table 5.2.2(c) Measurements of ellipses on sections of QM65 taken from the smaller fault zone (zone 2).

Section orientation		094/68	
	Aspect ratio	Theta	
	2.12	0	
	2.67	35	
	1.38	24	
	2	7	
harmonic mean	2.41	16.42	vector mean
Section orientation		315/36	
	4	1	
	2	0	
	2	145	
	2.67	1	
	2.33	0	
harmonic mean	2.43	174.33	vector mean
Section orientation		194/72	
	4.25	1	
	1.83	24	
	4	17	
	4	31	
harmonic mean	3.12	18.40	vector mean

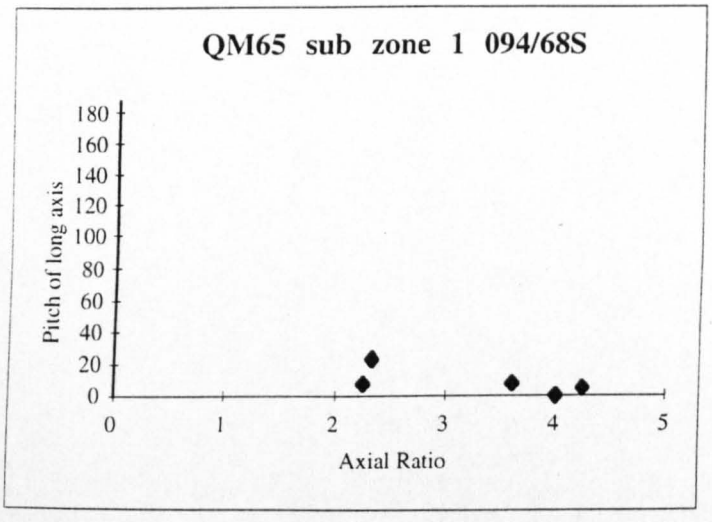

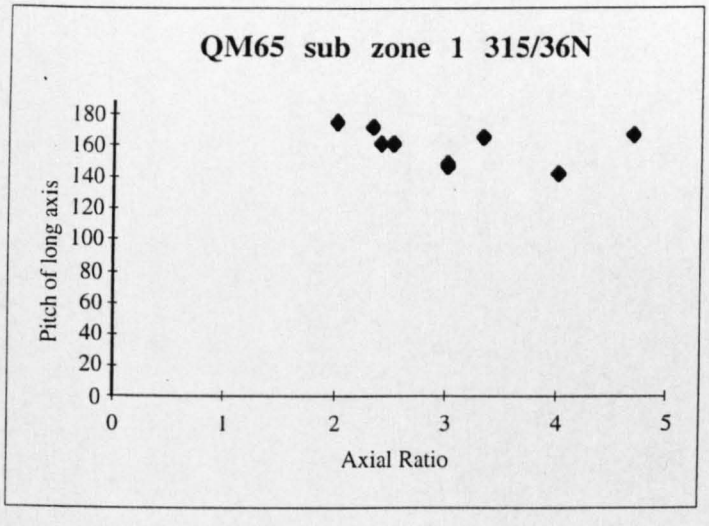

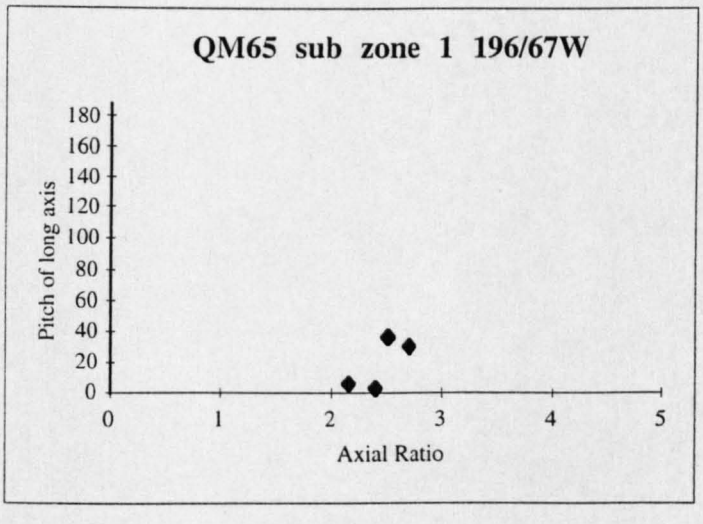

Figure 5.2.3 (c) The pitch and axial ratios of ellipses measured on approximately orthogonal surfaces in sub-zone 1 of sample QM65.

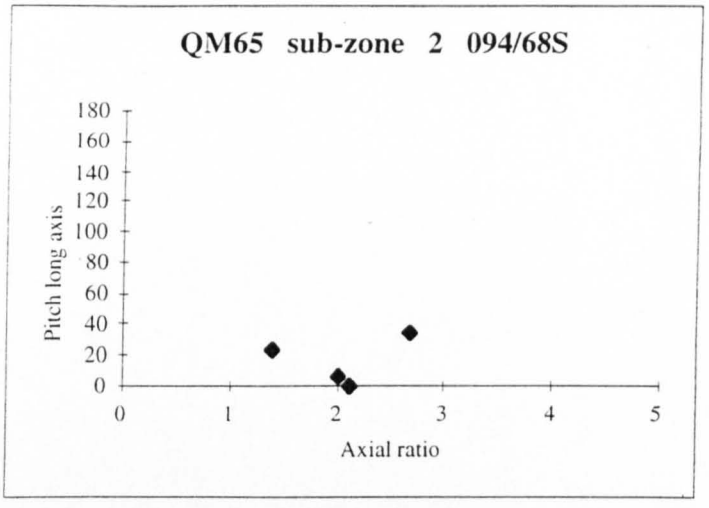

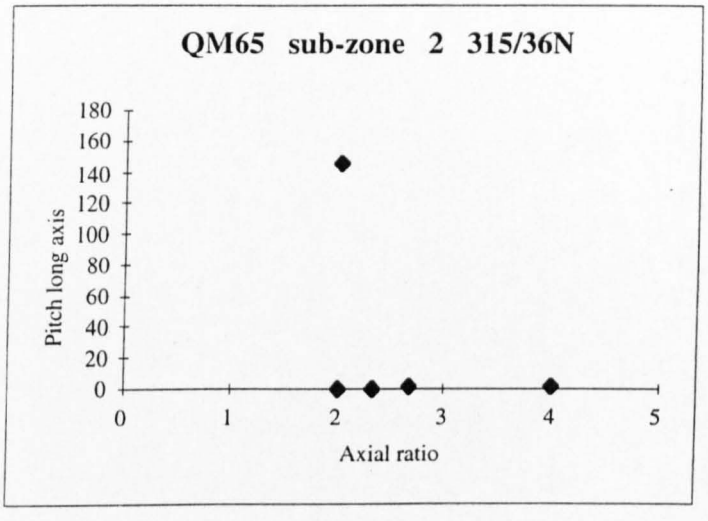

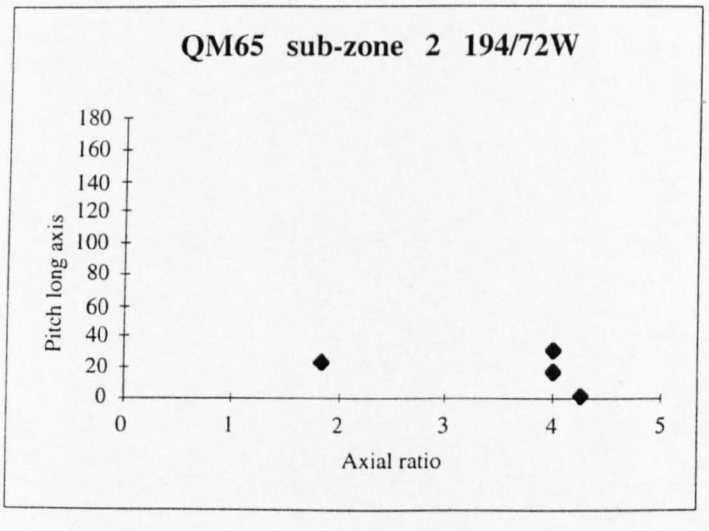

Figure 5.2.3 (d) The pitch and axial ratios of ellipses measured on approximately orthogonal surfaces in sub-zone 2 of sample QM65.

	Maximum Axis			Intermediate Axis			Minimum Axis		
basis	norm'd length	az.	plunge	norm'd length	az.	plunge	norm'd length	az.	plunge
q33	1.429	313.6	42.1	1.000	34.5	-9.9	0.298	294.0	-46.2
q11	1.515	307.6	43.2	1.000	31.5	-6.5	0.311	294.7	-46.0
q12	1.406	316.0	42.4	1.000	35.7	-11.1	0.292	294.2	-45.5
q13	1.563	317.1	41.9	1.000	36.6	-11.5	0.303	294.5	-45.8
q22	1.475	320.7	41.4	1.000	38.0	-14.0	0.301	293.5	-45.3
q23	1.483	314.6	42.3	1.000	34.8	-10.5	0.98	293.8	-45.8

Table 5.3.1 Six Tryel solutions for sample QM63. The normalised axis length is given in the first column followed by its azimuth and plunge. The axis length is proportional to the relative magnitude of the axis.

Q33=1 SOLUTION

			Input				Calculated		Undef
Weight	A	B	Strike	Dip	Pitch	A/B	Pitch	A/B	Ellip
1.00	2.40	1.00	223.0	82.0	25.0	2.40	21.1	2.33	1.14
1.00	2.80	1.00	158.0	54.0	127.0	2.80	122.7	2.93	1.21
1.00	3.40	1.00	329.0	29.0	40.0	3.40	38.3	3.43	1.10

LOGMEAN UNDEFORMED ELLIPSES = 1.15

Table 5.3.2 The detailed Tryel results for solution q33 above. For each Tryel solution the above data is available. Comparison of the calculated pitch and aspect ratio (A/B) show the ellipsoid fit is not exact, however the errors are not significant and are equally distributed between the sections. The low value of the log mean undeformed ellipse indicates a consistent data set.

The resulting ellipsoid is oblate, Figure 5.3.1. The orientation of the ellipsoid is shown in Figure 5.3.2. Comparison with Figure 5.1.2 shows the intermediate ellipsoid axis to plot near the intersection of fractures. The results from sample QM63 are plotted against the information known for the fault system in Figure 5.3.3, Ch 4.3. There is close coincidence of the maximum axis with the striae along system A faults and the intermediate ellipsoid axis with the intermediate strain axis. The maximum and intermediate axes lie in the plane defined by the striae and intermediate strain axis of system A. The maximum and minimum axes lie in the profile plane of the fault. The clasts are aligned to the strain regime of system A, not the bounding faults.

QM65

Quality Control

Table 5.3.4 shows the Bfel results for QM65 (and QM63). The log mean undeformed ellipses are seen to be low for both the QM65 larger scale ellipsoid and the ellipsoid calculated for sub-zone 1. The Tryel results for the larger ellipses measured and the smaller ellipses measured in sub-zone 1, both produce 6 successful solutions, which have similar orientations within each data set. The six solutions for each data set converge in Bfel towards an identical ellipsoid. The recalculated aspect ratio and pitch on the section surfaces for the calculated ellipsoid oscillate about the input values. The Tryel results for sub-zone 2 only produce one successful solution, which is unsuccessful in generating a refined solution in Bfel. The log mean undeformed ellipse for the Tryel solution is 1.31, significantly higher than those produced for sub-zone 1 and the larger ellipses. Sub-zone 2 is seen to have poorer internal consistency. This can be correlated with the increase in fault rock in sub-zone 2.

Results

Figure 5.3.1 shows the shape of each ellipsoid and Figure 5.3.2 shows the orientation of each ellipsoid on a stereonet. Comparison of QM65, the data for the larger ellipsoids measured across the whole fault zone, with the fracture distribution (Figure 5.1.2(b) and (c)) shows the maximum axis of the ellipsoid to be 2° different to the intersection of fractures. The ellipsoid axes are plotted against the kinematic data for system Ain Ch 4.3, in Figure 5.3.4. The maximum ellipsoid axis lies on the edge of the contoured region this corresponds to the intermediate strain axis. The intermediate strain axis lies within the contoured region denoting the striae distribution. The minimum ellipsoid axis does not have any apparent

Table 5.3.3 Bfel results for QM63. The writing in bold separates the different solutions. Dec and dip refer to azimuth and plunge of the ellipsoid axes.

q33

Length	Norm'd	DEC	DIP
0.298	-0.926	294.0	-46.2
1.000	0.285	34.6	-10.0
1.428	0.641	313.7	42.0
Length	Norm'd	DEC	DIP
0.338	-0.832	296.4	-48.5
1.000	0.252	31.9	-4.9
1.388	0.580	306.2	41.1
Length	Norm'd	DEC	DIP
0.340	-0.821	295.8	-48.7
1.000	0.259	30.7	-4.2
1.355	0.562	304.4	41.0
Length	Norm'd	DEC	DIP
0.340	-0.821	295.7	-48.6
1.000	0.258	30.8	-4.4
1.357	0.563	304.6	41.0

						Input		Calculated		Undef
Weight	A	B	Strike	Dip	Pitch	A/B	Pitch	A/B	Ellipse	
1.00	2.20	1.00	223.0	82.0	24.0	2.20	18.4	2.14	1.18	
1.00	2.60	1.00	158.0	54.0	129.0	2.60	125.8	2.62	1.13	
1.00	2.80	1.00	329.0	29.0	42.0	2.80	38.1	2.83	1.18	

WEIGHTED LOGMEAN UNDEFORMED ELLIPSES = 1.17

q11

Length	Norm'd	DEC	DIP
0.311	-0.916	294.7	-46.0
1.000	0.250	31.4	-6.4
1.516	0.666	307.5	43.2
Length	Norm'd	DEC	DIP
0.343	-0.830	296.4	-49.0
1.000	0.240	31.4	-4.4
1.420	0.590	305.2	40.7
Length	Norm'd	DEC	DIP
0.340	-0.821	295.8	-48.8
1.000	0.259	30.8	-4.4
1.354	0.562	304.6	40.9
Length	Norm'd	DEC	DIP
0.340	-0.821	295.7	-48.6
1.000	0.258	30.8	-4.4
1.356	0.563	304.6	41.1

						Input		Calculated		Undef
Weight	A	B	Strike	Dip	Pitch	A/B	Pitch	A/B	Ellipse	
1.00	2.20	1.00	223.0	82.0	24.0	2.20	18.4	2.14	1.18	
1.00	2.60	1.00	158.0	54.0	129.0	2.60	125.8	2.62	1.13	
1.00	2.80	1.00	329.0	29.0	42.0	2.80	38.1	2.83	1.18	

WEIGHTED LOGMEAN UNDEFORMED ELLIPSES = 1.17

q12

Length	Norm'd	DEC	DIP
0.292	-0.934	294.2	-45.5
1.000	0.297	35.6	-11.0
1.406	0.637	315.8	42.4
Length	Norm'd	DEC	DIP
0.339	-0.834	296.5	-48.5
1.000	0.249	31.6	-4.5
1.399	0.585	305.6	41.1
Length	Norm'd	DEC	DIP
0.340	-0.821	295.8	-48.8
1.000	0.258	30.7	-4.2
1.356	0.563	304.3	40.9
Length	Norm'd	DEC	DIP
0.340	-0.821	295.7	-48.6
1.000	0.258	30.7	-4.4
1.357	0.563	304.6	41.0

						Input		Calculated		Undef
Weight	A	B	Strike	Dip	Pitch	A/B	Pitch	A/B	Ellipse	
1.00	2.20	1.00	223.0	82.0	24.0	2.20	18.4	2.15	1.18	
1.00	2.60	1.00	158.0	54.0	129.0	2.60	125.8	2.62	1.13	
1.00	2.80	1.00	329.0	29.0	42.0	2.80	38.1	2.83	1.18	

WEIGHTED LOGMEAN UNDEFORMED ELLIPSES = 1.17

q13

Length	Norm'd	DEC	DIP
0.302	-0.946	294.5	-45.8
1.000	0.250	36.5	-11.5
1.563	0.697	317.0	41.9
Length	Norm'd	DEC	DIP
0.340	-0.833	296.8	-48.8
1.000	0.246	32.5	-5.0
1.406	0.587	306.9	40.8
Length	Norm'd	DEC	DIP
0.339	-0.821	295.9	-48.8
1.000	0.260	30.6	-4.1
1.352	0.561	304.1	40.9
Length	Norm'd	DEC	DIP
0.340	-0.821	295.7	-48.6
1.000	0.258	30.7	-4.4
1.357	0.563	304.5	41.0

						Input		Calculated		Undef
Weight	A	B	Strike	Dip	Pitch	A/B	Pitch	A/B	Ellipse	
1.00	2.20	1.00	223.0	82.0	24.0	2.20	18.4	2.15	1.18	
1.00	2.60	1.00	158.0	54.0	129.0	2.60	125.8	2.62	1.13	
1.00	2.80	1.00	329.0	29.0	42.0	2.80	38.1	2.83	1.18	

WEIGHTED LOGMEAN UNDEFORMED ELLIPSES = 1.17

q22

Length	Norm'd	DEC	DIP
0.301	-0.928	293.5	-45.3
1.000	0.273	38.0	-14.0
1.467	0.656	320.7	41.4
Length	Norm'd	DEC	DIP
0.338	-0.832	296.8	-48.4
1.000	0.252	32.4	-4.9
1.387	0.580	306.7	41.2
Length	Norm'd	DEC	DIP
0.340	-0.821	295.9	-48.8
1.000	0.259	30.5	-4.0
1.354	0.562	304.0	40.9
Length	Norm'd	DEC	DIP
0.340	-0.821	295.7	-48.6
1.000	0.258	30.7	-4.4
1.357	0.563	304.6	41.0

				Input			Calculated		Undef
Weight	A	B	Strike	Dip	Pitch	A/B	Pitch	A/B	Ellipse
1.00	2.20	1.00	223.0	82.0	24.0	2.20	18.4	2.15	1.18
1.00	2.60	1.00	158.0	54.0	129.0	2.60	125.8	2.62	1.13
1.00	2.80	1.00	329.0	29.0	42.0	2.80	38.1	2.83	1.18

WEIGHTED LOGMEAN UNDEFORMED ELLIPSES = 1.17

q23

Length	Norm'd	DEC	DIP
0.298	-0.939	293.8	-45.8
1.000	0.271	34.9	-10.6
1.487	0.668	314.7	42.3
Length	Norm'd	DEC	DIP
0.339	-0.834	296.6	-48.6
1.000	0.248	32.1	-4.8
1.401	0.585	306.3	41.0
Length	Norm'd	DEC	DIP
0.340	-0.821	295.9	-48.8
1.000	0.259	30.6	-4.1
1.354	0.562	304.2	40.9
Length	Norm'd	DEC	DIP
0.340	-0.821	295.7	-48.6
1.000	0.258	30.7	-4.4
1.356	0.563	304.5	41.0

				Input			Calculated		Undef
Weight	A	B	Strike	Dip	Pitch	A/B	Pitch	A/B	Ellipse
1.00	2.20	1.00	223.0	82.0	24.0	2.20	18.4	2.15	1.18
1.00	2.60	1.00	158.0	54.0	129.0	2.60	125.8	2.62	1.13
1.00	2.80	1.00	329.0	29.0	42.0	2.80	38.1	2.83	1.18

WEIGHTED LOGMEAN UNDEFORMED ELLIPSES = 1.17

Sample	Maximum Axis			Intermediate Axis			Minimum Axis			mean
	norm'd length	az.	plunge	norm'd length	az.	plunge	norm'd length	az.	plunge	undef ell
QM63	1.357	305	41	1.000	31	-4	0.340	296	-49	1.17
QM65	1.785	358	-23	1.000	283	31	0.465	238	-50	1.09
QM65 s.zon1	1.643	285	-07	1.000	17	-17	0.463	173	-72	1.07
QM65 s.zon2*	2.295	329	-18	1.000	241	08	0.482	174	-70	1.31

Table 5.3.4 Results of Bfel on samples QM65 and QM63. * indicates result taken from Tryel, as Bfel could not generate a solution. The orientation of the ellipsoid axes are given as azimuth and plunge.

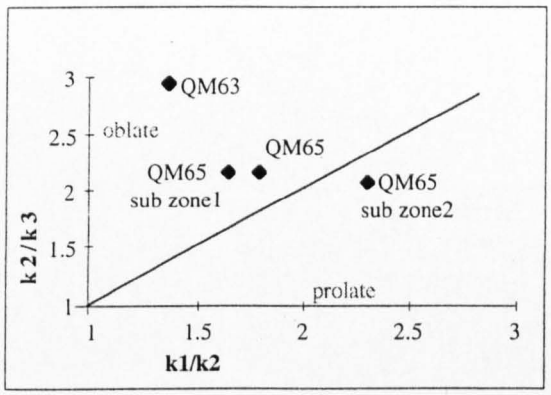

Figure 5.3.1 Flinn plot showing the shapes of the ellipsoidal clasts of rock in the localised fault zone.

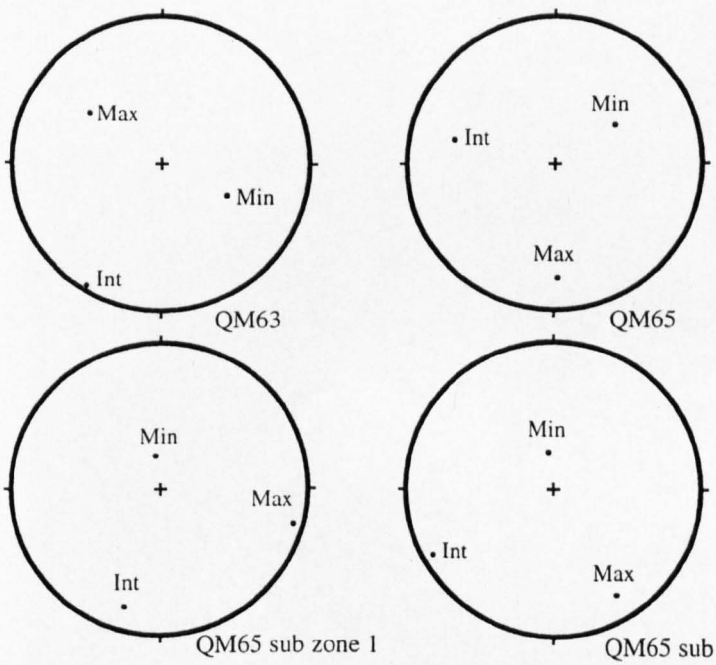

Figure 5.3.2 Representation of the ellispoid orientations on a stereonet.

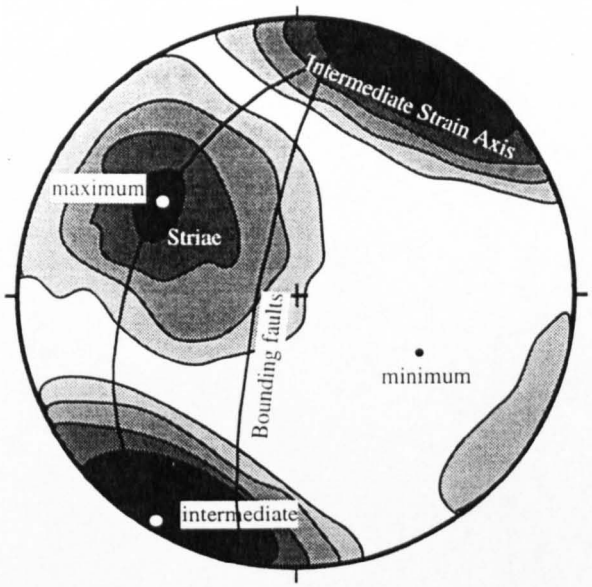

Figure 5.3.3 Ellipsoid axes determined for QM63. The contoured intermediate axes and striae for type A slip surfaces are shown also. The plane containing the maximum and intermediate axes is shown in black .

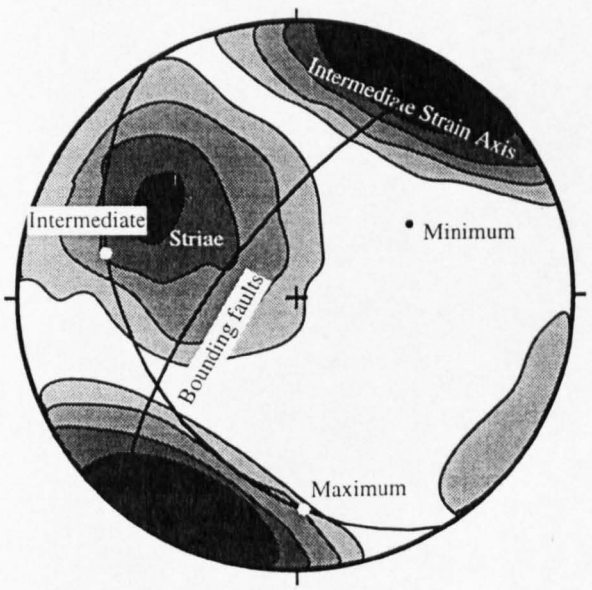

Figure 5.3.4(a) Ellipsoid axes determined for QM65, with ellipses defined byfractures>1mm. The contoured intermediate axes and striae for type A slip surfaces are shown. The plane containing the maximum and intermediate axes is shown in black. The intermediate and maximum axes are shown in white, the minimum axis in black.

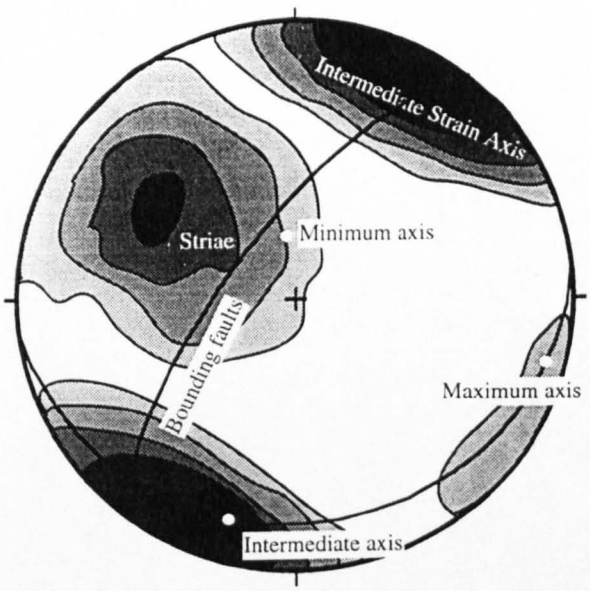

Figure 5.3.5(a) Ellipsoid axes determined for QM65, within the first smaller fault zone. The contoured intermediate axes and striae for type A slip surfaces are shown. The plane containing the maximum and intermediate axes is shown in black. All ellipsoid axes are shown in white.

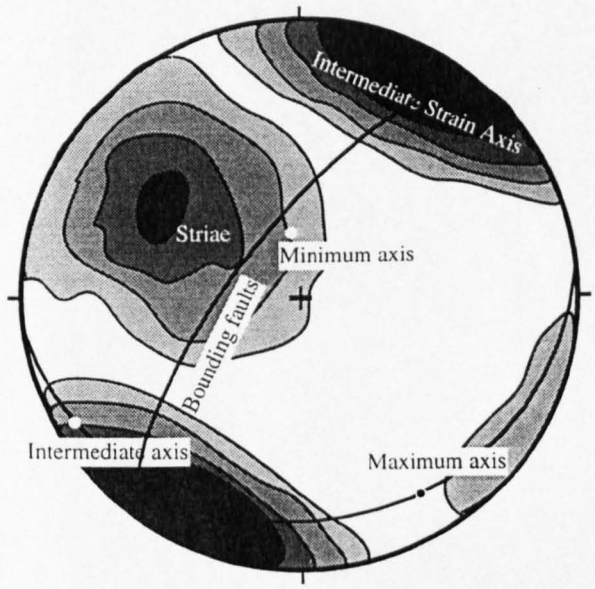

Figure 5.3.5(b) Ellipsoid axes determined for QM65, within the second smaller fault zone. The contoured intermediate axes and striae for type A slip surfaces are shown. The plane containing the maximum and intermediate axes is shown in black.

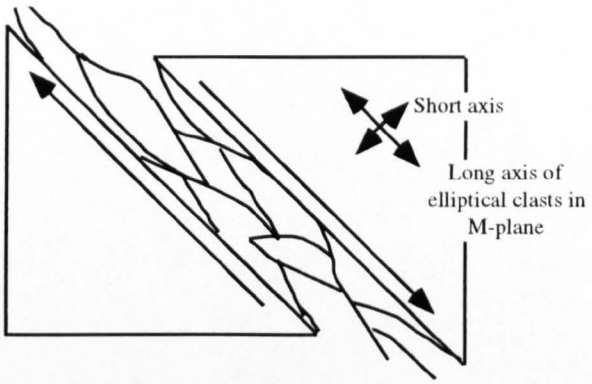

Figure 5.4.1 The profile plane of a fault zone with R, Y and P fractures developed. The fractures define intact clasts of rock with the short axes perpendicular to the bounding fault plane. The intermediate axes are parallel to the slip direction.

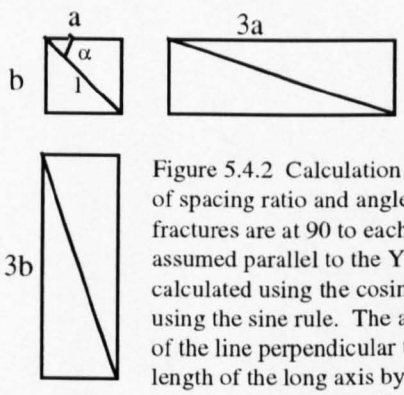

Figure 5.4.2 Calculation of long axis orientation and aspect ratio as functions of spacing ratio and angle between fractures. The spacing ratio = a/b : the fractures are at 90 to each other here. The orientation of the a fractures are assumed parallel to the Y fractures of the fault zone. The long axis length is calculated using the cosine rule and the angle of the long axis is calculated using the sine rule. The aspect ratio is calculated by determining the length of the line perpendicular to the mid point of the long axis and dividing the length of the long axis by this value. These calculations were carried out for fracture angles of 90, 75, 60, 45, 30 and 15. The aspect ratios ranged from 1:1 to 1:8 to 8:1. Comparison with Figure 5.2.1 shows this is the same technique as that used to measure ellipses.

relation to the kinematic data or data set A. The intermediate ellipsoid axis is almost within the plane defined by the striae and intermediate strain axis for system A.

Comparison of the ellipsoid axes for QM65 sub zone 1 with the fracture orientations in QM65 shows the intermediate axis plots near to the intersection of fractures. The ellipsoid axes calculated for sub zone 1 and the kinematic data for system Aare plotted together in Figure 5.3.5(a). The intermediate ellipsoid axis lies within the denser population of intermediate strain axes. The minimum axis lies within the contoured region of striae, but towards the edge. The maximum ellipsoid axis lies on the opposite side of the contoured region of striae. The intermediate and minimum ellipsoid axes lie in the plane of the bounding faults.

Comparison of the ellipsoid axes for QM65 sub zone 2, Figure 5.3.2, with the fracture orientations within QM65, Figure 5.1.2, shows the intersection direction of fractures to lie within the plane defined by the intermediate and maximum ellipsoid axes. The ellipsoid axes are plotted against the kinematic data for system Ain figure 5.3.5(b). The intermediate ellipsoid axis lies on the outskirts of the densely populated region of intermediate strain axes; and the minimum ellipsoid axis lies towards the edge of the region of contoured striae orientations. The minimum axis lies in the plane of the bounding faults.

Comparison of ellipsoid axes

None of the ellipsoids generated are parallel. The maximum axis of QM63 and the intermediate axis of QM65 are sub parallel, the other two axes are not. The intermediate axis of QM63 lies between the intermediate axes of QM65 sub zones 1 and 2. The minimum axes of QM65 sub zones 1 and 2 are parallel.

5.4 Significance of the clast shapes

Reidel's model of fractures generated during plane strain, simple shear predicts that all fracture intersections will have a parallel intersection lineation Figure 5.1.2(a). Theoretically this should produce clasts of rock that are infinitely long in the direction of the fracture intersection. Clasts of rock defined by the fractures will have their longest axis parallel to the intersection lineation of the fractures and parallel to the intermediate strain direction. The orientation of the intermediate and minimum ellipsoid axes are a function of

the fracture distribution in the M-plane. For example, a fault zone with many R, Y and P fractures, as shown in Figure 5.4.1, will produce an ellipse in the profile plane (M-plane) with the long axis parallel to the slip direction and the short axis perpendicular to the bounding fault. As the number of fractures which are asymmetric about the slip direction increases, the obliquity of ellipses in the profile plane increases.

In three dimensions within the fault plane, fractures have a curvi-planar geometry. This causes the clasts of intact rock defined by the fractures to terminate, Figure 5.1.3. The overlap of fractures is one of the parameters which causes modification of the fracture orientations. As the number of overlapping fractures increases, so the fractures increasingly deviate from planarity. In a fault zone with many R, Y and P type fractures, the interaction of fractures may cause the ellipsoid axis parallel to the ideal intersection of fractures and the ellipsoid axis parallel to the slip direction to swap magnitudes. Hence the maximum ellipsoid axis will parallel the slip direction, the intermediate will parallel the average intersection direction of fractures and the minimum axis will be the pole to the fault plane.

In a fault system with a significant amount of high angle fractures, for example R' and X fractures, the significance of the ellipsoid axes is more complex. The orientation of the long axis and the aspect ratio of the ellipse in the profile plane is dependent upon the distance between fractures and the angle between fractures. If the fractures defining the ellipses can be simplified to be represented by two fracture systems, the aspect ratio and orientation of the long axis of the ellipse can be used to determine the angle between fracture systems and the spacing ratio (ratio of lengths of fractures). It is theoretically possible to measure the orientation of the long axis of the ellipse and aspect ratio directly from the sample once the profile plane has been observed. Alternatively, an assumption can be made about the orientation of one set of fractures bounding the clasts of rock. The symmetric distribution of fractures about the intermediate strain axis and slip direction allows a simplification that enables the long axis and aspect ratio to be predicted for a suite of fracture sets. Any ellipse in the profile plane can be defined as a parallelepiped with the side orientations representing the average fracture sets defining the ellipse. One set of fractures can be assumed to parallel the slip direction. This is parallel to the long axis of ellipses in the profile plane that are formed by R, Y and P fractures. The assumption is based upon the close association of R, Y and P fractures in the temporal history of a fault zone and their presence in most studied brittle fault zones. A graph of long axis orientation and aspect ratio can be generated for different spacing ratios and angles between fracture systems, Figure 5.4.2. The long axis of

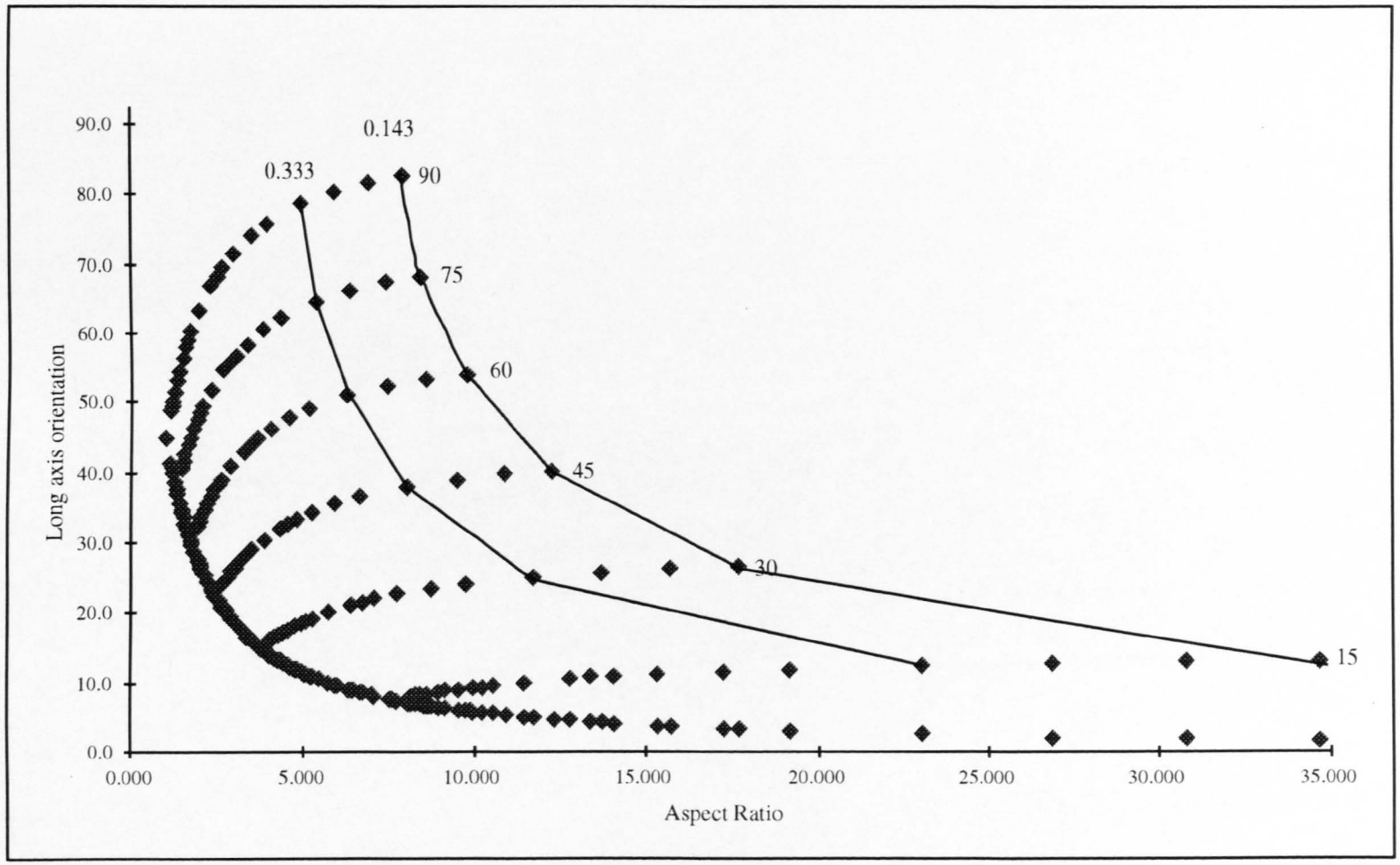

Figure 5..4.3 Long axis and aspect ratio of parallelipiped calculated for variations in spacing ratio and angles between fractures. The number at the end of the lines is the angle between fracture systems. Lines of constant spacing ratio are drawn for spacing ratios of 0.143 and 0.333. For spacing ratios >1 the lowest line shows the variation in aspect ratio and long axis orientation. The spacing ratios of fracture systems >1 cannot be distinguished. The long axes are measured relative to the Y fracture orientation.

the parallelepiped is measured with respect to the "top" fracture system, which in this case is the Y fracture system. Plotting the angle between the fault plane and the long axis of the ellipse and the aspect ratio in the profile plane, on this graph yields a position in terms of spacing ratio and angle between the fracture systems, Figure 5.4.3. It is equally simple to use geometrical relationships to calculate the specific spacing ratio and angle between fracture systems, as explained in figure 5.4.2.

Once the angle between the two simplified fracture sets is known, the "type" of fractures can be identified by comparison with the predicted fracture angles of Reidel, Figure 5.1.3(a). Identification of the slip direction and the pole to the fault plane can now be made. This analysis can be taken further by application of the observation that R' fractures tend to occur far more frequently than X fractures). Histograms of fractures (for example, Bartlett, 1981, Fig 15) show R' fractures to have a higher population than X fractures. Application of the assumption that a high angle fracture is an R' fracture, can lead to identification of the sense of movement along the system.

The effects of the high angle fractures on the three dimensional geometry of the fractures is uncertain. It is inferred that the fractures will intersect in the intermediate strain direction. A large number of high angle fractures will greatly reduce the length of the maximum ellipse axis in the profile plane. Comparison with the axis paralleling the intermediate strain axis, may find the axis paralleling the intermediate strain to be the maximum axis of the ellipsoid, with the intermediate and minimum axes within the profile plane.

5.5 Comparison of results with model

QM63

The coincidence of the maximum ellipsoid axis and the direction of slip along the fault plane (as defined by the contoured striae) and the intermediate ellipsoid and strain axes indicates a fault zone with a dominance of R, Y and P fractures. The number of fractures has caused increased clast termination in the direction of the fracture intersections (and intermediate strain axis).

QM65

The ellipsoid axes determined for the larger ellipses in sample QM65 do not have the same startling correlation with the kinematic data for system A, Figure 5.3.4. The intermediate axis is sub parallel to the direction of slip, while the maximum ellipsoid axis is at a low angle to the intermediate strain axis. The ellipsoid axes have been rotated anticlockwise about an axis oriented 49/261 as compared with QM63 (ignoring the relative swapping of maximum and intermediate axes). The fractures with a thickness >1mm which defined the larger elliptical clasts were all at low angles to the bounding faults. This discrepancy is attributed to the high angle fractures that define the smaller ellipses. Although they have not been recognised in definition of these larger ellipses, the rotations they have caused of the larger ellipses will affect the ellipsoid orientations. The orientation of the rotation axis does not coincide with the intermediate strain axis determined for system A. All fractures associated with this system Are anticipated to have the same rotation axis. Clearly this is not the case with these late stage high angle fractures. This may affect the ellipsoid axes, as a new fracture intersection orientation may occur. It is not suitable here to use the geometrical relationship to determine the angle between fracture systems (Figure 5.4.3) as the long axes are measured relative to the striae on the system, that is the Y fracture orientation in the profile plane. In this instance, the ellipsoid defining fractures are rotated from this orientation, so the orientation with which to measure the long axes with respect to is not known. It becomes necessary to consider the analysis of the smaller ellipses to define the angle between the fracture sets.

Sub zone 1

The ellipsoid axes determined for QM65 sub-zone 1, Figure 5.3.5(a) has its intermediate axis parallel to the intermediate strain axis. The maximum and minimum ellipsoid axes do not have any immediate significance with respect to the kinematic data from system A. The

minimum axis lies within the plane of the bounding faults. The orientation of the slip direction along the bounding faults has not been observed, however the projection of the striae associated with system A onto the orientation of the bounding fault, lies parallel to the minimum axis of the ellipsoid. The minimum axis is parallel to the striae and the maximum axis is approximately perpendicular to the bounding fault. This result indicates that the high angle, for example R', fractures are longer than those sub parallel to the bounding faults (R, T and P).

Alternatively, it may be more suitable to compare the orientation of the ellipsoids to the kinematic data determined for the whole system A. To make sense of the ellipsoid axes within this context, the long axis orientation and aspect ratio are used to calculate the angle between the fracture systems and spacing ratio, as shown on Figure 5.4.3. The long axis and aspect ratio are of the ellipse that occurs in the M-plane, in this case the ellipsoid maximum and minimum axes. As the long axis does not lie within the M-plane of system A, it is projected form the maximum ellipsoid axis. The long axis is measured relative to the striae orientation in the M -plane which is assumed to parallel the R-P-Y fractures (determined in Ch 4).

The angle between the striae and the intermediate axis is 52°.

The aspect ratio of the ellipse is modified to compensate for the projection of the two axes onto another plane. The aspect ratio in the M-plane is $(1.643/\cos\alpha)/(0.463/\cos\beta)$ where α is the angle between the maximum ellipsoid axis and the long axis projection on the M-plane, measured in the plane of the projection and β is the angle between the minimum ellipsoid axis and the projection on the M-plane.

$\alpha = 16°$, $\beta = 9°$, aspect ratio = 3.65

This yields an angle between the fracture systems of 67° and the spacing ratio of 0.429, Figure 5.5.1. Assuming that one set of fractures on the parallelepiped approximating the ellipse are parallel to the Y fractures, the second fractures are at an angle of 23° to the pole to the plane defined by the striae and intermediate strain axis of system A, Figure 5.5.2. This angular difference is compatible with the Reidel model of R' fractures. The orientation of the fractures within the M-plane is compatible with uplift to the east, Figure 5.5.2.

Sub zone 2

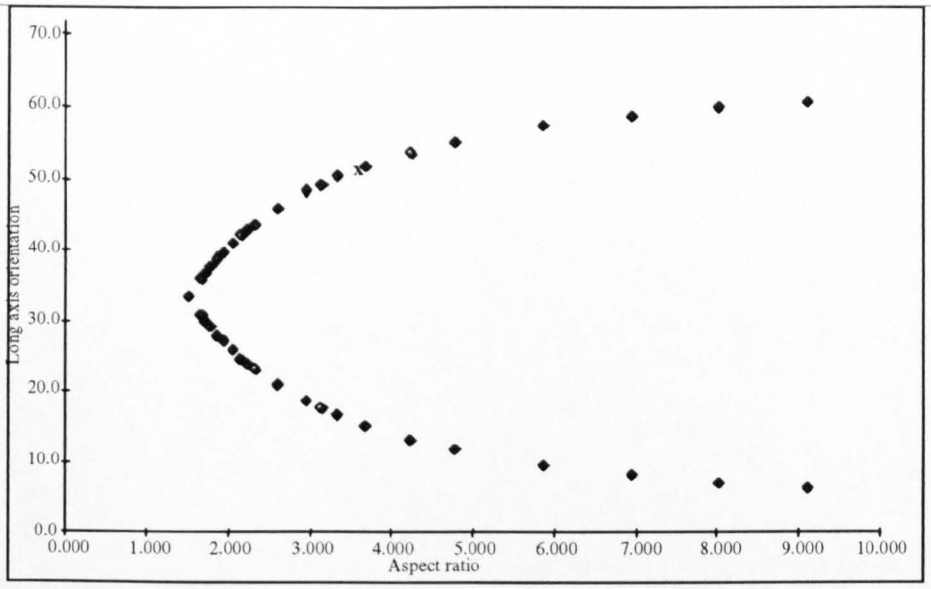

Figure 5.5.1 Long axis orientation and aspect ratio generated for parallelipiped defined by fractures at 67°. The angle between the fractures has been determined mathematically to be 67°. Spacing ratio increases from 0.125 at top right, to 8 at bottom right. A spacing ratio of 1 marks the inflection point. X marks the position of the M-plane ellipse for sample QM65, sub-zone 1.

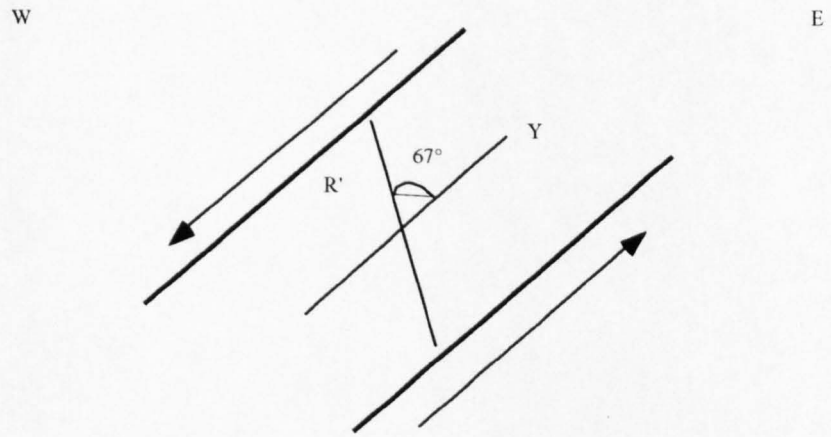

Figure 5.5.2 Schematic diagram of fracture sets in the M-plane that form the ellipses approximated by parallelipipeds in QM65 sub-zone 1. Bounding faults in thicker lines. See text for explanation.

The ellipsoid axes for sub zone 2 are shown in Figure 5.3.5(b). As with sub zone 1 , the results will be compared to both the orientation of the bounding slip surfaces and the system A kinematics. The minimum axis is parallel to the projection of striae from System A onto the bounding slip surface. The intermediate axis lies at a low angle to the bounding slip surfaces. Again, this is taken to indicate a dominance of R' fractures than R, Y and P fractures.

The projection of the maximum and minimum ellipsoid axes onto the profile plane of system A produces long axis orientation of 54° and an aspect ratio of 5.27. This gives an angle between the fracture systems of 65° and a spacing ratio of 0.234, Figure 5.5.3. The angle between the fracture systems is very close to that calculated for sub-zone 1. The reduction in spacing ratio may reflect generation of more high angle faults within this sub-zone. Again this is consistent with the interpretation of the secondary set of fractures (oblique to the Y fractures) as R' fractures. The sense determined from the orientation of fractures on the M-plane is also consistent with uplift to the east.

It would be possible to cut a sample of the fault zone parallel to the M-plane and, relating the spacing ratio and offset across each fracture system by geometrical formulae, calculate the net strain across the fractures defining the ellipses. This has not been carried out here as the samples were not large enough to warrant slicing in the M-plane and the majority of displacement is believed to have been taken up along the paired bounding faults.

Comparison of Ellipsoid axes and Fracture intersection points

The correspondence of the intermediate ellipsoid axis with the intersection direction of fractures in sample QM63 is good. The intersection direction of the fractures analysed in this way, Figure 5.1.2, must compensate for variations in the fracture geometries when a significant number of fractures are measured. The fractures measured for QM65 are probably biased against the thinner high angle fractures. The rapid change in orientation of the fractures resulted in difficulty measuring. Hence readings were accessible near intersections of sections, but not further away, and consequently did not reflect the number of these fractures present. Comparison of the orientation of the relevant larger ellipsoids axis from QM65 (in this case the maximum axis) with the intersection of fractures shows them to be approximately aligned. Without the rotation of these ellipsoids by the smaller, high angle fractures, the ellipsoid axis and intersection of fractures > 1mm thick, is expected to be coincident. The intermediate ellipsoid axis for QM65 sub zone 1 has a similar

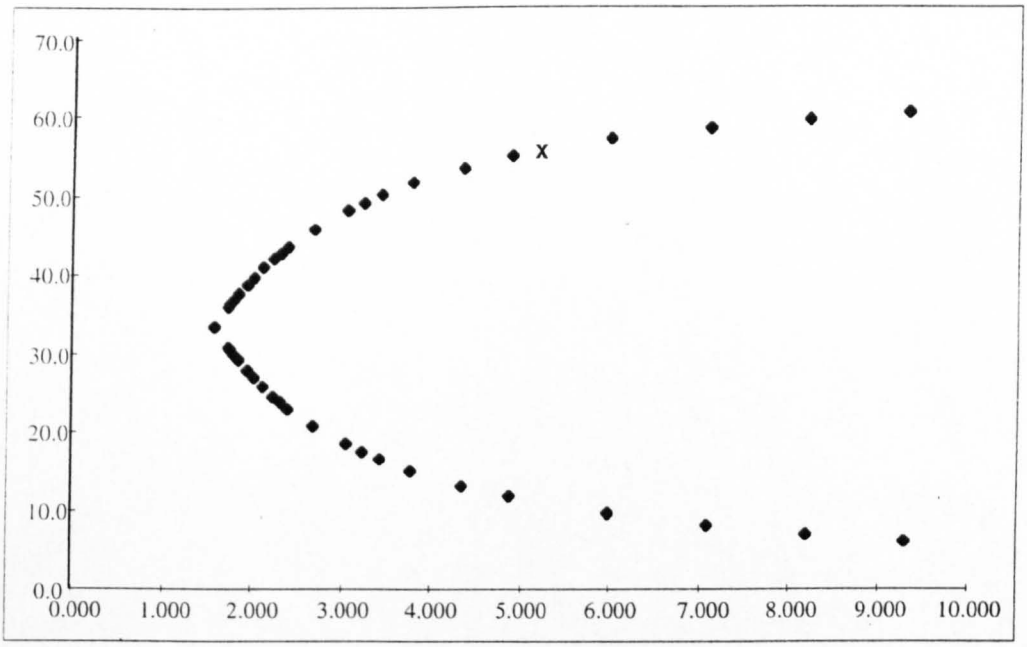

Figure 5.5.3 Long axis orientation and aspect ratio generated for parallelipiped defined by fractures at 65.° Spacing ratio increases form 0.125 at top right, to 8 at bottom right. A spacing ratio of 1 marks the inflection point. X marks the position of the M-plane ellipse for sample QM65, sub-zone 2.

orientation to the intersection of fractures, but again this discrepancy is expected, as the fracture readings only represent a fraction of the high angle fractures that are used to define the smaller ellipses.

Comparison of QM65 Ellipsoid Analysis with Fracture Distribution ofsystem A

The assumption that one set of fractures defining the parallelepiped parallels the Y fractures within the profile plane does not give any information as to exactly which fractures are present. The fracture set could be made up of R and P fractures only or R, P and Y fractures. Ellipsoid analysis has identified the angle between two sets of fractures defining the ellipsoids, to be ~66°. This is used to assign the two fracture sets which define the ellipses as R' and either R - P - Y or R - P fractures. The fracture distribution within the profile plane for system A (Figure 4.2.9(a)) shows the presence of R, Y, P and R' fractures. Depending which interpretation of fracture assignation is followed (in grey or black on Figure 4.2.9), the angle between the R' fractures and Y fractures is 60° and 80°, measured from this diagram. Either value is loosely compatible with the results from the ellipsoid analysis.

From the angular distance between the R and P fractures of slip system A an estimate of the angle of internal friction is 50° or 30 °, (Figure 4.2.9). From the angle between the fracture sets generating the ellipsoids in QM65 sub zones 1 and 2, the angle of internal friction is estimated at 46°. It is not known which estimate of the angle of internal friction from system A is correct. A genuine variation of the angle of internal friction between the rhyolite deforming as a series of discrete slip surfaces and deforming as a set of interdependent secondary fractures in a localised zone may be expected. The ratio of fault rock to intact rock will be different for the two deformation styles, which would have an effect on the rheology of the deforming medium, in this instance increasing the angle of internal friction.

5.6 Discussion

Orientation of primary structures which fractures are secondary to

QM63 ellipsoid axes correlate well with the anticipated kinematic features in system A. There is no immediate correspondence with the slip surfaces bounding the fault zone. The

projection of the maximum ellipsoid axis onto the orientation of the bounding slip surfaces would produce a maximum ellipsoid axis parallel to the inferred slip direction along the slip surfaces (the projection of striae from system A onto the great circle of the slip surfaces). Likewise, the ellipsoid axes determined from the larger elliptical sections in QM65 is apparently reflecting the strain within system A, more than the bounding slip surfaces. A projection of the ellipsoid axes onto the bounding structures would produce an intermediate ellipsoid axis at a low angle to the slip direction. The angular discrepancy is inferred to reflect rotation as a result of activity on the high angle faults.

The interpretation of the ellipsoid axes would not have been wrong if the orientation of the larger scale deformation system were unknown and the axes were projected onto the bounding slip surfaces. However, the non-coincidence of the ellipsoid axes and bounding slip surfaces in samples of predominantly low angle fractures (R, Y and P fractures) should cause alarm. Either the quality of the data or the presence of a larger scale structure should be assessed.

The ellipsoids determined for the sub zones apparently have a direct correlation with the bounding faults. This could be a chance occurrence, as the high angle faults complicate the intersection relationship between the fractures (and hence the ellipsoid axes), Section 5.5. When treated as reflecting the strain of system A, the resulting angle between fractures is compatible with an interpretation as R' fractures and R, Y and P fractures present in the fault zone. Alternatively, the coincidence of the minimum axis and the inferred slip direction on the bounding slip surfaces would indicate ellipsoids formed by fractures symmetrical about the pole to the bounding structures. Armed with the knowledge that one set of fractures is at a high angle to the bounding structures, the fracture sets can be interpreted as R, Y, P and R' and X. To produce an ellipsoid axis at 90° to the bounding structures, there must be an equal population of X and R' fractures. The first interpretation is favoured for two reasons. (i) Physical modeling and observations of real fault zones has highlighted a higher population of R' fractures than X fractures.
(ii) The high angle fractures on the sample are seen both to offset and be offset by the wider lower angle fractures.

The alignment of the clasts to the overall strain regime of system A, not just in accord with the bounding fault orientation, implies that the fault zone is equivalent to the local strain regime. Bounding structures do not dictate how the secondary fractures form, but the fault

zone can compensate for non-ideally oriented bounding structures to result in a net strain across the zone comparable with the local strain.

If the samples had been analysed without knowledge of the larger slip system A, and ellipsoid axes were compared to the bounding slip surface orientation, the results would not be erroneous. The slip direction would be determined, however the sense would not be known.

Differences in fracture development between samples

The width of fault rock is a measure of both the displacement (Scholz, 1987) and abrasion of the clasts. Despite local abrasion of clast asperities and possible extrusion of pseudotachylyte from the generation zone, this approximation still appears valid. Abrasion of clast asperities does not occur evenly along the fracture length, so visual averaging of fault rock is possible. The pseudotachylyte generation is subordinate to cataclasite generation, which remains within the fault zone. Hence weighting the fractures according to average thickness of fault rock along the length gives the relative displacement of the fractures. The fault zone is more developed in sample QM65, than in QM63. The fractures at a high angle to the bounding faults in sample QM63 are thicker in sub-zone 2 and thickest in sub-zone 3, indicating most offset along the system in the third sub-zone. This fracture set remains thinner than the fractures at lower angles to the bounding faults, indicating less activity on this system. This observation is again consistent with nominating these high angle fractures as R' fractures, which are expected to have less displacement than fractures parallel to the bounding slip surfaces.

The order of fracture development in a zone of brittle simple shear has been subject to much study. Bartlett et al (1981) found from physical modeling that R and P fractures form synchronously in the initial stages of fault zone development. With continued fault zone development, the fractures interlink to form a continuous set of surfaces parallel to the shear zone boundary. Later in the fault zone development, R', Y and X fractures are formed. This can be used to identify the ellipsoid orientations expected at different stages in fault zone development.

(i) Just after initiation of the faulting the zone will contain clasts of rock with ellipsoid long axes parallel to the intermediate strain axis. The intermediate ellipsoid axes will parallel the slip direction and the minimum axes will be the pole to the fault plane.

(ii) As the fault zone develops, The R and P fractures overlap and interlink. This promotes a deflection of the fracture orientations at the overlap, resulting in more common terminations of rock clasts parallel to the intersection of fractures. Unless many new R and P fractures are generated, the ellipsoid axis parallel to the slip direction will not be shortened, so the maximum and intermediate ellipsoid axes may swap orientation. The maximum ellipsoid axis will then be parallel to the slip direction and the intermediate axis will be parallel to the intermediate strain axis. If R and P fractures develop sufficiently close to other fractures, the ellipsoid axis parallel to the slip direction will be reduced, so the maximum ellipsoid axis could remain parallel to the intermediate strain axis and the intermediate ellipsoid axis parallel to the slip direction. These may be definite stages in all fault zone development, or may vary between fault zones.

(iii) The growth of Y fractures will not significantly modify the orientation of the axes, however could result in a shortening of the minimum axis (perpendicular to the bounding structures). Growth of R' and X fractures will have implications for the ellipsoid axes that lie in the profile plane. The axes will be rotated. The orientation of these newly formed ellipsoidal clasts will be dependent upon the spacing of the high angle fractures and the angle between the fracture systems. As the clast length parallel to the striae direction is shortened by cross cutting R' and X fractures, the long axis of the clasts will return to parallelism with the intersection of fractures, that is, the intermediate strain axis.

This predicted model of ellipsoid generation in a fault zone can be applied to the ellipsoid orientations determined to assign a relative stage in fault zone development to each sample. QM63 can be equated to stage (ii) in fault zone development; the fractures defining the larger ellipsoids from QM65 can also be equated with stage (ii) of fault zone development. QM65 contains more fault rock than QM63, even excluding the fault rock associated with the high angle fractures, however this may be an artifact of activity on the high angle fractures causing asperities to form along the lower angle fractures (R, Y and P fractures). If QM65 does contain more fault rock than QM63 from activity along R, Y and P fractures, it is a more developed fault zone. The swapping of the maximum and intermediate axes may be a secondary stage in stage (ii) of fault zone development. Alternatively the

swapping of maximum and intermediate axes between QM63 and QM65 may simply reflect less interaction of R, Y and P fractures and so fewer clast terminations in the direction of the intermediate strain axis. Sub zones 1 and 2 from samples QM65 can be equated with stage (iii) of fault zone development. Sub zone 3, with no fabric defined by the clasts can be equated a stage of fault activity when interaction of fractures has obscured the definition of a fabric.

5.7 Conclusions

Overlapping fault surfaces are found in fault systems of all sizes. Grocott (1981) found the chronology of deformation of a pseudotachylyte generation zone in the Amitsuarssuk brittle zone in West Greenland to begin with folding, then formation of the paired slip surfaces, followed by generation of secondary fractures. The pseudotachylyte was found along secondary fractures and tensile veins with geometries comparable with those expected in any zone of brittle simple shear. The presence of pseudotachylyte is not seen to modify the secondary fracture geometries. The geometries of pseudotachylyte zones are recognised to resemble fault zones on larger scales (Childs, 1996). As such, the results of this study provide a suitable analogue for brittle fault zones of any size in a non-layered medium. Clearly, these geometries will not be reproduced in a layered sequence, where layer parallel slip can occur.

Numerous physical modeling experiments (see Hancock, 1985, for brief summary, Bartlett et al, 1982) have produced a compilation of structures expected in a strike slip fault zone, based upon the Reidel fracture distribution including stylolites, folds and X fractures (antithetic, symmetrical to R' about the pole to the bounding faults). Equivalent structures have been reported on wide scales occurring in nature (for example, Tomlinson et al, 1994, report secondary fractures comparable to models mentioned above in the order of 10's of km; Reutter et al, 1991, report secondary fractures up to 1 km in length and; Petit, 1986, applied the fracture geometries to any brittle fault and so to apply to all zones of simple shear). Grocott (1981) showed the minor shears within a pseudotachylyte generation zone, to intersect at the orientation of the intermediate stress axis. System A and B slip surfaces analysed throughout the rhyolite dyke and fractures measured on samples QM63 and QM65 have demonstrated this relationship between fracture intersection direction and intermediate strain axis to hold. Hence the model of fracture patterns within a zone of simple shear is well established.

Analysis of deformation within a fault zone using the shape of the intact clasts of rock surrounded by fractures, rather than the orientations of the fractures themselves can avoid bias of the data set. Inconsistent fracture orientations are compensated for and highly curved fractures which are difficult to measure a representative orientation of, are automatically included in the data set.

The successful analyses of clast shape showed the intermediate axis, slip direction and M-plane across the localised fault zone, as defined by the clast shape, to relate to slip system A, not the orientation of the bounding faults. The secondary fractures thus have a complementary strain ellipse to that for slip system A. The strain is partitioned into A system slip surfaces exclusively along the length of the dyke that the samples are taken from. The fractures within the localised fault system do not have the geometrical relationship expected if they were secondary simply to the bounding surfaces. They appear to be secondary slip surfaces related directly to slip system A. The Reidel within Reidel model is not correct if the bounding slip surfaces are taken as the first generation of Reidel and associated fractures, however the fractures possess a Reidel distribution relative to system A. No satisfactory model has been postulated to explain this.

The results show a high degree in lateral variation along the fault in terms of development. This analysis could not therefore be used to predict connectivity within a fault zone. In all states of fault zone development, the R-Y-P system of fractures is formed, which produces an intersection direction of all fractures parallel to the intermediate strain axis. The effect of later, high angle fractures may rotate this orientation uniformly across the whole fault zone transect, or, as the division of sample QM65 into sub-zones would suggest, the intersection direction will be rotated differentially across a transect of the fault zone. A network of R-Y-P fractures also promotes connectivity in the direction of slip.

Many studied faults have paired slip surfaces bounding a zone which has undergone deformation (Childs et al 1997). Hence an analysis based upon clast shape without requiring slip direction on secondary fractures would prove useful. Use of clast shape as a kinematic indicator requires an estimate of the stage of fault zone development, in order to compare ellipsoid axes with the predicted results. Recognition of whether fracture sets form at a high or low angle to the bounding fault and an estimate of the percentage of fault rock : intact rock can be used. A percentage fault rock : intact rock greater than 45% is seen as an indication that the clasts may have an orientation with no dynamic significance. If a fabric cannot be seen defined by clasts it is not worth continuing the analysis. To determine the kinematics, a fault zone in stage (iii) is necessary, so the assymetric fracture distribution in the profile plane can be used to determine sense of slip. Once the angle between fracture sets is determined, designation of the type of fractures can lead to sense of motion.

Caution must be exercised when any ellipsoid axes do not coincide with the bounding structures, either the fault zone has developed to stage (iii) or beyond, or the fractures are responding to a larger fault system. The fracture symmetry with respect to the bounding structures can be mis-leading when the system the fractures are responding to is mis-recognised. In the sub zones of QM65, the fractures were symmetrical about the bounding structures, which could indicate pure shear had occurred. However, as the fractures were actually responding to a system with a different orientation of bounding surfaces, this would have been an erroneous conclusion.

The generation of secondary fractures within a fault zone is seen to agree with the literature (Bartlett et al, 1981, Tchalenko, 1970). Fault zone generation can be divided into four stages, the first three with a significance attached to shapes of intact clasts of rock bound by secondary fractures. As the slip on secondary fractures increases, to avoid lock up of the fracture system, abrasion of the clasts of intact rock increases. Whether by branching of the secondary fracture system or cataclasis, or some mixture of the processes, the result is a variation in thickness of fault rock along the length of the secondary fracture. This is comparable with the findings of Childs (1996) in sedimentary sequences bound by two slip surfaces.

Future work

The assumption that R' are more abundant than X fractures in fault zones needs a fuller evaluation. A literature search has shown this generally to be the case, but quantification of the relative magnitudes and any rheological effects or effects depending upon the orientation and movement sense of the fault also need evaluation.

It is not known whether the swapping of intermediate and maximum axes will occur in every brittle fault zone at the same stages in the development history, or whether the amount of dilation or compression across the zone is significant. That is, the effect of the shape factor of the strain axis is unknown on the clast shape. Physical modeling in a suitable medium would constrain this. Further field observations of the same laborious nature are also necessary, in a similar situation where the kinematic history of the region can be constrained independently.

The connectivity across the fault system is an important parameter to constrain where oil reservoirs or mineralisation are associated with faulting. The lateral variation in the fault zone development, however may mean that future research will produce a model that cannot predict the direction of maximum permeability across a fault zone.

The shape of the ellipsoids have not been considered in any depth in this study. Clarification of how the shape of the ellipsoid is linked to rheology, strain magnitudes and stages in fault zone development could be interesting. It may even prove possible to distinguish the sub-stages within fault stage (ii), based upon the shape of the ellipsoid.

Chapter 6

Regional Synthesis

CHAPTER 6 REGIONAL SYNTHESIS

Table 6.1 shows the relative chronology of events determined form each chapter; Table 6.2 interrelates these events. It is assumed that faults with the same orientations and displacement sense occurred during the same event, if this is consistent with the rest of the chronology. Folding is the oldest structure in all of the relative chronologies. It is possible that the reverse faults that cut the Jurassic sediments 9Ch 2.1) and displace the Sierra de Varas fault (Chapter 3) occurred at the same time (structural features 2 and 4 in Table 6.2). The compatible kinematics of the thrusts with the folds, Chapter 2.1, suggests that they formed in response to the same tectonic regime. The en echelon folds in the Jurassic sediments could have formed in response to sinistral transpression along the north-south strike of the DFS, which would indicate the shortening and sinistral displacements are contemporaneous. The low angle of the fold axes to the hypothetical N-S bounding structures suggest sinsitral shear and coaxial shortening across the zone (Sanderson and Marchini, 1984). It is concluded that structural features 1 - 4 formed during one tectonic phase.

Some thrusting must have occurred after the sinistral shear and prior to dextral displacement to cause offset of the Sierra de Varas fault (Chapter 3). Later reactivation of the Sierra de Varas fault in a dextral sense and dextral components of motion along some minor dip-slip faults (for example, fault number 3 , Section 3, Fold out 3.1) occurred. The palaeomagnetic rotations indicate the dextral displacements are less than the sinistral displacements. The relative timing of dextral displacements and NNE - SSW normal faulting is uncertain.

Normal faulting along NW-SE striking faults associated with the sinistral offsets along the Profeta thrust forming the s-shaped fold in Q. del Viento, appears to fracture the Mid Miocene pediment surface. There is no trace of the normal fault in Q. Las Mulas in the Miocene cover or later ignimbrites along its strike. ENE striking normal faulting with a WNW-ESE extension direction, possibly with a sinistral component of lateral movement (Chapters 2.1 and 4) is thought to predate activity of the NW-SE striking normal faults (Chapter 21.). The later normal faults, are conjugate faults while the earlier normal faults have a consistent dip to the west.

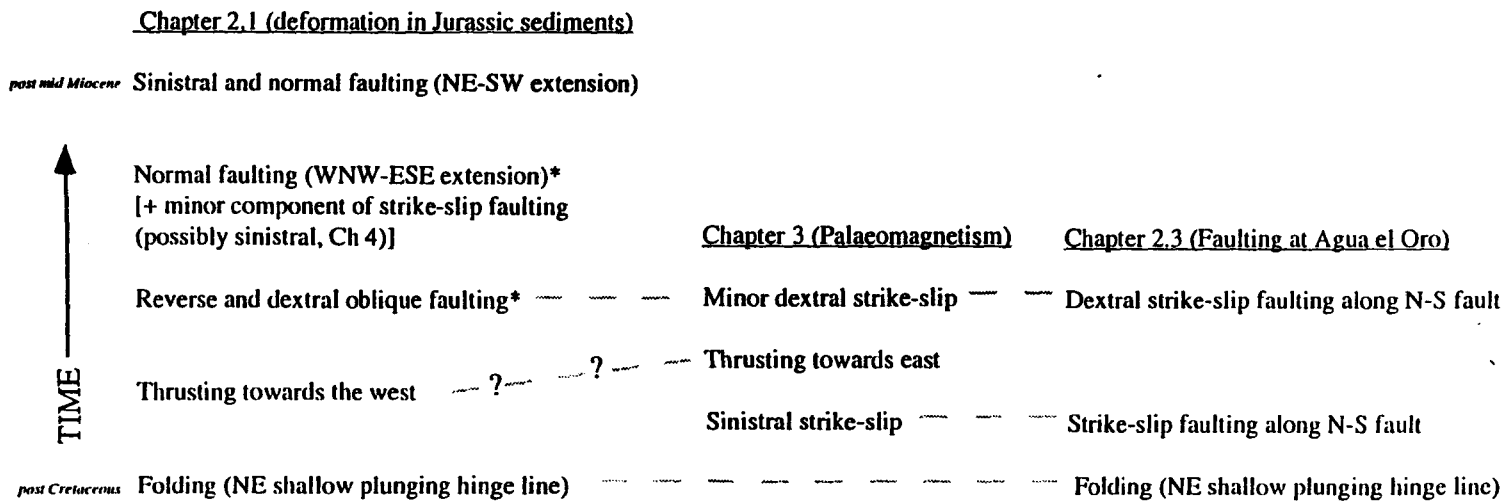

Table 6.1 Summary of relative chronologies determined throughout this study. Events that may correlate with each other are aligned. * indicates relative timing unknown.

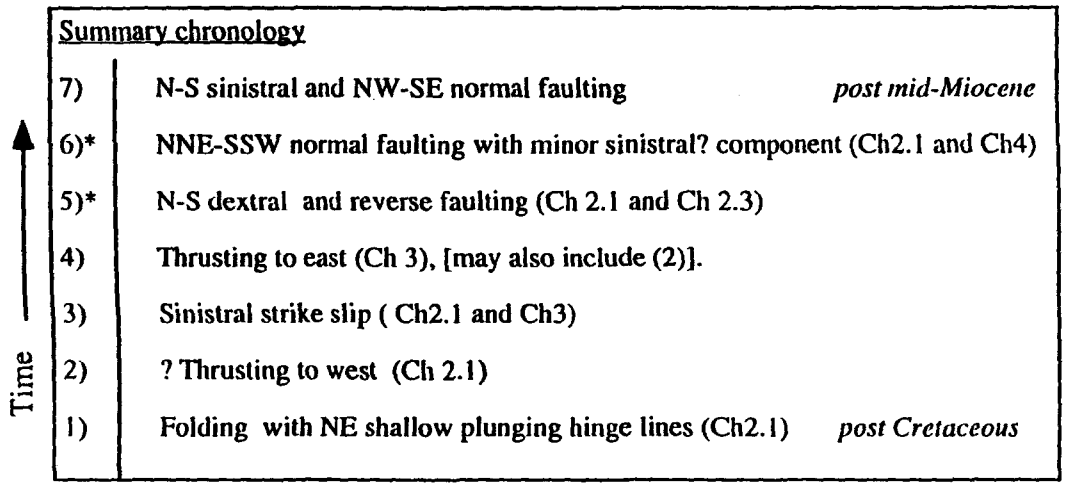

Table 6.2 Combined relative chronology of deformation inferred from all aspects of this study.

Epoch	Ma	Northern segment	Ma	Central segment	Ma	Southern segment
Miocene - Pliocene	<3	dextral, reverse and normal significant uplift [1]		normal faulting [10]		shortening [19]
	17		24	Punta Negra depression formed [11]		
Early Miocene- End Oligocene		sinistral ~ 36 or 25 km displacement post mineralisation [2,3,4]		reactivation of reverse fault [12]		
	31		30	dextral (Oligocene) [13]	32	
Upper Eocene		dextral ~ 2km displacement + shortening [5]		La Escondida mineralisation [14]	35	dextral [20]
	34	syn-mineralisation dextral [6,7]	34		36	
			40			sinistral and shortening [21]
Incaic Event	37			uplift [15, 16]		
		shortening [8]			42	
		Limon Verde + Chuquicamata hills rotated clockwise, translated N-wards [9]		sinistral ~30 km displacement timing poorly constrained [17]		
	44					
				dextral history throughout [18]		
Palaeocene			45			

Table 6.3 Chronology of deformation along the DFS as shown in Table 1.3.1. Numbers in square brackets refer to references in Table 1.3.2.

Comparison with previous deformation chronologies in the central segment of the DFS

Table 6.3 shows the deformation history of the DFS as defined prior to this study. Reutter et al's (1991) proposal of dextral displacement dominating the strike slip history of this zone does not appear valid for the study area. Dextral faulting has occurred but seem to have been subordinate to sinistral strike slip movements. The deformation history determined by Mpodozis et al (1993) is more consistent with observations from this study. Mpodozis et al 91993) ascribe the folding of the Jurassic sediments to the Late Cretaceous during the initial uplift of the Tarapaca basin floor (Chapter 1.2); they also recognise an episode of folding during the Incaic Phase. Reutter et al 91994) ascribe the folding of the Jurassic sediments to the Incaic Phase. Chong (1985) determined the age of folding to be ~40Ma. There is not enough evidence to independently determine the age of the folding from this analysis.

If the structural features 1 - 4 (Table 6.2) formed during one tectonic phase as postulated, comparison with previous work indicates that this is the Incaic phase (Steinmann, 1929). Comparison with Table 6.3 indicates the dextral offset inferred along the Sierra de Varas fault and the oblique faulting with reverse and dextral components of motion can be equated with the Oligocene dextral event recognised by Mpodozis et al (1993). The normal fault oriented NNE-SSW could be contemporaneous with the NNE-SSW normal faults that opened the Salar de Punta Negra depression at 24 Ma (Mpodozis et al, 1993). Finally, of the sinistral faulting along the Profeta thrust and contemporaneous with the NW-SE normal faults, Mpodozis et al (1993) had only seen evidence of normal faulting. Neogene to Recent sinistral faulting has not been recognised in the central segment of the DFS previously.

The chronology of deformation determined form this study is based upon much smaller scale observations than those of Mpodozis et al 91993). The complementary deformation histories produced form these separate studies verify the reliability of the chronology. The exact timing of each episode of deformation is still only loosely constrained.

Each segment of the DFS has undergone sinistral deformation and shortening during 45 - 40 Ma in the Incaic event. Each segment has also undergone later Oligocene dextral faulting. The large (36km) sinistral offset along the northern segment of the DFS is not evident elsewhere along the DFS. The post-middle-Miocene sinsitral faulting evidenced from Q. del Viento is much younger than this sinistral offset, Table 6.3.

It appears that the three segments of the DFS have a shared Eocene and Oligocene history, then behave as separate systems. In the Late Oligocene, thermal uplift and weakening of the present High Cordillera and Altiplano began (Isacks, 1988). The deformation front moved eastward to the High Cordillera and sub-Andean Ranges, although no major strike slip faults have been recognised within this region. This is though to have coincided with initiation of segmentation of the Andes related to variation in the dip of the subducting slab along the continental margin. The southern limit of the DFS is situated at a margin between a segment with a shallower subduction dip than the segment further south. This prompted variations in the width of the deforming zone between the segments. Miocene deformation may reflect local accommodation of deformation styles between the two Andean segments.

It is possible that the later sinistral components of faulting associated with NNE striking normal faults, documented I Chapters 2 and 4, is contemporaneous with the large sinistral offset (36 km) along the northern segment in the Oligo-Miocene. Even if this is the case, the magnitude of the displacement in the central segment is much smaller than that seen in the north. This would indicate that most of the displacement is not transmitted between the segments and it originated in the vicinity of the northern segment. Tomlinson and Blanco (1997) have related this event to contemporaneous sinistral faulting in Bolivia along N-S faults, possibly driven by differential shortening across the zone, Figure 6.1. Block rotation between these sinistral fault systems are thought to respond to an inferred dextral E-W shear couple. One unexplained feature of the large displacement evident in the northern but not central segments is how the displacement is accommodated. The 36 km displacement may sole into the master E-W fault, rotating and possibly uplifting the Calama basin. An erosional unconformitty occurred within the basin dated between 27 - 20 Ma (Pers. Commun. Hartley, 1996). This unconformity is only present within the Calama basin. Deposition recommenced towards the end of sinistral displacement along the northern segment of the DFS. This may explain why the displacement is not transmitted to the central DFS segment.

Model for Incaic deformation within the central segment of the DFS

Boundaries of the deforming zone

Jesinkey et al (1987) identified a ChRM consistent with the APW in Sierra Argomedo to the west, so the western margins of the deforming zone are constrained to the western limits of the Domeyko range, probably coincident with the fault bounding the western margin of the Jurassic sediments. The en echelon folding of Jurassic sediments indicates folding occurred

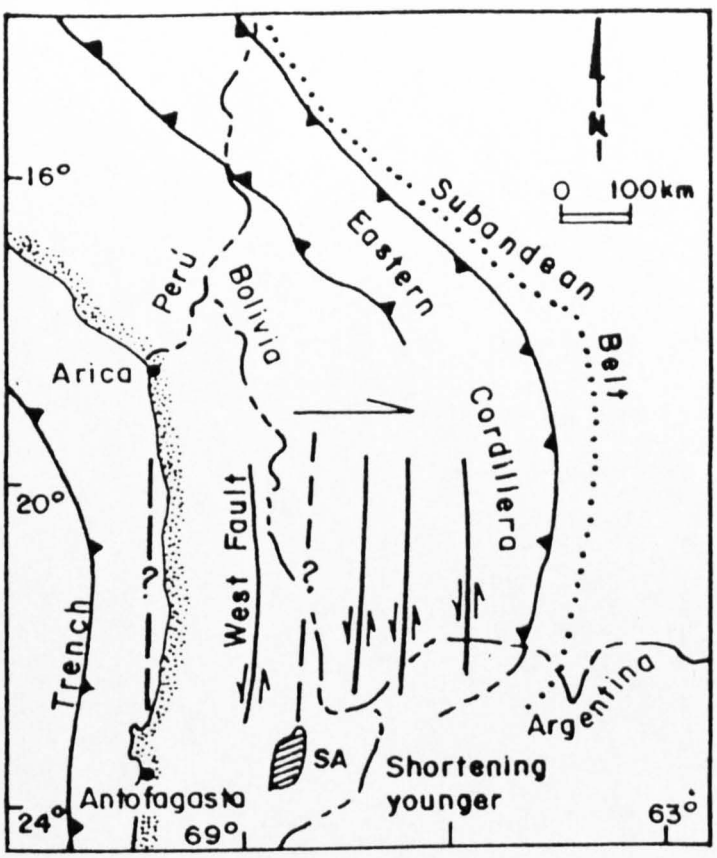

Figure 6.1 Structural model for the northern segment of the DFS during the ~27-18 Ma period. SA: Salar de Atacama. The north-south striking sinistral fault systems are idealized, their known strike length is considerably less. Contemporaneous reverse faults in the Eastern Cordillera are also shown. From Tomlinson and Blanco, 1997.

in a transpressional system, however the shorter lengths of the boundary thrusts and the obliquity of slip (if not pure dip slip) suggests the rotation within this zone will be less than within the La Escondia shear lens. The Sierra de Varas fault is recognised as the master fault of the segment (Herve et al, 1984). Mpodozis et al (1993) recognised a 50° clockwise rotation in the basement blocks to the east of the La Escondida shear lens. The 160° of clockwise rotation identified in Chapter 3, at the western margin of the DFS indicates a distributed deformation and a gradation in rotation across this zone, Figure 6.2. The fault zone can be divided into segments perpendicular to strike, with decreasing amounts of clockwise rotation to the east. This can be expressed as a decreasing amount of lateral transport along the faults while passing eastward. Most of the strike slip motions along the DFS at this latitude is concluded to have been taken up within the La Escondida shear lens.

This implies that the DFS was not active in conjunction with another fault system, so movement along the fault system could have a simple relationship with the driving stresses.

Comparison with Plate Motion Vectors

Oblique subduction to the northeast during the Eocene has been recognised by Pardo-Casas ans Molnar (1987) and Zonenshayn et al (1984). If the DFS directly reflected the relative motion of the South American and Farallon plates, a dextral shear is anticipated. Dextral movements along the Liquiñi-Ofqui fault in southern Chile (Cembrano et al, 1996) at this time indicate the plate reconstructions are valid. The presence of an as yet unidentified Eocene spreading ridge between north and south Chile could account for this discrepancy. Alternatively the regional stress regime may have a more complex relationship to the relative plate motions. Yañez et al (1994) suggested the ancestral Arica bend prevented northward movement of the frontal arc sliver (from dextral displacements); decoupling between the rigid upper crust and ductile lower crust prompted anticlockwise shear at the base of the lithosphere, Figure 6.3. After significant sinistral displacement had released the locked Arica bend, upper crustal dextral deformation in the Oligocene proved an easier way to take up the strain. This model is clearly a simplification of a highly complex system. Whilst it produces results compatible with the observations, it is not a unique solution. The modification of crustal stresses caused by thickening at the Arica bend could have caused tectonic escape form the bend. This may have been enough to modify the movement along the DFS from a simple reflection of the subduction direction.

Oroclinal bending

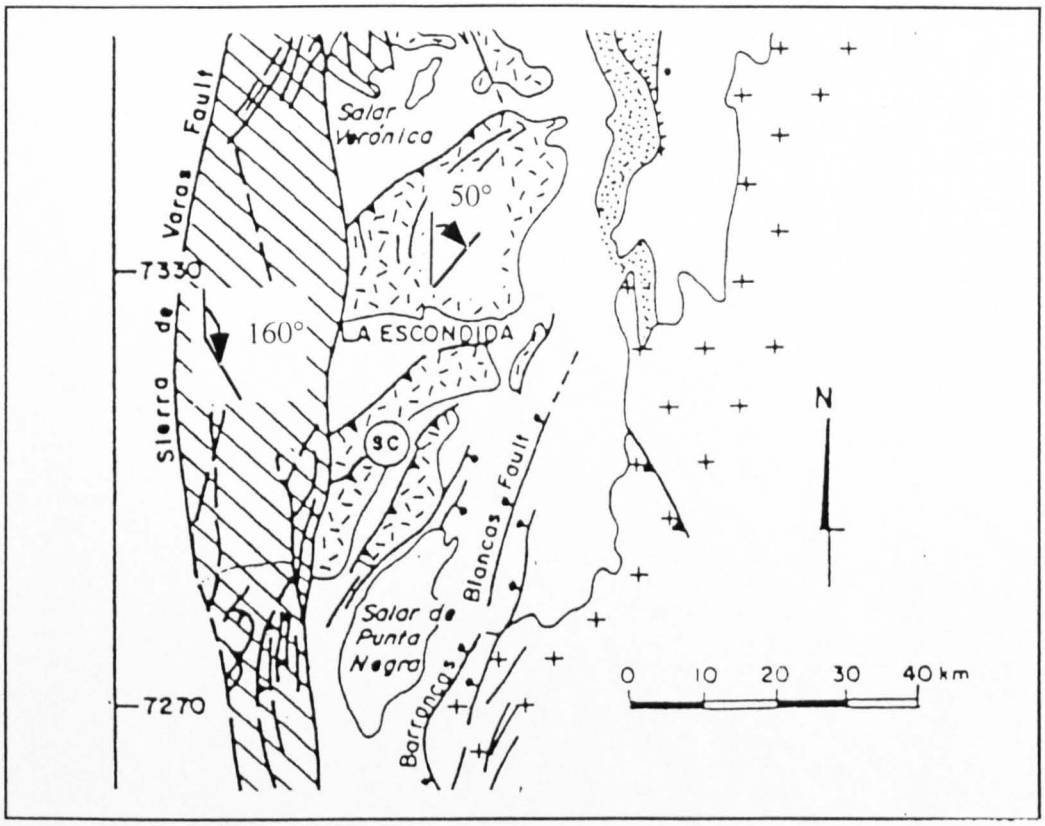

Figure 6.2 Variation in the amount of rotation across the structural domains in the central segment of the DFS.

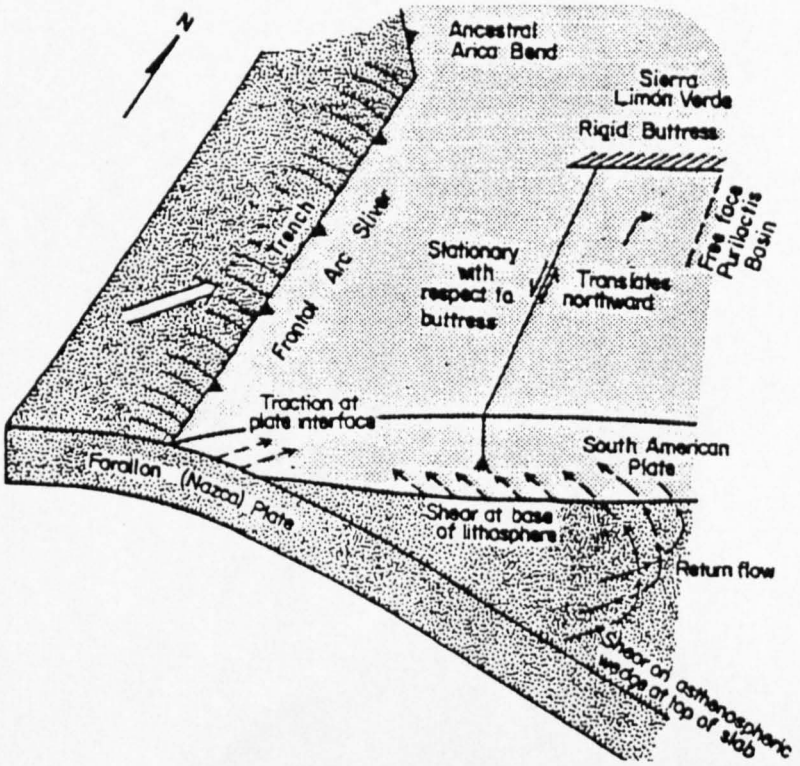

Figure 6.3 Conceptual dynamic model for the Incaic sinistral displacements observed along the DFS, from Yanez et al 1994.

Oroclinal bending as advocated by Isacks (1988) involves the passive rotation of two rigid crustal blocks either side of the arica bend in post-Miocene times. Palaeomagnetic rotations from this study, Chapter 3, indicate rotations associated with individual faults within the DFS. The ChRM's measured from Miocene samples have not been rotated from the expected palaeofield magnetic directions. Hence rotations along the Chilean Precordillera at 25°S are concluded to have been prompted by local fault activity.

Conclusions

CONCLUSIONS

Regional Conclusions

1) Deformation at the site of the Domeyko range began with uplift of the Tarapaca basin (Chapter 1).

2) Strike-slip activity along the central segment of the Domeyko Fault System began in the Eocene Incaic Phase with folding, thrusting and sinistral strike-slip along the Sierra de Varas fault (Chapters 2,3 and 6). Sinistral activity may also have occurred along the La Escondida fault to the east of the main range. The deformation was distributed across a region of ~60 km, with most lateral motion occurring at the western margin. Oligocene reactivation of the system involved dextral and reverse faulting. Later NNE-SSW normal faulting may have been contemporaneous with Late Oligocene opening of the Punta Negra basin. Finally, post mid - Miocene sinistral displacement along the west of the Domeyko range was accompanied by normal faulting along NW-SE normal faults.

3) The deformation histories of the three segments of the Domeyko Fault System are similar for the Eocene - mid Oligocene (the sinistral and dextral displacements). After this the segments behave separately (Chapter 6).

4) Comparison with plate motion vectors in the Cenozoic shows that the DFS does not simply reflect the margin parallel component of the relative plate motions (Chapter 6).

5) There is no evidence for passive rotation of the Domeyko Range related to formation of the Bolivian orocline (Chapter 3).

Geometry and Kinematics of Fault Zones

6) The distribution of secondary faults can be used to determine the sense of shear of the larger system, however the profile plane for the system must be determined, either using

the fracture intersection point or resolving the incremental strain axes. It is also necessary to establish that plane strain has occurred, otherwise the fracture distribution may be more complex. Plain strain can be identified if the intermediate incremental strain axis for the secondary faults are closely grouped (Chapter 4).

7) The shapes of rock clasts bound by secondary fractures are determined by the kinematics of the fault system. In the early stages of fault zone development the axes of an ellipsoid approximating the shape of the clast tend to parallel the slip direction, pole to the boundary surfaces and intermediate strain axis. Which axis parallels which structural feature varies as the fault zone develops (Chapter 5).

8) The orientation and shape of an ellipse approximating the shape of the rock clasts in the profile plane of the fault system can be used to identify the fracture types, according to the Reidel classification (Chapter 5).

9) R, Y and P fractures form ellipsoids with their maximum and intermediate axes parallel to the slip direction and intermediate strain axis of the fault system. Which axis parallels which structural feature varies, depending on the spacing between fractures and the curvature of the fracture surfaces (Chapter 5). The minimum axis parallels the pole to the boundary faults.

10) If the fault zone has R' fractures developed, the orientation of an elliptical section through the ellipsoid can be used to determine the sense of displacement of the fault system, when viewed in the profile plane with respect to the boundary structures (Chapter 5). The development of R' fractures modifies the intersection lineation of secondary fractures.

11) Beyond a critical level of development, the rock clasts do not have a shape that has a simple relation to the kinematics of the fault zone. The fault rock : intact rock ratio can provide a guide as to whether this level has been reached (Chapter 5).

12) Analysis of the shapes of rock clasts defined by fractures, rather than analysis of the fractures directly can avoid bias of the data set towards larger fractures or against irregular fractures (Chapter 5).

13) When analysing the shapes of rock clasts defined by secondary fractures in a non-layered medium that has undergone brittle faulting, it is necessary to identify the orientation of the boundary structures driving the system or, as in the system studied, well constrained options for the boundary fault orientations and kinematics are necessary.

14) It may prove possible to use this technique on 2 dimensional data, for example maps or satellite images, to determine the kinematics of a large scale fault system or to establish whether strain partitioning has a geographical distribution. Comparison of the plane perpendicular to the intersection of the faults with the mapped plane would indicate the suitability of this technique in different circumstances. This technique would not be valid where fault reactivation has occurred.

Fault Zone

15) Differences in fault zone development can vary over relatively small distances and influences the shape of rock clasts between fractures. There does not seem to be a way to predict the degree of development. Once developed beyond a certain point the clast shape does not have a simple relationship to the primary fault system.

References

REFERENCES

Aleksandrowski, P., 1985, Graphical determinations of principal stress directions for slickenside lineation populations: an attempt to modify Arthaud's method: Journal of Structural Geology, v. 7 No1, p. 73-82.

Allmendinger, R. W., Figueroa, D., Snyder, D., Beer, J., Mpodozis, C., and Isacks, B. L., 1990, Foreland shortening and crustal balancing in the Andes at 30 ° S: Tectonics, v. 9, p. 789-809.

Andriessen, P. A. M., and Reutter, K. J., 1994, K-Ar and fission track mineral age determinations of igneous rocks related to multiple magmatic arc systems along the 23 ° S latitude of Chile and NW Argentina, *in* Reutter, K. J., Scheuber, E., and Wigger, P., eds., Tectonics of the Southern Central Andes [1st ed.]: Berlin, Springer-Verlag, p. 141-155.

Angelier, J., 1989, From orientation to magnitudes in palaeostress determinations using fault slip data: Journal of Structural Geology, v. 11 No 1/2, p. 37-50.

Arabasz, W. J., 1971, Geological and geophysical studies of the Atacama Fault Zone in northern Chile: Ph.D. Thesis, California Institute of Technology, 275 p.

Ardill, J. R., 1996, Sequence stratigraphy of the Mesozoic Domeyko Basin, Northern Chile: Ph.D. Thesis, Liverpool University, 151 p.

Arthaud, F., 1969, Methode de determination graphique des directions de racourcissement, d'allongement et intremediare d'une population de failles: Bulletin Geological Society France., v. 7ser11, p. 729-737.

Bahlberg, H., 1987, Sedimentology, petrology and geotectonic significance of the Palaeozoic flysch in the Coastal Cordillera of Nortern Chile: N. Jb. Geol. Palaeont.Mh., v. 9, p. 527-599.

---, 1993, Hypothetical southeast continent revisited: new evidence from the middle Palaeozoic basins of Northern Chile: Geology, v. 21, p. 909-912.

Bahlberg, H., and Breitkreuz, C., 1991, The evolution of marginal basins in the Southern Central Andes of Argentina and Chile during the Palaeozoic: Journal of South American Earth Sciences, v. 4, p. 171-188.

---, 1993, Differential response of a Devonian-Carboniferous platform-deeper basin system to sea level changesand tectonics,N Chilean Andes: Basin research, v. 5, p. 21-40.

Bahlberg, H., Moya, M., and Zeil, W., 1994, Geodynamic evolution of the Early Palaeozoic continental margin of Gondwana in the Southern Central Andes of Northwest Argentina and Northern Chile, *in* Reutter, K. J., Scheuber, E., and Wigger, P. J., eds., Tectonics of the Southern Central Andes [1st ed.]: Berlin, Springer-Verlag, p. 333.

Bartlett, W. L., Friedman, M., and Logan, J. M., 1981, Experimental folding and faulting of rocks under confining pressure: part IX. Wrench faults in limestone layers: Tectonophysics, v. 79, p. 255-277.

Bathal, R. S., 1971, Magnetic anisotropy in rocks: Earth Science Reviews, v. 7, p. 227-253.

Beck, M. E., 1988, Analysis of Late Jurassic - Recent palaeomagnetic data from active plate margins of South America: Journal of South American Earth Sciences, v. 1, p. 39-52.

Beck, M. E., Garcia, A., R, Burmester, R. F., Munizaga, F., Herve, F., and Drake, R., 1991, Palaeomagnetism and geochronology of late Palaeozoic granitic rocks from the Lake District of Southern Chile: Implications for accretionary tectonics: Geology, v. 19, p. 332-335.

Bell, C. M., 1982, The lower Palaeozoic metasedimentary basement of the Coastal Ranges of Chile between 28.5° and 27 ° S: Revista Geologica de Chile, v. 17, p. 21-29.

---, 1987, The origin of the Upper Palaeozoic Chanaral melange of North Chile: Geological Society of London, v. 144, p. 599-610.

Berger, G. W., and York, D., 1981, Geothermometry for 40Ar/39Ar of biotite containg excess Ar-40: Geochimica et Cosmochima, v. 45, p. 795-811.

Besse, J., and Courtillot, V., 1991, Revised and synthetic apparent polar wander paths of the African, Eurasian, North American and Indian plates, and true polar wander since 200Ma: Journal of Geophysical Research, v. 96, p. 4029-4050.

Bond, G. C., Nickeson, P. A., and Kominz, M. A., 1984, Break up of a supercontinent between 625Ma and 555Ma: new evidence and implications for continental histories: Earth and Planetary Science Letters, v. 70, p. 325-345.

Boric, R., Diaz, F., and Maksaev, V., 1990, Geologia y Yacimientos mataliferous de la region de Antofagasta: Santiago, Servicio Nacional de Geologia y Mineria - Chile, v. Boletin 40, 246 p.

Breitkreuz, C., and Zeil, W., 1984, Geodynamics and magmatic stages on a traverse through the Andes between 20 and 24 ° S (N. Chile, S. Bolivia, N.W. Argentina): Geological Society of London, v. 141, p. 861-868.

---, 1994, The Late Carboniferous to Triassic volcanic belt in Northern Chile, *in* Reutter, K. J., Scheuber, E., and Wigger, P., eds., Tectonics of the Southern Central Andes [1st ed.]: Berlin, Springer-Verlag, p. 333.

Brown, M., 1988, Comparative geochemical interpretation of Permian-Triassic plutonic complexes of the Coastal Range and Altiplano, 25.5 - 26.5 ° south, *in* Harmon, R., and Rapela, C., eds., Andean magmatism and its tectonic setting [1st ed.]: Geological Society of America Special Publication, p. 157-177.

Brown, M., Diaz, F., and Grocott, J., 1993, Displacament history of the Atacama fault system, 25 - 27 ° S, Northern Chile: Geological Society of America Bulletin, v. 105, p. 1165-1174.

Bussell, M. A., 1989, A simple method for the determination of the dilation direction of intrusive sheets: Journal of Structural Geology, v. 11 No 6, p. 679-687.

Butler, R. F., 1992, Palaeomagnetism [1st ed.]: Cambridge, Masachusetts, Blackwell Scientific Publications, 319 p.

Butler, R. F., Herve, F., Munizaga, F., Beck, M. E., Burmester, R. F., and Oviedo, E. S., 1991, Palaeomagnetism of the Patagonian plateau basalts, southern Chile and Argentina: Journal of Geophysical Research, v. 96, p. 6023-6034.

Cande, S. C. and Leslie, R. B., 1986, Late Cenozoic tectonics of the Southern Chile trench: Journal of Geophysical Research, v. 91, p471-496.

Cande, S. C., La Brecque, J. L., and Haxby, W. F., 1988, Plate kinematics of the South Atlantic: Chron C34 to present: Journal of Geophysical Research, v. 93, p. 13479-13492.

Carey, E., 1976, Analyse numerique d'un moedele mecanique elementaire applique a l'etude d'une population de failles: calcul d'un tenseur moyen des contraintes a partir de stries de glissement: Ph.D. Thesis, Universite de Paris Sud.

Carey, S., 1955, The orocline concept in geotectonics: Proceeds of the Royal Society of Tasmania, v. 89, p. 255-258.

Cembrano, J., Herve, F. and Lavenu, A., 1996, The Liquini-Ofqui fault zone: a long lived intra arc fault system in Southern Chile: Tectonophysics, 259 (special issue on Andean Geodynamics), 55-66.

Charrier, R., and Reutter, K. J., 1994, The Purilactis Group of Northern Chile, *in* Reutter, K. J., Scheuber, E., and Wigger, P., eds., Tectonics of the Southern Central Andes [1st ed.]: Berlin, Springer-Verlag, p. 189-203.

Charrier, R., and Vicente, J. C., 1970, Liminary and geosynclinal Andes: major orogenic phases and synchronical evolution of the Central and Austral sectors of the Southern Andes: Upper Mantle Symposium, Buenos Aires, v. 2, p. 451-470.

Childs, C., Walsh, J. J., and Watterson, J., 1997, Complexity in fault zone structure and implications for fault seal prediction, *in* Moller-Peredsen, P., and Koestler, A. G., eds., Hydrocarbon seals: importance for exploration [1st ed.]: Singapore, Elsevier, v. Norewegian Petroleu Society, Spec Pub 7., p. 61-72.

Childs, C., Watterson, J., and Walsh, J. J., 1996, A model for the structure and development of fault zones: Journal of the Geological Society, v. 153 No Pt3, p. 337-340.

Chong, G. D., 1973, Reconocimiento Geologico del area Catalina-Sierra de Varas y Estratigrafia del Jurasico del Profeta: Ph.D. Thesis, Universidad de Chile, Santiago.

---, 1977, Contributions to the knowledge of the Domeyko Range, Northern Chile: Geologische Rundschau, v. 66, p. 374-404.

Choukronne, P., Gapais, D., and Merle, O., 1987, Shear Criteria and Structural Symmetry: Journal of Structural Geology, v. 9 No 5/6, p. 525-530.

Cobbing, E. J., 1985, The Central Andes-Peru and Bolivia: Ocean Basins and Margins, v. 7 No.PA, p. 219-264.

Coira, B., Davidson, J., Mpodozis, C., and Ramos, V., 1982, Tectonic and magmatic evolution of the Andes of northern Argentina and Chile: Earth Science Reviews, v. 18, p. 303-332.

Cominguez, A. H., and Ramos, V. A., 1991, La estructura profunda entre la Precordillera y Sierra Pampeanas (Argentina): Evidencias de la seismica de reflexion profunda: Revista Geologia de Chile, v. 18 (1), p. 3-14.

Cornejo, P. and Mpodozis, C., 1996, Geologia de la region de Sierra Exploradora (25° - 26°S): Servicio Nacional de Geologia y Mineria -CODELCO, Registered report IR-96-09, p330, Santiago.

Cornejo, P., Tosdal, R. M., Mpodozis, C., Tomlinson, A. J., Rivera, O., and Fanning, C. M., 1997, El Salvador, Chile porphyry copper deposit revisited: geologic and geochronologic framework: International Geology Review, v. 39, p. 22-54.

Cox, K. G., Bel, J. D., and Pankhurst, R. J., 1993, The interpretation of Igneous Rocks [2nd ed.]: London, Chapman and Hall, 450 p.

Dalla Salda, L., Cingolani, C., and Varela, R., 1992, Early Palaeozoic orogenic belts of the Andes in South America:Result of Laurentia Gondwana collision: Geology, v. 20, p. 616-620.

Dalla-Salda, L. H., Lopez de Luchi, M. G., Cingolani, C., and Vorela, R., 1996, extended abstract: 3rd ISAG, St Malo, France, p. 767-770.

Dallmeyer, R. D., Brown, M., Grocott, J., Taylor, G. K., and Treloar, P. J., 1996, Mesozoic magmatic and tectonic events within the Andean plate boundary zone, 26-27.5 ° S, North Chile: constraints from Ar-40/Ar-39 mineral ages: Journal of Geology, v. 104, p. 19-40.

Dalrymple, G. B., and Lanphere, M. A., 1971, 40Ar/39Ar technique of K/Ar dating: a comparison with the conventional technique: Earth and Planetary Science Letters, v. 12, p. 300-308.

Dalziel, I. W. D., Dalla Salda, L. H., and Gahagan.LM, 1994, Palaeozoic Laurentia-Gondwana interaction and the origin of the Appalachian-Andean mountain system: Geological Society of America Bulletin, v. 106, No2, p. 243-252.

Damm, K. W., Harmon, R. S., and Kelley, S., 1994, Some isotopic and geochemical constraints on the origin and evolution of the Central Andean Basement (19-24 ° S), *in* Reutter, K. J., Scheuber, E., and Wigger, P., eds., Tectonics of the Southern Central Andes [1st ed.]: Berlin, Springer-Verlag, p. 263-277.

Davidson, J., Mpodozis, C., and Rivano, S., 1983, El Palaeozoico de Sierra Almeida, al oeste de Manturaqui, Alta Cordillera de Antofagasta, Chile: Revista Geologica de Chile, v. 12, p. 3-23.

Davidson, J., and Mpodpzis, C., 1991, Regional geological setting of epithermal gold deposits, Chile: Economic Geology, v. 86, p. 1174-1186.

Dodson, M. H., 1973, Closure temperature in cooling geochronological and petrological systems: Contributions to mineralogy and petrology, v. 40, p. 259-274.

Edelman, S. H., 1989, Limitationsof the concept of stress in structural analysis: Journal of Geological Education, v. 37, p. 102-106.

Ernesto, M., and Pacca, I. G., 1988, Palaeomagnetism of the Parana Basin flood volcanics, southern Brazil, *in* Piccirillo, E. M., and Melfi, A. J., eds., The Mesozoic Flood volcanism of the Parana Basin: petrogenetic and geophysical aspects [1st ed.]: Sao Paulo, University of Sao Paulo, p. 229-255.

Faure, G., 1986, Principles of Isotope Geology [2nd ed.]: New York, Wiley.

Fisher, R. A., 1953, Dispersion on a sphere: Proceeds of the Royal Society of London, v. 217, p. 295-305.

Forsythe, R., and Chisholm, L., 1994, Palaeomagnetic and structural constraints on rotations in the North Chilean Coastal Ranges: Journal of South American Earth Sciences, v. 7, p. 279-294.

Gaber, L. J., Foland, K. A., and Corbato, C. E., 1988, On the significance of argon released from biotite and amphibole during 40Ar/39Ar vacuum heating: Geochimica et Cosmochima, v. 52, p. 2457-2465.

Gallagher, J. J., 1989, Andean Chronotectonics, *in* Ericksen, G. E., Canas-Pinochet, M. T., and Reinemund, J. A., eds., Geology of the Andes and its relation to hydrocarbon and mineral resources [1st ed.]: Houston, Circum-Pacific Council for Energy and Mineral Resources Earth science Series, v11.

Gamond, J. F., 1983, Displacement features associated with fault zones: a comparison between observed examples and experimental models: Journal of Structural Geology, v. 5 No1, p. 33-45.

Garcia, F., 1967, Geologia del Norte Grande de Chile.Simp.Geosincl.,Andino: Society Geologia de Chile Publicacion, v. 3, p. 138.

Grocott, J., Brown, M., Dallmeyer, R. D., Taylor, G. K., and Treloar, P. J., 1994, Mechanisms of continental growth in extensional arcs: an example from the Andean plate boundary zone: Geology, v. 22, p. 391-394.

Grocott, J., and Wilson, J., 1997, Ascent and emplacement of granitic complexes in subduction related extensional environments, *in* Holness, M. B., ed., Deformation enhanced fluid transport in the earth's crust and mantle [Mineralogical Society Special series 9 ed.]: London, Chapman and Hall.

Grocottt, J., 1981, Fracture geometry of pseudotachylyte generation zones: a study of shear fractures formed during seismic events: Journal of Structural Geology, v. 3, p. 169-178.

Gygi, R. A., and Hillebrandt, A., 1991, Ammonites (mainly Gregoryoceras) of the Oxfordian, (Late Jurassic) in Northern Chile and time correlation with Europe: Memoires Suisses de Palaeontologie, v. 113, p. 136-167.

Hancock, P. L., 1985, Brittle microtectonics - principles and practice: Journal of Structural Geology, v. 7 No3-4, p. 437-457.

Harland, W. B., Armstrong, R. L., Cox, A. V., Smith, A. G., and Smith, D. G., 1989, A geologic time scale [1st ed.]: Avon, Cambridge University Press, 263 p.

Hartley, A. J., Turner, P., Williams, G. D., and Flint, S. S., 1988, Palaeomagnetism of the Cordillera de la Costa, Northern Chile:evidence for local forearc rotation: Earth and Planetary Science Letters, v. 89, p. 375-386.

Heki, K., Hamono, Y., Kono, M., and Ui, T., 1985, Palaeomagnetism of Neogene Ocros dyke swarm, the Peruvian Andes:implicationfor the Bolivian orocline: Geophysical Journal of the Royal Astronomical Society, v. 80, p. 527-534.

Herve, M., Marinovic, N., Mpodozis, C., and Smoje, I., 1991, Mapa geologico de la hoja Sierra de Varas: Servicio Nacional de Geologia y Mineria Map 2, scale 1:100,000.

Hillbrandt, A., Smith, P., Westermann, G. E. G., and Callomon, J. H., 1992, Ammonite zones of the circum-Pacific region, *in* Westermann, G. E. G., ed., The Jurassic of the circum-Pacific [1st ed.]: New York, Cambridge University Press, p. 247-272.

Hrouda, F., 1982, Magnetic anisotropy of rocks and its applications in geology and geophysics: Geophysical Survey, v. 5, p. 37-82.

Irving, E., and Park, J. K., 1972, Hairpins and superintervals: Canadian Journal of Earth Sciences, v. 9, p. 1318-1324.

Irving, E. J., and Irving, G. A., 1982, Apparent polar wander paths, Carboniferous through Cenozoic, and the assembly of Gondwana: Geophysical Survey, v. 5, p. 141-188.

Isacks, 1988, Uplift of the Central Andean plateau and bending of the Bolivian Orocline: Journal of Geophysical Research, v. 93, p. 3211-3231.

Jesinkey, C., Forsythe, R. F., Mpodozis, C., and Davidson, J., 1987, Concordant late Palaeozoic palaeomagnetisations from the Atacama Desert: implications for tectonic models of the Chilean Andes: Earth and Planetary Science Letters, v. 85, p. 461-472.

Jordan, T. E., and Gardeweg, M., 1989, Tectonic evolution of the late Cenozoic Andes, 20-33 ° south, *in* Ben-Avraham, Z., ed., The evolution of the Pacific Ocean margins [Monographs on Geology and Geophysics ed.]: Oxford University Press, p. 193-207.

Kay, S. M., Ramos.V, and Kay, R., 1984, Elementos mayoritarios y trazas de las vulcanitas Ordovicias en la Precordillera Occidental: basaltos de rift oceanicos tempranos proximos al margen continental: Buenos Aires IX Congreso Geologico Argentino, v. Actas 2, p. 48-65.

Kelly, S., 1997, The laser argon dating technique, *in* Potts, Bowles, Reed, and Cave, eds., Microprobe techniques in the earth sciences [1st ed.]: London, Chapman and Hall.

Kirshvink, J. L., 1980, The least squares line and plane and the analysis of palaeomagnetic data: Geophysical Journal of the Royal Astronomical Society, v. 62, p. 699-718.

Lamb, S. H., 1987, A model for tectonic rotations about a vertical axis: Earth and Planetary Science Letters, v. 84, p. 75-86.

Larson, R. L., and Pitman, W. C., 1972, World-wide correlation of Mesozoic magnetic anomalies and its implications: Geological Society of America Bulletin, v. 83, p. 3645-3662.

Lawyer, L. A., and Scotese, C. R., 1987, A revised reconstruction of Gondwanaland, *in* McKenzie, G. D., ed., Gondwana 6 : Structure, tectonics and geophysics [1st ed.]: Washington DC, AGU, v. Geophysical Monogr.Ser. Vol 40, AGU, p. 17-23.

Lindsay, D. D., Zentilli, M., and Rivera, J. R. de la, 1995, Evolution of an active ductile to brittle shear system controlling mineralisation at the Chuquicamata porphyry copper deposit, Northern Chile: International Geology Review, v. 37, p. 945-958.

Lisle, R. J., 1985, Geological Strain Analysis: A manual for the RF/Phi technique [1st ed.]: Oxford, Pergamon Press, 99 p.

Magloughlin, J. F., 1992, Microstructural and chemical changes associated with cataclasis and frictional melting at shallow crustal levels: the cataclasite-pseudotachylyte connection: Tectonophysics, v. 204, p. 243.

Magloughlin, J. F., and Spray, J. G., 1992, Frictional melting processes and products in geological materials: introduction and discussion: Tectonophysics, v. 204, p. 197.

Maksaev, V., 1978, Geolgia de los Cuadrangulos Chitigua y Cerro Palpana al oeste del curso superior del rio Loa, Region de Antofagasta: Mem. Departamiento Geologia de Universidad de Chile, p. 1-245.

---, 1990, Metallogeny,geological evolution and thermochronology of the Chilean Andes between latitudes 21 and 26 South and the origin of major porphyry copper deposits: Ph.D. Thesis, Dalhousie University, Halifax, Nova Scotia.

Marinovic, N., and Lahsen, A., 1984, Hoja Calama:Carta Geologia de Chile: Servicio Nacional de Geologia y Mineria de Chile Map 58 pp1-140.

Marinovic, N., Smoje, I., Herve, M., and Mpodozis, C., 1992, Hoja Aguas Blancas: Servicio Nacional de Geologia y Mineria, Santiago Carta Geologia de Chile Map 70, scale 1:100000.

Marquillas, R., and Salfity, J. A., 1988, Tectonic framework and correlations of the Cretaceous-Eocene Salta group; Argentina, *in* Bahlberg, H., Breitkreuz, C., and Giese, P., eds., The Southern Central Andes, Lecture notes in earth sciences, 17: Berlin,Heidelberg,New York, Springer, p. 119-136.

Marret, R., and Allmendinger, R. W., 1990, Kinematic analysis of fault slip data: Journal of Structural Geology, v. 12 No 8, p. 973-986.

McDougall, I., and Harrison, T. M., 1971, Geochronology and thermochronology by the 40Ar/39Ar method [1st ed.]: Oxford, Oxford University Press.

McNutt, R., Crocket, J. H., Clark,AH, Caelles, J. C., Farrar, E., Haynes,S, and Zentilli, M., 1975, Initial Sr87/86 ratios of plutonic and volcanic rocks of the Central Andes between latitudes 26° and 29 ° south: Earth and Planetary Science Letters, v. 27, p. 305-333.

Merrihue, C. M., and Turner, G., 1966, Potassium argon dating by activation with fast neutrons: Journal of Geophysical Research, v. 71, p. 2852-2857.

Merrill, R. T., and McElhinny, M. W., 1983, The Earth's Magnetic Field [1st ed.]: London, Academic Press, 401 p.

Mitchell, J. G., 1968, The argon40/argon39 method for potassium argon determination: Geochimica et Cosmochima, v. 32, p. 781-790.

Morel, P., and Irving, E. C., 1978, Tentative palaeocontinental maps for the early Phanerozoic and Proterozoic: Journal of Geology, v. 86, p. 535-561.

Mpodozis, C., and Allmendinger, R., 1993, Extensional tectonics, Cretaceous Andes, Northern Chile: Geological Society of America Bulletin, v. 105, p. 1462-1477.

Mpodozis, C., Marinovic, C., and Smoje, I., 1993, Estudio geologico-estructural de la Cordillera de Domeyko entre Sierra Limon Verde y Sierra Mariposas, Region de Antofagasta: Santiago, Servicio Nacional geologia y mineria, 1-231 p.

Mpodozis, C., Marinovic, N., Smoje, I., and Cuitino, L., 1993, Estudio Geologico-Estructural de la Cordillera de Domeyko entre Sierra Limon Verde y Sierra Mariposas, Region de Antofagasta: Informe registrado, Servicio Nacional Geologia y Mineria - Corporacion Nacional del Cobre de Chile, 281 p.

Mpodozis, C., and Ramos, V., 1990, The Andes of Chile and Argentina: Circum-Pacific Council for Energy and Mineral Resources, v. 11, p. 59-90.

Nagata, T., 1961, Rock magnetism [1st ed.]: Tokyo, Maruzen, 350 p.

Nance, R. B., Worsley, T. R., and Moody, J. B., 1988, The supercontinent Cycle:, p. 177-187.

Naranjo, J. A., and Puig, A., 1984, Hojas Taltal y Chanaral: Servisio Nacional Geologia y Mineria Carta Geologia de Chile Map 62-63, scale 1:250000.

Naylor, M. A., Mandl, G., and Sijpesteijn, C. H. K., 1986, Fault geometries in basement induced wrench faulting under different initial stress states: Journal of Structural Geology, v. 8, p. 737-752.

Niemeyer, H., Urazua, A., Acenola, F., and Gonzales, C., 1985, Progresos recients en el conocimiento del Palaeozoico de la region de Antofagasta, Chile: Congreso Geologico Chileno,, v. 4, p. 410-438.

Noblet, C., Lavenu, A., and Marocco, R., 1996, Concept of continuum as opposed to periodic tectonism in the Andes: Tectonophysics, v. 255,1-2, p. 65-78.

Norris, D. K., 1958, Structural conditions in Canadian coal mines: Bulletin Geological Survey of Canada, v. 44, p. 1-53.

Owens, W. H., 1983, The calculation of a best fit ellipsoid from elliptical sections on arbitrarily oriented planes: Journal of Structural Geology, v. 6, p. 571-578.

Pardo-Casas, F. and Molnar, P., 1987, Relative motion of the Nazca (Farallon) and South American plates since Late Cretaceous time: Tectonics, v. 6 No. 3, p233-248.

Pickles, C. S., 1997, : Ph.D. Thesis, Liverpool University, Liverpool.

Piper, J. D. A., 1976, Palaeomagnetic evidence for a Late Proterozoic supercontinent: Philosophical Transactions of the Royal Society of London, v. 280, p. 469-290.

---, 1983, Proterozoic palaeomagnetism and single continent plate tectonics: Geophysical Journal of the Royal Astronomical Society, v. 74, p. 163-197.

Prinz, P., Wilke, H., and Hillebrandt, A., 1994, Sediment accumulation and subsidence history in the Mesozoic marginal basin of Northern Chile, *in* Reutter, K. J., Scheuber, E., and Wigger, P. J., eds., Tectonics of the Southern Central Andes [1st ed.]: Berlin, Springer-Verlag, p. 219-232.

Quirt, G. S., 1972, A potassium -argon geochronological investigation of the Andean mobile belt of north-central Chile: Ph.D. Thesis, Queen's University, Kingston, Ontario, 240 p.

Ramirez-R, C., F. and Gardeweg-P, M., 1982, Hoja Toconoa, carta Geologica de Chile, 1:250000: Servicio Nacional de Geologia y Mineria, Santiago.

Ramos, E. D., and Ramos, V. A., 1979, Los ciclos magmaticos de la Republica Argentina: Actas 7th Congreso Geologico Argentino, v. 1, p. 771-786.

Ramos, V. A., 1994, Terranes of southern Gondwanaland and their control in the Andean Structure (30-33 ° S latitude), *in* Reutter, K. J., Scheuber, E., and Wigger, P., eds., Tectonics of the southern Central Andes [1st ed.]: Berlin, Springer-Verlag, p. 249-263.

Ramos, V. A., Jordan, T. E., Allmendinger, R. W., Mpodozis, C., Kay, S. J., Cortes, L., and Palma, L. A., 1986, Palaeozoic terranes of the Central Andes: Tectonics, v. 5, p. 855-880.

Randall, D. E., Taylor, G. K., and Grocott, J., 1996, Major crustal rotations in the Andean margin:palaeomagneyic results form the Coastal Cordillera of northern Chile: Journal of Geophysical Research, v. 101, p. 15783-15798.

Rapalini, A. E., Abdeldayem, A. L., and Tarling, D. H., 1993, Intracontinental movements in Western Gondwanaland: a palaeomagnetic test: Tectonophysics, v. 220, p. 127-139.

Rapalini, A. E., Tarling, D. H., Turner, P., Flint, S. S., and Vilas, J. F., 1994, Palaeomagnetism of the Carboniferous Tepuel Group, Central Patagonia, Argentina: Tectonics, v. 13, p. 1277-1294.

Rapalini, A. E., and Vilas, J. F., 1991, Tectonic rotations in the Late Palaeozoic continental margin of southern South America determined and dated by palaeomagnetism: Geophysical Journal International, v. 107, p. 333-351.

Raposos, M. I. B., and Ernesto, M., 1995, An early Cretaceous palaeomagnetic pole from the Ponta Grossa dikes (Brazil): implications for the South American Mesozoic apparent polar wander path: Journal of Geophysical Research, v. 100, p. 20095-20109.

Reches, Z., and Dieterich, J. H., 1983, Faulting of rocks in three dimensional strain fields. I and II: Tectonophysics, v. 95, p. 111-156.

Reutter, K. J., Scheuber, E., and Helmcke, D., 1991, Structural evidence of orogen parallel strike slip displacements in the Precordillera of Northern Chile: Geologische Rundschau, v. 80, p. 135-153.

Reutter, K. J., Giese, P., Gotze, H. J., Scheuber, H., Schwab, K., Schwartz, G., and Wigger, P., 1988, Structures and crustal development of the central Andes between 21 and 25 ° south, *in* Bahlberg, H., Breitkreuz, C., and Giese, P., eds., The Southern Central Andes, lecture notes in Earth Sciences, 17: Berlin, Springer, p. 231-261.

Reutter, K. J., Scheuber, E., and Helmcke, D., 1991, Structural evidence for orogen parallel strike slip displacements in the Precordillera of Northern Chile: Geologische Rundschau, v. 80/1, p. 135-153.

Riley, P. D., Beck, M. E., Burmester, R. F., Mpodozis, C., and Garcia, A., 1993, Palaeomagnetic evidence of vertical axis block rotations from the Mesozoic of Northern Chile: Journal of Geophysical Research, v. 98, p. 8321-8333.

Rojas, J., and Lindsay, D. D., in press, Evolucion estructural de Chuquicamata, su relacion con la intrusion del porfido y eventos de alteracion-mineralizacion: .

Roperch, P., and Carlier, G., 1992, Palaeomagnetism of Mesozoic rocks from the Central Andes of Southern Peru: importance of rotations in the development of the Bolivian Orocline: Journal of Geophysical Research, v. 97, p. 17233-17249.

Salfity, J. A., 1980, Desarrollo palaeogeographico del Palaeozoic inferior del Noroeste Argentino: Reunion Annuales Proyecto 44 IGCP, Lower Palaeozoic South America, Lima.

Sanderson, D. J., and Marchini, W. R. D., 1984, Transpression: Journal of Structural Geology, v. 6 (5), p. 449-458.

Scheuber, E., Bogdanic, T., Jensen, A., and Reutter, K. J., 1994, Tectonic development of the North Chilean Andes in relation to plate convergence and magmatism since Jurassic, *in* Reutter, K. J., Scheuber, E., and Wigger, P. J., eds., Tectonics of the Southern Central Andes [1st ed.]: Berlin, Springer-Verlag, p. 333.

Scheuber, E., Hammerscmidt, K., and Friedrichsen, H., 1995, Ar-40/Ar-39 and Rb/Sr analyses from ductile shear zones from the Atacama Fault Zone, Northern Chile: the age of deformation: Tectonophysics, v. 250, p. 61-87.

Scholz, C. H., 1987, Wear and gouge formation in brittle faulting: Geology, v. 15, p. 493-495.

Scholz, C. H., Dawers, N. H., YU, J.-Z., Anders, M. H., and Cowie, P. A., 1993, Fault growth and fault scaling laws:Preliminary results: Journal of Geophysical Research, v. 98, p. 21951-21961.

Scotese, C. R., Lawver, L. A., Norton, I., and Royer, J. Y., 1987, Plate tectonic evolution of the circum-Antarctic passive margins: American Association of Petroleum geologists Bulletin, v. 71, p. 611.

Scotese, C. R., Lawver, L. A., Sclater, J. G., Mayer, C. L., Norton, I., and Royer, J. Y., 1987, Plate tectonic evolution of circum-Antarctic passive margins: American Association of Petroleum geologists Bulletin, v. 71 no5, p. 611.

Scotese, C. R., and McKerrow, W. S., 1990, Revised world maps and introduction: Geological Society of London, p. 1-21.

Shimamoto, T., and Ikeda, Y., 1976, A simple algebraic method for strain estimation from deformed ellipsoidal objects.1.Basic theory: Research Papers, p. 315-335.

Sibson, R. H., 1975, Generation of pseudotachylyte by ancient seismic faulting: Geophysical Journal of the Royal Astronomical Society, v. 43, p. 775-794.

Spray, J. G., 1992, A physical basis for the frictional melting of some rock forming minerals: Tectonophysics, v. 204, p. 205.

Steiger, and Jager, 1977, Subcommission on geochronology: convention on the use of decay constants in geo- and cosmochronology: Earth and Planetary Science Letters, v. 36, p. 359-362.

Steinmann, G., 1929, Geologie von Peru: Heidelberg, 448 p.

Sylvester, A., G, 1988, Strike slip faults: Geological Society of America Bulletin, v. 100, p. 1666-1703.

Tarling, D. H., 1983, Palaeomagnetism: principles and applications in geology, geophysics and archaeology [1st ed.]: London, Chapman and Hall ltd, 379 p.

Tchalenko, J. S., 1970, Similarities between shear zones of different magnitudes: Geological Society of America Bulletin, v. 81, p. 1625-1640.

Thiele, R., and Pincheira, 1987, : Mining Geology, v. 34(1), p. 21-31.

Thornburg, and Kulm, 1981, Sedimentary basins of the Peru continental margin - Structure, stratigraphy and Cenozoic tectonics for 6 - 16 degress south latitude: Geological Society of America Memoirs, v. 154, p. 393-422.

Tomlinson, A. J., and Blanco, N., 1997, Structural evolution and displacement history of the west fault system, Precordillera, north Chile. Parts I and II: Congreso Geologico Chileno,, v. VIII, p. 1873-1882.

Tomlinson, A. J., Mpodozis, C., Cornejo, P., and Ramirez, C. F., 1993, Structural geology of the Sierra Castillo-Agua Amarga fault system, Precordillera of Chile, El-Salvador-Potrerillos: Proceedings of the 2nd International Symposium on Andean Geodynamics, v. 2, p. 259-262.

Truco, S., and Rapalini, A. E., 1996, New evidence of a widespread Permian remagnetising event in the Central Andean zone of Argentina: 3rd International Symposium on Andean Geodynamics, St Malo, France, v. Extended Abstracts, p. 799-802.

Turner, J. C. M., and Mendez, V., 1979, Puna, *in* Segundo Symposio Geologico Regional de Argentina [1st ed.]: Cordoba, Academia Nacional Ciencias.

Ulriksen, C., 1979, Regional geology, geochronology and metallogeny of the Coastal cordillera between 23.5 and 26 ° south: MSc Thesis, Dalhousie University, Canada, 180 p.

Uyeda, S., Fuller, M. D., Belshe, J. C., and Girdler, R. W., 1963, Anisotropy of magnetic susceptibility of rocks and minerals: Journal of Geophysical Research, v. 68, p. 279-291.

Valencio, D. A., 1979, Palaeomagnetism of Lower Ordovician and Upper Precambrian rocks from Argentina, *in* McElhinny, M. W., Khramov, A. N., and Valencio, D. A., eds., Global reconstruction and the geomagnetic field during the Palaeozoic [1st ed.]: Advances in EPSL 10, p. 71-75.

Valencio, D. A., and Mitchell, J., 1972, Edad potasio-argon y palaeomagnetismo de rocas igneas de las formaciones Quebrada del Pimiento y Las Cabras, Provincia de Mendoza: Revista de la Asociation Geologica Argentina, v. 24, p. 191-198.

Van der Voo, R., 1994, True Polar Wander during the middle Palaeozoic?: Earth and Planetary Science Letters, v. 122, p. 239-243.

Vicente, J. C., 1985, Early Late Cretaceous overthrusting in the Western Cordillera of Central Peru: Geology of the Andes and its relation to hydrocarbon and mneral resources, v. Circum-Pacific Council for Energy and Mineral Resources.

Vilas, J. F., and Valencio, D. A., 1982, Implicancias geodinamicas de los resultados palaeomagneticos de formaciones asugnadoas al Palaeozoico Tardio-Mesozoico Temprano del centro-oeste Argentina: V Congreso Latinoamericano Geologia Actas, v. III, p. 743-758.

Vilas, J. F. A., 1981, Palaeomagnetism of South American rocks and the dynamic processes related to fragmentation of western Gondwana, *in* McElhinny, M. W., and Valencio, D. A., eds., Palaeoreconstruction of the continents [1st ed.]: American Geophysical Union Geodynamics Series, v. 2, p. 106-114.

Wallbrecher, E., and Fritz, H., 1989, Quantitative evaluation of the shape factor and the orientation of a palaeostress ellipsoid from the distribution of slickenside striations: Annales Tectonicae, v. III, p. 110-122.

Wallbrecher, E., Fritz, H., and Unzog, W., 1996, Estimation of the shape factor of a palaeostress ellipsoid by comparison with theoretical slickenline patterns and application of an eigenvalue method: Tectonophysics, v. 255, p. 177-187.

Wilson, J., 1996, The emplacament of the Las Tazas plutonic complex, N Chile: Ph.D. Thesis, Kingston University, London, 223 p.

Yañez, G., Mpodozis, C., and Tomlinson, A., 1994, Eocene dextral oblique convergence and sinistral shear along the Domeyko Fault System; a thin viscous sheet approach with asthenospheric drag at the base of the crust: Congreso Geologico Chileno,, v. 7, Actas, V2, p. 11478-11482.

York, D., 1978, A Formula describing both magnetic and isotopic blocking temperatures: Earth and Planetary Science Letters, v. 39, p. 89-93.

Zeigler, A. M., Parrish, J. T., and Scotese, C. R., 1981, Cambrian world palaeogeography: U.S. Geological Survey, v. 81-743, p. 252.

Zeil, W., 1979, Vulkanismus und geodynamik an der wende Paluozoikum-Mesozoikum in den zentralen und sudlichen Anden (Chile - Argentinien): Zentralblatt Geologie Palaeontologie, v. 3-4, p. 298-318.

Zentilli, M., 1974, Geological evolution and metallogenic relationships in the Andes of northern Chile between 26 and 29 ° S: Ph.D. Thesis, Queen's University, Kingston, Ontario, 295 p.

Zonenshayn, L. P., Savostin, L. A. and Sedov, A. P., 1984, Global Palaeogeodynamic Reconstructions for the last 160 Million Years: Geotectonics, v. 18 No. 3, 181-195.

Appendices

Page	Plane	Lineation		Fabric?	Dykes	Data set
39	172 40 w				178 35 w	
Ag el Oro	01 174					
	179 44 w					
	152 56 sw	15 149				Y
	157 80 w	20 f S				Y
40	318 66 ne					
	204 57 se					
	338 29 n	02 158	weak ep	bt- 165 69 w		Y
41	318 49 ne	39 099				X
	199 16 w					
	326 63 ne	32 121		153 85 n	146 55 ne	X
	091 65 s					
	116 18 e					
	250 25 nw	16 312				Y
	190 56 e	42 166				Y
	308 55 ne					
	221 75 w					
	311 47 n					
	023 64 nw	38 f NE				N-S
	334 67 sw	27 f N				Y
	067 46 se	12 f NE				Z
	074 40 s	08 081	S to NE			Y
	319 54 ne				014 85 w	
	326 54 ne	32 014				Z
	020 57 s					
	335 45 e					
	351 58 sw	56 233				Z
	324 33 n					
45	043 80 se		chl			
	056 78 se		chl			
	356 60 e		chl			
	345 54 w		ep			
	356 59 w	41 f S	ep			Z
	152 62 w	52 f N	ep			X
	315 09 e	03 344	chl			Y
	319 27 ne	18 111	ep+chl		303 70 E	Y
	038 44 w					
	197 52 w	48 f S				Z
	201 71 W	37 f S				Z
	187 84 w	57 f S	ep			Z
	003 64 e		ep			
	164 63 e		weak			
	323 78 e					
	352 68 w	38 fN				Y
	020 82 w					
	122 64 n					
	359 74 e	77 f N				Z
	019 89 w	64 f S				Z
	333 31 e		ep			
	335 58 e	67 f N				Z
47	019 27 e		chl + ep			
Q to N	096 46 s		chl + ep			
	074 43 s		ep			
	167 56 w	19 f N	chl + ep			Y
	140 46 sw	8 fN				Y
	223 55 n		chl+ ep			
	151 32 w	47 fN				X
	060 24 S	36 f E				X
	053 18 S					
	005 41 E		chl+ ep			
	336 54 e	29 f S				Y
	005 39 E	~ horiz'l				N-S
	102 43 S		chl			
	081 35 S	53 f E				Y
	345 52 NE		ep			

Page	Plane	Lineation		Fabric?	Dykes	Data set
49	142 50 W		ep + chl			
	320 31 ne		ep			
	094 70 s		chl			
	169 44 sw	58 f SE	chl			Z
	158 44 sw	24 f NW				Y
	261 73 n	5 fE				Z
	196 76 w	49 fN		ep v'n-5mm	014/20 e	Y
	132 41 W	79 f NW				Z
	189 62 w		ep vn			
	181 66 W	85 f N				X
	222 54 N					
	341 21 E					
	180 67 W	64 f N	ep vn			Y
	022/~90		ep vn			
	056 32 S					
	176 49 w	75 fN	chl + ep			X
	125 40 SW	38 f N				X
	158 80 W	61 f N	ep + chl			X
	065 38 S	71 f E				Y
	044 38 e	56 f N				X
	101 41 s	81 f E	ep + chl			N-S
	133 60 SW	32 f W				Y
	172 70 w	45 f N				Y
	197 47 w		ep +chl			
	121 36 ne		ep			
	194 22 w		ep + chl			
	213 75 w	46 f S				Z
	163 46 w	90				Z
51	080 60 s	36 f E	ep?			X
	350 48 e	90				X
	069 31 s	12 f E				X
	347 54 NE	43 f NW	chl			Z
	105 48 s		chl + ep			
	106 44 s		ep vn			
	195 29 w	27 f N	chl			N-S
	101 30 s	54 f E				
	102 51 s	75 f E	chl			Y
	154 46 sw	57 f NW	chl			Y
	129 48 sw	34 f Se	chl			Y
	183 26 w	22 f N				Y
	204 37 nw	35 f SE	ep + chl			Z
	266 38 n	54 f W	ep			Y
	116 39 n		ep vn			
	213 34 w	60 f sw	chl + ep			x
	093 70 s	51 f W	ep + chl			z
	192 48 w	90				x
	174 70 w	86 f s	ep			z
	011 90	90	ep			z
	023 47 e	66 f N	chl + ep	This + next c'd be conj. frac's		x
	140 55 w	57 f N	chl + ep			x
	104 66 s	37 f e	ep + qtz			y
	104 78 s	38 f E				y
	106 58 s	38 f E	ep.			y

APPENDIX 3 Magnetic Theory

This brief introduction is intended to familiarise the non-palaeomagnetic reader with the concepts necessary to understand chapter 3. It is not an exhaustive, quantitative review and a fuller account of the techniques and theory can be found elsewhere (Tarling, 1983 or Butler, 1992).

A3.1 Terminology

A glossary of the terms commonly used in palaeomagnetism is given below.

Apparent Polar Wander Path (APWP) The time sequence of palaeomagnetic poles determined from a tectonically coherent unit.

Blocking Temperature The temperature at which the time taken for the magnetism of grains with the same magnetic properties to move into a new field direction changes from a short relaxation time to periods comparable with geological time. In practice, rocks contain grains with a range of magnetic properties so that the magnetisations are blocked over a range of temperatures called the *blocking temperature spectrum.*

Characteristic Relaxation Time Time after which the magnetisation has fallen to 1/e of its original value.

Characteristic Remanent Magnetisation (ChRM) The highest stability component isolated by progressive demagnetisation. This magnetisation does not necessarily have the same age as the rock.

Chemical Remanent Magnetisation Remanent magnetism acquired from the geomagnetic field at ambient temperatures by chemical changes within the ferromagnetic grains.

Coercivity Value of the applied magnetic field required to reduce ferromagnetism of a grain to zero.

Curie Temperature The temperature at which ferromagnetic properties are lost as exchange couplings between neighbouring atoms are broken down.

Demagnetisation Removal of magnetism possessed by ferromagnetic particles. A laboratory procedure used to subtract the magnetism in a rock. Increasing temperature or alternating fields are used to achieve this.

Dipole A system comprising an oppositely directed north and south seeking magnetic pole.

Domains Sub-divided volume of a ferromagnetic grain with uniform magnetisation.

Ferromagnetic minerals Minerals capable of retaining a memory of the magnetic field after the field has been removed.

Geocentric Axial Dipole The magnetic field produced by a magnetic dipole at the centre of the earth and aligned to the rotation axis. This is the time averaged model of the magnetic field used to calculate the palaeomagnetic pole.

Induced Magnetisation (**J**) Net magnetic moment per unit volume acquired in an applied field.

Isothermal Remanent Magnetisation (IRM) Remanent magnetism imparted by short term exposure to strong magnetic fields at constant temperature (eg lightning strikes)

Magnetic Component Constituent part of the magnetism in a rock, acquired at a discrete point in time. Partial demagnetism in the laboratory aims to isolate and resolve the components comprising the total magnetisation.

Magnetic Moment (**M**) (magnetic dipole moment) Charge x Distance between two opposite magnetic charges.

Magnetic Field Strength (**H**) The force on a unit positive charge placed in a magnetic field.

Magnetic Susceptibility (χ) Magnetisability of a substance $J_i = \chi H$

Natural Remanent Magnetisation (NRM) The total remanent magnetisation of a rock prior to laboratory treatment.

Primary Remanence Magnetisation acquired at time of rock formation.

Remanant Magnetisation The ferromagnetism in a rock sample recording the memory of one or more ancient magnetic fields.

Secular Variation Short term changes in direction and magnitude of the surface geomagnetic field with periodicity of 1 - 10^5 years.

Superparamagnetic Ferromagnetic grains which are so small that alignment of their ferromagnetism is continually upset by thermal vibrations.

Thermoremanent Magnetisation (TRM) Acquired by cooling from above the Curie temperature in the presence of a magnetic field. This is the form of magnetisation acquired by most igneous rocks during initial cooling.

Virtual Geomagnetic Pole (VGP) Pole position calculated from an observation of the direction of the geomagnetic field at a point in time, that is, an instantaneous record of secular variation.

Viscous Remanent Magnetisation (VRM) A soft magnetisation acquired over geologically short periods of time as ferromagnetic particles relax their prior orientation to realign with the ambient field.

A3.2 The Geomagnetic Field

About 90% of the earth's magnetic field observed at the surface can be explained in terms of the field produced by a geocentric dipole inclined to the axis of rotation. The magnetic north and south poles of this model are located where the inclination of the magnetic field is 90°. The magnetic poles are not precisely coincident with the *geo*magnetic poles because up to 10% of the field has an external origin. When the best fitting dipole field is subtracted from the observed magnetic field, a non-dipole field is apparent.

Both the dipole and non-dipole fields vary with time. Directional changes of the magnetic field can be characterised as a random motion about a mean direction and non-dipole fields are observed to grow, decay and deform over periods of $\sim 10^3$ years. Merrill and McElhinny (1983) compiled geomagnetic pole positions from all over the globe, for 100 year intervals, over the last 2000 years. The time averaged geomagnetic field is the geocentric axial dipolar field and the non-dipole field is observed to be transient.

Variations in the observed magnetic field with a periodicity of 10^3 - 10^5 years can be attributed to secular changes in the dipolar field. Both the orientation and intensity of the geomagnetic field thus vary with time. Normal polarity, as exemplified by the present field, points towards geographic south as in Figure A3.2

Thus over time periods of the order of 10^3-10^4 years the Earth's geomagnetic field approximates to that of a geocentric axial dipole (GAD). The field can be considered equivalent to that produced by a single magnetic dipole at the centre of the earth and aligned with the rotation axis, Figure A3.1 The magnetic field, **H**, produced by the GAD at the surface is a vector quantity:

$$\mathbf{H} = \frac{M}{r_e^3}\sqrt{1+3\sin^2\lambda} \qquad \text{[A3. 1]}$$

I is the inclination of the magnetic field from the horizontal, λ is the geographic latitude, M is the magnetic dipole and r_e is the radius of the earth, (Figure A3.2). The derivation is given in Butler (1992, p 294).

Figure A3.1. A magnetic dipole created between positive and negative magnetic charges. The magnetism, **M** is equal to the charge multiplied by the distance.

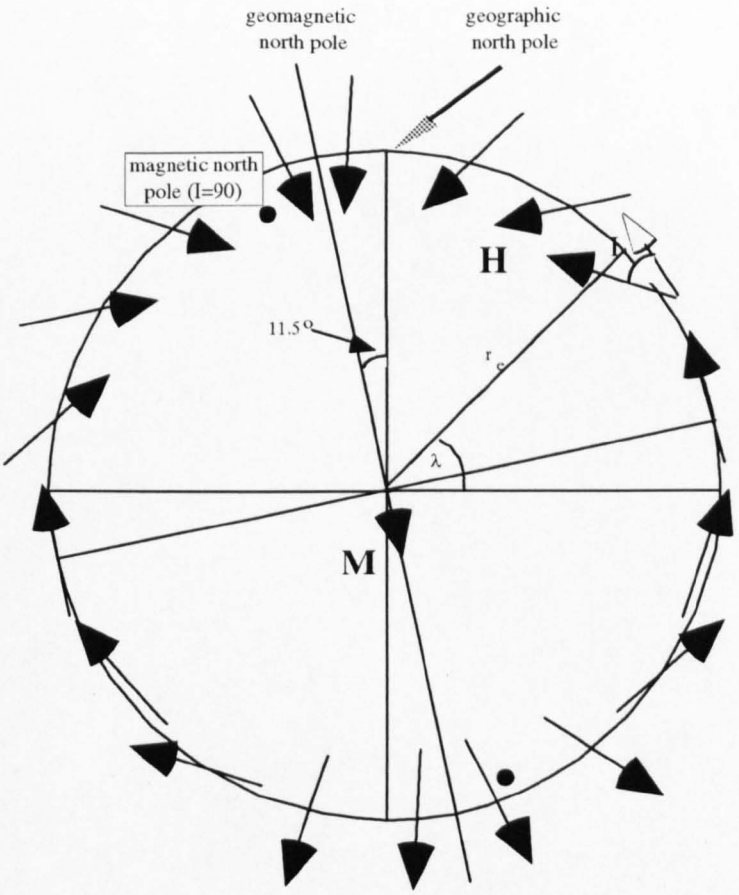

Figure A3.2 The geocentric axial dipole model. The magnetic field of the earth is modelled as that produced by a single dipole at the centre of the earth inclined to the axis of rotation. See section 7.1 for explanation. Redrawn after Butler 1992.

Implications of Palaeomagnetic Directions

Volumes of rock which contain remanent magnetisations acquired over timescales in excess of 10^3 years, will record the directions approximating to the geocentric axial dipole field at the sample locality. The orientation of the magnetism will then include a record of the latitude at the time the magnetism was acquired. As shown in equation [A3.2], the latitude is related to inclination of the magnetism in the GAD model by the relationship

$$\tan I = 2 \tan \lambda \qquad [A3.2]$$

where I is the inclination and λ is the latitude. In this way, the former latitude of exotic terranes may be identified by comparing inclinations of their magnetisation with palaeolatitudes of local autochthonous units of similar age. Rotational movements are determined by contrasts in declination. It is easy to calculate a virtual geomagnetic pole (VGP) for the sampling site, that is the location of the dipole required to produce the observed magnetic inclination and declination of the sample. Comparison of the VGP with the apparent polar wander path (APWP) for that continent, at the given rock age, can be used to highlight the effects of tectonic activity, but components of declination and inclination must be assessed separately to evaluate the discrepancy. In this study the magnetic direction recorded in units of known age immediately adjacent to faults are compared to the stable, age equivalent directions derived from the APWP to determine tectonic rotation. In addition, a palaeomagnetic sampling site in a Miocene lava flow without visible tectonic disturbance is compared to the APWP. A brief overview of how rocks can record this information is given below.

Acquisition of Remanent Magnetisation

Ferromagnetic minerals are capable of acquiring a record of the intensity and direction of the ambient magnetic field as they pass through critical lattice energy levels. This can occur as the minerals grow through a certain volume to surface area ratio, for example, or cool below a blocking temperature influenced by crystal size and chemistry. The magnetic signal then becomes "locked in" as a natural remanent magnetisation (NRM).

A ferromagnetic particle, exposed to an external magnetic field, will align its magnetic moment into parallelism with the field. A surface magnetic charge will result. An internal magnetic field, called an *internal demagnetising field,* is produced which is antiparallel to

the external field, Figure A3.3. The internal demagnetising field arises from the mutual magnetostatic attraction between the north and south poles in the particle.

As the particle size increases, the internal demagnetising field also increases. Above a critical size the magnetic forces operating in the particle cause it to split into magnetic domains, to minimise the magnetic energy. Within a domain the magnetisation is uniform and the domain boundaries *(Bloch walls)* are narrow zones across which the magnetic moments are canted around from the orientation of one domain in to the next, as shown in Figure A3.4. Grains that are small enough consist of only one domain, single domain (SD) grains. Between multiple domain (MD) and SD grains, pseudo-single domain grains occur (PSD). These grains are initially MD grains, however have been subject to a magnetic field which caused expansion of one domain at the expense of others. Removal of the field did not result in the return to a SD grain, as the domain boundaries are pinned by imperfections or shape effects. The remanence in an MD grain is more susceptible to change than an SD grain, unless domain walls are pinned by lattice imperfections or shape effects.

Figure A3. 5 shows a *hysteresis loop,* a graph of induced magnetisation as a function of applied magnetic field. The sample is representative of a whole rock with single domain grains distributed with random orientations. At point 0, the external field is zero, the sample has no net magnetisation.

At point 1 the external magnetic field is increasing. Naturally aligned domains have begun to increase in size at the expense of opposed domains and unaligned domains have been slightly deflected towards parallelism with the external field.

At point 2 saturation magnetisation (J_s) is reached. All possible domains are aligned to the external field and no more magnetisation can be acquired by the sample.

When the field is removed at point 3 some relaxation of the grain alignment has occurred and the enlarged domains preserve a reduced magnetisation parallel to the applied field as a memory.

To remove this memory a reversed field must be applied , point 4; this is the coercive force.

A characteristic relaxation time of a magnetic grain, τ, has been defined by Néel such that

$$J_r = J_{ro} \exp(-t/\tau) \qquad [A3.3]$$

so that, when $t=\tau$ $J_r(t) = J_{ro}/e$

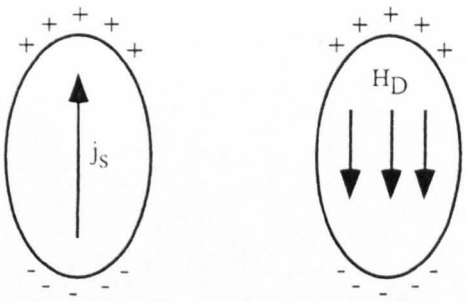

Figure 3.1..3 The induced magnetisation (j_S) in a ferromagnetic particle and the internal demagnetising field,H_D, which is uniform within the grain and opposes the external field.

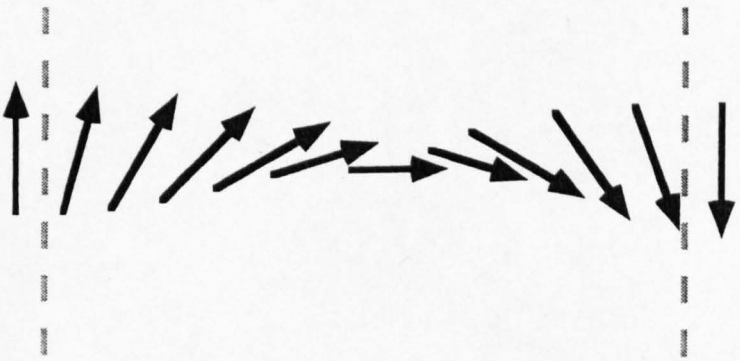

Figure 3.1.4. a) The Magnetic moments across the Bloch wall. The individual dipoles gradually rotate until aligned with the neighbouring domain. The grey dashes mark the domain boundaries.

where J_r is the remanent magnetisation at time, t and J_{ro} is the original magnetisation.

$\tau = 1/C[\exp(vh_cJ_s/2kT)]$

where C = frequency factor (approximately constant except near the Curie temperature), v = volume, h_c = coercivity, J_s = saturation magnetisation, k = Boltzman constant and T is the temperature. τ is dependent on the ratio of magnetic to thermal energies. As the magnetic energy increases, τ increases. Volume and temperature are the main variables in this equation (C, J_s, h_c and k are all approximately constant below the Curie temperature).This equation predicts that the relaxation time increases very rapidly as temperature falls to the "blocking" temperature. The variation of relaxation time with volume and temperature is shown in Figure A3.6.

Remanent Magnetisation

The total magnetisation in a rock is the vector sum of the remanent magnetisation and the induced magnetisation. The remanent magnetisation is typically composed of more than one component. The primary remanent magnetisation is acquired as the rock is forms. Secondary components are acquired later and can add to or replace the primary component. The total NRM is the vector sum of all the remanence components. Secondary components can be caused by chemical change or thermal resetting. There are three main types of magnetisation in rocks, these are thermoremanent magnetisation (TRM), chemical remanent magnetisation (CRM) and detrital remanent magnetisation (DRM). Since all samples used in Chapter 3 and 4 have an igneous origin, DRM will not be discussed here.

Cooling of a rock from above the Curie temperature through the blocking temperature imparts a TRM. Since all rocks contain a range of grains with varying magnetic properties, in practice this TRM is acquired over a temperature range known as the blocking temperature spectrum.

Chemical changes that result in the growth of new ferromagnetic minerals, or convert paramagnetic minerals into ferromagnetic minerals, can produce a CRM at ambient temperatures. As the ferromagnetic mineral grains grow, they pass through a critical blocking volume and pass from superparamagnetic to single domain grain properties. This is the origin of CRM in sedimentary rocks. It usually imparts a new remanence although

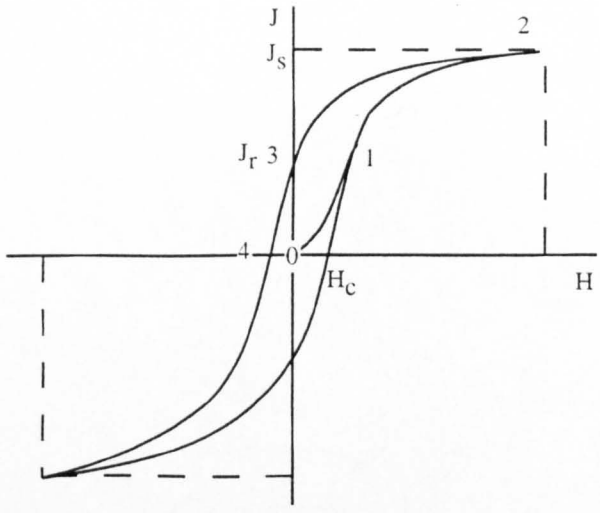

Figure A3.5 Idealised plot of magnetisation, J, as a function of applied magnetic field, H in a ferromagnetic material. J_S is the saturation magnetisation of the sample, J_r is the remanent magnetisation and H_c is the bulk coercive force (after Butler, 1992).

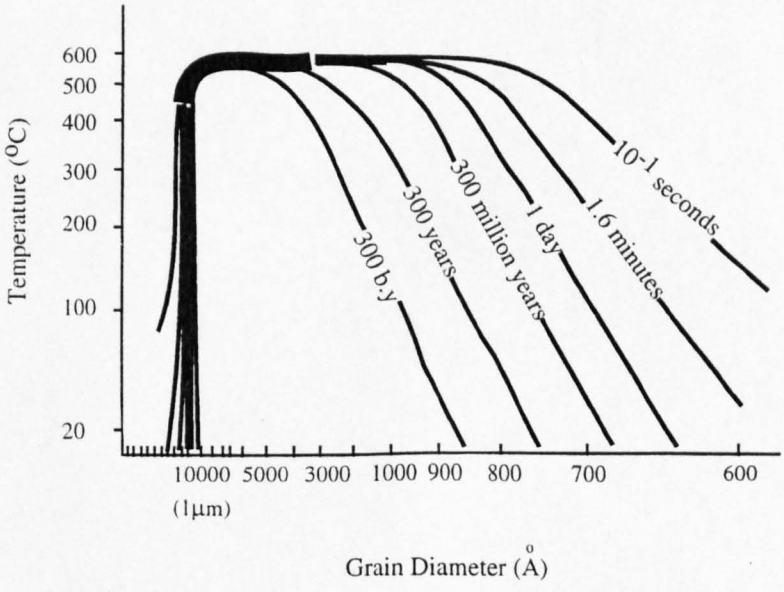

Ficure A3.6 Graphical representation of the relationship between temperature, volume and relaxation time, for titanomagnetite. The general shape is valid for all ferromagnetic minerals, but the values vary. (After Tarling, 1983.)

alteration of titanomagnetite to titanomaghaemite without a fundamental change in crystal structure can result preservation of in the original remanence in the final record.

Haematite and magnetite are the most common magnetic minerals. Figure A3.7 shows the chemical ternary phase diagram incorporating these minerals. Titanomagnetites are a solid solution series between ulvospinel and magnetite end members. A linear dependence of saturation magnetisation upon composition is observed. The Curie temperature reduces linearly with increasing Ti substitution for Fe. Haematite (Fe_2O_3) and ilmenite ($FeTiO_3$) are end members of the titanohaematite solid solution series. A Ti:Fe ratio of between 2 and 1:3 produces a maximum saturation magnetisation in the particle. This falls off sharply however, as a Fe:Ti ratio of 1 reduces the saturation magnetisation to zero. Magnetic mineralogy can be determined from a thermomagnetic curve (saturation magnetisation, J_s, versus temperature) using a Curie balance. The small sample is free to move and is heated in the presence of a strong saturating magnetic gradient. Changes in saturation remanence are translated into motion (the equilibrium of the sample position is disturbed and it moves within the magnetic gradient) which is monitored and recorded. Inflections or cusps in the curve result as mineral components are passed to progressively isolate components with a higher Curie point. Tangents drawn on either side of the cusp are used to define the Curie point. Table A3.1 lists Curie points for pure magnetite and haematite.

When determining Curie temperatures by means of a thermomagnetic curve, strong minerals such as magnetite can obscure the expression of the Curie temperatures of the lower saturation remanence minerals such as haematite. Thus it is also useful to note the temperature range over which the ChRM in each core has been resolved to identify the contribution of haematite.

Measurement of Magnetic components

From equation [A3.3] it can be seen that increasing the thermal energy of the ferromagnetic particle will greatly reduce the relaxation time. Incremental heating of the sample to elevate the thermal energy, followed by cooling a in zero field will gradually remove the remanent magnetism. Measuring the direction and magnitude of magnetisation in the sample between these stages of heat treatment allows the NRM of the sample, with the constituent components to be evaluated by vector subtraction retrospectively.

	Haematite	Magnetite
Curie Temp ^{O}C	675	575
coercivity	high	low
anisotropy	magnetocrystalline	shape
susceptibility	low	high

Table A3.1 Some important magnetic properties of magnetite and haematite.

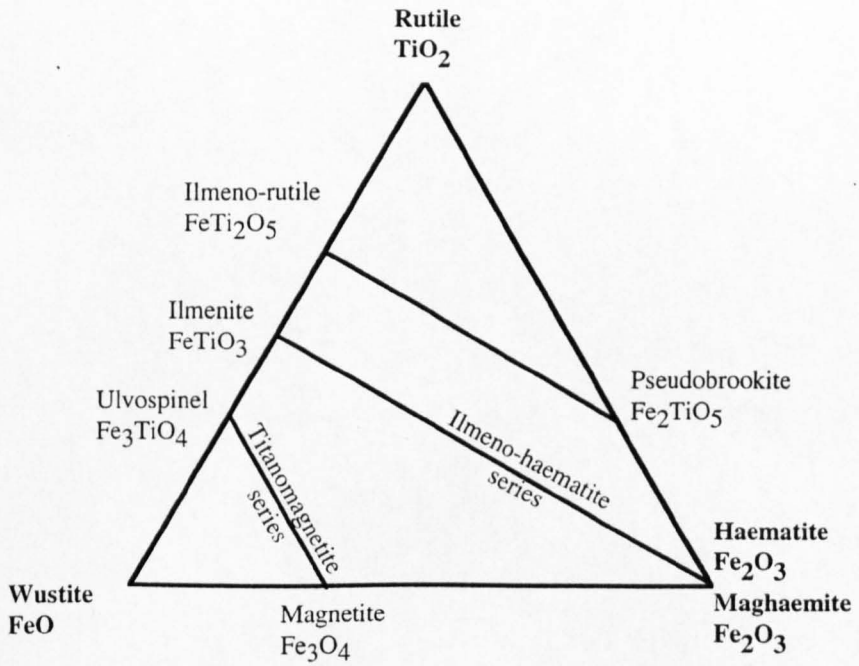

Figure A3.7 FeO - TiO_2 - Fe_2O_3 Ternary diagram. Low temperature oxidation tends to shift the chemistry to the right, parallel with the Fe^{2+} - Fe^{3+} boundary and form maghaemite by conversion of magnetite. Generally an increase in Ti content decreases the susceptibility and Curie point.

Anisotropy of Magnetic Susceptibility

A grain will be more readily magnetised along its long axis as this increases the separation of the surface magnetostatic poles. An alignment of elongate grains within the rock can thus cause a *shape anisotropy*. The second possible type of anisotropy is *magnetocrystalline anisotropy*. This occurs in non-isotropic crystals when there is an alignment of crystallographic axes and the crystals have an "easy" direction of magnetisation. Haematite has a high magnetocrystalline anisotropy and the susceptibility on the basal plane is at least two orders of magnitude higher than along the c axis (Hrouda, 1982). Alignment of crystal axes within the rock will result in a crystalline anisotropy. Haematite has a low susceptibility (10^{-3} - 10^{-2}) so any grain shape anisotropy will not be reflected in a magnetic anisotropy. Magnetite alternatively, has high susceptibility (0.5 - 13) so an anisotropic grain shape will result in a shape anisotropy. The magnetite crystal lattice is magnetically isotropic so when exposed to a weak magnetic field like the Earth's, it will not exhibit a magnetocrystalline anisotropy. The contrasting magnetic properties of magnetite and haematite are summarised in Table A3. 1. Less significant causes of magnetic anisotropy include an alignment of magnetic domains, stress induced alignment and close contact between rows or planes of magnetic minerals (Bathal 1971). The anisotropy of magnetic susceptibility (AMS) can be described by a second order tensor; diagrammatically this is approximated to a triaxial ellipsoid with maximum and minimum suscpetibility axes of k_1 and k_3, where $k_1>k_2>k_3$.

Numerous equations have been used as a measure of anisotropy. Here the degree of anisotropy,P where

$$P=k_1/k_3 \qquad [A3.4]$$

(Nagata, 1961) is used in this study.

The magnitude and orientation of AMS tend to reflect the processes that produced alignment. Volcanic rocks exhibit low anisotropies (typically with P ranging from 1, isotropic, to 1.1). The anisotropy is believed to reflect the dimensional orientation of titanomagnetites aligned by lava flow, a mechanism of rotation which is not effective in producing a pervasive magnetic fabric. The magnetic foliation reflects the flow plane and the magnetic lineation is either perpendicular or contained within the flow plane. The minimum axis in ignimbrites (k_3) is often perpendicular to the flow plane, in a fabric enhanced by flattening. Plutonic rocks may exhibit a range of anisotropy values. Lower anisotropy values are usually interpreted as a consequence of magmatic flow, with the

principal susceptibility directions correlating with flow directions. When P is greater than 2, ductile deformation is likely to have been involved in fabric enhancement and at higher values mimetic magnetite is involved (Hrouda 1982).

Above certain values of AMS, the remanent magnetisation is significantly deflected from the ambient magnetic field direction. Irving and Park (1973) show that this deflection is not as much as anticipated when the magnetic carriers are a mixture of both high and low coercivity particles (e.g. haematite and magnetite). In anisotropic rocks, the ferromagnetic grains are rarely in contact, so the magnetic direction varies slightly as the anisotropy varies through the volume of the rock.

For this study any samples with mixed haematite and magnetite assemblages, or rock samples with a degree of anisotropy less than 1.05 are assumed to have faithfully recorded the direction of the ambient field, within the limits of orientation and measurement accuracy. A degree of AMS greater than 1.05 is assumed to cause an anisotropy in the remanence. Uyeda et al's (1963) formula, with some modifications, is used to translate laboratory measurements of AMS into compensatory deflections of the remanence directions. A direct equivalence between anisotropy of susceptibilty and remanence is assumed.

For a thermoremanent magnetisation (TRM) vector, the deflection of remanence by AMS is defined by Uyeda et al (1963) as

$\tan \alpha = \tan \beta \ / \ P_0 P_B$ [A3.5]

α = inclination of the TRM vector relative to the k_1 axis of magnetic anisotropy.

β = inclination of the external field

P_0 and P_B are the degrees of AMS at room temperature and at the blocking temperature respectively. The geometries are shown in Figure A3.8. It can be seen that Uyeda's equation resolves the ambient magnetism into components parallel to the k_1 and k_3 orientations. No distinction is made between prolate and oblate magnetic ellipsoid shapes. It is possible to compensate for k_2 in calculations for the effect of anisotropy on the deflection of the ambient magnetic field: the component of the NRM on the plane defined by k_1 and k_2 is determined (this can be done with a stereo net projecting from the k_3 orientation) and its length determined (using the angle made with the semi-axes and their susceptibility measurements). The angle between the NRM and the k_1-k_2 plane is now equivalent to α; P_0 and P_B are calculated for the dimension of the NRM component in the

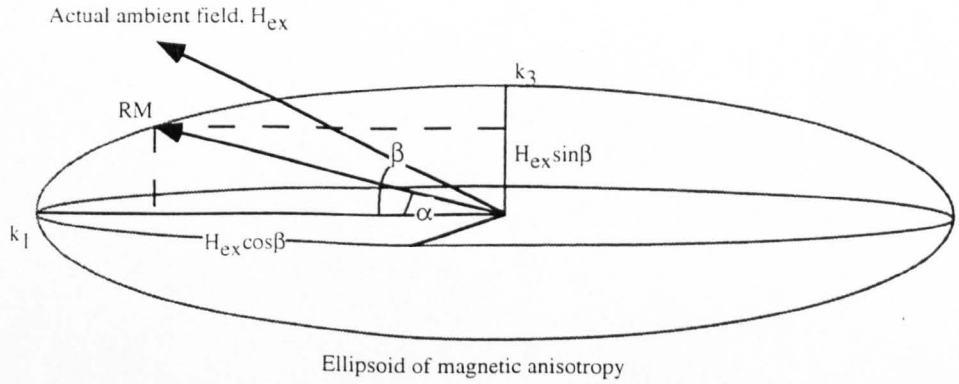

Figure A3.8 The geometric basis of Uyeda et al's equation, 1963.

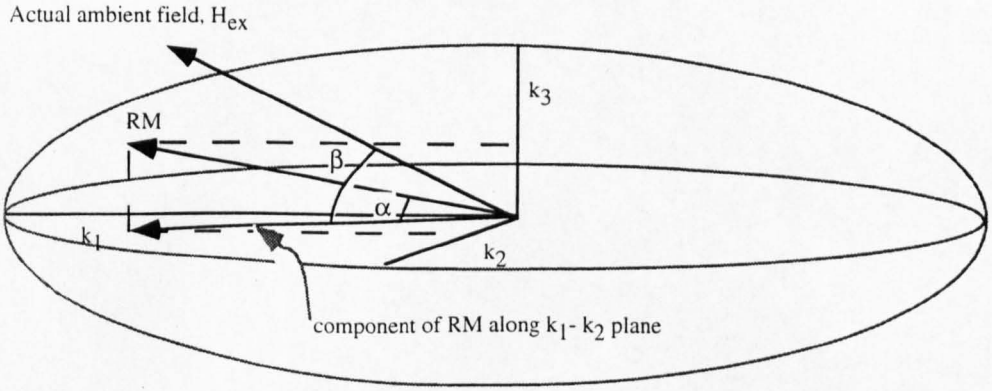

A modification of the calculations by Uyeda et al, 1963 to include compensation for the relative magnitude of the k_2 axis.

plane defined by the k_1-k_2 axes and the k_3 component; β remains the angle between the k_1-k_2 plane and the corrected NRM (measured in the plane containing the k_3 axis and the uncorrected NRM).

The AMS has been measured at room temperature, after no heating, and again after thermal cleaning to 500°C. The correction shows the AMS, above the degree of 1.05, will cause a significant deflection in the recorded magnetisation, even if the actual ambient direction lies within the magnetic ellipsoid.

Dist	Extens'n vein	rel tim'		shear fracture		dark seam	rel tim'g	sense	lintn	data set	comment
-0.4	038 66 E	I									
0	123 51 S	II									
0.2	050 50 E	I		138 80 S				sin			
0.5				107 90							
1.3									19 fr W		
				140 90							
2			1	098 83 S				5 sin	15 fr W	A	
	150 80 S										
						127 63 S	II	3 dex			
				113 82 S		040 78 W	I				
						165 23 S					
						145 06 S	I				
						125 77 S					
5m				009 59 W				3 dex			
						024 69 W					
7.7			2	034 16 W					15 308	A	
8.5					1	111 33 S		S dwn	24 254	A	
						090 0					
8.7					2	007 02E	Ib *		00 144	A	
						162 21 S	Ia *				
8.7					3	151 83 S	II *		71 fr E	B	
						155 73 N	II *	N dwn			
						154 90	I				
9					4	114 88 N	II		67 fr E	B...	
						141 80					
9.4			3	141 42 S					35 fr E	B / A	
10					5	118 90	II *		65 fr E	A	
10.15					6	156 83 S	I *		22 197	B	
10.9			4	175 43 W					11 192	B	
	096 38	br									
14					7	077 89 S			76 fr W	A	
						127 82 N	I				
	135 81 S	II									
15											
20											
25											
						113 68 S	I *				
28.6	058 42 E	III *			8	167 40 W	II *		16 217	B	
						009 69 W	IV *	4 E dwn			
						143 76 S	V *	20 dex			
28.5					9	113 82 S	V *		79 fr E	B	
29.3					10	004 82 E	VI *		60 fr N	A	
						027 74 W	I				
29.3					11	103 58 S	I		86 fr W	B	
						149 90	II=V *?				
30											
57.7					12	016 40 W			38 277	A	
						010 80 W		W dwn			yell/pple contact
						018 75 W	I	W dwn			pple
	092 70 N	br, CaCo3				166 37 W	II	Wdwn			pple
						082 80 S					pple
						167 80 W					yell
59.3					13	006 70 W			80 fr N	A	yell
58.8					14	176 27 W			22 096	A	yell
58.8					15	004 86 W			83 fr N	A	yell
59.4					16	016 68 W		W dwn	75 fr N	A	yell/pple contact
60			5	195 70 W					75 fr N	A	yell
						013 81 W					yell

Dist	Extens'n vein	rel tim'		shear fracture		dark seam	rel tim'g	sense	lintn	data set	comment
						104 81 N					pple
61.8					17	025 62 W			87 fr S	A	yell
61.8					18	026 63 W			83 fr S	A	yell
61.8					19	045 73 W			84 fr S	A	yell
61.8					20	026 69 W			85 fr S	A	yell
61.8					21	026 63 W			82 fr S	A	y/p contact
62.5					22	048 04 W				A	
62.5					23	017 60 W			90	A	yell
62.5					24	007 57 W			85 fr N	A	yell
						132 32 S					yell
						132 46 S					yell
						186 78 W					pple
65.4						244 72 N					
					25	158 70 S			90	A	
						183 61 W					
						293 90					
						120 59 S					
56.8					26	170 52 W			46 fr N	A	
						168 64 W					
67.5					27	208 29 W	III		32 110	A	
68.8					28	198 15 W	II		09 247	B	
69.1					29	198 19 W	I		19 306	A	
									07 329		
69.6					30	162 25 W			24 257	A / B	
70.1					31	221 42 W			247 21	B / A	
						143 70 SW					
						196 36 W					
71.3					32	184 55 W			70 fr N	A	
72					33	217 58 W			62 fr N	A	
80	324 58 N										
83.4	317 46 N		6	269 62 N					34 fr W	A	
83.9			7	349 65 E					26 fr S	A	
	141 63 N										
	074 64 S										
85									17 046		
88.1	314 60 N		8	143 51 S					49 201	B	
87.9			9	156 63 S					54 205	B	
88.4	356 45 E		10	154 36S					36 fr E	B	
	244 64 N										
	113 58 S										
	262 54 N										
	154 45 W										
92			11	022 49 E					68 fr S	A	
	129 62 N										
	033 58 E	III									
	136 44 N	II									
	113 50 N	I									
93			12	024 71 E					77 fr S	A	
	275 41 N	CaCO3									
93.5			13	027 79 E					76 fr S	A	
	232 32 w										
96.2	134 83 S		14	165 32 E					8 fr W	A...	
	301 64 N										
96	190 38 W		15	156 51 W					40 231	B	
	159 60 W	II *		009 84 E							
96.6			16	184 85 W					26 fr S	B	
96.8					34	136 77 S			63 fr E	B	
				285 80 N							
97.6					35	199 29 W			11 352	?	
97.9					36	095 75 N	I		37 frE	B	yell

Dist	Extens'n vein	rel tim'		shear fracture		dark seam	rel tim'g	sense	lintn	data set	comment
						192 57 W					yelll
98.3					37	065 54 S	II		72 fr W	A	yell
						120 81 N					yell
98.5					38	110 90	III		71 fr E	B	yell
98.75					39	129 90	I		60 fr E	B	yell
											yell
99.5			17	226 45 W					34 316	A	yell
				012 78 W		119 67 W					yell
	235 32 N			015 68W							pple
	125 90										pple
	329 90										pple
99.9	177 59 W								84 fr S		pple
									50 fr S		pple
100						138 75 S					yell
						188 84 N					yell
						002 84 E					yell
						218 53 W					pple
102.3					40	166 35 W			23 199	B	pple
	225 19 W					174 75 W					pple
104	124 55 S				41	117 75 S			25 fr E	B	pple
106					42	194 44 W			44 fr S	B	pple
107.1					43	144 24 S			19 170	B	yell
107.6					44	104 49 N			59 fr E	B	pple
						197 77 W	III				pple
						149 43 S	II				pple
108.2					45	102 53 S			56 fr E	B / A	pple
						206 38 W					yell
						112 58 N					pple
						144 40 W					pple
						261 44 N					pple
						096 46 S					pple
						124 80 S					pple
110.8			18	212 55 W					82 fr N	B	pple
110.8					46	039 03 W			02 314	A	pple
						209 48 W					pple
						277 59 N					pple
						203 65 W					pple
						159 43 W					pple
116.7					47	187 48 W			69 fr S	B	pple
117.2					48	200 45 W			90	A	pple
				169 32 W							pple
117.3					49	141 41 W			46 231	B	pple
	282 32 N										pple
116.7					50	000 15 E			116 08	A	pple
117			19	267 27 N					18 030	B	pple
	128 72 S										pple
	286 28 N										
	208 36 W										pple;wi.ig clasts
118.1					51	211 50 W			79 fr N	A	pple
118.4					52	203 46 W			82 fr N	A	pple
118.4					53	193 49 W			82 fr N	A	pple
118.3					54	175 48 w			42 fr S	B	pple
118.3	203 37 W				55	210 43 W			90	A	pple
118.3				026 59 E		028 71 W				A	yell
119.7					56	255 56 N			45 fr E	B	yell
	235 55 W					192 14 W					pple
121					57	143 18 S			06 307	A	pple
	251 28 W										pple
121					58	247 45 w			15 fr E	B	pple
121.2					59	187 17 W			90 304	A	pple

Las Mulas rhyolite dyke structural data

Appendix 4

Dist	Extens'n vein	rel tim'		shear fracture		dark seam	rel tim'g	sense	lintn	data set	comment
									03 341		pple
						344 82 n					pple
122.6					60	232 12 W			10 305	A	pple
122.5			20	032 12 W					12 219		pple
122.7			21	191 26 W					26 281		pple
123					61	196 18 W			09 304	B	pple
						201 24 W					pple
123.3					62	233 50 w			28 fr E	B	pple
124.3					63	238 42 w			05 226	B	pple
124.8					64	254 41 W			31 023		pple
	249 26 N										pple
125.9	258 19 N								13 038		pple
125.6					65	225 42 W			41 330	A	pple
126.6			22	353 42 W					09 193	B	pple
126.8					66	207 43 W			75 fr S	A	pple
	204 43 W										pple
125.6					67	225 42 W			41 330	A	pple
	175 33 W										pple
	213 44										yell

QM63	slip surfaces			QM65	slip surfaces	
strike	dip	dip direction		strike	dip	dip direction
213	81	n		183	73	W
218	83	n		181	87	W
212	57	n		163	72	W
37	39	s		163	46	W
53	82	s		88	90	E
192	24	w		135	84	S
228	39	n		159	19	W
205	89	w		10	86	E
220	46	w		33	72	E
221	50	n		29	85	E
170	66	w		125	43	S
215	59	w		274	26	N
217	83	n		168	86	W
91	47	s		214	66	W
216	41	n		320	89	N
210	51	w		12	65	E
234	61	n		195	84	W
189	46	w		226	70	N
222	72	n		163	68	W
158	54	w		201	40	W
222	51	n		125	85	S
197	59	w		125	85	S
228	68	n		172	44	W
250	69	n		193	48	W
273	12	n		182	70	W
339	85	e		5	33	E
51	66	e		350	38	E
267	68	n		293	18	E
253	84	n		141	37	S
188	84	W		87	44	S
329	66	E		167	36	W
321	59	E		135	31	S
191	55	W		135	35	S
15	77	E		85	36	S
223	40	W		16	11	S
220	57	N		137	30	S
201	59	W		127	35	S
220	20	W		352	63	E
206	77	W		181	25	W
193	78	W		75	35	E
120	43	S		135	30	W
336	55	E		277	63	E
221	24	W		135	67	W
207	27	W		114	64	S
160	78	W		78	20	S
318	36	N				
342	33	E				
193	30	W				
216	42	W				
231	57	N				
252	42	N				
160	72	W				
129	39	W				
34	53	W				
110	27	E				

Slip surfaces in localised fault zone

strike	dip	dip direction		strike	dip	dip direction
210	34	S				
133	9	W				
125	1	S				
125	6	S				
214	42	S				
210	28	N				
227	35	n				

LIVERPOOL
UNIVERSITY
LIBRARY

FOLD - OUT 2.1

Section 1 Folded Jurassic sediments in Quebrada Profeta. Scale 1:10 000.

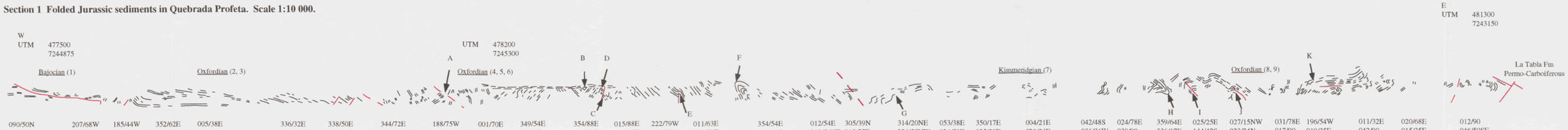

090/50N | 207/68W 191/48W 181/82W | 185/44W 193/77W 032/33SE | 352/62E 300/43N 004/07E 352/38E 024/24E 317/24NE | 005/38E 324/17NE 034/16E

336/32E 289/27N 145/10W 320/17NE | 338/50E 286/31N 004/43E 305/33NE 316/39NE | 344/72E 341/49E 329/22NE 346/60E 336/64E

188/75W 034/72E 353/39E 004/25E 359/48E fault 109/81N 001/26E 315/26N 215/42NW 220/87W | 001/70E 029/76E 025/90 008/79E 042/37SE 181/72W 003/56E 053/53E | 349/54E 357/7E 292/83S 175/86S 018/90

354/88E 176/80E 023/64E 322/28E 312/26N 003/15E 288/31E 224/50NW 198/80W 200/84W 017/82E Ax Tr: 28/172 | 015/88E 356/47E 262/52N 252/59N 219/59NW 208/52W 019/81E 352/36E 287/47N 174/88W 018/60E 017/82E 018/19E | 222/79W 236/75W 030/82E 034/90 011/63 227/64W 240/70W 241/70N 255/58N 278/52N 332/38NE 025/43E 024/87E | 011/63E 014/53E *340/34E* *27/145* *265/64N* *338/64NE* *4 from N* 025/90 020/68E 342/52E 237/47NW 233/57NW 358/81E 355/46E 011/90 193/71W 349/50E 233/40NW

354/54E 042/28E 354/42E 004/63E 005/52E 002/78E 040/72E 037/31E 234/56NW 307/32N 016/27E 345/47E 359/72E 009/59E *175/77W* *70 from S*

012/54E 190/21W | 305/39N 013/55E 009/42E 254/79W 235/55NW

314/20NE 226/55NW 315/42N 220/85W 040/48E 203/66E 320/29E

053/38E 024/50E 241/32NW 067/32SE 022/47E 299/23W 064/77W 003/19E 270/53N 043/90 045/43SE 334/86SE | 350/17E 025/29E

004/21E 020/34E 176/26W 050/90

042/48S 036/36W 031/90 024/90 | 024/78E 039/90 236/63NW 269/24N 249/56NW

359/64E 336/17E 250/26N 266/32N 318/18NE 263/56N 208/66NW | 025/25E 144/42S 329/42NE 290/14N 077/22S 136/32SW 314/40NE 201/58W 341/52E 359/64E 336/17E 250/24N 266/32N 202/57W | 027/15NW 023/24N 070/04N 206/82W 197/46W 217/28W 223/30W 036/27E 346/28E 014/36E 012/22E 036/57E 022/89W conj frac: 324/40E 219/84W | 031/78E 017/90

196/54W 019/35E 208/75W 023/61e 021/77e 033/73e 018/90

011/32E 042/90 227/32NW 203/25W 030/84E 012/52E

020/68E 015/35E 041/62E 026/90

012/90 046/50SE 032/61E

Age assignment along the section has combined recognition of key fossils, (pers. comm. G Chong, 1996, and Hillebrandt et al, 1992) and a comparison of lithologies with a regional stratigraphy as defined in Ardill, 1996, and Prinz et al, 1994.

(1) pers. comm G Chong (1996), lithology cf Prinz et al, 1994.
(2) Perisphinctes sp. Oxfordian (Chong, 1996, Hillebrandt, 1992)
(3) Bositra sp. Oxfordian
(4) Ostrea Commonly Oxfordian, not key fossil
(5) Perisphinctes sp. Oxfordian
(6) lithology cf. Ardill (1996) and Prinz et al (1994)
(7) Evaporites Kimmeridgian (Ardill, 1996, Prinz et al, 1994)
(8) Gregoryceras sp. Oxfordian (Chong, pers.comm, Giye and Hillebrandt, 1991).

Poles to bedding from whole section.

Poles to bedding from the whole Jurassic section in Q. Profeta give a common fold axis of 18/025.

Poles to bedding from individual small scale folds.

Poles to bedding from site A give a fold axis of 20/041 which lies within the observed axial plane of 022/49E.

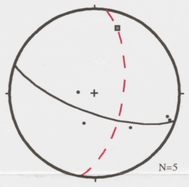

Poles to bedding from B have a fold axis of 19/020, which combined with the axial trace, 28/172, produces an axial plane of 009/61E.

Poles to bedding from site C produce a fold axis of 34/035.

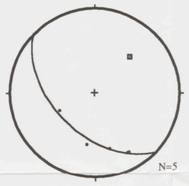

Poles to bedding from site D have a fold axis of 40/045.

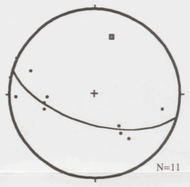

Poles to bedding from site E have a fold axis of 31/017.

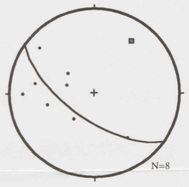

Poles to bedding from site F have a fold axis of 26/036.

Poles to disturbed evaporite bedding from site G have a fold axis of 09/053. Fracturing of the evaporites has occurred to accommodate the strain.

Poles to bedding at site H have a fold axis of 01/303.

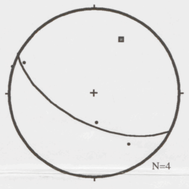

Poles to bedding at site I produce a fold axis of 30/027. The fault that cuts the core of the fold is not axial planar to the fold.

Poles to bedding from site J produce a fold axis of 04/018.

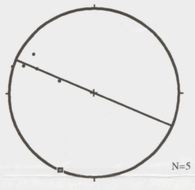

Poles to bedding from site K produce a fold axis of 00/203.

Section 3 Folded Jurassic sediments in Quebrada Las Mulas. Scale 1:10 000.

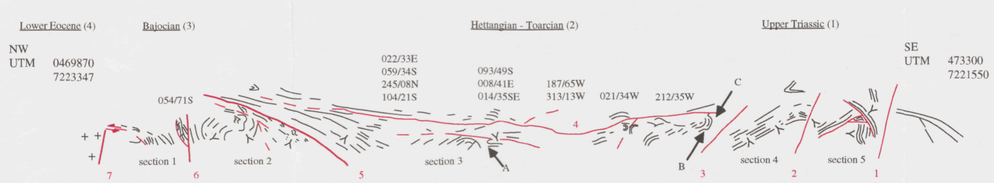

Bedding

158/24W | 047/23W 053/53S 061/76S 045/48S 100/82N | 020/59W 164/70W 149/60W 010/42E 015/64E 010/72W 006/70W | 129/40S 013/40E 207/85E 039/69SE 045/34SE 030/45SE 042/27S | 013/31E 083/29S 049/04E 159/81W 171/54W 008/37E 064/20S | 019/62SE 016/69NW 011/60NW 003/36NW 337/16W 146/15W AP 087/12S | 016/44E 038/70E 192/72W 181/63W 126/09S 016/40W 040/42W 023/40W 025/38W 017/16W | 203/79W 074/73S 237/90 225/62N 075/42S 075/47S 194/56W 059/80S 190/47W 205/25W 227/50W 066/17W 052/20W 042/40NW 093/26N | 036/34N 038/18N 051/40N 085/35N 097/28N Ax Tr 81/235 | 114/35S 28/226 115/42S 091/82N 083/72N 003/62W 044/65W

Veins | *277/69N 290/41E 84 from W* | *118/76N 65 from W* | *196/40W 85 from N* | *106/84N*

127/34S 141/21W 154/54E 063/82S

Source of age assignments:
(1,2) lithology cf Ardill (1996), Prinz et al (1994)
(3) Pers. comm. Chong (1996), lithology cf Ardill (1996)
(4) Ar dating Ch 4.2.

KEY

- Fault
- Inferred fault
- Bedding as seen in hillside
- Topography
- A → Site of detailed measurements (eg fold hinge)
- Ax Tr Axial Trace
- AP Axial Plane
- Y younging in direction of stalk.
- *italic* vein orientations.
- N/E no exposure.

Readings are placed near locations.

The best fit great circles of poles to bedding were generated by the computer, using Stereonet 4.9.6, Allmendinger, 1988. All stereo nets are equal area, axial planes are represented by red dashed great circles, profile planes are black great circles.

Poles to bedding from whole section.

Poles to bedding across whole section define a fold axis of 08/209.

Poles to bedding from fault bounded sections.

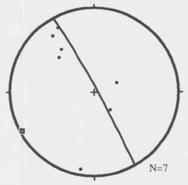

Poles to bedding from the westernmost fault bounded section, section 1, define a fold axis of 03/241.

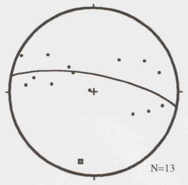

Poles to bedding from fault bound section 2 define a fold axis of 16/191.

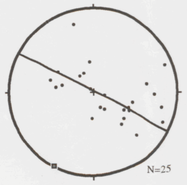

Poles to bedding from section 3 define a fold axis of 01/208.

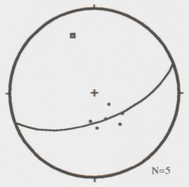

Poles to bedding from section 4 weakly define a fold axis; bedding is approximately planar, so no significance is attached to this result.

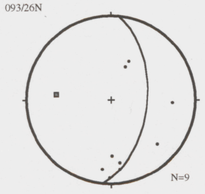

Poles to bedding in section 5 define a fold axis of 36/275. The units are cut by antithetic faults with differing strain axes, so no significance is attached to this result.

Poles to bedding from individual small scale folds.

Poles to bedding within the upper fault bounded unit produce a fold axis of 09/201.

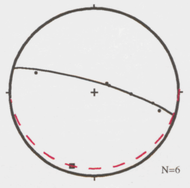

Poles to bedding from A define a fold axis of 10/197, which lies within the observed axial plane of 087/12S.

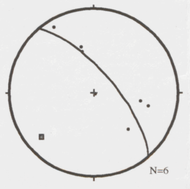

Poles to bedding from B define a fold axis of20/230.

Poles to bedding from C define a fold axis of 01/048.

Section 4 Folded Jurassic sediments at the western end of Quebrada Las Mulas. Scale 1:50 000

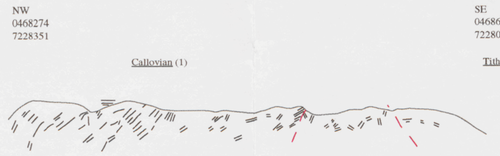

Source of age assignment:

(1) Reineckeia sp. Callovian Chong, pers. comm. 1996, Hillebrandt, 1992.

231/37 NW 232/30 N 222/70 N 214/33 NW | 327/75 N 010/90 349/71 E 341/45 E | 202/85 W 003/64 E 004/70 W 355/74 E | 327/55 NE 162/80 W 001/90 | 318/45 NE 011/57 E 206/28 N 240/42 N | 233/54 N | 211/17 N 183/70 W 020/85 W | 194/43 W

Poles to bedding define a common fold axis of 27/003

Section 2 Folded Jurassic in Quebrada del Viento. Scale 1:50 000.

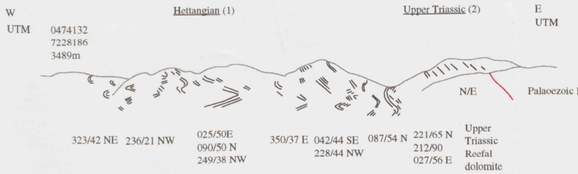

323/42 NE 236/21 NW | 025/50E 090/50 N 249/38 NW | 350/37 E 042/44 SE 228/44 NW | 087/54 N | 221/65 N 212/90 027/56 E

Upper Triassic Reefal dolomite expected to cut through here, if exposed.

Source of age assignments:

(1) lithology cf. Ardill (1996), Prinz et al (1994)
(2) *E. bidenta,* Choristoceras Rhaetian (Ardill, 1996, Chong, 1973, Hillebrandt, 1992)

Poles to bedding define a common fold axis of 24/040.

Poles to bedding from all of the Jurassic sections.

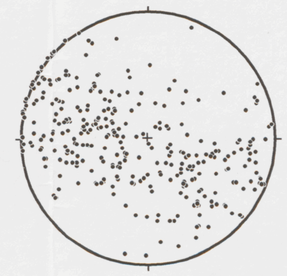

Poles to bedding from all of the Jurassic sections.

Fold out 2.2

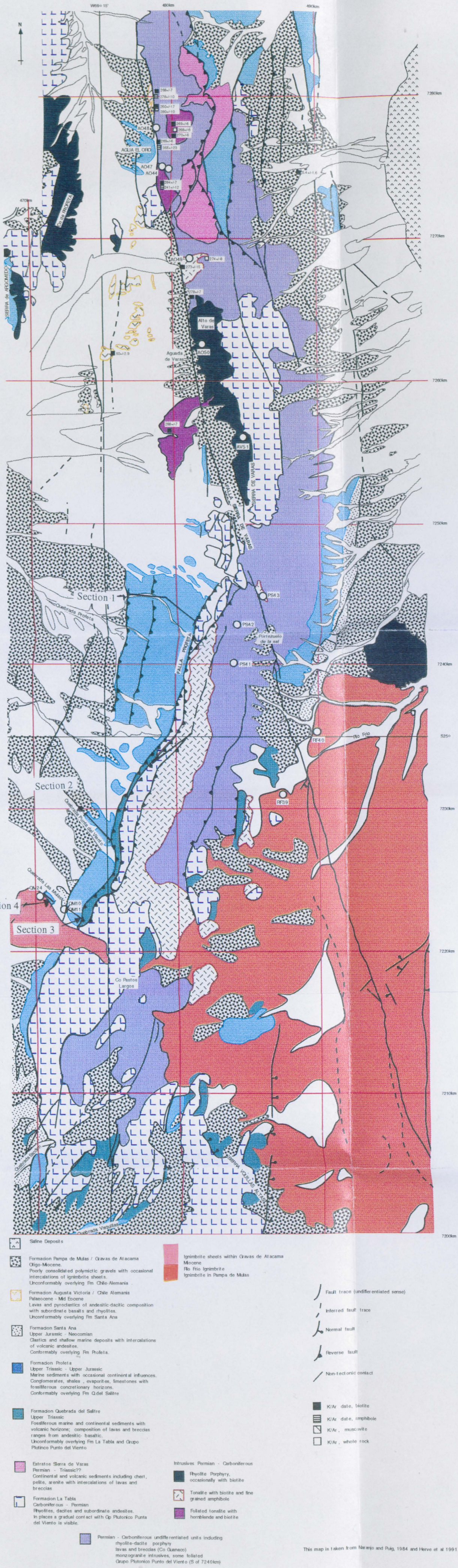

Saline Deposits

Formacion Pampa de Mulas / Gravas de Atacama
Oligo-Miocene.
Poorly consolidated polymictic gravels with occasional intercalations of ignimbrite sheets.
Unconformably overlying Fm Chile-Alemania .

Formacion Augusta Victoria / Chile Alemania
Palaeocene - Mid Eocene
Lavas and pyroclastics of andesitic-dacitic composition with subordinate basalts and rhyolites.
Unconformably overlying Fm Santa Ana

Formacion Santa Ana
Upper Jurassic - Neocomian
Clastics and shallow marine deposits with intercalations of volcanic andesites.
Conformably overlying Fm Profeta.

Formacion Profeta
Upper Triassic - Upper Jurassic
Marine sediments with occasional continental influences.
Conglomerates, shales , evaporites, limestones with fossiliferous concretionary horizons.
Conformably overlying Fm Q.del Salitre

Formacion Quebrada del Salitre
Upper Triassic
Fossiliferous marine and continental sediments with volcanic horizons; composition of lavas and breccias ranges from andesitic- basaltic.
Unconformably overlying Fm La Tabla and Grupo Plutinco Punto del Viento

Estratos Sierra de Varas
Permian - Triassic??
Continental and volcanic sediments including chert, pelite, arenite with intercalations of lavas and breccias

Formacion La Tabla
Carboniferous - Permian
Rhyolites, dacites and subordinate andesites.
In places a gradual contact with Gp Plutonico Punta del Viento is visible.

Ignimbrite sheets within Gravas de Atacama
Miocene
Rio Frio Ignimbrite
Ignimbrite in Pampa de Mulas

Intrusives Permian - Carboniferous

Rhyolite Porphyry, occasionally with biotite

Tonalite with biotite and fine grained amphibole

Foliated tonalite with hornblende and biotite

Permian - Carboniferous undifferentiated units including
rhyolite-dacite porphyry
lavas and breccias (Co Guanaco)
monzogranite intrusives, some foliated
Grupo Plutonico Punto del Viento (S of 7240km)

Fault trace (undifferentiated sense)

Inferred fault trace

Normal fault

Reverse fault

Non-tectonic contact

K/Ar date, biotite

K/Ar date, amphibole

K/Ar , muscovite

K/Ar , whole rock

This map is taken from Naranjo and Puig, 1984 and Herve et al 1991.

FOLD OUT 4.1 Slip surfaces mapped in detail from a normal fault along Q. Las Mulas

1

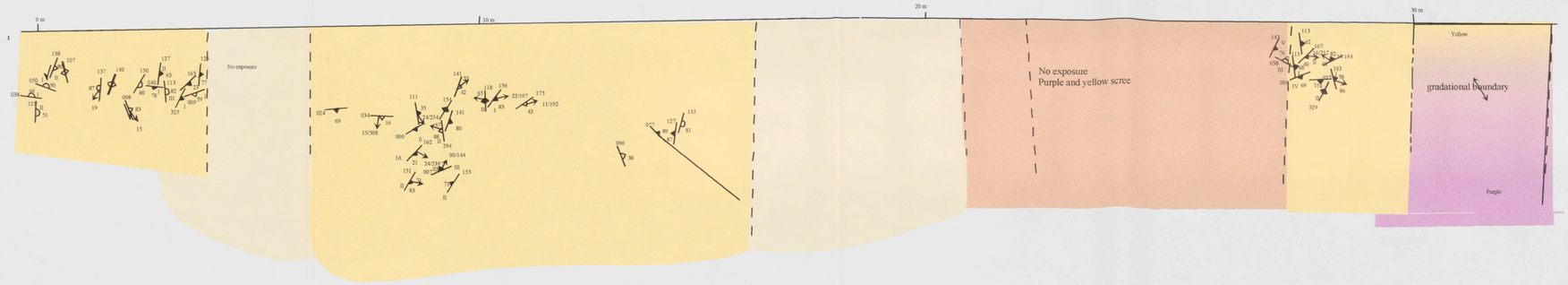

2

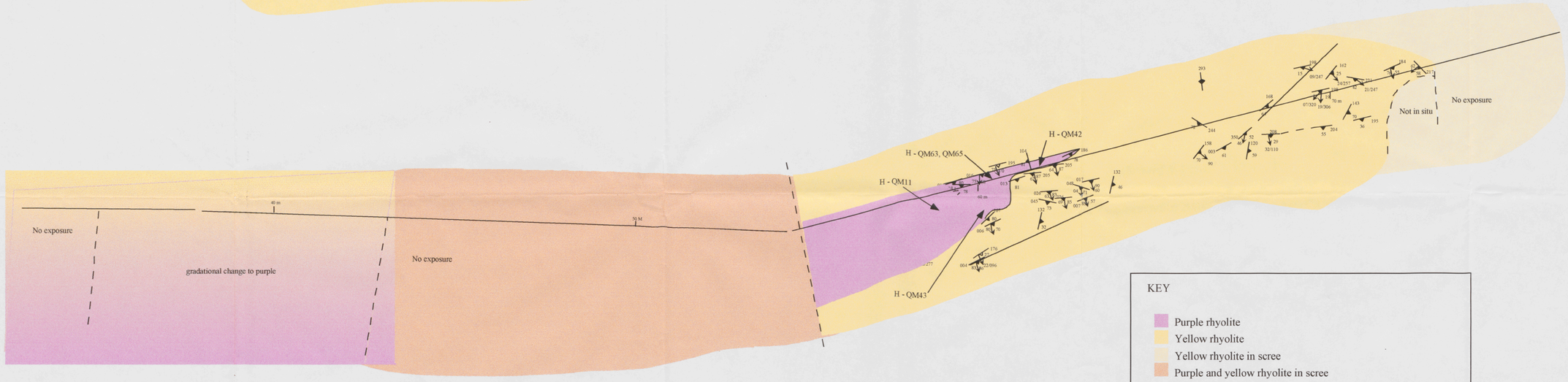

3

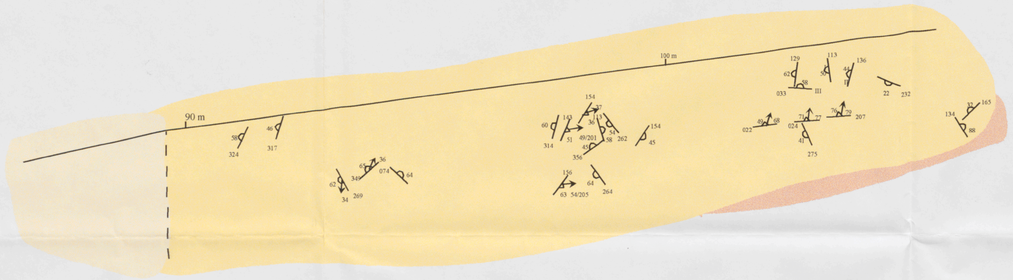

KEY

- Purple rhyolite
- Yellow rhyolite
- Yellow rhyolite in scree
- Purple and yellow rhyolite in scree
- Vein
- Slip surface with fine grained, dark fault rock
- Slip surface without negligible fault rock
- ↑ Lineation
- Line of tape measure
- H Hand sample

Strike, dip, pitch or lineation are written beside the relevant symbol. Each section follows on directly from the last. All the sections have the same North direction.

Neopolitan effects copyright McElderry 98

Copy of Figure 4.1.1 The rhyolite dyke mapped in fold out 4.1. The reference distances relate to the distances in the rest of the foldout. The tape measure used for mapping was parallel to the strike of the outcrop.
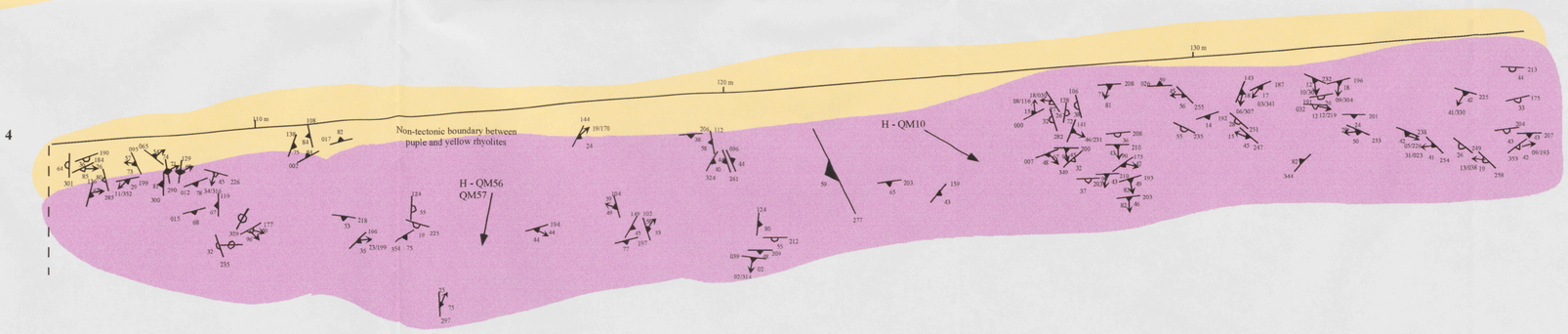
4